Measuring cross-section data for prompt gammas emitted during proton-nucleus collisions

Vijitha Ramanathan

Supervisor

Dr.Steve Peterson

Thesis Presented for the Degree of

DOCTOR OF PHILOSOPHY

in the Department of Physics

UNIVERSITY OF CAPE TOWN

January 2017

Abstract

In Radiation Oncology, proton therapy has become an increasingly popular treatment modality due to the superior dose distribution of the proton beam while sparing more surrounding normal healthy tissues and critical organs. This advantage can quickly turn into a disadvantage if there is any uncertainty in the delivery of the proton beam. To fully utilize the benefits of proton therapy, it is important to monitor the in-vivo dose deposition. Due to the fact that the treatment protons stop within the patient as they deliver the dose, secondary radiation is the potential method to obtain a dose verification measurement. The detection of secondary prompt gamma rays have been proposed as an in-situ method to determine the proton range since the location of the prompt gamma emission is strongly correlated with the proton depth dose profile. This correlation has been confirmed in both experimental measurements and in Monte Carlo simulations, but absolute prompt gamma productions have been unsuccessful, due to discrepancies the Monte Carlo prompt gamma production data particularly for the prominent elements found in tissue within the therapeutic range (50-200 MeV).

The goal of this work was to evaluate the prompt gamma production for both carbon and oxygen at energies relevant for proton therapy. The first part of this study was to experimentally measure the interaction cross section for proton-nucleus collisions in both carbon and oxygen. In order to determine these cross-sections, measurements using thin targets of natural Carbon and Mylar over the energy range of 66-125 MeV were performed using the AFRODITE detector system at iThemba LABS in Cape Town, South Africa. Energy and efficiency calibrations of the detection system were performed using three standard gamma emitting sources (^{137}Cs, ^{60}Co, and ^{152}Eu). The second part of this work was to model the AFRODITE detector system using the Geant4 Monte-Carlo radiation transport code in order to compare the simulated to the measured results and to evaluate the previously observed discrepancies for prompt gamma production in the Geant4 code.

In the experimental study, the standard gamma sources were used to obtain individual absolute efficiency response curves for each of the 30 high purity germanium crystals (2 crystals were not functioning). The differential cross section was calculated at five different energies (66, 80, 95, 110, 125 MeV) using three angles (90^0, 130^0 and 140^0) for the 4.438 MeV gamma peak using both the carbon and Mylar targets, and for the 6.129 MeV gamma peak using the Mylar target. The total cross-section for the 4.438 and 6.129 MeV peaks were calculated by fitting the angular measurements to a Legendre polynomial.

In the simulation study, the geometry of the AFRODITE detection system was carefully modelled to mimic the actual geometry by importing CAD models into the Geant4 code. The physics of the AFRODITE model was tested by comparison to the three standard gamma emitting sources, by testing the Compton suppression system and evaluating various hadronic physics processes. Once the model was validated, the experimental runs were simulated and the same procedures were followed in order to obtain absolute detector efficiency curves for the germanium crystals, as well as, differential cross-section data and total cross-section data for the 4.438 and 6.129 MeV gamma peaks.

The overall absolute gamma energy spectra from the experimental and simulation runs were compared and displayed excellent agreement for the total prompt gamma production values. Comparisons of the cross-section values for the individual peaks (4.438 and 6.129 MeV) produced mixed results. There was strong agreement (difference of 1.2% to 14.0%) for the total experimental cross-section results for the 4.438 MeV peak from the two targets (carbon and Mylar), providing internal validation for the experimental measurements. However, the total cross-section data for both peaks was slightly higher than the sparse previously available measured data points.

When comparing to the simulated results, the cross-section values for the individual peaks (4.438 and 6.129 MeV) did not agree quite as well. The simulated results for the total cross-section for the 4.438 MeV peak from the carbon target, the ^{12}C(p, p$'$)^{12}C* reaction, produced values 50% higher than the measured results. This over-estimation has been attributed to an unusually high number of ^{12}C(p, d)^{11}C* and ^{12}C(p, np)^{11}C* reactions

produced during the simulation. The total cross-section for the 4.438 MeV peak from the Mylar target, the ^{12}C(p, p$'$)^{12}C* reaction, also produced an over-estimation (32%) for the same reason; this result was also boosted by the ^{16}O(p, x)^{12}C* reactions that occur from the oxygen found in Mylar. The 6.129 MeV peak from the Mylar target, the ^{16}O(p, p$'$)^{16}O* reaction, was virtually non-existent in the simulations making it impossible to calculate a simulated total cross-section value.

Overall, the experimental measured data provided results that compare favourably to existing data. The available experimental data for the ^{12}C(p, p$'$)^{12}C* and ^{16}O(p, p$'$)^{16}O* reactions has been extended up to 125 MeV. The AFRODITE Geant4 model successfully re-produced the gamma spectra from the experimental runs and will be used again in further studies. As seen before, the Geant4 physics over-estimates (or neglects) the individual prompt gamma peaks. Further testing will be done to identify these errors and work to improve the Geant4 physics models.

Contents

1 Background **1**

1.1 Aim and outline of the study 1

1.2 Structure of the dissertation 2

1.3 Radiation oncology 2

1.4 Rationale for proton therapy 3

1.5 Physics of proton therapy 5

1.5.1 Stopping power 5

1.5.2 Multiple Coulomb scattering 7

1.5.3 Nuclear interactions 7

1.5.4 Prompt gamma production 7

1.6 Review of prompt gamma cross section measurements 8

1.6.1 Discrete gamma ray line from ^{12}C 8

1.6.2 Discrete gamma ray lines from ^{16}O 9

1.7 Introduction to reaction cross section 13

1.8 Range uncertainty in proton therapy 15

1.9 Range verification techniques for proton therapy 16

1.9.1 In-patient point dose measurement 16

1.9.2 Range probe 17

1.9.3 Positron emission tomography (PET) imaging 18

1.9.4 Prompt gamma imaging 18

1.10 Prompt gamma imaging and Monte-Carlo simulations 22
1.10.1 Challenges of prompt gamma imaging 25
1.11 Motivation 27

2 GEANT4 model of the AFRODITE detector system 29
2.1 Geant4 toolkit 29
2.2 Geometry in Geant4 29
2.3 Physics in Geant4 30
2.3.1 Nuclear collisions 31
2.3.2 Electro-magnetic interactions 31
2.3.3 Nuclear models 32
2.4 iThemba Laboratory for Accelerator-Based Sciences (iThemba LABS) . . . 34
2.4.1 AFRODITE array 35
2.4.2 Clover detectors and detection modes 37
2.4.3 Compton escape suppression 39
2.5 Geometry of Geant4 AFRODITE model 40

3 Measurement of prompt gamma cross-section using AFRODITE clover detectors 44
3.1 Experimental cross section measurement 44
3.1.1 Detector arrangement and target setup 45
3.1.2 Proton irradiations 49
3.2 Acquisition of experimental cross-section data 49
3.2.1 Digital Data Acquisition System (DDAS) 49
3.2.2 Experimental data processing 51
3.2.3 Dead time and background subtraction 51
3.3 Procedures for experimental cross-section measurements 53
3.3.1 Energy calibration procedures 53
3.3.2 Detection efficiency 53

3.3.3 Calculating the total cross-section 54
3.3.4 Calculating the differential cross section 56
3.3.5 Uncertainty propagation for differential cross section 56
3.3.6 Uncertainty propagation for total cross section 58

4 Measurement of prompt gamma cross section using Geant4 AFRODITE model 60

4.1 Performance of Compton-suppression detector 60
4.2 Validation of Geant4 AFRODITE model 62
4.3 Simulated absolute detector efficiency 63
4.3.1 Calculating simulated detector efficiency 63
4.4 Calculating simulated differential Cross-section 64
4.5 Target thickness optimization for simulation 65
4.6 Simulation of prompt gamma production cross-section 68
4.6.1 Comparison of physics list 69
4.6.2 Full AFRODITE simulations 69

5 Results from experimental prompt gamma cross-section measurements 72

5.1 Energy calibration 72
5.2 Absolute Detection efficiency 77
5.3 Calculating prompt gamma cross section from experimental data 83
5.3.1 Experimental prompt gamma spectra 84
5.3.2 Differential cross section 87
5.3.3 Angular distribution of 4.438 MeV 91
5.3.4 Angular distribution of 6.129 MeV 95
5.3.5 Total cross-section measurement 97

6 Results from prompt gamma cross-section measurements 99

6.1 Performance of the simulated Compton suppression 99
6.2 Validation of Geant4 AFRODITE model 102

6.3 Absolute detector efficiency for simulation 104
6.4 Calculating prompt gamma cross section from simulated data 107
6.4.1 Simulated prompt gamma spectra 107
6.4.2 Investigation into Geant4 Physics 109
6.4.3 Calculating simulated differential cross-section 115
6.4.4 Angular distribution of 4.438 MeV in Geant4 simulation 117
6.4.5 Total cross-section measurement in Geant4 simulation 120

7 Comparison of experimental and simulated results 122
7.1 Prompt gamma spectra from carbon target 122
7.1.1 Comparison of simulated and experimental 4.438 MeV photo peak from ^{12}C 124
7.2 Prompt gamma spectra from mylar target 126
7.2.1 Comparison of simulated and experimental 4.438 MeV photo peak from Mylar target 127
7.3 Comparison of experimental and simulated total cross section results . . . 131
7.3.1 Experimental and simulated cross-section comparison for the 4.438 MeV photo peak 131
7.3.2 Experimental and published cross-section comparison for the 6.129 MeV photo peak 134

8 Conclusion 136

Bibliography 148

Appendix:

A Geant4 Electromagnetic processes 150
A.0.3 Photoelectric effect 150
A.0.4 Compton scattering 151

A.0.5 Gamma conversion 152
A.0.6 Ionization 154
A.0.7 Bremsstrahlung 155
A.0.8 Positron-electron annihilation 156

B Experimental results **157**
B.1 Energy calibration results 157
B.2 Experimental absolute detector efficiency results 160

List of Figures

1.1 Depth dose profile of a single Bragg peak (gray line), a spread out Bragg peak (solid black line) and 10 MV X-ray beam (dashed black line). Source: Yock and Tarbell (2004) 3

1.2 Dose conformity comparison with photon and proton beams for boost radiation to the posterior fossa of medulloblastoma radiotherapy. As depicted by arrows, the proton beam is able to spare the cochlea better than either techniques of photons. Source: Yock and Tarbell (2004) 4

1.3 Radiation dose distribution to the spine and other anterior structure using photons and protons for medulloblastoma whole spine irradiation. The color-wash dose clearly shows difference between photon and proton dose distribution. Source: Yock and Tarbell (2004) 4

1.4 Depth dose profile for a 250 MeV proton beam, showing the characteristic Bragg peak. Source: Paganetti and Bortfeld (2005) 6

1.5 The energy level diagram for ^{12}C nucleus with its excited states. Source: Aubrecht (2003) 8

1.6 Available experimental cross-section data for the ^{12}C 4.438 MeV peak. This figure shows the gaps in the cross-section data in the range 50 - 90 MeV and there is no data beyond 90 MeV. 9

1.7 The energy level diagram for the ^{16}O nucleus with its excited states. Left side axis shows energies in keV and right side axis shows angular momentum and parity. Source: Galt.J.C (2005) 10

1.8 Available experimental cross-section data for the ^{16}O 6.129 MeV photo peak. This figure shows the gaps in the cross-section data in the range 50 - 90 MeV and there is no data beyond 90 MeV. 11

1.9 Comparison of the potential depth dose difference resulting from a 1.0 cm water equivalent depth (WED) variation for a 10 MV photon beam and a proton spread out Bragg peak delivery, producing a 3% or 90% dose difference in photon and proton beam deliveries, respectively. Source: Lu (2007) 16

1.10 Model for range probe measurement setup. Source: Mumot et al. (2010) . 18

1.11 Correlation between proton dose distribution measured by ionization chamber (IC) and measured prompt gammas using a prompt gamma scanning system (PGS) in a water phantom at proton energies at 100, 150, and 200 MeV. Source: Min.C et al. (2006) 19

1.12 Right panel: Three stage Compton camera setup which illustrates prompt gamma production during proton beam irradiation in a tissue phantom. The prompt gamma interacts with the three stage Compton camera. The energy deposition due to the interaction of the photon with each detector and the interaction positions are also shown. Left panel: Parallel plane geometry of the Compton camera where θ_1 and θ_2 are the Compton scatter angles and E_0, E_1, and E_2 are the gamma ray energies as the gamma ray traverses through the detectors D_1, D_2, and D_2. The projected cone is then used to reconstruct the images. Source: Peterson et al. (2010) 20

1.13 Arrangement of double scattering Compton camera. Source: Richard et al. (2011) 21

1.14 Knife edge slit camera. Source: Smeets et al. (2012) 22

1.15 Left: experimental setup for prompt gamma measurement modeled in Geant4 Monte-Carlo code. Right: Experimentally measured prompt gamma spectra (black circle from lucite phantom and gray squares from bone equivalent plastic) have been compared with Geant4 Monte-Carlo simulation (red line from lucite and blue line from bone equivalent plastic phantom). Source: Polf et al. (2009) 23
1.16 Geometry of simulated setup including a 160 MeV incident proton beam on the PMMA ($C_5O_2H_8$) target, detector at 50 cm, and the lead collimator in between the target and collimator. All distances are in cm. Source: Smeets et al. (2012) 23
1.17 Simulated and measured prompt gamma spectra for a 160 MeV proton beam at 50 cm distance for different collimator positions as shown in the figures. Source: Smeets et al. (2012) 24
1.18 Left: Schematic diagram of experimental setup modeled in Geant4. Right: prompt gamma spectra comparison for a 200 MeV proton beam using water phantom. Source: Jeyasugiththan (2014) 24
1.19 Left: γ-ray production cross section for ^{12}C 4.438 MeV photo peak using total inelastic cross-section data from Wellisch and Axen. Right: γ-ray production cross section for ^{12}C 4.438 MeV photo peak using total inelastic cross-section data from Tripathi. Source: Jeyasugiththan and Peterson (2015) 26

2.1 Schematic diagrams of currently available CAD import methods in Geant4 geometry. CAD interface indicates CADMesh in this figure. Source: Poole et al. (2012) 30
2.2 Geant4 hadronic models. Source: G4HadModels (2015) 30

2.3 Schematic diagram of cascade modelling sequence. Upper left: hadron incident upon target nucleus. Upper right: development of cascade process and secondary nucleons leaving the nucleus. Lower left: higher energy hadrons leaving the nucleus and creating highly excited particle hole state. Lower right: evaporation process of de-excited nucleus. 33
2.4 Layout of the iThemba LABS facilities. TR is proton therapy, TC is neutron therapy, TL is proton therapy beam line 2(unfinished), SSC is the cyclotron, and AFRODITE vault is for AFRODITE detector system. 35
2.5 A segment of the AFRODITE array showing the rhombicuboctahedron shaped target chamber 36
2.6 The AFRODITE array, the eight clover detectors, the target chamber, and the beam line. This figure shows the detector frame when the fixed clover detectors are moved apart in order to place the target inside the target chamber. 36
2.7 Schematic diagram of four high purity germanium crystals in a clover detector. Source: Jones.P.M et al. (1995) 38
2.8 Left: Individual high purity germanium crystal. Right: Closely packed four high purity germanium crystals in a clover detector. Source: Duchene.G et al. (1999) 38
2.9 Top panal: Schematic diagram of clover with BGO Compton suppression shield (yellow) connected to liquid nitrogen dewar. Bottom left: The cross section view of germanium crystals and BGO. Bottom right: Closely packed germanium crystals. Source: Szücs et al. (2010) 39
2.10 Left hand side: BGO Compton suppression shield. Right hand side: Clover detector. Source: Duchene.G et al. (1999) 40
2.11 Geant4 model of the closely packed germanium crystals in an AFRODITE clover. 41
2.12 Geant4 model of the germanium crystal assembly inside the aluminium case. 41

2.13 Geant4 model of the Compton escape suppression shielding in the AFRODITE detector system. 42
2.14 Geant4 model of the closely packed germanium crystals housed inside the Compton escape shielding. 42
2.15 Complete simulated clover detector setup identical to experimental arrangement of AFRODITE array. 43

3.1 AFRODITE clover detector arrangement for the cross-section measurement experiment. Clovers were placed at the following positions: C_1, C_5, C_6, C_7 at 135^0. C_2, C_3, C_4, C_8 at 90^0. 45
3.2 This figure shows the prepared mylar (in the middle) and carbon (on the right) targets at iThemba LABS for cross-section measurement. 46
3.3 The target ladder in which four targets can be accommodated. The one on the left is the ruby which is used for beam focusing. 47
3.4 The rhombicuboctahedron shaped target chamber which is supported by the beam line, and the target ladder fixed to the top of the target chamber. . . 47
3.5 The control panel for changing the targets and the beam current measurement is located in the data room 48
3.6 The experimental setup of AFRODITE array with the clover detectors in final measurement position. 48
3.7 System control. Left panel: The base frame window. Right panel: The experiment control window. The system can be operated using STOP and GO button. This procedure is only required when changing the parameters or setting up the system. Source: iThemba LABS (2016) 50
3.8 The digital data acquisition set up window which shows different parameters that can be adjusted to optimize the resolution of the system. Source: iThemba LABS (2016) 50
3.9 The flow diagram of SimSort code. Source: Papka.P (2007) 51
3.10 Dead time correction in percentage as a function of beam current. 52

4.1 Clover detectors setup for testing Compton shield with no Compton shield and an isotropic gamma source. 61
4.2 Clover detectors setup for testing Compton shield with Compton shield and an isotropic gamma source. 62
4.3 Prompt gamma spectrum for a 66 MeV proton bombardment on a 0.5 mm ^{12}C target. Inset: Gaussian peak fit for the 4.438 MeV photo peak using the OriginPro data analysis program. 66
4.4 Simulated cross-section values versus thicknesses for 66, 80, 95, 110, and 125 MeV proton bombardments on a ^{12}C target. 67
4.5 Simulated cross-section values versus thicknesses for a 66 MeV proton bombardment on a ^{12}C target. Inset: Zoomed picture of the experimental (0.04 mm) and the simulated (0.5 mm) target thicknesses. 67
4.6 Geometry setup of the AFRODITE model for prompt gamma production with the incident proton entering as a pencil beam and interacting with the target. Track colours: blue - proton, green - gamma, and red - electron . . 70

5.1 Identified photo peak in the ^{137}Cs spectrum from crystal A in clover 1. There were a total of 32 spectra for each calibration source. 73
5.2 Identified photo peaks in the ^{60}Co spectrum from crystal A in clover 1. . . 73
5.3 Identified photo peaks in the ^{152}Eu spectrum from crystal A in clover 1. . . 74
5.4 Peak fitting using OriginPro to find centroid of ^{137}Cs 662 keV photo peak in the spectrum from high purity germanium crystal A in clover 1. 76
5.5 Peak fitting using OriginPro to find centroid of ^{60}Co 1173 keV and 1332 keV photo peaks in the spectrum from high purity germanium crystal A in clover 1. 76
5.6 The energy calibration curve for crystal A in clover 1. 77
5.7 Absolute detection efficiency for the four high purity germanium crystals in clover 1. 78

5.8 The absolute detector efficiency difference between the experimental results and the simulated results for high purity germanium crystal A in clover 1. This figure shows that the Geant4 model of the AFRODITE detector had a higher efficiency than the actual AFRODITE detector system. 79
5.9 The absolute efficiency response curve for crystal A in a clover 1. The red triangle points are experimentally measured absolute detector efficiencies, the blue hollow circle points and green star points are simulated efficiencies using single-energy gamma sources and standard gamma emitting sources, respectively. Solid line is the third-order exponential fit. 81
5.10 The absolute efficiency response curve for crystal B in a clover 1. The red triangle points are experimentally measured absolute detector efficiencies, the blue hollow circle points and green star points are simulated efficiencies using single-energy gamma sources and standard gamma emitting sources, respectively. Solid line is the third-order exponential fit. 82
5.11 The absolute efficiency response curve for crystal C in a clover 1. The red triangle points are experimentally measured absolute detector efficiencies, the blue hollow circle points and green star points are simulated efficiencies using single-energy gamma sources and standard gamma emitting sources, respectively. Solid line is the third-order exponential fit. 82
5.12 The absolute efficiency response curve for crystal D in a clover 1. The red triangle points are experimentally measured absolute detector efficiencies, the blue hollow circle points and green star points are simulated efficiencies using single-energy gamma sources and standard gamma emitting sources, respectively. Solid line is the third-order exponential fit. 83
5.13 The red line shows the raw data for the 95 MeV proton bombardment of the carbon target, cyan color line is room background, the blue line indicates the background radiation from the frame with the beam on, and the gray line shows the background from the target frame with the beam off. These spectra were measured by the clovers placed at 90 degrees to the beam line. 84

5.14 The red line shows the raw data for the 95 MeV proton bombardment of the mylar target, cyan color line is the room background, the blue line indicates the background radiation from the frame with the beam on, and the gray line shows the background from the target frame with the beam off. These spectra were measured by the clovers placed at 90 degrees to the beam line 85
5.15 Prompt gamma spectrum for the 95 MeV proton collision with the carbon target measured by the clovers placed at 90 degrees to the beam direction. PP: Photo peak, SE: Single escape peak, and DE: Double escape peak. . . 86
5.16 Prompt gamma spectrum for the 95 MeV proton collision with the mylar target measured by the clovers placed at 90 degrees to the beam direction. PP: Photo peak, SE: Single escape peak, and DE: Double escape peak. . . 86
5.17 The 4.438 MeV photo peak with manually added spectrum background line (black line) for the 95 MeV proton collisions on the carbon target for one of the high purity germanium crystals at 90^0 (a) - crystal A in clover 3, 130^0 (b) - crystal A in clover 1, and 140^0 (c) - crystal C in clover 1. 87
5.18 The 6.129 MeV photo peak with spectrum background subtraction for the 95 MeV proton collisions on Mylar target in a crystal C of clover 3 located at 90^0. 88
5.19 The 6.129 MeV photo peak with the spectrum background subtraction for the 95 MeV proton collisions on Mylar target in a crystal B of a clover 6 located at 130^0. 89
5.20 The 6.129 MeV photo peak with the spectrum background subtraction for the 95 MeV proton collisions on Mylar target in a crystal C of clover 6 located at 140^0. 89
5.21 Angular distribution for the ^{12}C 4.438 MeV gamma-ray line at 66 (a), 80 (b), 95 (c), 110 (d), 125 (e) MeV proton energies. The solid lines are the fitted curves from the 4^{th} order Legendre polynomial python fit. The circle indicates the measured angular dependence term (differential cross section) with associated uncertainty. 92

5.22 Angular distribution for the mylar 4.438 MeV gamma-ray line at 66 (a), 80 (b), 95 (c), 110 (d), 125 (e) MeV proton energies. The solid lines are the fitted curves from the 4^{th} order Legendre polynomial python fit. The circle indicates the measured angular dependence term (differential cross section) with associated uncertainty. 94
5.23 Angular distribution for the ^{16}O 6.129 MeV (Mylar) gamma-ray line at 66 (a), 80 (b), 95 (c), 110 (d), 125 (e) MeV proton energies. The solid lines are the fitted curves from the 6^{th} order Legendre polynomial python fit. The blue circle indicates the measured angular dependence term (differential cross section) with associated uncertainty and red hollow circle indicates the virtual points. 96
5.24 Experimental cross-section results for the 4.438 MeV gamma-ray line from ^{12}C and mylar targets 97
5.25 Experimental cross-section results for the 6.129 MeV gamma-ray line from ^{16}O (Mylar) 98

6.1 Spectra from the ^{137}Cs gamma source with Compton suppression and without Compton suppression in six different modes: crystal-green line, suppressed crystal-dark blue line, clover-blue line, suppressed clover-pink line, detector system (all clovers)-black line, and suppressed detector system-orange line. About 45% suppression was observed. 100
6.2 Spectra from ^{60}Co gamma source with Compton suppression and with no Compton suppression for entire AFRODITE detector system. Black line - No Compton suppressed spectrum. Red line - Compton suppressed spectrum. 101
6.3 Spectra from ^{152}Eu gamma source with Compton suppression and with no Compton suppression for entire AFRODITE detector system. Black line - No Compton suppressed spectrum. Red line - Compton suppressed spectrum. 101

6.4 Comparison of the simulated and experimental gamma spectra from ^{137}Cs for the AFRODITE clover detector system. The green line shows the simulated spectrum and red line shows the experimental spectrum. Normalization was done according to the number of gammas emitted by the source in the experiment and number of gamma histories in the simulation. 102
6.5 Comparison of the simulated and experimental gamma spectra from ^{60}Co for the AFRODITE clover detector system. The green line shows the simulated spectrum and red line shows the experimental spectrum. Normalization was done according to the number of gammas emitted by the source in the experiment and number of gamma histories in the simulation. 103
6.6 Comparison of the simulated and experimental gamma spectra from ^{152}Eu for the AFRODITE clover detector system. The green line shows the simulated spectrum and red line shows the experimental spectrum. Normalization was done according to the number of gammas emitted by the source in the experiment and number of gamma histories in the simulation. 103
6.7 Fitted Gaussian photo peak (red line) to find area under the 662 keV peak from ^{137}Cs for germanium crystal A of clover 1. 104
6.8 Fitted Gaussian photo peaks to find area under the 1173 keV and 1332 keV peaks from ^{60}Co for germanium crystal A of clover 1. Horizontal green and red lines are the background. 105
6.9 Fitted Gaussian photo peaks to find area under the 779 keV and 867 keV peaks from ^{152}Eu for germanium crystal A of clover 1. Horizontal green and red lines are the background. 105
6.10 Absolute detector efficiency response curve for germanium crystal A of clover 1. The green points are the simulated efficiencies for the standard gamma emitting sources and the blue color points are the efficiencies for the single-energy gamma sources. 106

6.11 Simulated prompt gamma spectra from a 80 MeV proton collision with the carbon target. The blue line is the 90^0 spectrum and the black line is the 130^0 spectrum. The gap between two spectra shows a higher gamma production in crystals placed at 130^0 than at 90^0 108
6.12 Simulated prompt gamma spectra from a 80 MeV proton collision with the mylar target. The blue line is the 90^0 spectrum and the black line is the 130^0 spectrum. 108
6.13 Prompt gamma spectrum comparison for binary cascade with two different inelastic cross-section data set (Geisha and Tripathi). 110
6.14 Binary cascade prompt gamma spectrum comparison against the precompound model using the Tripathi and Geisha cross-section data set. 110
6.15 Binary cascade prompt gamma spectrum comparison against the precompound model with modified number of exciton as 1 using the Tripathi and Geisha cross-section data set. 111
6.16 Prompt gamma spectrum with Doppler broadening ignored for the precompound model using the Geisha inelastic cross-section data set with the carbon target and 80 MeV incident proton. Note the sharp increase in the 4.438 MeV peak when the exciton number is changed to 1. 112
6.17 Prompt gamma spectra comparison for mylar target using different physics lists with available cross-section data set and modified and default exciton number. 113
6.18 Prompt gamma spectrum with Doppler broadening ignored for the precompound model using the Tripathi inelastic cross-section data set with the Mylar target. 113
6.19 Prompt gamma spectra comparison for the mylar target using different physics lists with the latest version of Geant4 (10.3) 114

6.20 4.438 MeV photo peak with a manually added background line (red line) for the 95 MeV proton collision with the Carbon target for germanium crystals placed at 90^0, germanium crystals placed at 130^0, and germanium crystals placed at 140^0 respectively. 115
6.21 6.129 MeV photo peak with a manually added background line (red line) for the 95 MeV proton collision with the Carbon target for germanium crystals placed at 90^0, germanium crystals placed at 130^0, and germanium crystals placed at 140^0 respectively. 116
6.22 Angular distribution for the simulated ^{12}C 4.438 MeV gamma-ray line at 66 (a), 80 (b), 95 (c), 110 (d), 125 (e) MeV proton energies. The solid line are the fitted curve according to the 4^{th} order Legendre polynomial using python. The circle are the differential cross section values with their associated uncertainty. 118
6.23 Angular distribution for the simulated mylar 4.438 MeV gamma-ray line at 66 (a), 80 (b), 95 (c), 110 (d), 125 (e) MeV proton energies. The solid line are the fitted curve according to the 4^{th} order Legendre polynomial using python. The circle are the differential cross section values with their associated uncertainty. 119
6.24 Simulated cross-section results for the 4.438 MeV gamma-ray line for ^{12}C and mylar targets 121

7.1 Prompt gamma spectra comparison of the experimental and simulated results for a 95 MeV proton collision on the carbon target. The red line shows the corrected Geant4 simulated spectrum and the black line shows the experimental spectrum. Inset: Enlarged view of the 4.438 MeV gamma peak. 123
7.2 Simulated and experimental 4.438 MeV photo peak comparison for a 95 MeV proton collision on the Carbon target at 90^o, 130^o, and 140^o clovers, respectively. The simulated spectra was not corrected for absolute comparison in this figure in order to better see the shape of the two spectra. 125

7.3 Prompt gamma spectra comparison of the experimental and simulated results for a 95 MeV proton collision on the mylar target. The red line shows the corrected Geant4 simulated spectrum and the black line shows the experimental spectrum. Inset: Enlarged view of the 4.438 MeV gamma peak. 127
7.4 Simulated and experimental 4.438 MeV photo peak comparison for a 95 MeV proton collision on the Mylar target at 90°, 130°, and 140° clovers, respectively. The simulated spectra was not corrected for absolute comparison in this figure in order to better see the shape of the two spectra. 128
7.5 Experimental 4.438 MeV photo peak comparison for a 95 MeV proton collision on the Carbon and Mylar targets at 90°, 130°, and 140° clovers, respectively. The spectra were intentionally shifted in order to better see the shape of the two spectra. 129
7.6 Simulated 4.438 MeV photo peak comparison for a 95 MeV proton collision on the Carbon and Mylar targets at 90°, 130°, and 140° clovers, respectively. The spectra were intentionally shifted in order to better see the shape of the two spectra. 130
7.7 Comparison of experimental total cross-section results against simulated results for 4.438 MeV gamma from carbon and mylar targets. 133
7.8 Comparison of measured and simulated total cross-section values for the 4.438 MeV photo peak with available experimental cross-section data. . . . 134
7.9 Comparison of measured total cross-section values for the 6.129 MeV photo peak from ^{16}O with available experimental cross-section data. 135

B.1 The absolute efficiency response curve for crystal A in a clover 2. The red triangle points are experimentally measured absolute detector efficiencies the blue hollow circle points and green star points are simulated efficiencies using single-energy gamma sources and standard gamma emitting sources, respectively. Solid line is the third-order exponential fit. 160

B.2 The absolute efficiency response curve for crystal B in a clover 2. The red triangle points are experimentally measured absolute detector efficiencies the blue hollow circle points and green star points are simulated efficiencies using single-energy gamma sources and standard gamma emitting sources, respectively. Solid line is the third-order exponential fit. 160
B.3 The absolute efficiency response curve for crystal C in a clover 2. The red triangle points are experimentally measured absolute detector efficiencies the blue hollow circle points and green star points are simulated efficiencies using single-energy gamma sources and standard gamma emitting sources, respectively. Solid line is the third-order exponential fit. 161
B.4 The absolute efficiency response curve for crystal D in a clover 2. The red triangle points are experimentally measured absolute detector efficiencies the blue hollow circle points and green star points are simulated efficiencies using single-energy gamma sources and standard gamma emitting sources, respectively. Solid line is the third-order exponential fit. 161
B.5 The absolute efficiency response curve for crystal A in a clover 3. The red triangle points are experimentally measured absolute detector efficiencies the blue hollow circle points and green star points are simulated efficiencies using single-energy gamma sources and standard gamma emitting sources, respectively. Solid line is the third-order exponential fit. 162
B.6 The absolute efficiency response curve for crystal C in a clover 3. The red triangle points are experimentally measured absolute detector efficiencies the blue hollow circle points and green star points are simulated efficiencies using single-energy gamma sources and standard gamma emitting sources, respectively. Solid line is the third-order exponential fit. 162

B.7 The absolute efficiency response curve for crystal D in a clover 3. The red triangle points are experimentally measured absolute detector efficiencies the blue hollow circle points and green star points are simulated efficiencies using single-energy gamma sources and standard gamma emitting sources, respectively. Solid line is the third-order exponential fit. 163
B.8 The absolute efficiency response curve for crystal A in a clover 4. The red triangle points are experimentally measured absolute detector efficiencies the blue hollow circle points and green star points are simulated efficiencies using single-energy gamma sources and standard gamma emitting sources, respectively. Solid line is the third-order exponential fit. 163
B.9 The absolute efficiency response curve for crystal B in a clover 4. The red triangle points are experimentally measured absolute detector efficiencies the blue hollow circle points and green star points are simulated efficiencies using single-energy gamma sources and standard gamma emitting sources, respectively. Solid line is the third-order exponential fit. 164
B.10 The absolute efficiency response curve for crystal C in a clover 4. The red triangle points are experimentally measured absolute detector efficiencies the blue hollow circle points and green star points are simulated efficiencies using single-energy gamma sources and standard gamma emitting sources, respectively. Solid line is the third-order exponential fit. 164
B.11 The absolute efficiency response curve for crystal D in a clover 4. The red triangle points are experimentally measured absolute detector efficiencies the blue hollow circle points and green star points are simulated efficiencies using single-energy gamma sources and standard gamma emitting sources, respectively. Solid line is the third-order exponential fit. 165

B.12 The absolute efficiency response curve for crystal A in a clover 5. The red triangle points are experimentally measured absolute detector efficiencies the blue hollow circle points and green star points are simulated efficiencies using single-energy gamma sources and standard gamma emitting sources, respectively. Solid line is the third-order exponential fit. 165
B.13 The absolute efficiency response curve for crystal B in a clover 5. The red triangle points are experimentally measured absolute detector efficiencies the blue hollow circle points and green star points are simulated efficiencies using single-energy gamma sources and standard gamma emitting sources, respectively. Solid line is the third-order exponential fit. 166
B.14 The absolute efficiency response curve for crystal C in a clover 5. The red triangle points are experimentally measured absolute detector efficiencies the blue hollow circle points and green star points are simulated efficiencies using single-energy gamma sources and standard gamma emitting sources, respectively. Solid line is the third-order exponential fit. 166
B.15 The absolute efficiency response curve for crystal D in a clover 5. The red triangle points are experimentally measured absolute detector efficiencies the blue hollow circle points and green star points are simulated efficiencies using single-energy gamma sources and standard gamma emitting sources, respectively. Solid line is the third-order exponential fit. 167
B.16 The absolute efficiency response curve for crystal B in a clover 6. The red triangle points are experimentally measured absolute detector efficiencies the blue hollow circle points and green star points are simulated efficiencies using single-energy gamma sources and standard gamma emitting sources, respectively. Solid line is the third-order exponential fit. 167

B.17 The absolute efficiency response curve for crystal C in a clover 6. The red triangle points are experimentally measured absolute detector efficiencies the blue hollow circle points and green star points are simulated efficiencies using single-energy gamma sources and standard gamma emitting sources, respectively. Solid line is the third-order exponential fit. 168
B.18 The absolute efficiency response curve for crystal D in a clover 6. The red triangle points are experimentally measured absolute detector efficiencies the blue hollow circle points and green star points are simulated efficiencies using single-energy gamma sources and standard gamma emitting sources, respectively. Solid line is the third-order exponential fit. 168
B.19 The absolute efficiency response curve for crystal A in a clover 7. The red triangle points are experimentally measured absolute detector efficiencies the blue hollow circle points and green star points are simulated efficiencies using single-energy gamma sources and standard gamma emitting sources, respectively. Solid line is the third-order exponential fit. 169
B.20 The absolute efficiency response curve for crystal B in a clover 7. The red triangle points are experimentally measured absolute detector efficiencies the blue hollow circle points and green star points are simulated efficiencies using single-energy gamma sources and standard gamma emitting sources, respectively. Solid line is the third-order exponential fit. 169
B.21 The absolute efficiency response curve for crystal C in a clover 7. The red triangle points are experimentally measured absolute detector efficiencies the blue hollow circle points and green star points are simulated efficiencies using single-energy gamma sources and standard gamma emitting sources, respectively. Solid line is the third-order exponential fit. 170

B.22 The absolute efficiency response curve for crystal D in a clover 7. The red triangle points are experimentally measured absolute detector efficiencies the blue hollow circle points and green star points are simulated efficiencies using single-energy gamma sources and standard gamma emitting sources, respectively. Solid line is the third-order exponential fit. 170
B.23 The absolute efficiency response curve for crystal A in a clover 8. The red triangle points are experimentally measured absolute detector efficiencies the blue hollow circle points and green star points are simulated efficiencies using single-energy gamma sources and standard gamma emitting sources, respectively. Solid line is the third-order exponential fit. 171
B.24 The absolute efficiency response curve for crystal B in a clover 8. The red triangle points are experimentally measured absolute detector efficiencies the blue hollow circle points and green star points are simulated efficiencies using single-energy gamma sources and standard gamma emitting sources, respectively. Solid line is the third-order exponential fit. 171
B.25 The absolute efficiency response curve for crystal C in a clover 8. The red triangle points are experimentally measured absolute detector efficiencies the blue hollow circle points and green star points are simulated efficiencies using single-energy gamma sources and standard gamma emitting sources, respectively. Solid line is the third-order exponential fit. 172
B.26 The absolute efficiency response curve for crystal D in a clover 8. The red triangle points are experimentally measured absolute detector efficiencies the blue hollow circle points and green star points are simulated efficiencies using single-energy gamma sources and standard gamma emitting sources, respectively. Solid line is the third-order exponential fit. 172

List of Tables

1.1 Gamma ray lines in proton induced reactions on ^{12}C and ^{16}O. Source: Kozlovsky et al. (2002) 12

1.2 γ-ray selection rules and multi-polarities 15

2.1 Specifications of AFRODITE clover detectors. Source: Newman.R.T et al. (1995). 37

4.1 Calculated cross-section values using actual target thickness (0.042 mm) and simulated target thickness (0.5 mm) and percent difference. σ_{ATT}: cross-section value for actual target thickness. σ_{STT}: cross-section value for simulated target thickness 68

5.1 The standard decay data for the three calibration sources. Source: IAEA (2016) 75

5.2 Experimental absolute efficiencies and associated uncertainties for high purity germanium crystal A in clover 1. 79

5.3 The correction factors for each high purity germanium crystal used to fit the efficiency response curves. Here, C - Clover, HpGe - High purity germanium crystal 80

5.4 Details of the functional fitting for the absolute efficiency response curve for crystal A in clover 1. 81

5.5 Average differential cross-section values for 4.438 MeV carbon target 90

5.6 Average differential cross-section values for 4.438 MeV mylar target 90

5.7 Average differential cross-section values for 6.129 MeV mylar target 90
5.8 Obtained Legendre coefficients during the angular distribution fit using python for the 4.438 MeV ^{12}C gamma 91
5.9 Obtained Legendre coefficients during the angular distribution fit using python for the 4.438 MeV gamma from the mylar target 93
5.10 Obtained Legendre coefficients during the angular distribution fit using python for the 6.129 MeV ^{16}O gamma 95
5.11 Experimental cross-section results for the 4.438 MeV gamma-ray line from ^{12}C and mylar targets 97
5.12 Experimental cross-section results for the 6.129 MeV gamma-ray line from ^{16}O (Mylar) 98

6.1 Fitting details for the absolute detector efficiency response curve for germanium crystal A in clover 1 of the Geant4 model of the AFRODITE detector. 106
6.2 Average differential cross-section values for 4.438 MeV carbon target 116
6.3 Average differential cross-section values for 4.438 MeV mylar target 117
6.4 Legendre coefficients from the angular distribution fit using python for the simulated 4.438 MeV gamma from the carbon target 120
6.5 Legendre coefficients from the angular distribution fit using python for the simulated 4.438 MeV gamma from the mylar target 120
6.6 Simulated cross-section results for the 4.438 MeV gamma-ray line for ^{12}C and mylar targets 120

7.1 Comparison of experimental total cross-section (σ) results against simulated results for 4.438 MeV gamma-ray line for ^{12}C 132
7.2 Comparison of experimental total cross-section results against simulated results for 4.438 MeV gamma-ray line for mylar target 132

B.1 The energy calibration curve details for each high purity germanium crystals for first four clover detectors 158

B.2 The energy calibration curve details for each high purity germanium crystals for remaining four clover detectors 159
B.3 Absolute detector efficiency for the 4.438 MeV energy for each high purity germanium crystals with associated uncertainty 173
B.4 Absolute detector efficiency for the 6.129 MeV energy for each high purity germanium crystals with associated uncertainty 174
B.5 Measured differential cross-section values(4.438 MeV) for each high purity germanium crystals for the 66 MeV proton collision on natural carbon target 175
B.6 Measured differential cross-section values(4.438 MeV) for each high purity germanium crystals for the 80 MeV proton collision on natural carbon target 176
B.7 Measured differential cross-section values(4.438 MeV) for each high purity germanium crystals for the 95 MeV proton collision on natural carbon target 177
B.8 Measured differential cross-section values(4.438 MeV) for each high purity germanium crystals for the 110 MeV proton collision on natural carbon target178
B.9 Measured differential cross-section values(4.438 MeV) for each high purity germanium crystals for the 125 MeV proton collision on natural carbon target179
B.10 Measured differential cross-section values(4.438 MeV) for each high purity germanium crystals for the 66 MeV proton collision on mylar target 180
B.11 Measured differential cross-section values(4.438 MeV) for each high purity germanium crystals for the 80 MeV proton collision on mylar target 181
B.12 Measured differential cross-section values(4.438 MeV) for each high purity germanium crystals for the 95 MeV proton collision on mylar target 182
B.13 Measured differential cross-section values(4.438 MeV) for each high purity germanium crystals for the 110 MeV proton collision on mylar target . . . 183
B.14 Measured differential cross-section values(4.438 MeV) for each high purity germanium crystals for the 125 MeV proton collision on mylar target . . . 184
B.15 Measured differential cross-section values(6.129 MeV) for each high purity germanium crystals for the 66 MeV proton collision on mylar target 185

B.16 Measured differential cross-section values(6.129 MeV) for each high purity germanium crystals for the 80 MeV proton collision on mylar target 186
B.17 Measured differential cross-section values(6.129 MeV) for each high purity germanium crystals for the 95 MeV proton collision on mylar target 187
B.18 Measured differential cross-section values(6.129 MeV) for each high purity germanium crystals for the 110 MeV proton collision on mylar target . . . 188
B.19 Measured differential cross-section values(6.129 MeV) for each high purity germanium crystals for the 125 MeV proton collision on mylar target . . . 189

Acknowledgements

First and foremost, I would like to express my sincere gratitude to my supervisor Dr.Steve Peterson of the Department of Physics, University of Cape Town for giving me the opportunity to work under his supervision. Without his thoughtful guidance, support and encouragement my PhD dissertation would not have been possible to accomplish.

I am also indebted to my friends Dr.T.Pathmathas and Dr.J.Jeyasugiththan for introducing me to Steve to get this wonderful opportunity and their help.

I take this opportunity to sincerely acknowledge Dr.Elena Lawrie for her assistance regarding the AFRODITE experiment at iThemba LABS. I expand my thanks to the collaborators (Prof. Saad Ouichaoui et al.) from Université des Sciences et de la Technologie H.Boumediéne (USHB), Faculté de Physique, Laboratoire des Sciences nucléaires, Algeria and the collaborators (Dr. Jurgen Kiener et al.) from Centre de Spectrométrie Nucléaire et de spectrométrie de Masse (CSNSM), CNRS-IN2P3 et Université Paris-Sud , 91405 Orsay Campus, France. Specially, I would like to thank Walid Yahia-cherif for his help in the cross section measurement experiments.

I gratefully acknowledge Prof.Paul Papka of the Department of Physics, University of stellenbosch for his SimSort code to unpack the bulk of experimental data and his assistance.

I would also like to extend my sincere thanks to Kevin Li, University of stellenbosch for his AFRODITE basic code.

My sincere thanks also goes to Centre for High Performance Computing (CHPC), 15 Lower Hope Rd, Rosebank, Cape Town for providing me their clusters for my simulations. I would also like to thank UCT ICTS for giving me the access to HPC cluster.

I am grateful for the award of Science Faculty PhD fellowships for 2014-2016.

It is my pleasure to thank Prof.Andy Buffler, Head of the Department and other academic staffs, all postgraduate students and administrative staffs of the Physics Department, University of Cape Town for being just wonderful environment for my research work. I really

appreciate excellent UCT library services also.

Words are short to express my gratitude towards my friend, Claire Van Den Berg for her help in using Origin data analysis program and her moral support.

My special thanks to my sisters Rathy and Nisha, and my brothers Sri and Sarathy for their love and continuous support.

Last but not least, I would like to express a deep sense of gratitude to my parents for their love, encouragement, moral support and blessings.

A timely favour, however trivial

its material value is, is invaluable

-Thiruvalluvar

Part I
Introduction

Chapter 1

Background

1.1 Aim and outline of the study

Over the last few decades remarkable progress has been made in radiotherapy treatment modalities towards effectively delivering the radiation dose to the planning target volume (PTV) while increasing the survival rates and reducing the side effects for cancer patients. However, there are still plenty of improvements that can be done in the fields of photon and, more particularly, particle radiotherapy (proton therapy and carbon ion therapy). Specifically, the range verification of a proton beam during treatment delivery is a challenging task since the treatment protons stop within the patient. Therefore, the potential method to verify the range of the protons is by measuring the secondary gammas during the treatment. Proton range verification using prompt gamma imaging is the basis for this work.

The aim of this study is to compare the measured prompt gamma cross-section against simulated cross-section data for the elements of carbon and oxygen, two of the most prominent elements found in the human body. One aspect of this work was to model the AFRODITE detector system using the Geant4 Monte-Carlo particle transport code (version 10.01.p03) to evaluate the simulated prompt gamma cross-section data. A second aspect was to experimentally measure the prompt gamma cross-sections for carbon and oxygen using thin targets of natural carbon and mylar (^{12}C, ^{16}O). The cross-section measurement experiment was conducted at iThemba LABS in Cape Town, South Africa.

1.2 Structure of the dissertation

This dissertation is divided into three main parts. The first part (Chapter 1) includes the introduction which describes the background information for this study including rationale for using proton therapy, physics of proton therapy, possible uncertainties during a proton radiotherapy treatment, previous research works related to range verification in proton radiation therapy and literature review for experimental prompt gamma cross section measurements of proton collisions on ^{12}C and ^{16}O. The introduction concludes with a motivation for this study.

The second part describes the materials and methodology for this work and is composed of three chapters (2, 3, and 4). Chapter 2 presents the Geant4 model of the AFRODITE detector system including a brief introduction of the Geant4 Monte-Carlo toolkit, Geant4 physics models and processes, and the AFRODITE detector system. Experimental methods for the prompt gamma cross-section measurements are reported in Chapter 3 and simulation procedures for the cross-section measurements are explained in Chapter 4.

Part 3 comprises of the results and discussion. The results of the experimental cross section measurements are described in chapter 5. Chapter 6 describes the results of the prompt gamma cross-section measurements using the Geant4 model of AFRODITE detector system. In chapter 7, a comparison of the experimental and simulated results are discussed. Finally, conclusions and future work are included in chapter 8.

1.3 Radiation oncology

Cancer is one of the leading causes of death worldwide among men and women. According to the World Health Organization [WHO (2015)], 8.2 million deaths and 14 million new cases were reported in 2012. Treatment of cancer can comprise of several modalities such as surgery, radiation therapy, chemotherapy, hormonal therapy and immunotherapy. About two-thirds of cancer patients receive radiotherapy during the course of their treatment. The radiation can be either an electromagnetic radiation (X-rays, gamma rays) or corpuscular radiation (electron, proton, carbon ion, etc.), which damages DNA to eradicate cancer cells by energy absorption through the processes of ionization and excitation of the atoms and molecules in the living tissue [Jayaraman and Lanzl (2011)]. Radiation can be administered as external beam radiation (EBRT) or internally via Brachytherapy. The radiation dose can be used as neoadjuvant treatment (pre-operative therapy) to shrink the tumour before surgery and/or adjuvant therapy to treat tumour after surgery. It can also be used in palliative care to control the pain in cancer patients. One major drawback to using radiotherapy is that healthy tissue can also be affected during the radiation treatment. Therefore, the foremost goal of radiation therapy is the precise targeting of the tumour volume with minimal exposure to the surrounding normal healthy tissue.

1.4 Rationale for proton therapy

In practice, there are many sophisticated radiotherapy treatment options using conventional X-ray based photons such as Image guided radiotherapy (IGRT), Intensity modulated radiation therapy (IMRT), three dimensional conformal radiation therapy (3DCRT), Volumetric modulated arc therapy (VMAT), Tomotherapy, etc.. However, proton therapy has become an increasingly popular treatment modality due to the superior dose distribution from a proton beam. In 1946, Robert R Wilson proposed that energetic protons could be used for therapeutic purposes [Wilson (1946)] and the first patient was treated with protons at Berkeley Radiation Laboratory, University of California in 1954. Proton therapy takes advantage of the steep dose fall-off at the end of the range of the protons in tissue, resulting in a significant reduction in the dose to the organ at risk and precise dose conformity while increasing tumor control probability. Conversely, the conventional X-ray based radiation treatment loses its effective dose within the first few centimeters of tissue and continues damaging healthy cells even beyond the target as shown in figure 1.1.

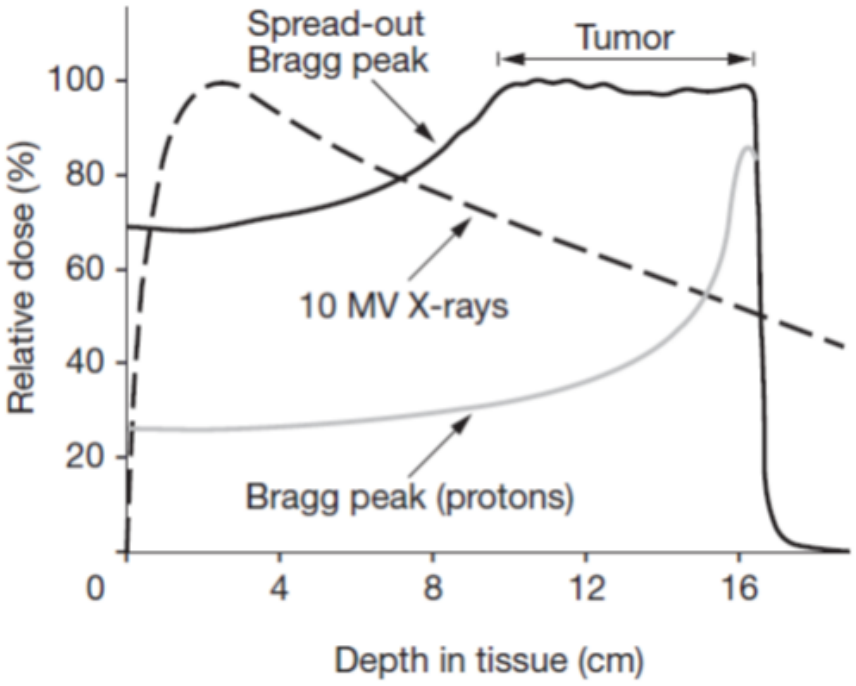

Figure 1.1: Depth dose profile of a single Bragg peak (gray line), a spread out Bragg peak (solid black line) and 10 MV X-ray beam (dashed black line). Source: Yock and Tarbell (2004)

To understand the advantage of proton therapy over traditional photon therapy, it is useful to consider a radiotherapy treatment plan. For example, for the treatment of medulloblastoma (the most common malignant pediatric brain tumour), radiation is delivered to the entire Craniospinal axis while sparing the cochlea, pituitary gland and hypothalamus. The

differences in the dose conformity using conventional X-ray based photon therapy and proton therapy are shown in figures 1.2 and 1.3. Due to the nature of the steep dose fall off for the proton beam, a significant dose reduction to the normal surrounding healthy tissue and critical organs can be seen. As shown in figure 1.2, the proton beam is able to spare the cochlea compared to other techniques such as three dimensional X-rays and intensity modulated radiotherapy (IMRT).

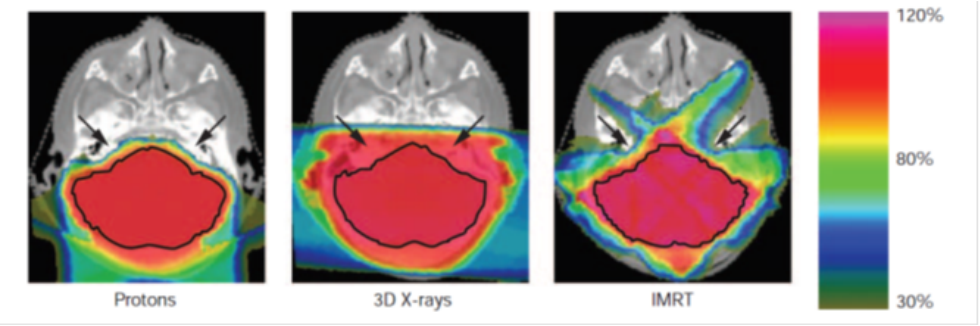

Figure 1.2: Dose conformity comparison with photon and proton beams for boost radiation to the posterior fossa of medulloblastoma radiotherapy. As depicted by arrows, the proton beam is able to spare the cochlea better than either techniques of photons. Source: Yock and Tarbell (2004)

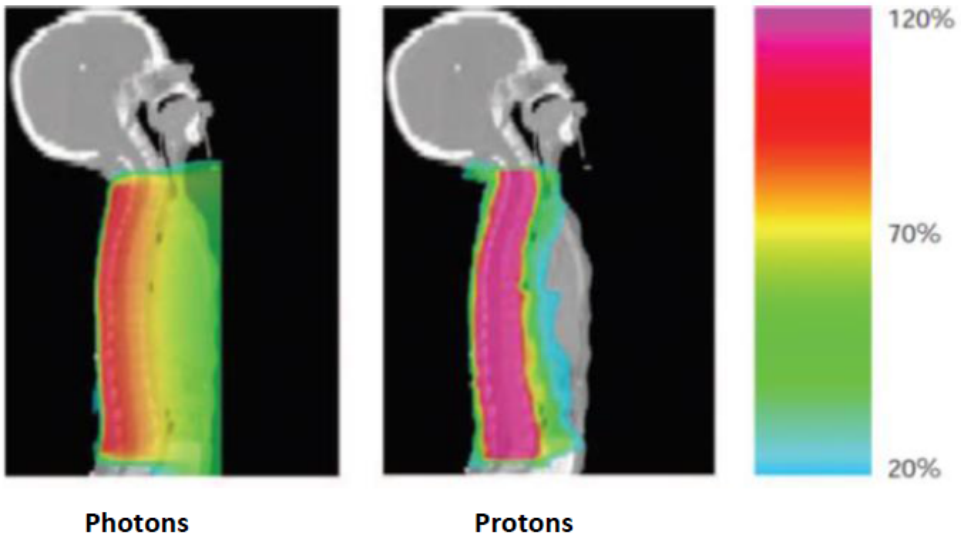

Figure 1.3: Radiation dose distribution to the spine and other anterior structure using photons and protons for medulloblastoma whole spine irradiation. The color-wash dose clearly shows difference between photon and proton dose distribution. Source: Yock and Tarbell (2004)

1.5 Physics of proton therapy

1.5.1 Stopping power

When a proton passes through matter, it will primarily lose energy through electromagnetic Coulomb interactions with the outer-shell electrons of the target material. The energy loss rate of ions (linear stopping power) is defined as dE/dX, where dE is the mean energy loss and dX is the distance. The stopping power of high velocity light ions in matter assumes two simplifications. The first assumption is that the ion is much faster than the target electrons and the second is that the ion is much heavier than the electrons [Ziegler.J.F (1999)].

The mass collision stopping power is given by the Bethe-Bloch equation [ICRU (1993)],

$$\frac{S_{col}}{\rho} = -\frac{1}{\rho}\left(\frac{dE}{dX}\right)_{el} = \frac{4\pi^2 r_e^2 m_e c^2}{\beta^2}\frac{1}{u}\frac{Z}{A}L(\beta)\, z^2 \qquad \frac{MeV}{g/cm^2} \tag{1.1}$$

where, ρ is the mass density of the material, $r_e = e^2/m_e c^2$ is the classical electron radius, $m_e c^2$ is the rest mass energy of the electron, β is the projectile velocity in units of light speed ($\beta = v/c$), u is the atomic mass unit, Z and A are the atomic number and atomic weight of the target material and z is the charge of the incident particle. The quantity $L(\beta)$ is defined as the stopping number and the expansion of $L(\beta)$ includes the corrections to the basic energy loss process of two particles which is given by,

$$L = L_0(\beta) + zL_1(\beta) + z^2 L_2(\beta), \tag{1.2}$$

where

$$L_0(\beta) = \frac{1}{2} ln\left(\frac{2m_e c^2 \beta^2 W_m}{1-\beta^2}\right) - \beta^2 - ln(I) - \frac{C}{Z} - \frac{\delta}{2}, \tag{1.3}$$

and C and δ are the shell and density corrections and I is the mean excitation energy of the absorbing material. L_1 and L_2 are called the Barkas and Bloch corrections respectively. The shell correction (C) is only applicable for low energies where the incident particle velocity is close to the velocity of the atomic electrons. The density correction (δ) arises from the shielding of distance electrons by near electrons and resulting in a reduction of energy loss at higher energies [Newhauser and Zhang (2014)]. Thus, these corrections (shell, density, Barkas and Bloch) can be neglected in the therapeutic proton ranges [Gottschalk (2004)]. Therefore, equation 1.1 can be re-written for the therapeutic energy range as follows [Paganetti (2012)],

$$\frac{S_{col}}{\rho} = 0.3072 \frac{Z}{A} \frac{1}{\beta^2} \left(ln \frac{W_m}{I} - \beta^2 \right) \qquad \frac{MeV}{g/cm^2} \tag{1.4}$$

where

$$W_m = \frac{2 m_e c^2 \beta^2}{1 - \beta^2}. \tag{1.5}$$

From equation 1.4, the energy loss of the projectile is inversely proportional to the square of its velocity ($\frac{S_{col}}{\rho} \propto \frac{1}{v^2}$). Therefore, when the proton slows down the probability of ionization and excitation events increases. At the end of the proton range, the rate of the energy loss of the proton becomes very high due to the low velocity. Ultimately, the proton loses all of its remaining energy and resulting in a dose peak known as the Bragg peak. Figure 1.4 shows a Bragg peak for 250 MeV protons.

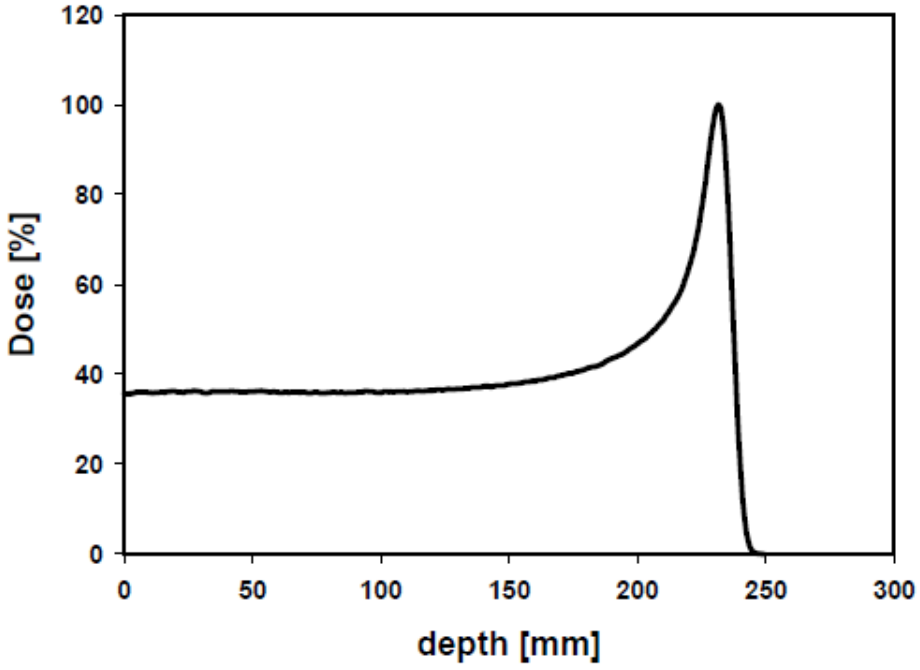

Figure 1.4: Depth dose profile for a 250 MeV proton beam, showing the characteristic Bragg peak. Source: Paganetti and Bortfeld (2005)

1.5.2 Multiple Coulomb scattering

Protons are also scattered laterally in addition to the energy loss. The first process for proton deflection is due to Coulomb interactions with electrons, which can be largely ignored since the protons are 1836 times heavier than the electrons. The more significant process is the proton deflection by the atomic nuclei caused by the electrostatic force between the positive charges of the atomic nucleus and of the proton. This effect is known as multiple Coulomb scattering (MCS), which contributes an approximately 2% widening of the proton beam at the Bragg peak in water [Goitein (2008)].

1.5.3 Nuclear interactions

In addition to the above mentioned processes, protons can also interact with the target nucleus by the strong interaction force. These interactions are generally divided into two processes namely, elastic and inelastic interactions. In an elastic interaction, the projectile is scattered off and the target nucleus is left intact while the total kinetic energy is conserved. During an inelastic scattering process, the characteristics of the target nuclei are changed upon absorption of the incident particle while the total kinetic energy is not conserved. Further, in an inelastic reaction, the target nucleus could be split up or excited to a higher energy state [Alburger.D.E et al. (2012) and Newhauser and Zhang (2014)].

1.5.4 Prompt gamma production

Nuclear gamma ray emissions take place during the de-excitation of the nucleus which means the excited nucleus emits gamma rays when it transitions to a lower or a ground state of the nucleus. The energy of the emitted gamma rays is equal to the energy difference between the two nuclear states involved in the transition. This process is analogous to the emission of characteristic X-rays at the atomic level [S.Krane (1987)]. During a proton-nucleus inelastic collision, the target nucleus may transition to an excited state due to the transfer of energy from the incident proton to the target nucleus. This process causes one or more nucleons to enter an excited state. The resulting de-excitation happens in less than a nano-second. Therefore, this process is known as prompt gamma emission. The energy of emitted gamma ray emission is dependent on the target material and energy of the incident proton. Due to these characteristics, the instant emission of prompt gammas and the well known emitted gamma ray energy for particular elements (carbon and oxygen are prominent elements in human tissue), measuring prompt gammas has been suggested as a potential method to verify the proton range in proton therapy. In addition, the distribution of prompt gamma emission has been correlated against the proton depth dose profile [Min.C et al. (2006), Polf.J.C et al. (2009a)]. More details of prompt gamma imaging is discussed in section 1.9.4.

1.6 Review of prompt gamma cross section measurements

A literature review yielded a number of gamma ray cross-section studies that have been performed experimentally for proton-nucleus collisions on ^{12}C and ^{16}O specifically for the astronomical environment. A brief overview of the experimental prompt gamma cross section measurements for ^{12}C and ^{16}O is given in the following sections.

1.6.1 Discrete gamma ray line from ^{12}C

The gamma ray line emission at 4.438 MeV is produced by de-excitation of the first excited state (2^+) of ^{12}C. This reaction is written as ^{12}C (p, p$'\gamma^{4.44MeV}$) ^{12}C. Experimentally, the measured peak for this gamma ray line includes the ^{12}C (p, 2p) ^{11}B$^{*4.445}$ reaction since these two line cannot be separated due to Doppler broadening. Doppler broadening is the widening of the spectral lines due to the Doppler shift caused by the random motions of atoms and molecules [Kutner (2003)]. The gamma emission mechanism is described in table 1.1. Other possible excited states of ^{12}C are shown in figure 1.5.

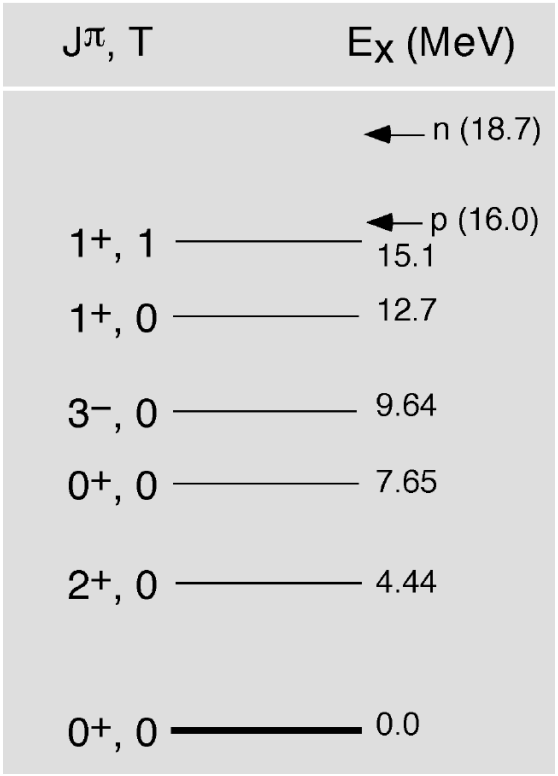

Figure 1.5: The energy level diagram for ^{12}C nucleus with its excited states. Source: Aubrecht (2003)

The cross-section for the 4.438 MeV gamma ray line production in proton induced reactions has been measured from threshold (least energy value that produced nuclear reaction) to 23 MeV by Dyer et al. (1981). Lang et al. (1987) studied the reactions at 40, 65, and 85 MeV proton energies. Lesko et al. (1988) measured this cross-section in the range of 8 MeV-50 MeV proton energies and Kiener et al. (1998) performed measurements in the range of 8.4 MeV to 20 MeV proton energies. Belhout et al. (2007) measured the 4.438 MeV from threshold to 25 MeV protons. Figure 1.6 shows the available experimental cross-section data for ^{12}C 4.438 MeV peak.

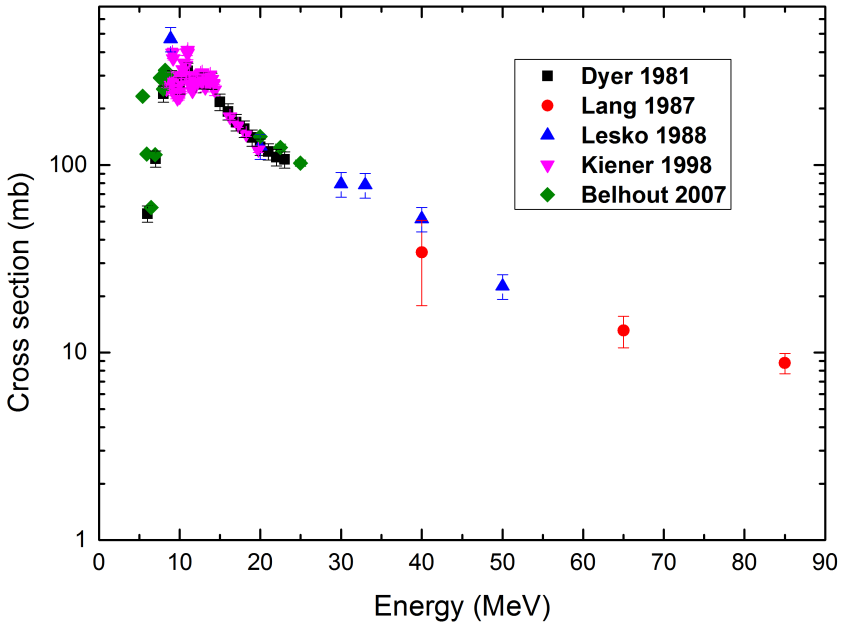

Figure 1.6: Available experimental cross-section data for the ^{12}C 4.438 MeV peak. This figure shows the gaps in the cross-section data in the range 50 - 90 MeV and there is no data beyond 90 MeV.

1.6.2 Discrete gamma ray lines from ^{16}O

Nuclear excitation of ^{16}O creates several γ- ray lines. The important reactions of ^{16}O are ^{16}O(p, p$'\gamma^{2.74MeV}$)^{16}O, ^{16}O(p, p$'\gamma^{6.13MeV}$)^{16}O, ^{16}O(p, p$'\gamma^{6.92MeV}$)^{16}O, and ^{16}O(p, p$'\gamma^{7.12MeV}$)^{16}O. The corresponding emission mechanisms are shown in table 1.1. The first excited state of ^{16}O at 6.049 MeV decays by electron and positron pair emission. The second excited state of ^{16}O at 6.130 MeV(3^-) de-excites to the ground state producing γ - rays at 6.129 MeV. The third and fourth excited states are 2^+ (6.917 MeV) and 1^- (7.117 MeV) respectively. The fifth excited state of ^{16}O at 8.872 MeV decays 75% to the 6.130 MeV level and produces γ-ray lines at 2.741 and 6.129 MeV [Ramaty (1977)]. The energy level diagram for ^{16}O is shown in figure 1.7.

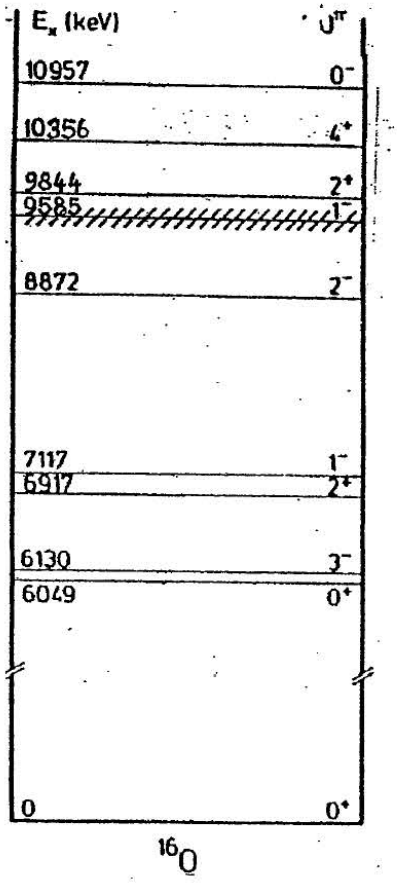

Figure 1.7: The energy level diagram for the ^{16}O nucleus with its excited states. Left side axis shows energies in keV and right side axis shows angular momentum and parity. Source: Galt.J.C (2005)

The prompt gamma cross section studies for 6.129 MeV ^{16}O have been studied by Dyer et al. (1981) from threshold to 23 MeV proton energies. Narayanaswamy et al. (1981) measured this cross-section at 23.7 and 44.6 MeV proton energies. Lang et al. (1987) studied this cross-section at 40, 65, 85 MeV proton energies. Lesko et al. (1988) measured this cross-section in the range of 8 MeV - 50 MeV proton energies and Kiener et al. (1998) from 8.4 MeV to 20 MeV. Belhout et al. (2007) measured up to a proton energy of 25 MeV. Figure 1.8 shows the available experimental cross-section data for the ^{16}O 6.129 MeV peak.

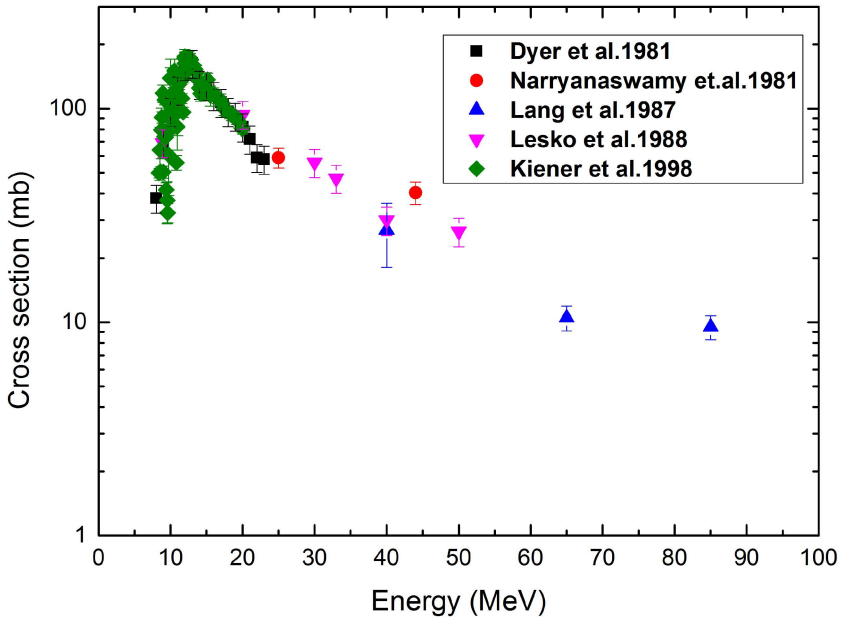

Figure 1.8: Available experimental cross-section data for the ^{16}O 6.129 MeV photo peak. This figure shows the gaps in the cross-section data in the range 50 - 90 MeV and there is no data beyond 90 MeV.

Table 1.1: Gamma ray lines in proton induced reactions on ^{12}C and ^{16}O. Source: Kozlovsky et al. (2002)

Energy (MeV)	Transition	Reaction	Mean Life (Sec)
0.718	$^{10}B^{*0.718} \rightarrow$ g.s	$^{12}C(p,x)^{10}B^*$	1.0×10^{-9}
		$^{12}(p,x)^{10}C(\epsilon)^{10}B^*(100\%)$	27.8
		$^{16}O(p,x)^{10}B^*$	1.0×10^{-9}
1.022	$^{10}B^{*1.740} \rightarrow {}^{10}B^{*0.718}$	$^{12}C(p,x)^{10}B^*$	7.5×10^{-15}
		$^{16}O(p,x)^{10}B^*$	7.5×10^{-15}
1.635	$^{14}N^{*3.948} \rightarrow {}^{14}N^{*2.313}$	$^{16}O(p,x)^{14}N^*$	6.9×10^{-15}
2.000	$^{11}C^{*2.000} \rightarrow$ g.s	$^{12}C(p,x)^{11}C^*$	1.0×10^{-14}
2.124	$^{11}B^{*2.125} \rightarrow$ g.s	$^{12}C(p,x)^{11}B^*$	5.5×10^{-15}
2.313	$^{14}N^{*2.313} \rightarrow$ g.s	$^{16}O(p,x)^{14}N^*$	9.8×10^{-14}
2.742	$^{16}O^{*8.872} \rightarrow {}^{16}O^{*6.130}$	$^{16}O(p,p')^{16}O^*$	1.8×10^{-13}
3.684	$^{13}C^{*3.685} \rightarrow$ g.s	$^{13}C(p,p')^{13}C^*$	1.6×10^{-15}
		$^{16}O(p,x)^{13}C^*$	1.6×10^{-15}
3.853	$^{13}C^{*3.854} \rightarrow$ g.s	$^{13}C(p,p')^{13}C^*$	1.2×10^{-11}
		$^{16}O(p,x)^{12}C^*$	1.2×10^{-11}
4.438	$^{12}C^{*4.439} \rightarrow$ g.s	$^{12}C(p,p')^{12}C^*$	6.1×10^{-14}
		$^{16}O(p,x)^{12}C^*$	6.1×10^{-14}
4.444	$^{11}B^{*4.445} \rightarrow$ g.s	$^{12}C(p,2p)^{11}B^*$	5.6×10^{-19}
5.105	$^{14}N^{*5.106} \rightarrow$ g.s	$^{16}O(p,x)^{14}N^*$	6.3×10^{-12}
5.180	$^{15}O^{*5.181} \rightarrow$ g.s	$^{16}O(p,x)^{15}O^*$	$< 4.9 \times 10^{-14}$
5.240	$^{15}O^{*5.241} \rightarrow$ g.s	$^{16}O(p,x)^{15}O^*$	3.25×10^{-12}
5.269	$^{15}N^{*5.270} \rightarrow$ g.s	$^{16}O(p,x)^{15}N^*$	2.58×10^{-12}
5.298	$^{15}N^{*5.299} \rightarrow$ g.s	$^{16}O(p,x)^{15}N^*$	1.2×10^{-14}
6.129	$^{16}O^{*6.130} \rightarrow$ g.s	$^{16}O(p,p')^{16}O^*$	2.7×10^{-11}
6.175	$^{15}O^{*6.176} \rightarrow$ g.s	$^{16}O(p,x)^{15}O^*$	$< 2.3 \times 10^{-14}$
6.322	$^{15}N^{*6.324} \rightarrow$ g.s	$^{16}O(p,x)^{15}N^*$	1.0×10^{-15}
6.337	$^{11}C^{*6.339} \rightarrow$ g.s	$^{12}C(p,x)^{11}C^*$	$< 1.1 \times 10^{-13}$
6.476	$^{11}C^{*6.478} \rightarrow$ g.s	$^{12}C(p,x)^{11}C^*$	$< 8.7 \times 10^{-15}$
6.741	$^{11}B^{*6.743} \rightarrow$ g.s	$^{12}C(p,x)^{11}B^*$	4.3×10^{-20}
6.916	$^{16}O^{*6.917} \rightarrow$ g.s	$^{16}O(p,p')^{16}O^*$	6.8×10^{-15}
7.115	$^{16}O^{*7.117} \rightarrow$ g.s	$^{16}O(p,p')^{16}O^*$	1.2×10^{-14}

1.7 Introduction to reaction cross section

When an incident particle hits a target nucleus, the resulting interaction is called a nuclear reaction. Different nuclear reactions can occur at different probabilities. In nuclear physics, the probability of a reaction taking place during a collision between the incident particle and the target material is defined as the cross section. This nuclear reaction probability depends on the target composition, the target thickness, and the incident particle energy.

If the particle passes perpendicularly through a thin target, the probability of a certain type interaction (dW) and the cross section (σ) are related by the following equation [Tavernier (2010), Sober (2005)],

$$dW = dxN\sigma \tag{1.6}$$

where, dx is the target thickness and N is the number of scattering centres per unit volume.

The probability of a certain type of interaction (dW) can be written in terms of the number of incident particles ($N_{incident}$) and the number of detected events (N_{events}) for that particular type of interaction,

$$dW = \frac{N_{events}}{N_{incident}} \tag{1.7}$$

The number of scattering centres per unit volume (N) is defined as,

$$N = \frac{\rho N_{Avo}}{A} \tag{1.8}$$

where ρ is the density of the target, N_{Avo} is Avogadro's number, and A is the mass number. From equations 1.6, 1.7, and 1.8, the cross section for a particular interaction can be defined as,

$$\sigma = \frac{N_{events}}{N_{incident}} \quad \frac{A}{dx\rho N_{Avo}} \tag{1.9}$$

If N_{events} refers to any kind of interaction within the target material, then σ is called the total reaction cross-section. It is also possible to define the cross-section according to specific types of interactions such as the elastic cross-section, the inelastic cross-section, the fission cross-section, etc.. These are called partial cross-sections. It is also possible to restrict the N_{events} measured to a specific angle using a finite detector size, giving the differential cross section. This is defined as,

$$\frac{d\sigma}{d\Omega} = \frac{N_{events(\Delta\Omega)}}{N_{incident}} \quad \frac{A}{dx\rho N_{Avo}\epsilon} \tag{1.10}$$

where, ϵ is the absolute detector efficiency.

The total cross section (σ_{tot}) is related to the differential cross section by,

$$\sigma_{tot} = \int_{4\pi} \frac{d\sigma}{d\Omega} d\Omega = 2\pi \int_{-1}^{1} \frac{d\sigma}{d\Omega} d(cos\theta), \tag{1.11}$$

If the differential cross section has been measured at a finite number of angles then the differential cross section can be expanded as [Brune (2002)],

$$\frac{d\sigma}{d\Omega} = \frac{\sigma_{tot}}{4\pi} W(\theta), \tag{1.12}$$

where $W(\theta)$ is an angular distribution function composed of Legendre polynomial ($P_l(cos\theta)$), and is given by [Brune (2002) and Kiener et al. (1998)],

$$W(\theta) = \sum_{i}^{l_{max}} a_l Q_l P_l(cos\theta) \quad (l - even) \tag{1.13}$$

where l_{max} is the smaller of the following two quantities: the first quantity is that twice the spin of the decaying state (I_f), and the second quantity is that twice the value of multipolarity of the gamma ray transition state (E_l/M_l).

a_l are the Legendre coefficients, and Q_l are angle dependent attenuation coefficients [Ferguson.A.J (1965), Rose (1953)]. The Legendre coefficient a_0 directly gives the angle integrated cross-section ($\sigma = 4\pi a_0$).

The multi-polarity of the photon is a quantity of angular momentum carried by the photon. To find the state of multipolarity of a gamma emission, the selection rules can be used. The angular momentum (L) and parity (π) selection rules for a photon are given by [S.Krane (1987)],

$$|I_i - I_f| \leq L \leq I_i + I_f \qquad (no \quad L = 0) \tag{1.14}$$

$\Delta\pi$ (change in parity) = no; even electric multipoles, odd magnetic multipoles

$\Delta\pi$ (change in parity) = yes; odd electric multipoles, even magnetic multipoles

The γ-ray selection rules and multi-polarities are given in table 1.2.

For example, the 4.438 MeV gamma emission from ^{12}C is a transition from the first excited state ($I_i = 2^+$) to the ground state ($I_f = 0^+$). If we apply the selection rules (equation 1.14) to find the multipolarity state of the gamma emission, the angular momentum of this gamma emission is 2 ($L = 2$), and since there is no parity change, therefore the state of the multipolarity of the 4.438 MeV gamma emission is an electric quadrupole (E_2).

Table 1.2: γ-ray selection rules and multi-polarities

Multipolarity state of gamma	Name	$L = \Delta I$	$\Delta\pi$
E_1	electric dipole	1	yes
M_1	magnetic dipole	1	no
E_2	electric quadrupole	2	no
M_2	magnetic quadrupole	2	yes
E_3	electric octupole	3	yes
M_3	magnetic octupole	3	no
E_4	electric haxadecapole	4	no
M_4	magnetic haxadecapole	4	yes

1.8 Range uncertainty in proton therapy

In radiotherapy, sources of uncertainty are a recognized concern. The uncertainties found in conventional X-ray based photon therapy are also applicable in proton therapy. Most of these uncertainties can be addressed using the same techniques as in photon therapy. However, a more important uncertainty that is unique to proton therapy is range uncertainty. The main cause of range uncertainty in proton therapy is the uncertainty during the conversion of CT (computerized tomography) Hounsfield unit to stopping power due to tissue heterogeneities. And other possible uncertainties are morphological changes during treatment fractions, internal organ motion during treatment, set up errors, and imaging artifacts [Min (2011)].

To illustrate the importance of range uncertainty in proton therapy, a 1.0 cm water equivalent depth (WED) variation in the proton range could cause a 90% dose difference in the proton beam delivery if it occurred near the Bragg peak of the proton beam as shown in figure 1.9. Meanwhile, for the same 1.0 cm WED variation would produce only a 3% dose difference in conventional X-ray based photon therapy because of the exponential nature of the photon beam. A dislocation of a Bragg peak due to range uncertainty could cause severe under dosage or over dosage in proton therapy. Therefore, it is very important to verify the location of the Bragg peak during the treatment delivery to fully take advantage of proton therapy.

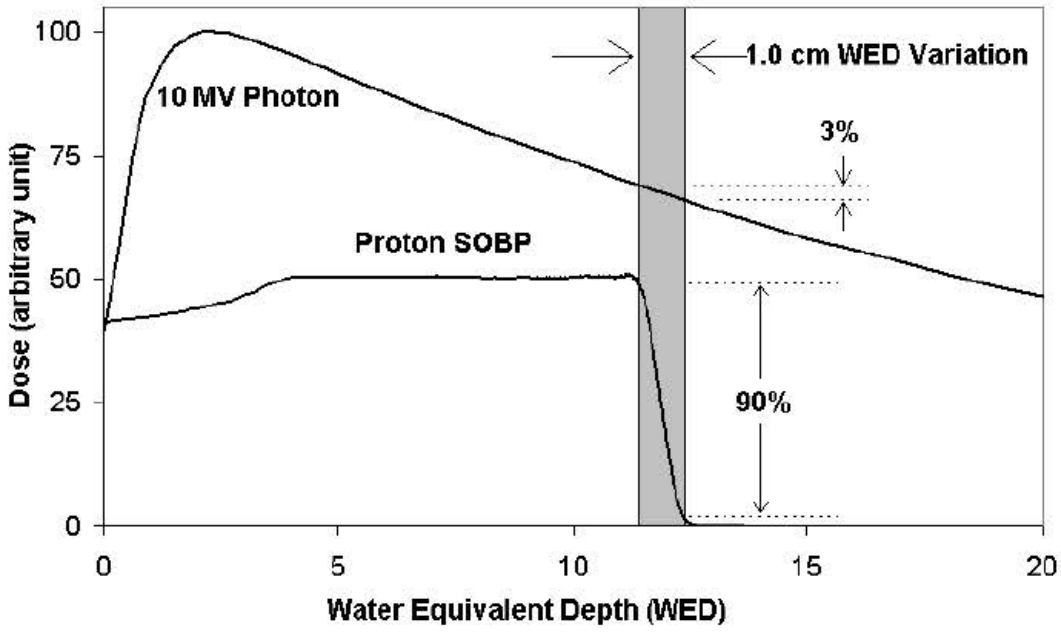

Figure 1.9: Comparison of the potential depth dose difference resulting from a 1.0 cm water equivalent depth (WED) variation for a 10 MV photon beam and a proton spread out Bragg peak delivery, producing a 3% or 90% dose difference in photon and proton beam deliveries, respectively. Source: Lu (2007)

1.9 Range verification techniques for proton therapy

As discussed in the previous section, the location of the Bragg peak during treatment is essential, thus various methods have been proposed in the literature to more accurately verify the proton range. Due to the fact that the treatment protons fully stop within the patient, monitoring the delivered dose and locating the Bragg peak using the primary protons is not possible. The secondary radiation which escapes the patient is the best option to verify the proton dose distribution. This secondary radiation includes both prompt gammas as discussed in section 1.5.4 and delayed gamma emission from unstable nuclei. This section briefly discusses the different approaches which have been reported regarding range verification in proton radiation therapy.

1.9.1 In-patient point dose measurement

In conventional X-ray based photon therapy or electron therapy, in-vivo point dose measurement (placing the dosimeters on the patient's skin or in natural cavities) is the most-used direct method to monitor the delivered radiation dose during the radiotherapy [Essers

and Mijnheer (1999)]. Implantable dosimeters have been investigated by Scarantino et al. (2008), Beyer et al. (2007) and Black et al. (2005) for X-ray based photon therapy. The same method was implemented for passively scattered proton beams to verify the range of proton beam. However, it did not provide much information due to the homogeneous dose distribution in the target volume. Dose measurements performed at the distal edge of the proton beam in the target volume proved difficult and was very sensitive to the detector placement.

Two different approaches were proposed to overcome these problems. The first approach was a time-dependent point dose measurement [Lu (2008b)]. Using the timing information, the measured dose was unique at each point of the delivered spread out Bragg peak (SOBP), thus the depth information can be encoded. If the measurements were acquired at a particular point, the data could be decoded to obtain the residual depth dose measurements. Lu (2008b) first investigated this method using a small ionization chamber. Gottschalk et al. (2011) proposed semiconductor diodes which are inexpensive and small. This method has experienced difficulties due to the complex heterogeneity of the human body structure and due to limitations in determining the exact position of the detectors [Knopf and Lomax (2013)].

The second method proposed splitting the conventional spread out Bragg peak (SOBP) into a complementary field pair [Lu (2008a)] where the fields are sloped and opposite. The ratio of the dose at a point in the target volume from each field can be measured, which provides the water equivalent path length of the implanted dosimeter. This method can be implemented easily in both passively scattered and active scanning proton beams. Although, it is fairly straight forward to implement this method of dose verification, it is restricted to a limited number of verification points [Lu (2008b)] for obvious clinical reasons and the dosimeters must be implanted in the target volume. Unfortunately, the implantation of dosimeters is a very difficult process and impossible for head and neck cancer patients. This method appears to have been abandoned for proton range verification [Knopf and Lomax (2013)].

1.9.2 Range probe

Due to the implantation difficulties of in-vivo point dose measurements, an alternative concept for one dimensional dose verification is the range probe (figure 1.10) [Romero et al. (1995), Mumot et al. (2010)]. In this method, a pencil beam of high energy protons is applied to pass through the patient and the integrated Bragg peak is measured using a multi layer detector. While this is a viable option, the primary limitation is the requirement of a much higher proton energy especially for the lateral field of the pelvis. Most proton therapy facilities cannot provide high enough energy. Furthermore, spatial resolution is poor and it can only verify the range through the patient whole body and not the target volume. Although it may prove difficult for therapy purposes, a promising application

of this idea is proton computed tomography (CT) to correct the CT Hounsfield problem (discussed in section 1.6) [Schulte and Penfold (2012)].

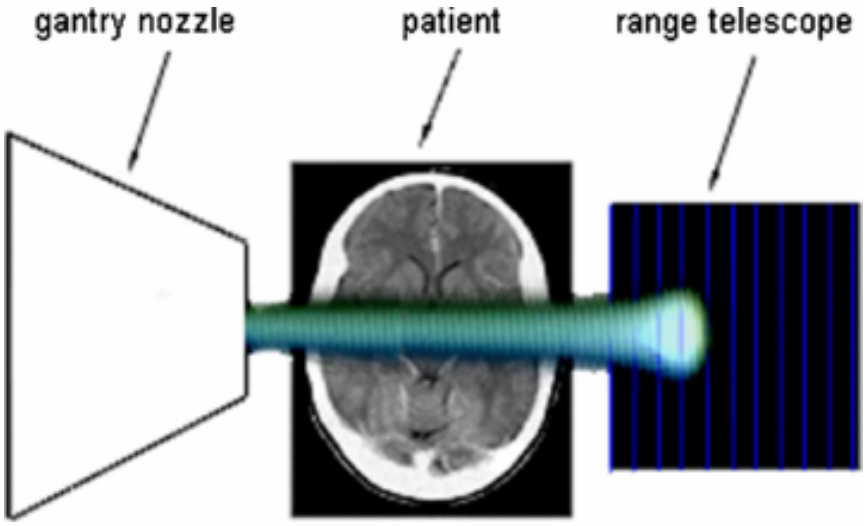

Figure 1.10: Model for range probe measurement setup. Source: Mumot et al. (2010)

1.9.3 Positron emission tomography (PET) imaging

Using positron emitters to verify the proton range was suggested by G.W.Bennett et al. in 1978 [Bennett.G.W et al. (1978)]. In proton therapy, positrons are produced when the protons interact with tissue via the (p,pn) reactions which can occur in both ^{12}C and ^{16}O. These reactions produce short lived isotopes ^{11}C ($T_{1/2}$ = 20.39 min) and ^{15}O ($T_{1/2}$ = 2.04 min), the emitted positrons interact with the surrounding electrons in the tissue and produce back-to-back gammas with equal energy of 511 keV which can then be observed by a PET camera. Considerable research has been carried out regarding this approach [Litzenberg et al. (1992), Paans and Schippers (1992), Vynckier et al. (1993), Litzenberg et al. (1994), Parodi and Enghardt (2000), Parodi et al. (2002), Parodi et al. (2005), Parodi and Bortfeld (2006), and Knopf et al. (2011)]. This was the first method to be used clinically to verify the proton range. This approach does have some limitations because of the short half life of the positron emitters, and the poor resolution is due to organ motion and biological wash out.

1.9.4 Prompt gamma imaging

The detection of prompt gammas is a potential method to determine the proton range since the rate of production of prompt gammas is approximately ten times higher than gammas produced by positron emitters [Moteabbed et al. (2011)]. The advantage of prompt gamma

imaging is a real time measurement and there is no additional dose to the patient. Therefore, this method has been proposed as a suitable technique for proton range verification over PET imaging. The prompt gamma imaging was first proposed by Jongen and Stichelbaut (2003) in 2003. Parodi et al. (2005) observed prompt gammas as a noise in PET measurement. The first prompt gamma measurement was done by Min.C et al. (2006) and explained the correlation between the proton beam profile and the prompt gamma distribution. In his study, a prompt gamma scanning system was developed to locate the Bragg peak of a proton beam. Figure 1.11 shows the correlation between the proton dose distribution, measured using the ionization chamber, and the measured prompt gammas using the prompt gamma scanning system. This correlation clearly demonstrates the feasibility of prompt gamma imaging being used for range verification during the treatment delivery of a proton beam. Since then, the correlated result of prompt gammas was confirmed by Polf.J.C et al. (2009a), and Polf et al. (2009).

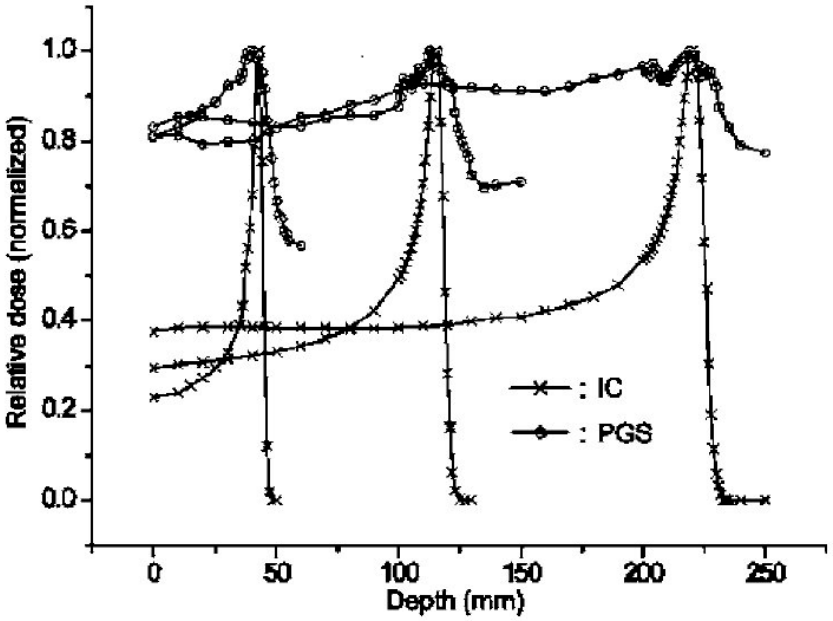

Figure 1.11: Correlation between proton dose distribution measured by ionization chamber (IC) and measured prompt gammas using a prompt gamma scanning system (PGS) in a water phantom at proton energies at 100, 150, and 200 MeV. Source: Min.C et al. (2006)

Since prompt gamma emission is typically in the range of 2 MeV-15 MeV during the proton irradiation [Polf.J.C et al. (2009a)], it is impractical to use a two-dimensional collimated imaging systems like SPECT (Single-photon emission computed tomography) due to the size of detector required to completely absorb the gamma. Thus, several research groups have attempted to develop clinical prompt gamma imaging devices since no device is currently available. The proposed methods for prompt gamma imaging are briefly explained below. Two different approaches have been proposed for prompt gamma imaging. The first approach is a Compton camera which is an electronically collimated detector system.

The second approach is using a physical collimator to produce a prompt gamma image. For physical collimator detection systems, parallel slit cameras, knife edge and pinhole collimators have been proposed.

In a Compton camera, for each photon interaction (Compton scattering and other interaction) in the detector, the position and the deposited energy of the interaction is determined. Multiple detector planes are used to build a Compton camera. To find the direction of the photon, this method depends on multiple interactions of the photon in the detector. Compton cameras were investigated as a possibility by Seo et al. (2007), Peterson et al. (2010), Kormoll et al. (2011), Roellinghoff et al. (2011), Richard et al. (2011), and Mackin et al. (2013). Figure 1.8 shows a three-stage Compton camera modeled by Peterson et al. (2010). In this model, three detection stages are considered; germanium detectors were used for each stage and the size of detectors were optimized according the detector performance (efficiency of the detector). Each detection stages could handle either two dimensional or three dimensional spatial resolution. This research work was focused on model design and not clinical application. Robertson et al. (2011) studied the Compton camera by using different materials and geometries.

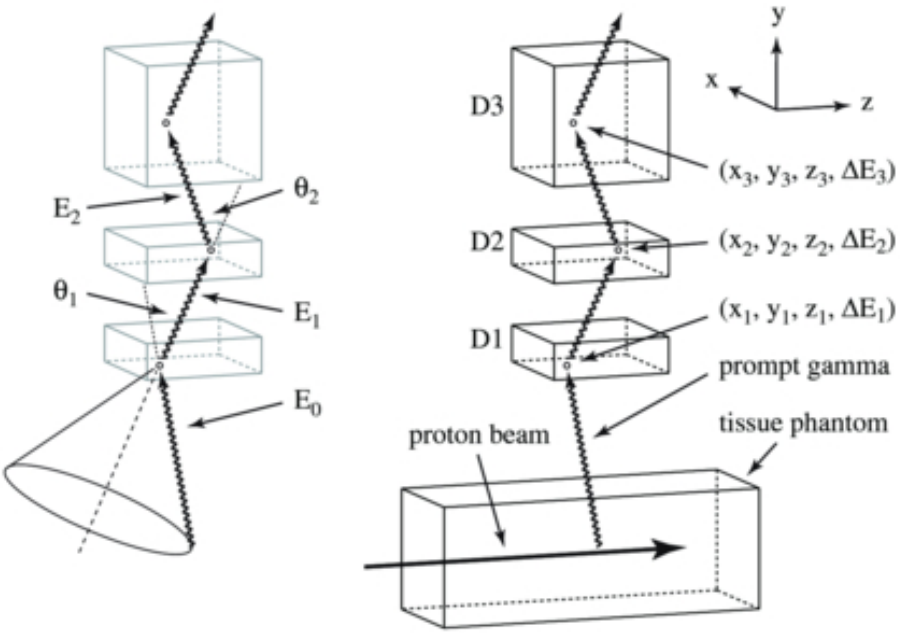

Figure 1.12: Right panel: Three stage Compton camera setup which illustrates prompt gamma production during proton beam irradiation in a tissue phantom. The prompt gamma interacts with the three stage Compton camera. The energy deposition due to the interaction of the photon with each detector and the interaction positions are also shown. Left panel: Parallel plane geometry of the Compton camera where θ_1 and θ_2 are the Compton scatter angles and E_0, E_1, and E_2 are the gamma ray energies as the gamma ray traverses through the detectors D_1, D_2, and D_2. The projected cone is then used to reconstruct the images. Source: Peterson et al. (2010)

Another example of a Compton camera [Richard et al. (2011)] is shown in figure 1.13. If a photon undergoes at least one Compton scattered event in either the first or second detector and there is at least one interaction in the third absorber, an active event can be produced. Accumulation of a large number of events will allow reconstruction of an image showing the location of the initial prompt gamma production. Further modifications to the Compton cameras, an electron tracking Compton camera (ETCC) was developed by Kabuki et al. (2009) and a combined Compton scattering and pair creation camera has been investigated by Frandes et al. (2010).

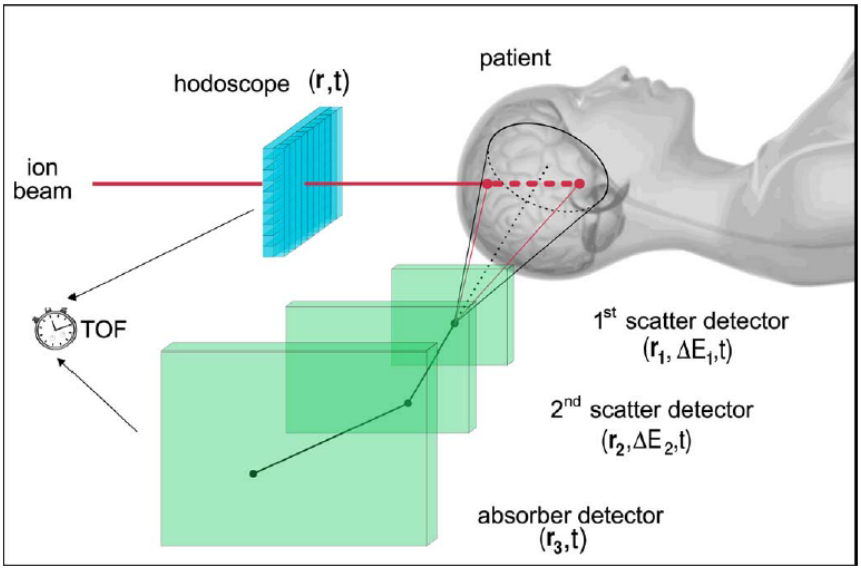

Figure 1.13: Arrangement of double scattering Compton camera. Source: Richard et al. (2011)

For physical collimator systems, several studies have been performed using a parallel slit collimator based detection system. Min.C et al. (2006), Kurosawa et al. (2012), and Verburg et al. (2013) measured prompt gammas for proton irradiation using a single slit within a parallel edge configuration. Testa et al. (2008) used the same method for carbon ion irradiation. In addition, a two dimensional parallel hole system was modeled in MCNPX Monte-Carlo code by Lee et al. (2012). A Parallel slit system was also modeled in MCNPX code by Min et al. (2012).

A number of knife-edge slit systems have also been developed, for 1D system; figure 1.14 shows a knife-edge system studied by Smeets et al. (2012). Diblen et al. (2012) and Bom et al. (2012) individually investigated a similar set up using different sizes of slit width openings. For 2D systems, Kim et al. (2009) developed a 2D pinhole system.

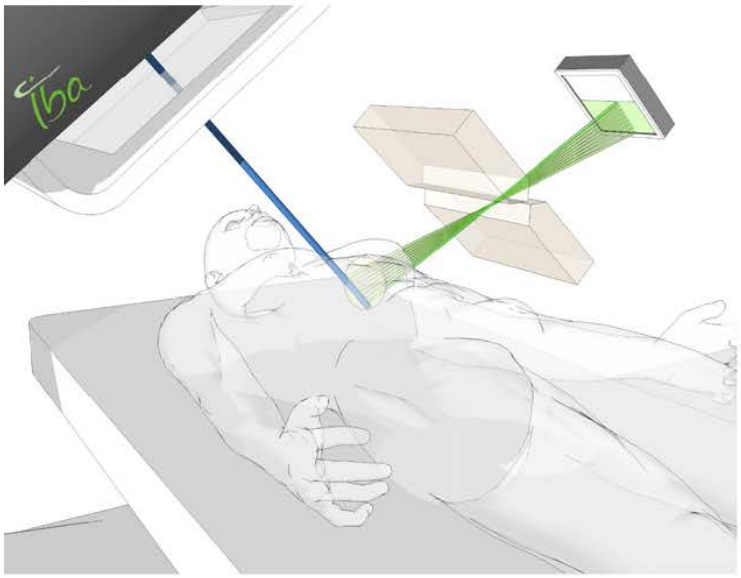

Figure 1.14: Knife edge slit camera. Source: Smeets et al. (2012)

1.10 Prompt gamma imaging and Monte-Carlo simulations

The precision of range verification using prompt gamma imaging strongly depends on the detector performance. Prompt gamma imaging detection systems are still in development. Due to the time and money require to build detectors, studying and optimizing detector performance using Monte-Carlo simulations is common. Monte-Carlo transport codes are software used to simulate nuclear processes and interactions. In prompt gamma imaging studies, both GEANT4 and MCNPX Monte-Carlo codes have been used. Recently, different approaches have been performed to improve the results from Monte-Carlo prompt gamma simulations. Unfortunately, there are still limitations for making absolute comparisons between simulation and experiment. Therefore, modelling the detection systems using Monte-Carlo codes has become a critical component during the development.

Efforts have been made to compare experimental results to Monte-Carlo simulations. Prompt gamma spectrum produced experimentally by Polf et al. (2009) using a plastic phantom was compared with Geant4 Monte-Carlo simulation. Figure 1.15 shows the experimental and simulated setups as well as the Geant4 and measured spectra comparison. Smeets et al. (2012) obtained prompt gamma spectra for the irradiation of a 160 MeV proton pencil beam on a PMMA target ($C_5O_2H_8$) using NaI detector (figure 1.16) and compared with simulated results using Monte-Carlo code MCNPX as shown in figure 1.17. Jeyasugiththan (2014) measured prompt gamma spectrum for the irradiation of a 200 MeV proton beam on water phantom and compared with Geant4 simulated results.

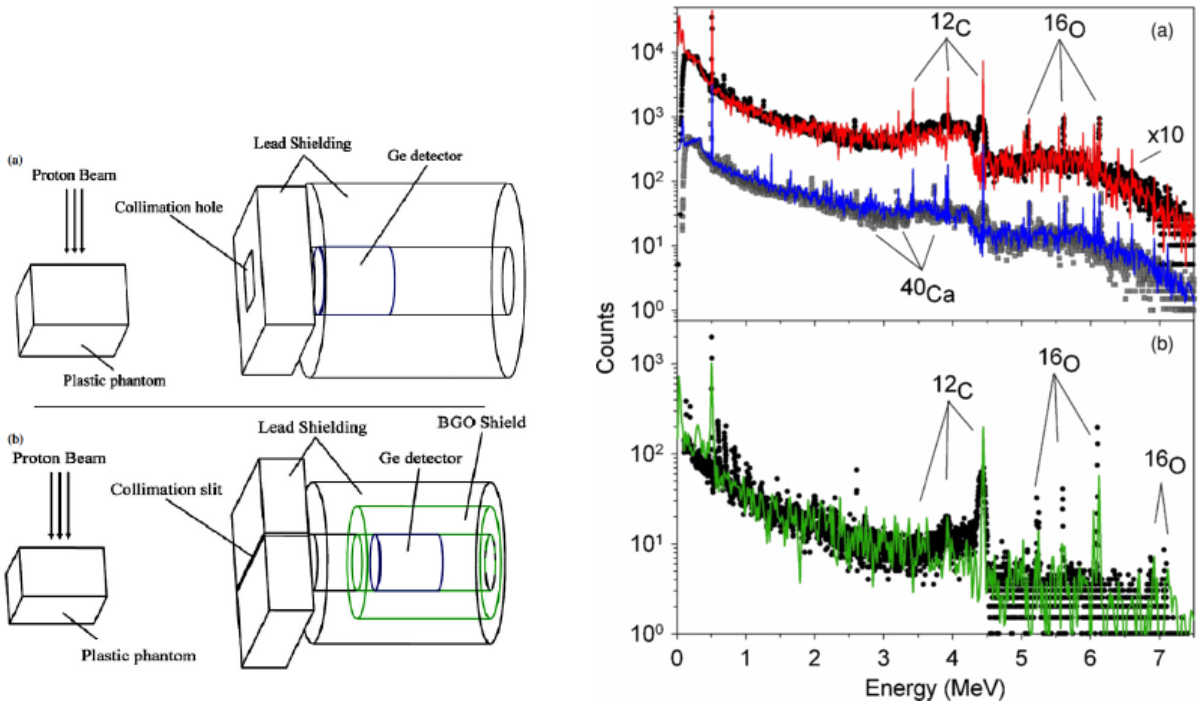

(a) (b)

Figure 1.15: Left: experimental setup for prompt gamma measurement modeled in Geant4 Monte-Carlo code. Right: Experimentally measured prompt gamma spectra (black circle from lucite phantom and gray squares from bone equivalent plastic) have been compared with Geant4 Monte-Carlo simulation (red line from lucite and blue line from bone equivalent plastic phantom). Source: Polf et al. (2009)

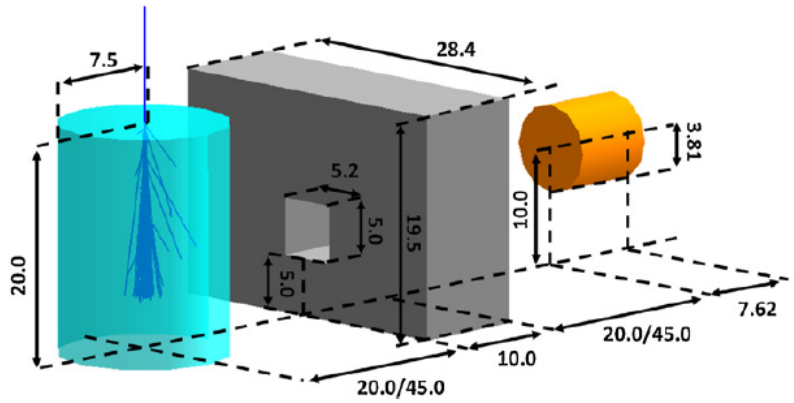

Figure 1.16: Geometry of simulated setup including a 160 MeV incident proton beam on the PMMA ($C_5O_2H_8$) target, detector at 50 cm, and the lead collimator in between the target and collimator. All distances are in cm. Source: Smeets et al. (2012)

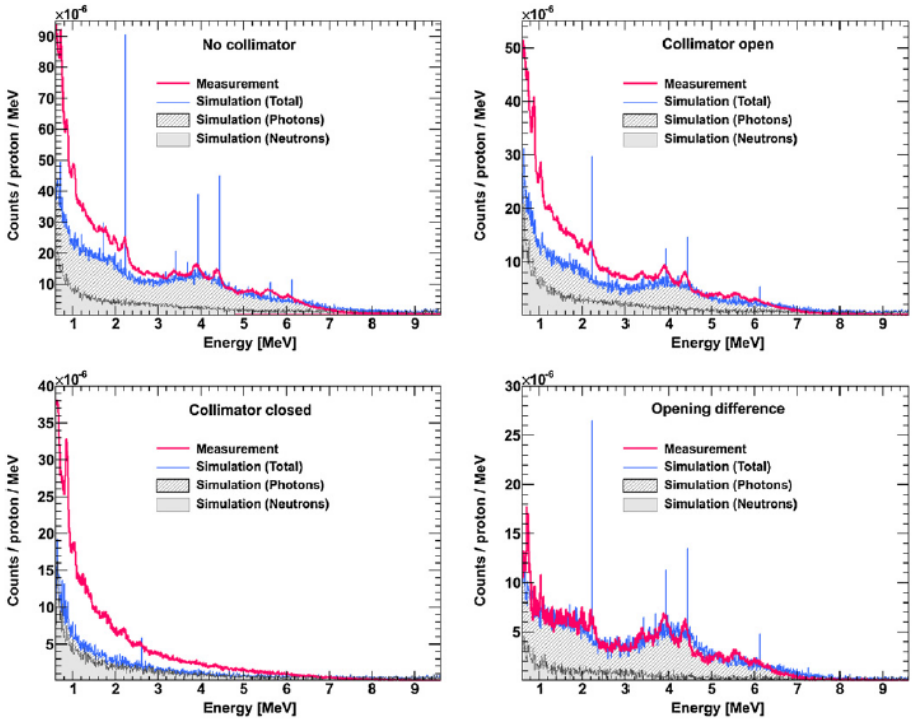

Figure 1.17: Simulated and measured prompt gamma spectra for a 160 MeV proton beam at 50 cm distance for different collimator positions as shown in the figures. Source: Smeets et al. (2012)

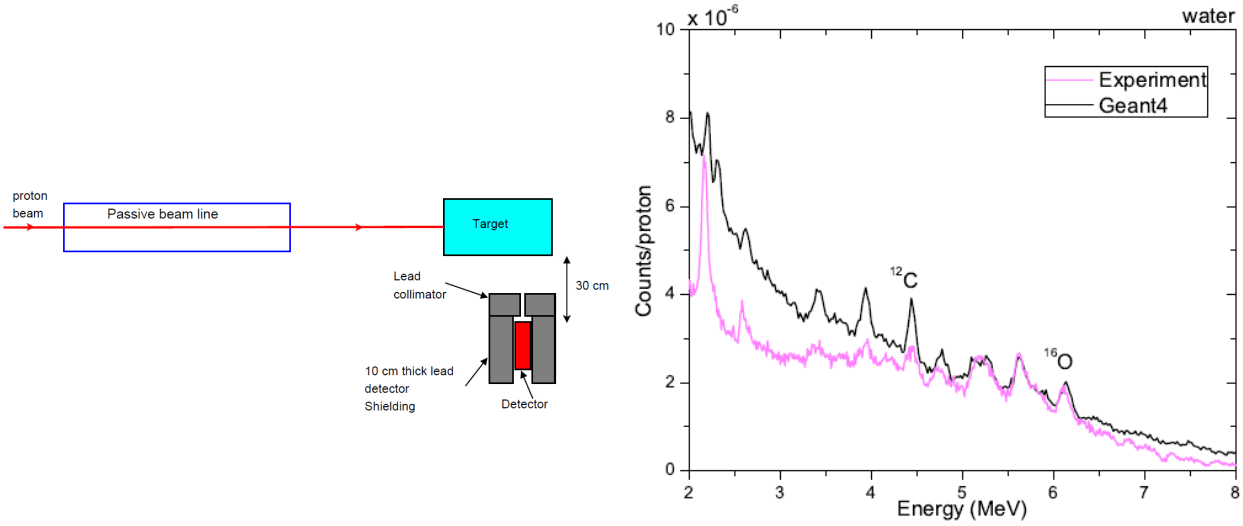

(a) (b)

Figure 1.18: Left: Schematic diagram of experimental setup modeled in Geant4. Right: prompt gamma spectra comparison for a 200 MeV proton beam using water phantom. Source: Jeyasugiththan (2014)

1.10.1 Challenges of prompt gamma imaging

Even though considerable research has been done towards developing a prompt gamma imaging device, there is still no complete system to clinically verify the proton range [Smeets et al. (2016), Smeets et al. (2012), Richard et al. (2011), Peterson et al. (2010), Polf et al. (2009)] . To produce a clinically usable prompt gamma imaging device, there are number of challenges that need to be overcome in the area of detector development and design, and particularly the efficiency of the detector. Monte-Carlo transport code has played a major role in detector development, particularly the Geant4 Monte-Carlo transport code due to its versatility and flexibility for different applications. Although Geant4 has been an invaluable tool for the development of devices, previous work has found problems with the prompt gamma production (cross-section) data, particularly for the elements carbon and oxygen. The following is a review of the discrepancies found in the literature regarding the prompt gamma spectrum and the Geant4 prompt gamma cross-section data.

Polf et al. (2009) performed a Geant4 (version 9.2) simulation to compare simulated prompt spectra (shown in figure 1.15) against measured spectra during a design study for a prompt gamma imaging device. They reported a much wider measured peak for the 4.438 MeV gammas from ^{12}C due to the absence of Doppler broadening in this version of the Geant4 code. Paganetti (2012) reported another limiting factor in Monte-Carlo simulations is the absence of prompt gamma cross-section data. Most of the required prompt gamma cross-section data are unavailable in the energy range of interest for proton therapy. In addition, Paganetti (2012) mentioned more experimental cross-section data is required to reduce the uncertainties in Monte-Carlo simulations.

In Verburg et al. (2012) Geant4 (version 9.5) simulation studies, the gamma peak from the ^{16}O(p,p$'$)^{16}O$^{*6.13}$ reaction was not observed at energies above 20 MeV. In addition, the total simulated gamma production near the Bragg peak was reported to be a factor of 2 higher than the experimental value. Further, Dedes et al. (2014) reported an overestimation of the total prompt gamma yields in Geant4 (version 9.6) simulations of 160 MeV protons on a water target. Jeyasugiththan (2014) reported a 50% of overestimation of prompt gamma production in Geant4 (version 9.6) simulation for 4.438 MeV photo peak from the water target. The prompt gamma spectra comparison of simulated against experiment is shown in figure 1.18b. In addition, Jeyasugiththan and Peterson (2015) tested various Geant4 proton inelastic reaction models with different cross-section data (Tripathi data and Wellisch and Axen cross-section data set). The variations of Geant4 prompt gamma cross-section data against available experimental cross-section data of ^{12}C for different Geant4 models (Precompound and binary cascade) using two different cross-section data reported, which are shown in figure 1.19.

These discrepancies in the Geant4 simulations are a cause for concern and will contribute to the uncertainties in the range verification of proton beams. Furthermore, figures 1.13 and 1.14 show the gaps in the available experimental cross-section data for ^{12}C and ^{16}O.

These gaps are unfortunately in the therapeutic range. In conclusion, the Geant4 Monte-Carlo code struggles to accurately model the proton interactions on ^{12}C and ^{16}O at energies relevant to proton therapy. In addition, more accurate prompt gamma production data are necessary to produce.

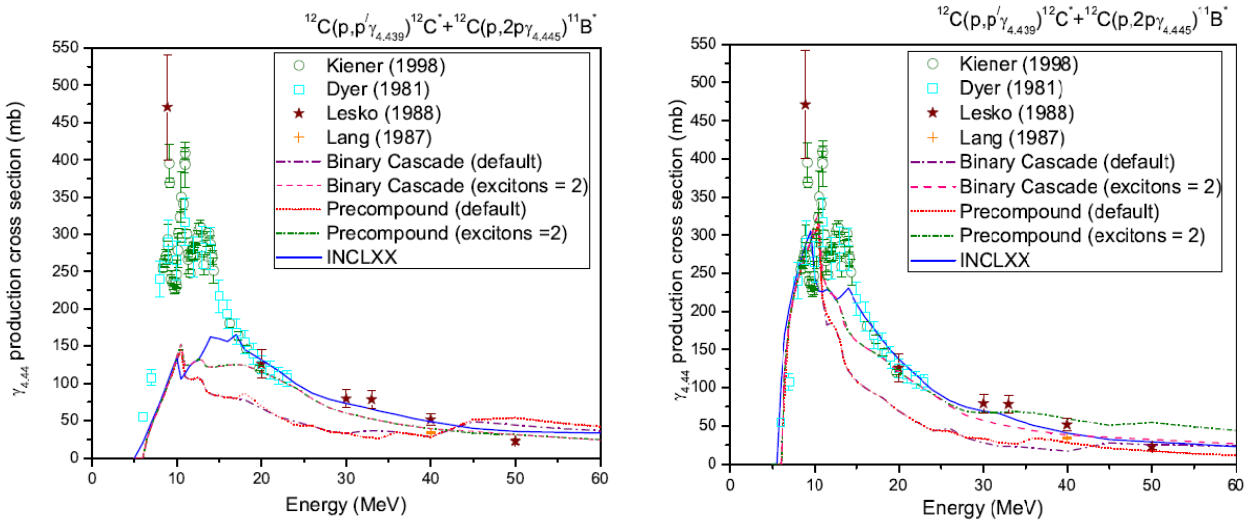

Figure 1.19: Left: γ-ray production cross section for ^{12}C 4.438 MeV photo peak using total inelastic cross-section data from Wellisch and Axen. Right: γ-ray production cross section for ^{12}C 4.438 MeV photo peak using total inelastic cross-section data from Tripathi. Source: Jeyasugiththan and Peterson (2015)

1.11 Motivation

As discussed in this chapter, on-line range verification in particle therapy still faces a variety of challenges in order to be implemented clinically. These challenges have motivated this research work, which consists of two specific aims. The first aim is the measurement of prompt gamma cross-section for the prominent elements (carbon and oxygen) found in human tissue. The second aim is developing a Geant4 model of the experimental cross-section set-up to produce simulated results to compare with the experimental results.

Specific Aim I

As discussed in section 1.6, the majority of the cross-section measurements have been performed specifically for the astronomical environment, and only provide a very limited amount of data as shown in figure 1.6. The gaps in the cross-section data and the lack of data beyond 90 MeV drives the cross-section measurement aspect in this work. This study focussed on measuring the prompt gamma cross-section for reactions in carbon and oxygen to extend the available cross-section data into the therapeutic range (50-200 MeV). The objective of this work is to measure the cross-section for the 4.438 MeV gamma peak from ^{12}C and the 6.129 MeV gamma peak from ^{16}O using the thin targets of natural carbon and mylar (^{12}C, ^{16}O) at proton energies of 66, 80, 95, 110, and 125 MeV.

Specific Aim II

As discussed in section 1.10.1, previous work reported discrepancies in the prompt gamma production in the Geant4 Monte-Carlo code, specifically at energies (40 MeV, 160 MeV, and 200 MeV) and reactions relevant to proton therapy and prompt gamma imaging, motivating investigation into Geant4 prompt gamma production. Therefore, the second specific aim of this work is to model (in Geant4) the AFRODITE detector system used for the cross-section measurements, run a series of simulations to mimic the experimental setup, and then compare these simulated results with the experimental cross-section results. The model will be validated using standard gamma emitting sources and the hadronic physics processes will be evaluated. The final Geant4 AFRODITE model simulation results will then be processed in an identical manner to the experimental results, completing a complete virtual cross-section measurement.

Part II
Materials and Methods

Chapter 2

GEANT4 model of the AFRODITE detector system

2.1 Geant4 toolkit

Geant4 is an object oriented Monte-Carlo toolkit which is implemented in the C++ programming language [Agostinelli et al. (2003)]. Geant4 stands for Geometry and Tracking. The first version of Geant4 can be traced back to the 1970s and was originally written in Fortran. The next version, Geant3, was released in 1982. For the development, Geant4 of CERN (European Organization for Nuclear Research) and HIP (Helsinki Institute of Physics) worked independently in 1993 [Amako (1994)]. This led to release of the first version of Geant4 in 1998 with its advanced computing techniques. It is used to simulate the interaction of particles with matter and it plays a major role in particle physics, nuclear physics, astrophysics and medical physics due to the versatility of the Geant4 code.

2.2 Geometry in Geant4

Due to the flexibility of the Geant4 toolkit, it is possible to create geometries using Constructed Solid Geometry (CSG), Boundary Represented Solids (BREPS), or Tessellated Solids. These geometries can be implemented either directly into the code or imported from a Geometry Description Markup Language (GDML) or STEP (Standardized graphic exchange file) tool. Another method to import geometries is CADMesh [Poole et al. (2012)] which is a CAD (Computed Aided Design) interface for Geant4. It allows for directly importing CAD models without any intermediate steps as shown in figure 2.1. This method was used to import the AFRODITE detector geometry.

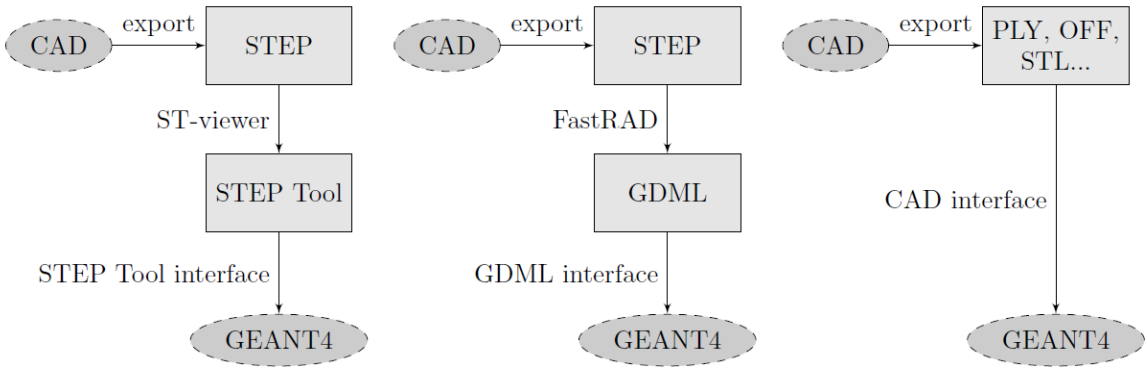

Figure 2.1: Schematic diagrams of currently available CAD import methods in Geant4 geometry. CAD interface indicates CADMesh in this figure. Source: Poole et al. (2012)

2.3 Physics in Geant4

Presently, there are 28 built in physics lists available in Geant4. Selecting a suitable physics list in Geant4 is the user's responsibility to decide which physics processes are required and then it can be included in the physics list. In addition, custom built physics lists are possible by invoking individual physics models. Each Geant4 model gives an example of how to invoke it, the energy range within which the model should be used, and a list of the particles to which it applies. Typically, alternate physics models are also available for each physics process. The Geant4 hadronic models are shown in figure 2.2.

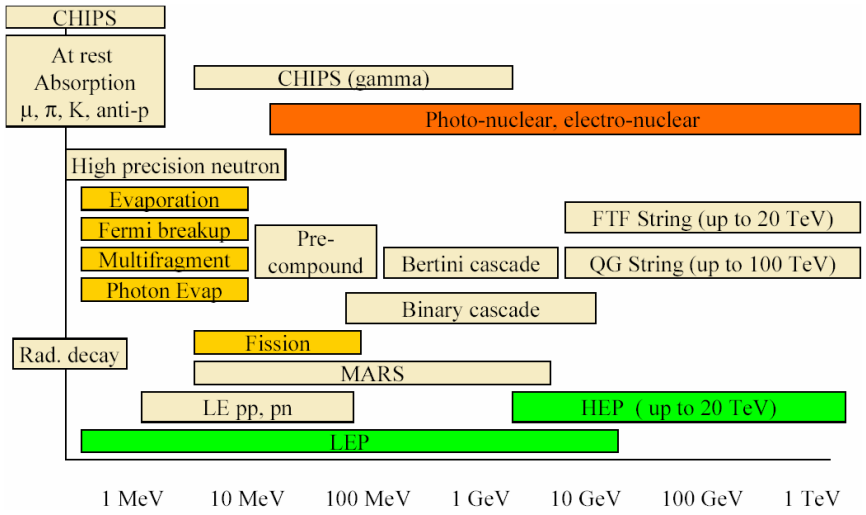

Figure 2.2: Geant4 hadronic models. Source: G4HadModels (2015)

In this work, the physics lists were chosen to measure prompt gamma cross section in the therapeutic range (50 - 200 MeV). The chosen physics lists in the prompt gamma measurement simulations included elastic scattering, inelastic scattering, electromagnetic interactions and radioactive decay physics. Physics processes explain how the particles interact with matter. There are seven major processes in Geant4 such as hadronic, electromagnetic, decay, photolepton-hadron, parameterization, optical, and transportation. The nucleus and incident particle interactions are tracked by nuclear models as described in section 2.3.3 while emitted photons are tracked by the interactions described in section 2.3.2.

2.3.1 Nuclear collisions

During a projectile and target collision, either of two interaction processes could take place. The incident particle may be deflected from the target nucleus with no change in the centre of mass energy. This process is called elastic scattering. On the other hand, the incident particle may interact with the target nucleus and lose some of its energy, resulting in the projectile being removed from the entrance channel and being absorbed by the target nucleus. This process is called inelastic scattering. This work will focus on inelastic scattering which leads to prompt gamma production.

In inelastic scattering, the absorption of the incident particle is followed by an intra-nuclear cascade where secondary nucleons leave the nucleus. In Geant4, this process can be simulated using the intra-nuclear cascade models. In the therapeutic proton energy range, the relevant models are: the binary cascade, the Bertini cascade, and the low energy parameterized models (figure 2.2). Once the cascade process has developed, the compound nucleus becomes an excited state. The de-excitation process of the nucleus is simulated by the pre-equilibrium model. There are two pre-equilibrium models (the precompound model and the pre-equilibrium model) in the Geant4 Monte-Carlo code. The cascade models automatically evoke this pre-equilibrium phase when the cascade model has reached a lower limit. The binary cascade invokes the precompound model while the Bertini cascade invokes the pre-equilibrium model. The compound nucleus also allows further processes to occur, for example, evaporation and/or Fermi breakup [Geant4 (2015), Dedes et al. (2014)]. In this study, the QGSP_BIC Physics package (QGS $\rightarrow$ Quark gluon string model, P $\rightarrow$ Precompound model, and BIC $\rightarrow$ Binary cascade) was used for hadronic inelastic interactions.

2.3.2 Electro-magnetic interactions

For the electromagnetic interactions, standard and low energy parameterized models are available. In the standard EM package, there are five different options available in Geant4. The default option is emstandard, with the other options being emstandard_opt1, emstan-

dard_opt2, emstandard_opt3, and emstandard_opt4. More details about these packages can be found on the Geant4 physics manual [Geant4 (2015)]. In these cross section measurement simulation studies, electromagnetic standard physics_option4 was used. This model is directly obtained from Quantum Electro Dynamics (QED) calculations and is designed to produce higher accuracy for electron, hadron, and ion tracking. The standard EM (electro magnetic) model covers the energy range from 1 keV to PeV and includes photoelectric effect, Compton scattering, gamma conversion, multiple scattering, ionization, Bremsstrahlung, and positron-electron annihilation into two gammas. More details about electromagnetic interaction are in appendix A.

2.3.3 Nuclear models

Geant4 binary cascade model

The Geant4 binary cascade model is a hybrid between a quantum molecular dynamics model and classical cascade model [Folger et al. (2004)]. This model is used to simulate inelastic scattering of protons, neutrons, and light ions with energies in the range 0 MeV -10 GeV. The propagation of incident hadrons through the target nucleus is modeled by a cascading series of binary inelastic collisions between the projectile and the target nucleons. The secondary particles which are produced in these reactions are allowed to interact further in one on one collisions with remaining target nucleons. The cascade modeling sequence is shown in figure 2.3.

The target nucleus is modeled by a three dimensional collection of nucleons. For heavy nuclei with $A > 16$, the nucleons are placed according to the Woods-Saxon density distribution and for light nuclei ($A < 17$) the harmonic oscillator shell model is used to place nucleons [Wright et al. (2006)]. In this binary cascade model, the cross sections of free particles are used. In the nucleus these cross sections are reduced to effective cross sections by Pauli blocking due to Fermi statistics. The interaction is suppressed if either of the two particles have a momentum below the Fermi momentum, the reaction products are discarded and the original primary particles are allowed to continue the cascade. If the reaction is allowed, the secondaries are treated as primary particles and allowed to continue producing collisions. All secondaries are tracked until they leave the nucleus or until the cascade terminates. Eventually, the cascade process is terminated when the secondaries have reached a given threshold energy. The precompound and de-excitation models are called to handle the remaining fragments [Geant4 (2015), Kraan (2015)].

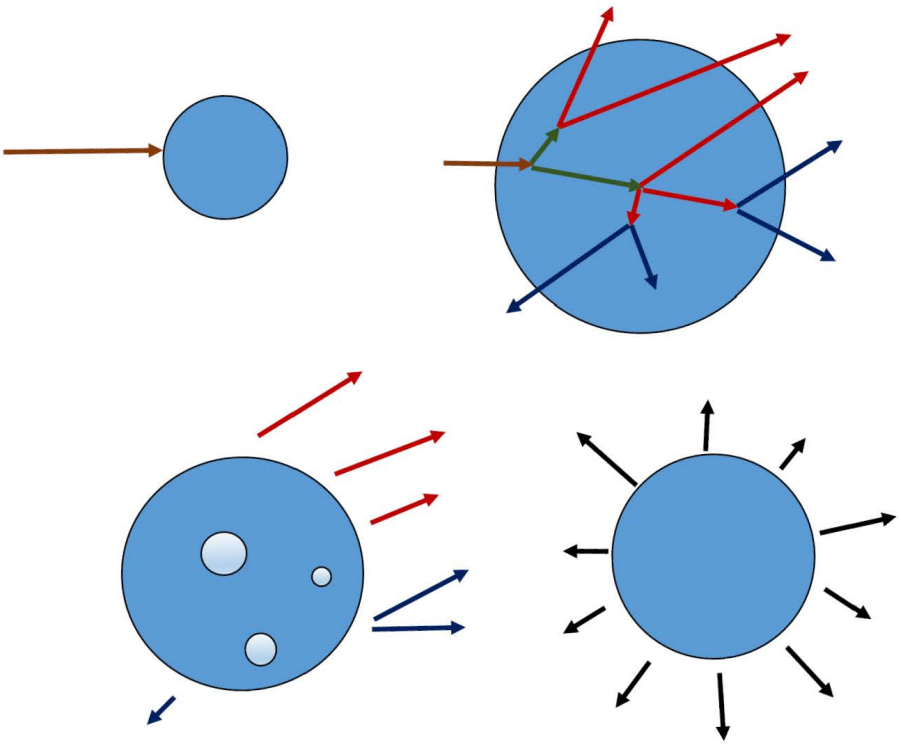

Figure 2.3: Schematic diagram of cascade modelling sequence. Upper left: hadron incident upon target nucleus. Upper right: development of cascade process and secondary nucleons leaving the nucleus. Lower left: higher energy hadrons leaving the nucleus and creating highly excited particle hole state. Lower right: evaporation process of de-excited nucleus.

Geant4 precompound model

This model is considered as an extension of the hadron kinetic model. The Geant4 hadron kinetic model addresses the intra-nuclear transport phase. The precompound model gives the possibility to extend the low energy range of the hadron kinetic model for nucleon-nucleus inelastic collisions. In the precompound model, the recommended maximum projectile energy is 170 MeV. It provides a smooth transition between the kinetic stage of a reaction described by the hadron kinetic model and the equilibrium stage where equilibrium de-excitation models take over. An algorithm is used for the transition from the binary cascade model to the precompound model. As long as there are still particles above the kinetic energy threshold (75 MeV), the cascade process will continue. If the mean kinetic energy of all participants is lower than the second threshold (15 MeV), the cascade process is stopped.

This model executes the exciton model proposed by Griffin [Griffin.J.J (1966)]. Nucleon states are characterized by the number of excited particles and holes (excitons). The

required initial information for calculation of the precompound nuclear stage are the atomic mass number A, charge (Z) of the residual nucleus, its four momentum P_0, the excitation energy U, and the number of excitons n. The number of excitons is the sum of the number of particles p and the number of holes h. The nucleons with a kinetic energy above the Fermi energy are called particles and holes are the nucleons below the Fermi level. At the pre-equilibrium stage of interaction, all possible transitions are taken into account. In the exciton model, the possible selection rules for particle-hole configurations in the source of cascade are: $\Delta h = 0, \pm 1$, $\Delta p = 0, \pm 1$, $\Delta n = 0, \pm 2$ [Gudima.K.K et al. (1983)]. This process only takes into account the emission of neutrons, protons, deutrons, tritium, and helium. The precompound model is implemented until the nuclear system is no longer in an equilibrium state. Further reactions like the emission of fragments or photon emission from excited nucleus are tracked by an equilibrium model [Geant4 (2015)].

De-excitation

After the collision and equilibration phase, the compound nuclei has reached statistical equilibrium but is still in an excited state. The excited nuclei are then de-excited by different processes depending on the excitation energy, the atomic number, and the atomic mass of the nuclei. This phase is treated by G4ExcitationHandler which handles five different de-excitation mechanisms. Evaporation (of light particles) is the main process in de-excitation, which is implemented according to the Weisskopf-Ewing approach [Weisskopf and Ewing (1940)]. Fission process is an evaporation competitive channel for heavy nuclei ($Z > 200$). The Fermi break up model is applicable for light nuclei ($A \leq 16$) and for small excitation energies, i.e. where comparable to their binding energies. The Multifragmentation model is applicable for more highly excited nuclei. Photon evaporation process is also a competitive channel for evaporation and other de-excitation processes [Dedes et al. (2014), Geant4 (2015)].

2.4 iThemba Laboratory for Accelerator-Based Sciences (iThemba LABS)

iThemba LABS is located at Old Faure Road, Faure, Cape Town, South Africa, which is a group of multi-disciplinary research laboratories administered by the National Research Foundation (NRF). It offers many basic and applied research opportunities using particle beams, particle therapy for cancer treatment, and accelerator products of radioisotopes for nuclear medicine and for research purposes. The variable energy Separated-Sector Cyclotron (SSC) provides proton beams with maximum energy of 200 MeV. The beam lines are directed to vaults for nuclear physics research, proton and neutron therapy and production of radioisotopes as shown in figure 2.4. A High intensity 66 MeV proton beam is employed for neutron therapy and radioisotope production while a 200 MeV energy proton

beam is used for proton radiation therapy. The nuclear physics department conducts research and training at post graduate levels in applied and basic nuclear physics. The main facilities in this department are the AFRODITE detector array, the K600 magnetic spectrometer, and the large D-line scattering chamber.

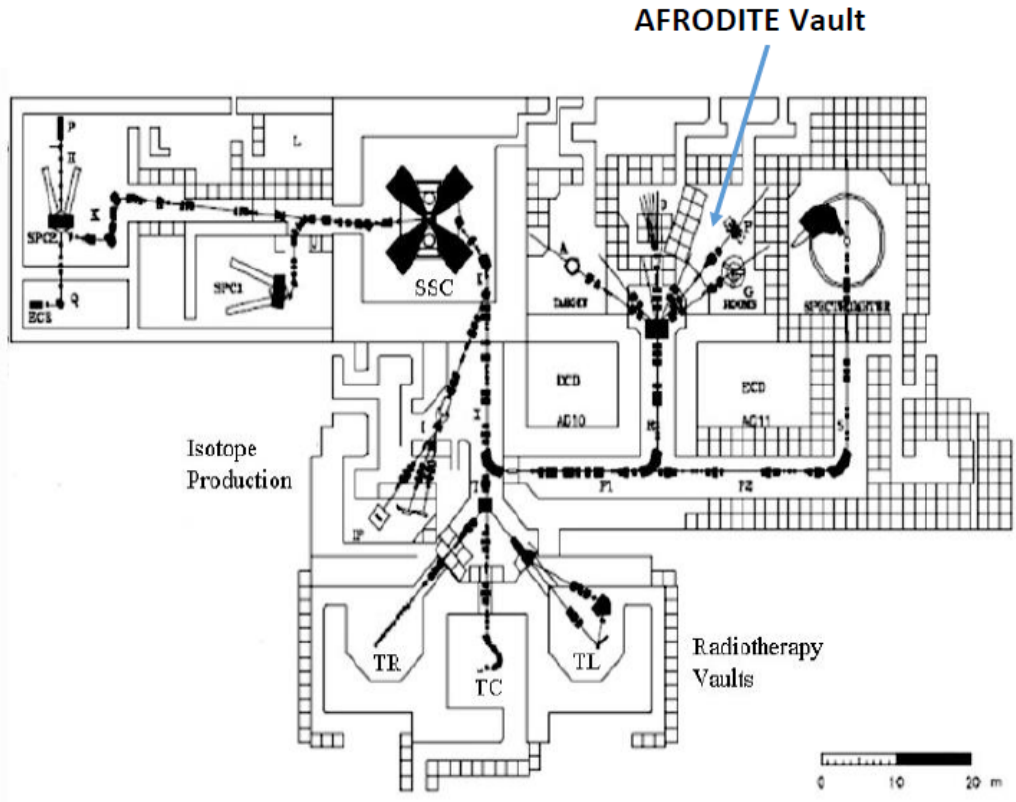

Figure 2.4: Layout of the iThemba LABS facilities. TR is proton therapy, TC is neutron therapy, TL is proton therapy beam line 2(unfinished), SSC is the cyclotron, and AFRODITE vault is for AFRODITE detector system.

2.4.1 AFRODITE array

AFRODITE stands for **AFR**ican **O**mnipurpose **D**etector for **I**nnovative **T**echniques and **E**xperiments. It is a medium-sized array that has the ability to detect both low and high energy photons with a reasonable efficiency by using escape suppressed n-type high purity Germanium (HpGe) clover detectors and p-type LEPS (Low Energy Photon Spectrometer) detectors. A segment of the AFRODITE array is shown in figure **??**. The AFRODITE frame has the shape of a small rhombicuboctahedron with sixteen detector positions. The target chamber also consists of the same geometry with thin Kapton windows. In this cross section measurement experiment, eight clover detectors were used with four clovers

placed at 90° angle and the remaining four clovers positioned at 135° angle to the beam direction with the support of rhombicuboctahedron frame as shown in figure 2.6.

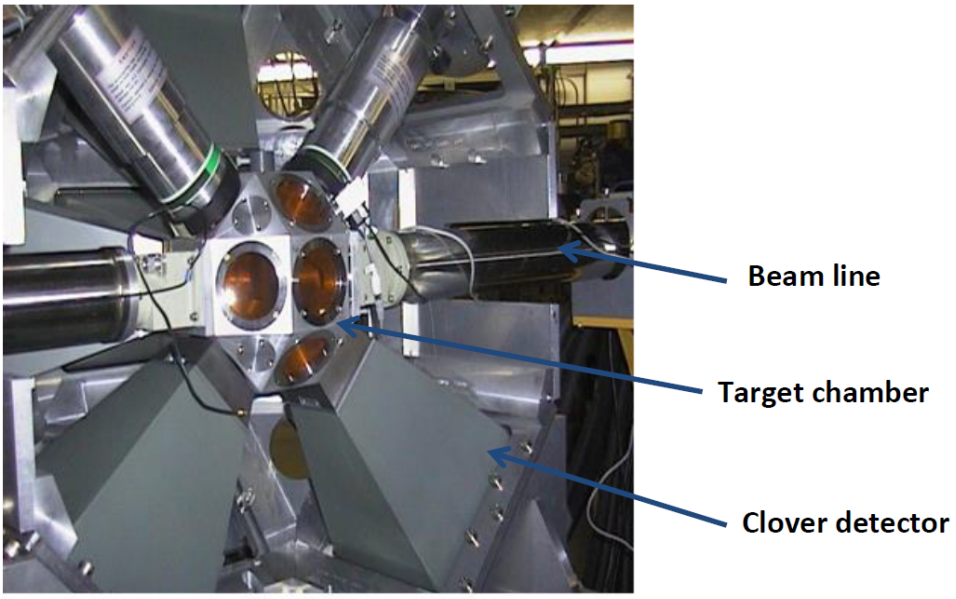

Figure 2.5: A segment of the AFRODITE array showing the rhombicuboctahedron shaped target chamber

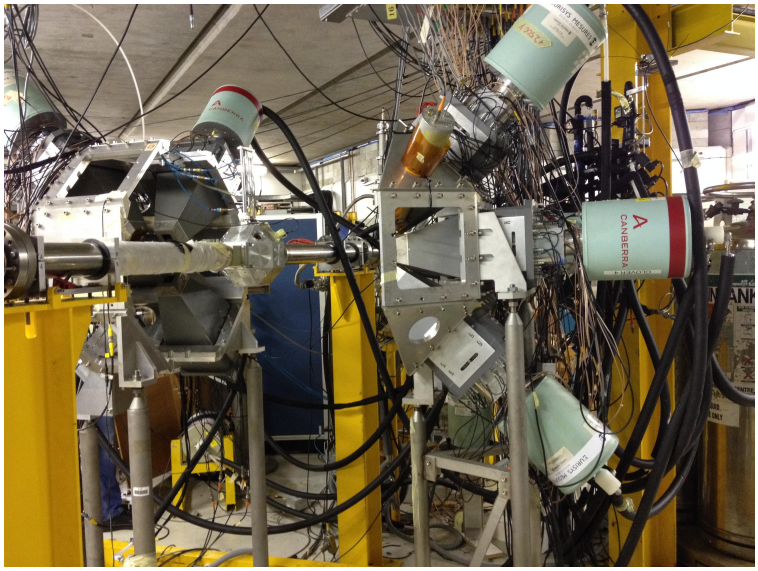

Figure 2.6: The AFRODITE array, the eight clover detectors, the target chamber, and the beam line. This figure shows the detector frame when the fixed clover detectors are moved apart in order to place the target inside the target chamber.

2.4.2 Clover detectors and detection modes

Each clover detector consists of four n-type separate coaxial HpGe crystals that are packed in the configuration of a four leaf clover and placed in the same cryostat. The geometric arrangement of the clover detectors is shown in figures 2.7 and 2.8. In order to optimize close packing, the high purity Germanium crystals are tapered at the front face providing a 41 mm X 41 mm square face. Additional details regarding the crystals can be found in table 2.1.

The detection of gamma rays is based on the three major interactions of photons with matter. These interaction processes are the photoelectric effect, the Compton effect, and pair production. In the clover detectors, there are two detection modes available, direct and addback modes. In direct mode, each of the segment of the clover detector are treated independently and the gamma energy deposition is measured separately for each crystal. This allows determination of the direct detection efficiency of each crystal. In addback mode, the four segments of the clover detector are treated as one detector and the gamma energy deposition for the crystals is summed together. The added signal from the adjacent crystals enhance the detector efficiency increasing the detection of Compton scattered gammas entering adjacent crystals or 511 keV annihilation photons escaping one crystal and then detected in a neighbouring crystal. In addback mode, the signals are added and stored in the addback spectrum giving the clover detectors higher detection efficiency and higher energy resolution.

Table 2.1: Specifications of AFRODITE clover detectors. Source: Newman.R.T et al. (1995).

Specification	Clover detectors	Escape suppressors
Supplier	Eurisys	Crismatec
Number of clovers	8	8
Crystal type	HpGe	BGO
Diameter (before shaping)	51 mm	
Length (before shaping)	71 mm	~ 26 cm
Thickness		$\sim (4-20)$ mm
Solid angle of detector (percentage of 4π)	1.34%	
Taper angle	7.1°	
Distance between target center and crystal surface	19.6 cm	

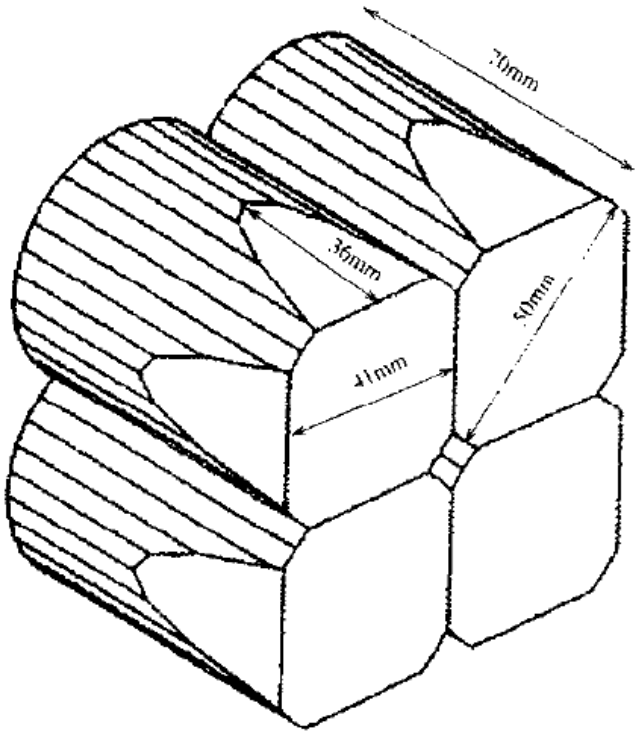

Figure 2.7: Schematic diagram of four high purity germanium crystals in a clover detector. Source: Jones.P.M et al. (1995)

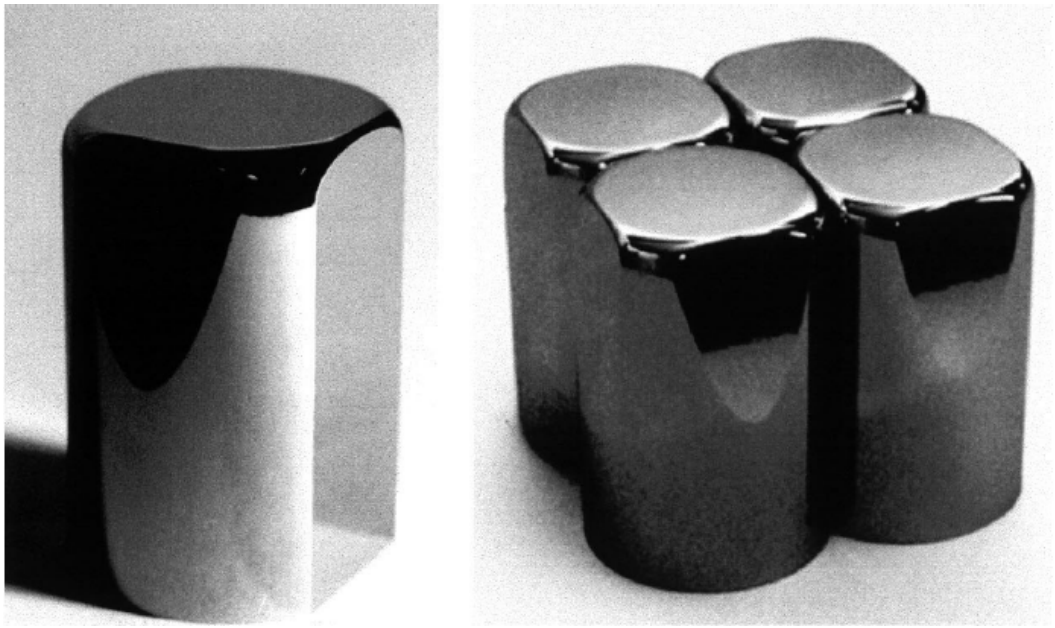

Figure 2.8: Left: Individual high purity germanium crystal. Right: Closely packed four high purity germanium crystals in a clover detector. Source: Duchene.G et al. (1999)

2.4.3 Compton escape suppression

Compton escape suppression is used to improve the signal to background ratio by reducing the background radiation. This background is normally produced by gamma rays which partially deposit their energy in the detector volume resulting in a large Compton continuum. In order to reduce the contribution of scattered gamma rays, the high purity germanium crystals are surrounded by BGO (Bismuth Germanate- $Bi_4Ge_3O_{12}$) scintillation detectors as shown in figures 2.9 and 2.10. The suppression of the Compton continuum is an effective way to increase photo peak efficiency. The clover detectors and BGO detectors are operated in an anti-coincidence mode which means that if an event is detected in both detectors simultaneously, then that event will be rejected. Both NaI and BGO scitillation detectors have been used for the purpose of Compton suppression, but BGO is more suitable since it has good timing properties and a higher density (7.13 g cm^{-3}). Due to its high density, a relatively small amount of BGO material is required to suppress the scattered events. Further, in the BGO scintillation crystal, Bi has a high atomic number (Z=83), resulting in a higher detection efficiency [Duchene.G et al. (1999), Glenn2010].

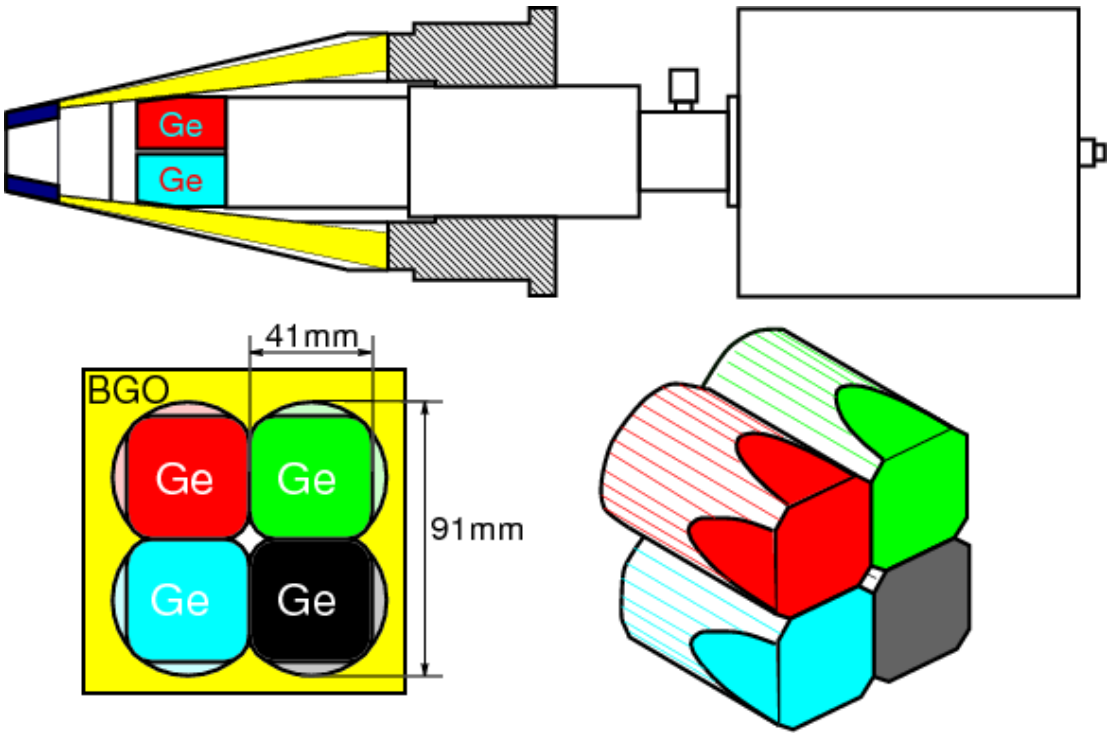

Figure 2.9: Top panal: Schematic diagram of clover with BGO Compton suppression shield (yellow) connected to liquid nitrogen dewar. Bottom left: The cross section view of germanium crystals and BGO. Bottom right: Closely packed germanium crystals. Source: Szücs et al. (2010)

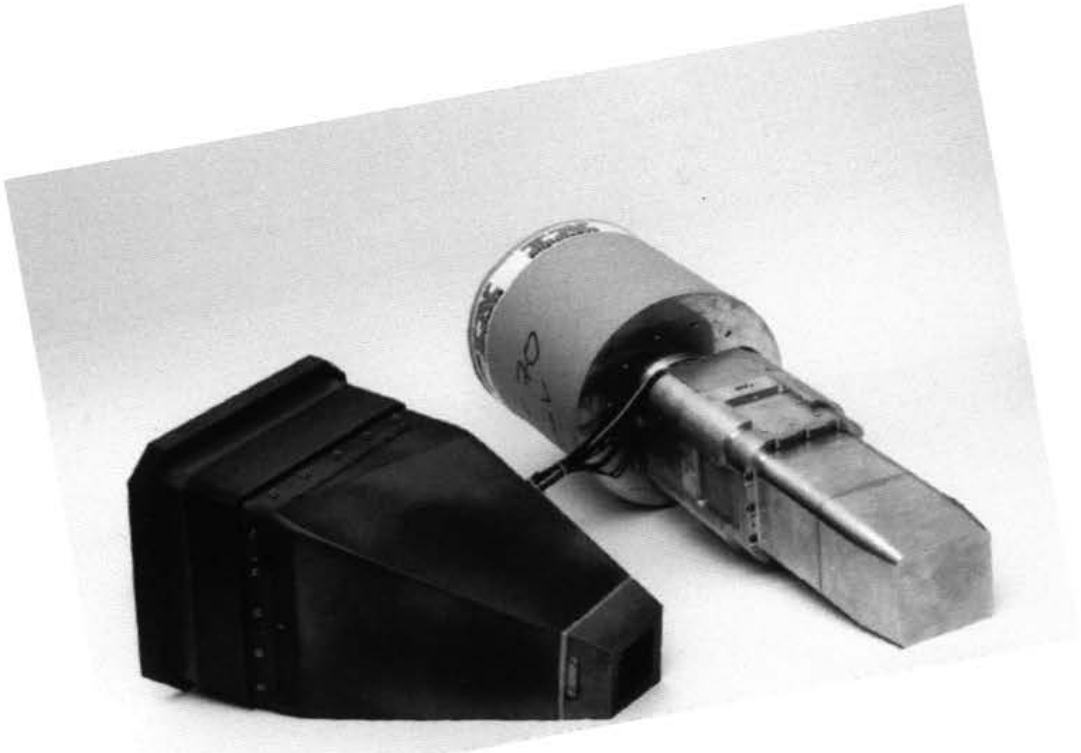

Figure 2.10: Left hand side: BGO Compton suppression shield. Right hand side: Clover detector. Source: Duchene.G et al. (1999)

2.5 Geometry of Geant4 AFRODITE model

The AFRODITE clover detector system was modelled using the Geant4 Monte-Carlo code (version 10.01.p03). The geometry of the germanium crystals, the BGO crystals, the rhombicuboctahedron shape target chamber, and the collimator were developed using CAD drawings. The complex geometry of the AFRODITE clover detector system was imported using the direct CAD model import interface, CADMesh. The CADMesh plugin for Geant4 can be found in the christopherpoole/CADMesh github repository [Poole.C (2012)].

A clover was designed by using four germanium crystals according to the HPGe crystal structure of iThemba LABS AFRODITE clover detector as discussed in section 2.4.2. The Geant4 model of closely packed germanium crystals is shown in figure 2.11. The entire germanium crystal assembly was placed inside the aluminium case as shown in figure 2.12. The crystal assembly was placed inside the 16 BGO crystals as shown in figures 2.13 and 2.14. In the Geant4 AFRODITE model, each BGO crystal is connected to photo multiplier tube (PMT) but the PMTs were not included in the simulation studies. The clover detector system as in the experimental setup is shown in figure 2.15. The complete geometry of the AFRODITE model can be found in the KevinCWLi/AFRODITE-PR239A github repository [Li (2015)].

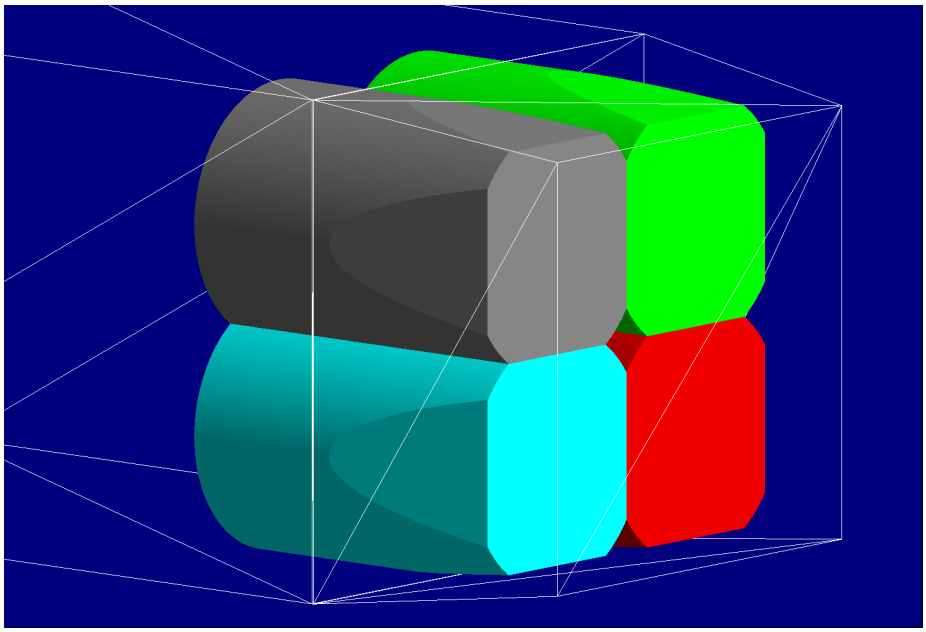

Figure 2.11: Geant4 model of the closely packed germanium crystals in an AFRODITE clover.

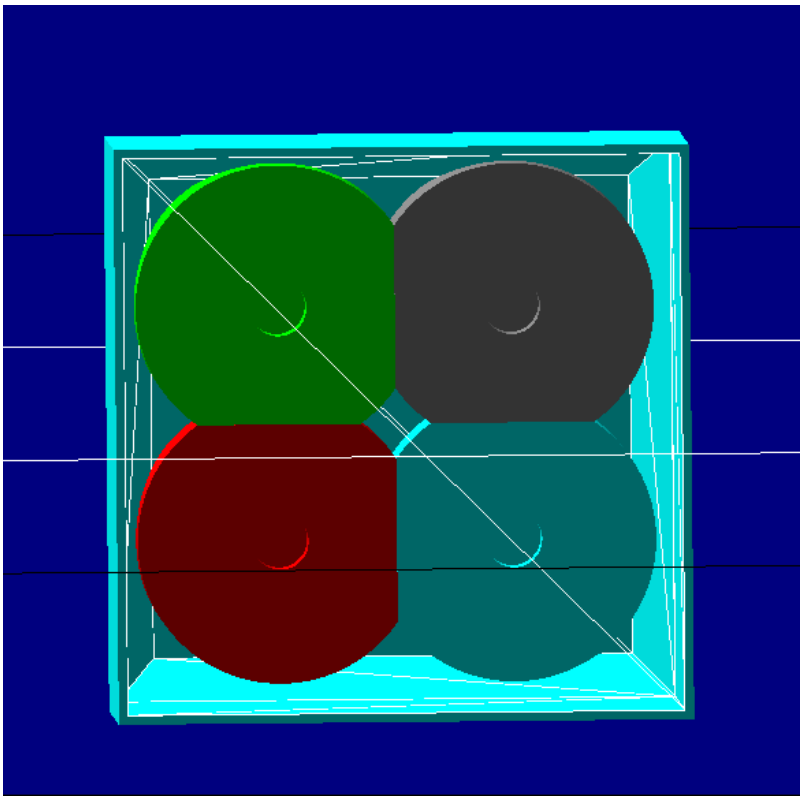

Figure 2.12: Geant4 model of the germanium crystal assembly inside the aluminium case.

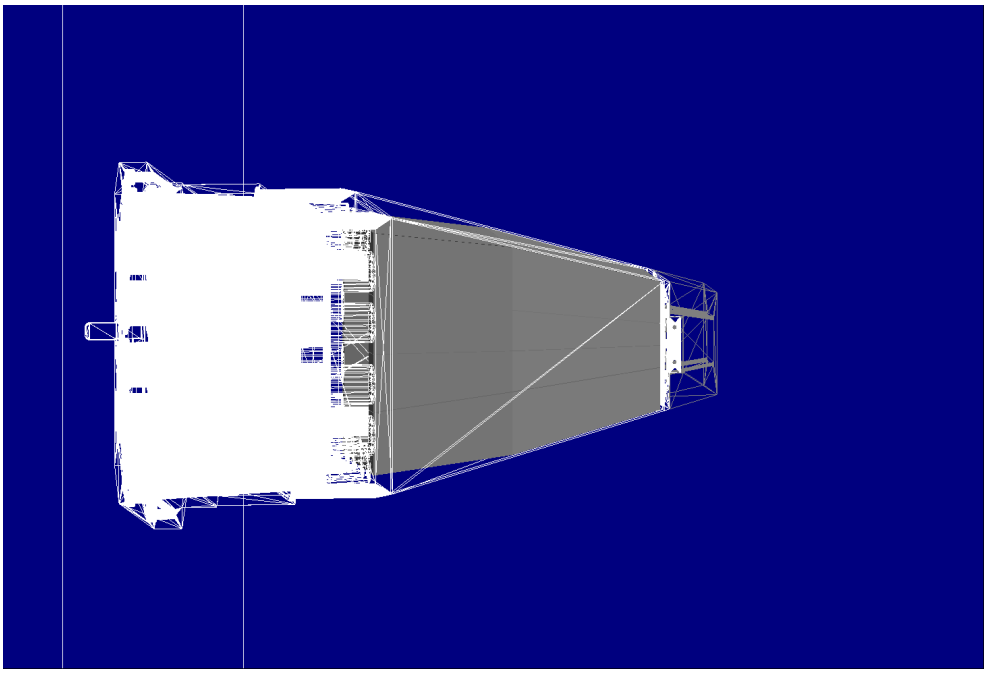

Figure 2.13: Geant4 model of the Compton escape suppression shielding in the AFRODITE detector system.

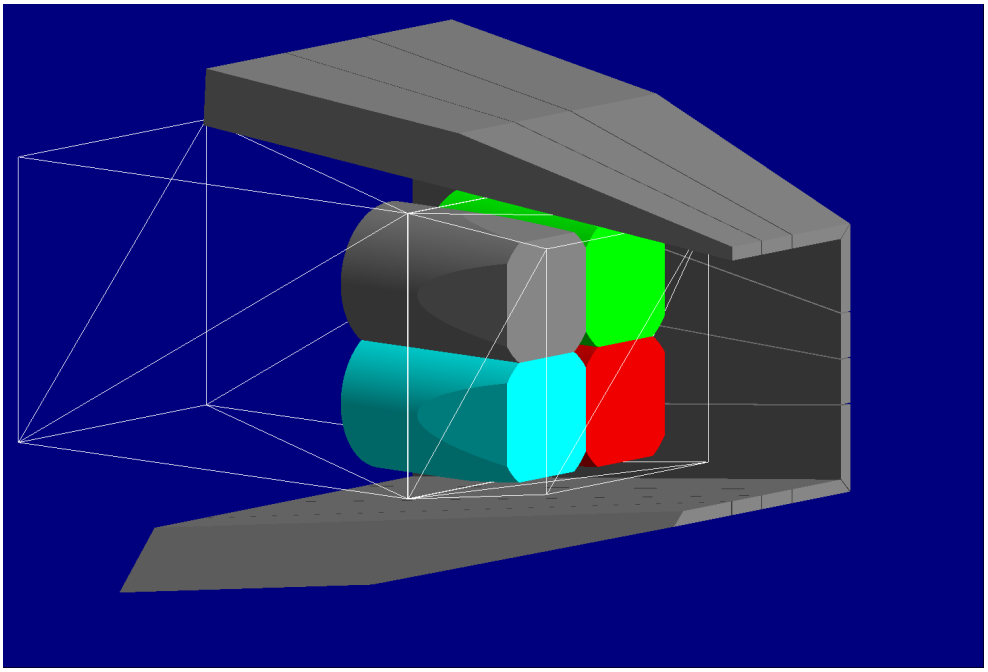

Figure 2.14: Geant4 model of the closely packed germanium crystals housed inside the Compton escape shielding.

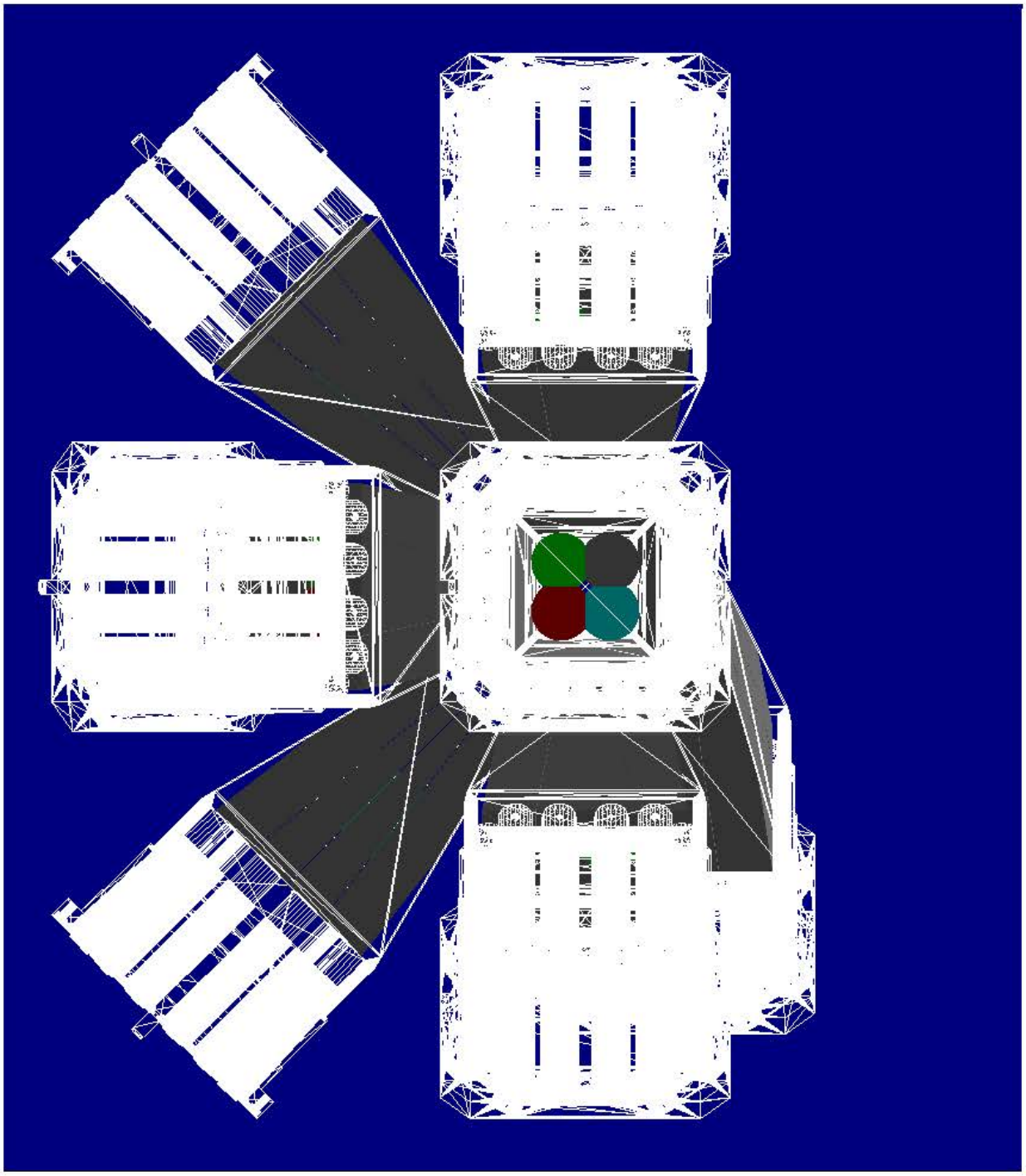

Figure 2.15: Complete simulated clover detector setup identical to experimental arrangement of AFRODITE array.

Chapter 3

Measurement of prompt gamma cross-section using AFRODITE clover detectors

This chapter reports on the cross-section measurements carried out using the AFRODITE detector at iThemba LABS, in Faure, Cape Town, South Africa. For these cross section measurements, five different proton beam energies were used. The clover detector arrangement for this experiment, the target setup, the proton irradiation procedures, the acquisition of experimental data, the energy calibration procedures, and the detection efficiency measurements will all be discussed in this chapter. Lastly, the differential and total cross-section measurement techniques will be explained.

3.1 Experimental cross section measurement

The measurements were carried out with the nuclear research division at iThemba LABS using the AFRODITE clover detector system. The experiment was performed from 26$^{\text{th}}$ January to 2$^{\text{nd}}$ February 2015 as the second phase of a three-part experiment. There are two injector cyclotrons (SPC1 and SPC2) (SPC- Solid-Pole Cyclotron) available at iThemba LABS. SPC1 is used for light ions while SPC2 is used for polarized hydrogen ions and heavy ions. The beam is extracted from the injector cyclotron and then accelerated in the separated sector cyclotron (SSC) until the required beam energy is acquired. The accelerated beam is delivered as a series of pulses and then guided through the high energy beam line to the nuclear experimental vault by using dipole and multipole magnets for bending and focusing respectively. Starting in 2014, the first part of this experiment covered the energy range of 26 MeV to 66 MeV for ^{12}C, Mylar ($C_{10}H_8O_4$), ^{24}Mg, ^{28}Si, and ^{56}Fe targets. For this measurement (second part of experiment), a proton beam was used

at the following energies 66, 80, 95, 110, 125 MeV for the same targets. A third set of experiments is planned for higher proton energies.

3.1.1 Detector arrangement and target setup

For these measurements, eight clover detectors were used in the AFRODITE array. Four clovers were placed at 90^0 and the other four clovers were placed at 135^0 to the beam line. The experimental clover detector arrangement is shown in figure 3.1. The proton beam used a typical beam current in the range of 1-3 nA. As mentioned in the above section, several targets were used to measure the cross-section. This work focused on measuring the cross-section using a natural carbon target (thickness = 8.40±0.07 mg/cm^2) and a Mylar ($C_{10}H_8O_4$) target (thickness = 7.00±0.08 mg/cm^2). Thin targets were selected to avoid multiple interactions and the solid targets were chosen for an easy handling in the experiment. These targets were prepared at iThemba LABS and are shown in figure 3.2.

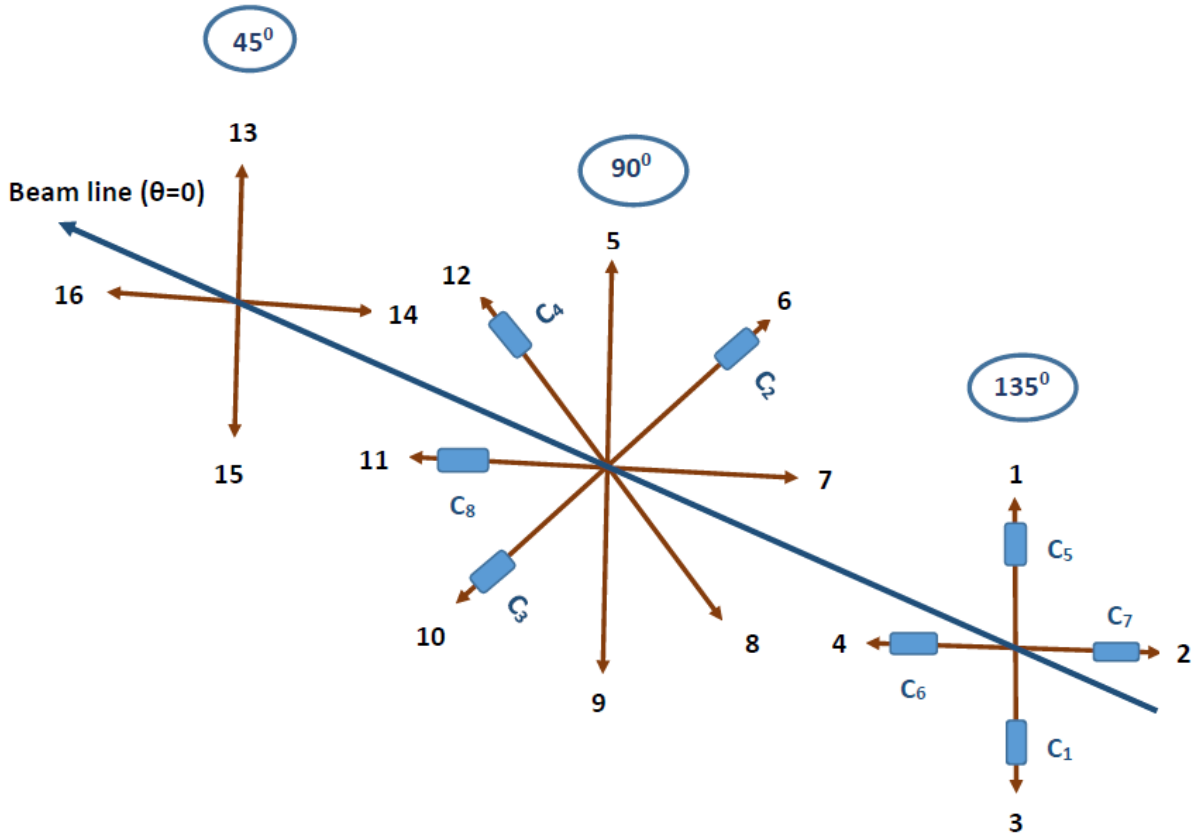

Figure 3.1: AFRODITE clover detector arrangement for the cross-section measurement experiment. Clovers were placed at the following positions: C_1, C_5, C_6, C_7 at 135^0. C_2, C_3, C_4, C_8 at 90^0.

Figure 3.2: This figure shows the prepared mylar (in the middle) and carbon (on the right) targets at iThemba LABS for cross-section measurement.

The targets were fitted in the target ladder as shown in figure 3.3 and then the target ladder was fixed into the target chamber as shown in figure 3.4. In addition to the targets, the target ladder typically includes an empty frame (used for background measurements) and the "ruby". The ruby is a metal plate with a small hole and is used to align the beam from the cyclotron. There is also a small transparent glass round window on the target chamber with a camera connected to the control room to verify visual alignment of the targets. The control panel for changing the targets and measuring the beam current is shown in figure 3.5. Figure 3.6 shows the eight clover detectors fixed in the left and right frames and the frames pushed together in measurement position, giving a distance of 19.6 cm between the target and the face of the detectors.

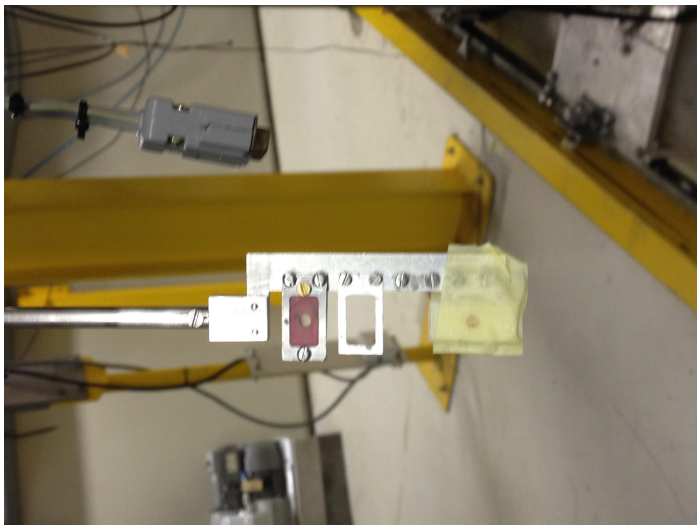

Figure 3.3: The target ladder in which four targets can be accommodated. The one on the left is the ruby which is used for beam focusing.

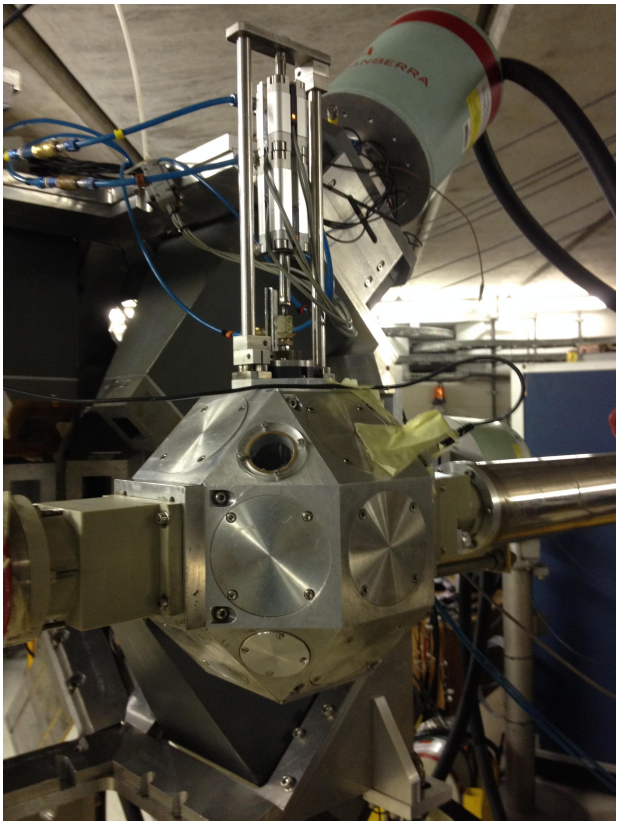

Figure 3.4: The rhombicuboctahedron shaped target chamber which is supported by the beam line, and the target ladder fixed to the top of the target chamber.

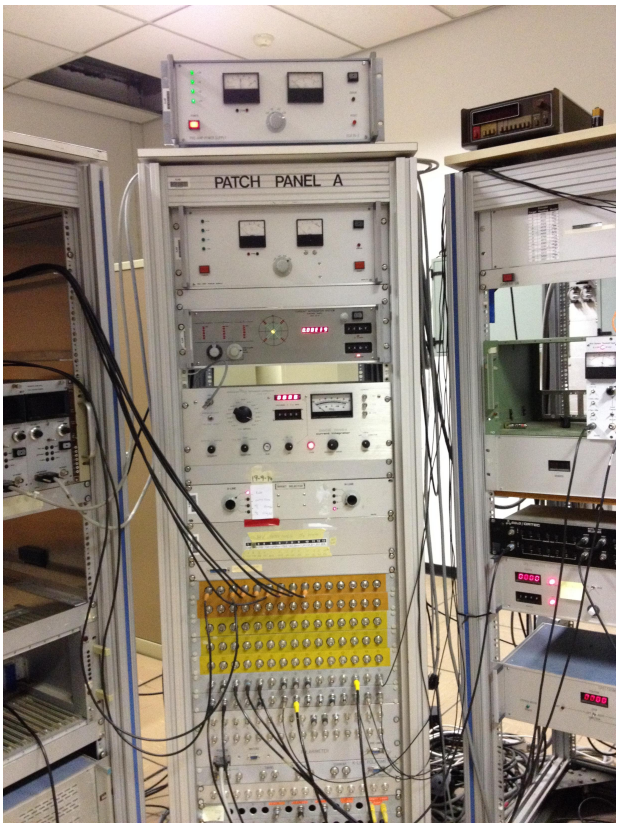

Figure 3.5: The control panel for changing the targets and the beam current measurement is located in the data room

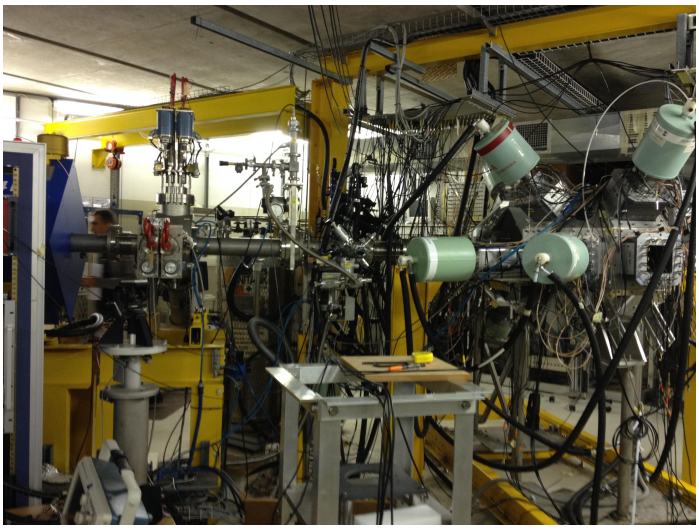

Figure 3.6: The experimental setup of AFRODITE array with the clover detectors in final measurement position.

3.1.2 Proton irradiations

The initial cross section measurement began with a proton beam energy of 80 MeV and a beam current of 2 nA and 3 nA for the carbon and mylar targets, respectively. The proton beam bombarded each target for 45 minutes and was then followed by 15 minutes for radioactive decay measurements. Background radiation measurements were performed with the empty frame for both beam-on and beam-off conditions. These background measurements were repeated for each energy employed in experiment. Each day, the proton beam energy was tuned to a new energy in this order: 95 MeV, 110 MeV, 125 MeV and measurements were taken. The final cross section measurements were done with a 66 MeV proton beam in repetition of measurements performed during the previous experiment. Lastly, the calibration source measurements were repeated and the room background was measured for three days.

3.2 Acquisition of experimental cross-section data

The following section briefly explains the data acquisition processes used in this experiment.

3.2.1 Digital Data Acquisition System (DDAS)

The DDAS is fabricated by two distinct processes, the front end and the control. The front end comprises of a PXI (**P**CI (Peripheral Component Interconnect) e**X**tensions for **I**nstrumentation) crate and XIA cards (produces X-ray and gamma-ray digital signal). The XIA cards are connected to a server PC (Personal Computer) which manipulates the data acquisition process and data collection modules. The control process runs on the server PC and consists of merge, filter, event-building, storage and Graphic Unit Interface (GUI) components. Merge is a standard TDR (Time-Domain Reflectometer) merge process, which receives data from the event collectors. The filter and event building processes read and filter the data. The TapeServer receives and stores the data [iThemba LABS (2016)]. Figure 3.7 shows the control GUI for operating the data acquisition system and figure 3.8 shows DDAS parameter setting GUI used to optimize the data acquisition.

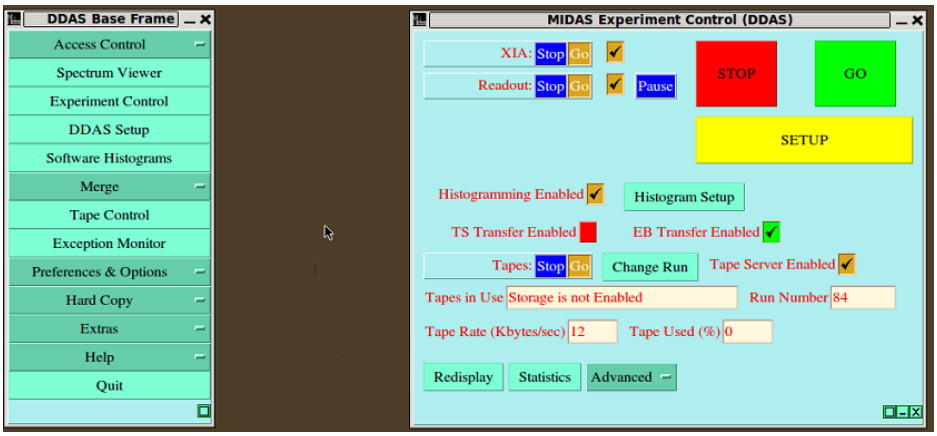

Figure 3.7: System control. Left panel: The base frame window. Right panel: The experiment control window. The system can be operated using STOP and GO button. This procedure is only required when changing the parameters or setting up the system. Source: iThemba LABS (2016)

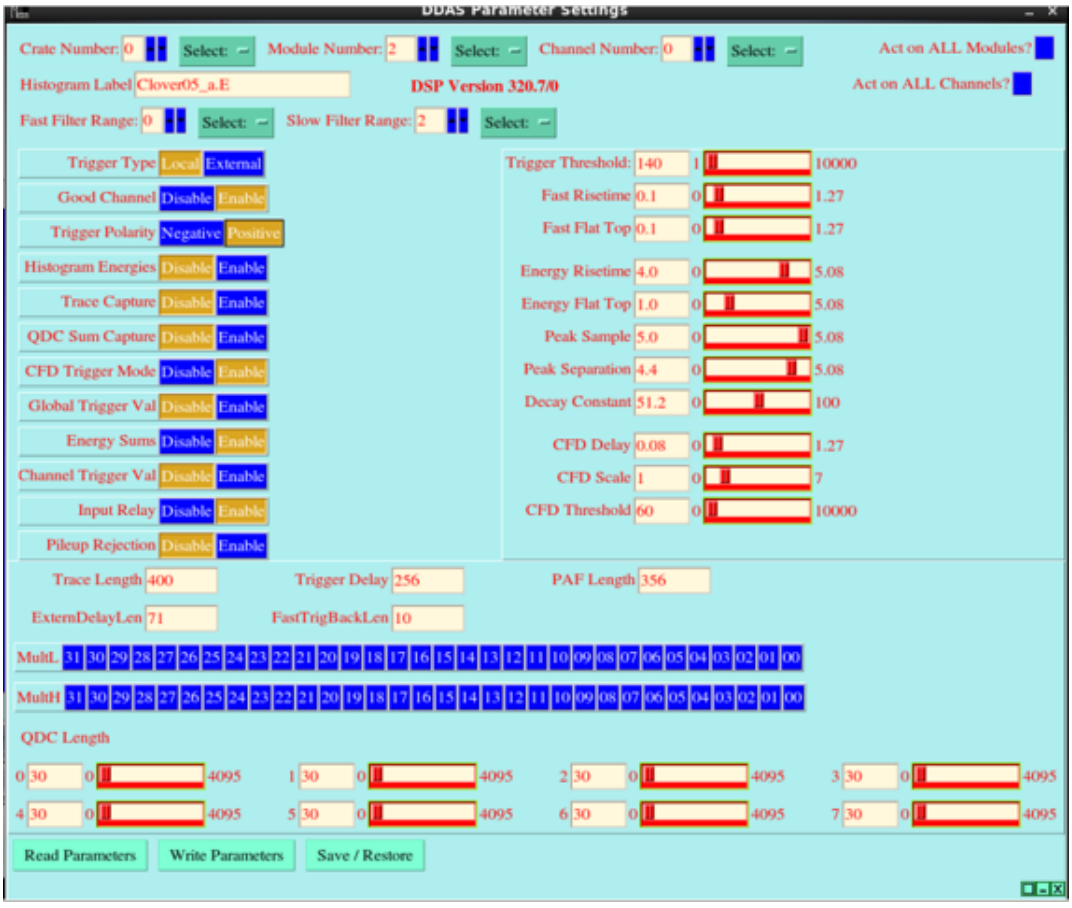

Figure 3.8: The digital data acquisition set up window which shows different parameters that can be adjusted to optimize the resolution of the system. Source: iThemba LABS (2016)

3.2.2 Experimental data processing

Once the data is captured, the first part of the data analysis process is conversion of the binary data into a easily readable format. Simsort [Papka.P (2007)] is a data analysis package to convert raw binary data into a ROOT file. ROOT is an object oriented data analysis program developed by CERN (European Organization for Nuclear Research). A main feature of ROOT is a data container called TTree. The TTree data structure in ROOT has branches (TBranch) and leaves (TLeaf). Simsort passes the binary source data into the TTree structure, making it more easily accessible. Finally, the complete data set is stored as a ROOT file and available for further analysis. The flow chart of SimSort code is shown in figure 3.9.

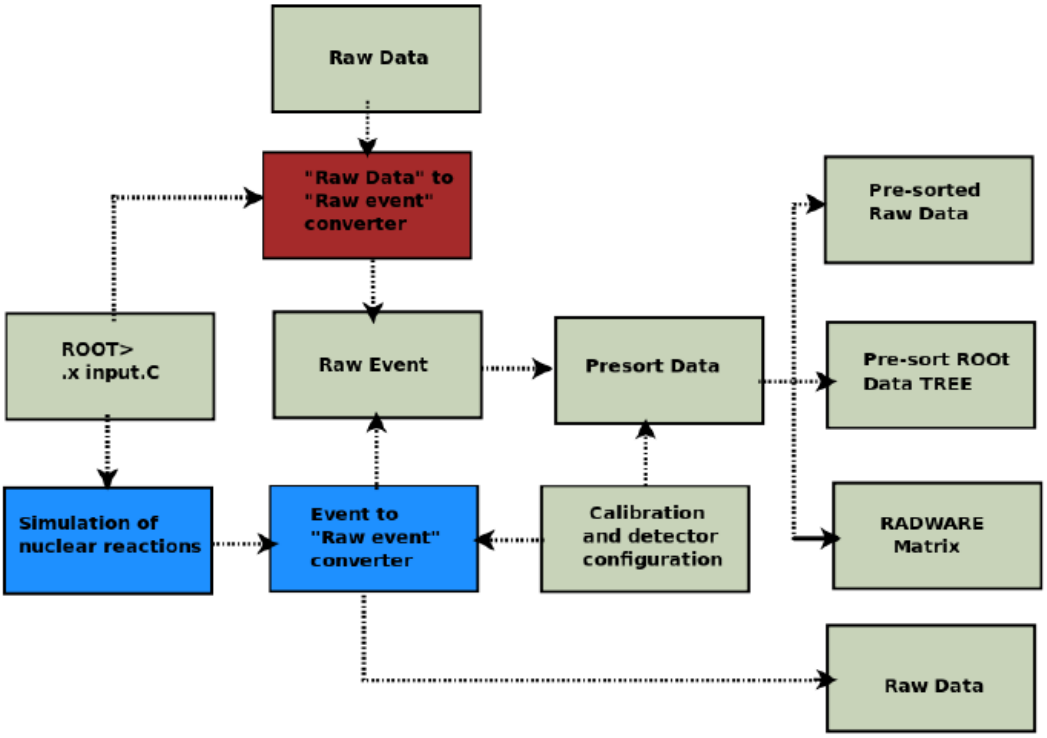

Figure 3.9: The flow diagram of SimSort code. Source: Papka.P (2007)

3.2.3 Dead time and background subtraction

The next step in the data analysis process is correction for dead time and background subtraction. The dead time is common to all detector systems. In order to detect two separate events, there is minimum amount of time required between the events to record the two separate pulses. This minimum time may arise either from the associated electronics

or may be set by the processes in the detector itself. The minimum time required for separation of two events is called the dead time of the system [Knoll.F.G (2010)]. If the detector system uses both analog and digital electronics, the dead time most likely arises from the electronics. The most likely contribution of dead time for the AFRODITE system is due to the data acquisition system when the system is busy with coding and data transferring.

For this experiment dead time was measured as a function of the beam current, shown in fig 3.10. The dead time measurements [Yahia-Cherif et al. (2015)] were performed as a part of the first phase of this experiment. The dead time was measured as a percentage of the total number of counts. For example, if the beam current is 1 nA, the dead time correction is 2% of the total counts. The dead time correction is then incorporated into the background subtraction.

For each of the 30 (2 crystals were not functioning) high purity germanium crystals used in the cross-section measurements, the raw energy spectra is background subtracted and dead time corrected. The spectra was first dead time corrected by adding the appropriate percentage based on the beam current. Then the room background was subtracted according the data acquisition time, followed by the empty frame background with beam-off again according the data acquisition time, then the empty frame background with beam-on (according the total number of incident protons). This results in the final energy spectra to be used to calculate the peak areas for each crystal.

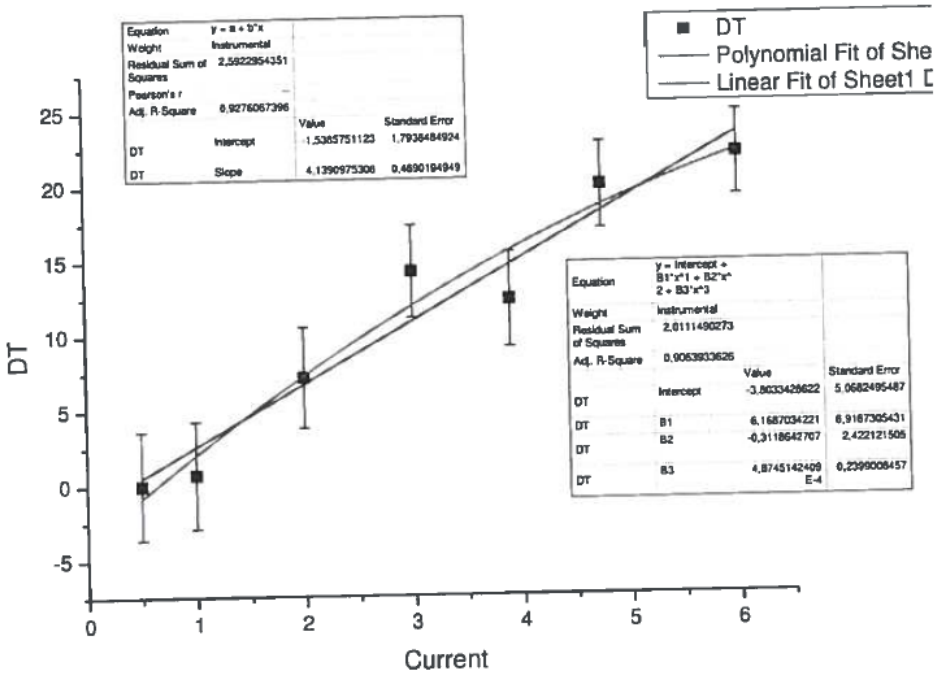

Figure 3.10: Dead time correction in percentage as a function of beam current.

3.3 Procedures for experimental cross-section measurements

Firstly, this section explains the energy calibration procedures and the absolute detector efficiency measurements. Then, this section illustrates the total cross-section calculation procedures for the 4.438 MeV ^{12}C and 6.129 MeV ^{16}O photo peaks. Finally, it explains the differential cross-section calculations and the associated uncertainty propagation.

3.3.1 Energy calibration procedures

The energy calibration was performed before running the cross section measurements by using three standard gamma emitting sources,^{152}Eu, ^{60}Co, and ^{137}Cs. In order to reproduce the distance between the target and the detectors, the gamma sources were placed at the target position. Aluminium (0.88 mm thickness) and Copper (1.21 mm) absorbers were used to reduce the counts from low energy X-rays, with the copper placed closest to the source followed by the aluminium. The data were collected for 30 minutes for each gamma emitting source in direct detection mode. These collected data sets were used to calibrate the energy by considering 17 photo peaks from the above gamma sources. The same data set was also used to determine the absolute detector efficiency for each high purity germanium crystal.

3.3.2 Detection efficiency

The efficiency of the detector system is an important parameter, which corresponds to the probability of a gamma being detected. It depends mainly on the type of detector, the distance between the source and the detector system, the shape and size of the detector, and the type of radiation (gamma, alpha, and beta radiation) and its energy. The different types of efficiency can be defined as follows [Gilmore and D.Hemingway (1996)].

Relative efficiency is generally defined as the measure of efficiency relating a detector's efficiency to that of a standard sodium iodide scintillation detector for a standard source, ^{60}Co 1332 keV photo peak. The **full energy/photo-peak efficiency** corresponds to the detection efficiency specific to full energy peak pulses only. **Intrinsic efficiency** is defined as the ratio between the number of pulses detected and number of radiation quanta striking the detector. It is independent of the detector and source geometry and this efficiency is a basic parameter of the detector type. **Absolute detector efficiency** relates the number of gammas emitted by the radioactive source to the number of counts produced by the detector at a specific location. The absolute efficiency is defined as [Rajput et al. (2002), Nikolic et al. (2014)],

$$\varepsilon = \frac{N}{N_0 P_\gamma(E) t e^{-\lambda t_d}} \tag{3.1}$$

where, N is the total area under the photo peak of γ ray energy E, N_0 is the activity of the gamma source in Becquerel, $P_\gamma(E)$ is the emission probability of a gamma ray at energy E (calibration source values shown in table 5.1), t is the acquisition time, t_d is the decay time, and $\lambda = ln2/T_{1/2}$, is the decay constant.

The uncertainty in the efficiency measurements can be calculated using the uncertainty propagation of error method.

In order to simplify the uncertainty calculations, the absolute detection efficiency equation can be rearranged as shown,

$$\varepsilon = \frac{N}{N_0 P_\gamma(E) t A} \tag{3.2}$$

where, $A = e^{-\lambda t_d}$.

Thus, the uncertainty in the absolute detector efficiency ($U(\varepsilon)$) can be written as,

$$\left(\frac{U(\varepsilon)}{\varepsilon}\right)^2 = \left(\frac{U(N)}{N}\right)^2 + \left(\frac{U(N_0)}{N_0}\right)^2 + \left(\frac{U(P_\gamma(E))}{P_\gamma(E)}\right)^2 + \left(\frac{U(t)}{t}\right)^2 + \left(\frac{U(A)}{A}\right)^2 \tag{3.3}$$

In this experiment, only the statistical uncertainty of net photo peak area ($U(N)$) was considered since the other uncertainties were negligible by comparison. Therefore, the uncertainty in the absolute detector efficiency was calculated using the following equation,

$$U(\varepsilon) = \varepsilon\left(\frac{U(N)}{N}\right) \tag{3.4}$$

where, $U(N)$ and N was measured by fitting of the photo peak to a Gaussian using the OriginPro data analysis program.

3.3.3 Calculating the total cross-section

Generally, the gamma emission from an excited nucleus is not isotropic [Alburger.D.E et al. (2012)]. Therefore, the total gamma ray production cross section cannot be measured by simply integrating the differential cross section since it depends on angular measurements. It must be determined by fitting a Legendre polynomial to the angular distribution of the gamma emission. As discussed in chapter 1, the angular distribution function for the case of the initial nucleus state (I_i) to the final state of the nucleus (I_f) is given by,

$$W(\theta) = \sum_{i}^{l_{max}} a_l Q_l P_l(cos\theta) \quad (l - even), \tag{3.5}$$

For these cross section measurements, two corrections were ignored. The first correction is the transformation of the laboratory frame to the center of mass frame. Typically, the measured angle between the detector and the proton beam (laboratory angle) needs to be

transformed into the center of mass frame for the application of the angular distribution function. However, ignoring this transformation has a very small impact in the cross section measurements [Lesko et al. (1988), Brune (2002)] and will thus be ignored for this experiment.

The second correction is the attenuation coefficients (Q_l) for the actual detector setup in equation 3.5. The attenuation coefficients can be analytically calculated according to the detector setup [Ferguson.A.J (1965), Rose (1953)] with the attenuation coefficient for point like detectors being one. For this cross section measurement, these coefficients are assumed to be one since the solid angle for the high purity germanium crystal is small and approximates a point detector. The angular distribution function can be rewritten when ignoring the attenuation coefficients as,

$$W(\theta) = a_0 + a_2 P_2(cos\theta) + a_4 P_4(cos\theta) + ... \tag{3.6}$$

where, $P(cos\theta)$ is the Legendre polynomials and a_0, a_2, and a_4 are the Legendre coefficients.

The angular distribution function for some multi-polarities are written below [S.Krane (1987), Iliadis (2007)].

For the E_1/M_1 transition,

$$W(\theta) = a_0 + a_2 P_2(cos\theta) \tag{3.7}$$

For the E_2/M_2 transition (4.438 MeV of ^{12}C (2^+, 4.439 MeV $\rightarrow 0^+$, ground state), (an E_2 transition)),

$$W(\theta) = a_0 + a_2 P_2(cos\theta) + a_4 P_4(cos\theta) \tag{3.8}$$

For the E_3/M_3 transition (6.129 MeV of ^{16}O (3^-, 6.130 MeV $\rightarrow 0^+$, ground state), (an E_3 transition)),

$$W(\theta) = a_0 + a_2 P_2(cos\theta) + a_4 P_4(cos\theta) + a_6 P_6(cos\theta) \tag{3.9}$$

where,

$$P_2(cos\theta) = \frac{1}{2}(3cos^2\theta - 1) \tag{3.10}$$

$$P_4(cos\theta) = \frac{1}{8}(35cos^4\theta - 30cos^2\theta + 3) \tag{3.11}$$

$$P_6(cos\theta) = \frac{1}{16}(231\cos^6\theta - 315cos^4\theta + 105cos^2\theta - 5) \tag{3.12}$$

For the 4.438 MeV gamma rays from ^{12}C (an E_2 transition), there are three terms in the angular distribution function (equation 3.8), so at least three points are required to fit the function and determine the total cross section. Consequently, the four high purity germanium crystals in the clover detectors placed at 135^0 were separated as two crystals at 130^0 angle to the beam direction, and two crystals at 140^0 angle to the incident beam. The 90^0 clover could not be separated since the angular distribution is symmetric about the 90^0 angle [Kiener et al. (1998), Lesko et al. (1988), Lang et al. (1987), Dyer et al. (1981)]

but these three angular positions (90^0, 130^0, 140^0) were sufficient to fit the fourth order polynomial.

For the 6.13 MeV gamma rays from ^{16}O (an E_3 transition), four different angles measurements are required to provide a fit since there are four terms in the angular distribution function. In order to find the total cross section for the 6.13 MeV peak, the symmetry of the angular function was used to mimic the additional data points and thus provide a fit to the function. More details of the total cross-section calculations are given in sections 5.3.4 and 5.3.5.

3.3.4 Calculating the differential cross section

As discussed in chapter 1, the differential cross section can be calculated by using this formula,

$$\frac{d\sigma}{d\Omega} = \frac{N_{events(\Delta\Omega)}}{N_{incident}} \quad \frac{A}{dx\rho N_{Avo}\varepsilon} \tag{3.13}$$

The number of detected events (N_{events}) in a particular photo peak can be calculated by measuring the area under the photo peak. The detected events for the ^{12}C 4.438 MeV peak were measured using the OriginPro data analysis program. Due to Doppler broadening and the very short life time of its excited state, the ^{12}C 4.438 MeV gamma has a broad peak and this peak does not have a Gaussian shape. Therefore, in order to find the area under the 4.438 MeV photo peak, the counts for each channel in the photo peak were added individually. The background for each photo peak was manually fit using a hand-drawn curve as shown in figure 5.17. The background for each channel in the photo peak was then subtracted from the total count.

3.3.5 Uncertainty propagation for differential cross section

In order to calculate the uncertainty in the differential cross section measurements, a simplified version of equation 3.13 is used. If, $dx\rho = t_a$ is area density, then:

$$\frac{d\sigma}{d\Omega} = \frac{N_{events(\Delta\Omega)}}{N_{incident}} \quad \frac{A}{t_a N_{Avo}\varepsilon} \tag{3.14}$$

The uncertainty in the differential cross section can then be written as (assuming no uncertainty in A and N_{Avo}),

$$U\left(\frac{d\sigma}{d\Omega}\right) = \left(\frac{d\sigma}{d\Omega}\right)\sqrt{\left[\frac{U(N_{events})}{N_{events}}\right]^2 + \left[\frac{U(N_{incident})}{N_{incident}}\right]^2 + \left[\frac{U(t_a)}{t_a}\right]^2 + \left[\frac{U(\varepsilon)}{\varepsilon}\right]^2} \tag{3.15}$$

The uncertainty in the number of events (N_{events}) was calculated statistically which is based on manual drawing for background subtraction and the uncertainty in the number of incident particles ($N_{incident}$) was calculated as 5% of the integrated charge measured by the Faraday cup during the experiment as used in all AFRODITE experiments. The uncertainty in the target thickness (t_a) was measured during target preparation. Finally, the uncertainty in the absolute detector efficiencies (ε) for the energies 4.438 MeV (^{12}C) and 6.129 MeV (^{16}O) was calculated by looking at the uncertainty in the fitting function coefficients, discussed below.

The fitting function for the absolute detector efficiency response curve is,

$$y = A_1 e^{-x/t_1} + A_2 e^{-x/t_2} + A_3 e^{-x/t_3} + y_0 \tag{3.16}$$

where $a_1 = A_1 e^{-x/t_1}$, $a_2 = A_2 e^{-x/t_2}$, and $a_3 = A_3 e^{-x/t_3}$, giving

$$y = a_1 + a_2 + a_3 + y_0 \tag{3.17}$$

The uncertainty in y can be written as

$$U(y) = \sqrt{[U(a_1)]^2 + [U(a_2)]^2 + [U(a_3)]^2 + [U(y_0)]^2} \tag{3.18}$$

In order to break down the uncertainty in a_1, two substitutions will be used: First, setting $b_1 = -x/t_1$ and assuming no uncertainty in x, giving

$$U(b_1) = b_1 \sqrt{\left[\frac{-U(t_1)}{t_1}\right]^2} \tag{3.19}$$

$$U(b_1) = b_1 \frac{U(t_1)}{t_1} \tag{3.20}$$

Second, using $c_1 = e^{b_1}$, the uncertainty in the natural antilogarithm can be written as,

$$U(c_1) = c_1 U(b_1) \tag{3.21}$$

thus,

$$a_1 = A_1 e^{-x/t_1} = A_1 e^{b_1} = A_1 c_1 \tag{3.22}$$

giving

$$U(a_1) = a_1 \sqrt{\left[\frac{U(A_1)}{A_1}\right]^2 + \left[\frac{U(c_1)}{c_1}\right]^2} \tag{3.23}$$

From equations 3.20, 3.21, 3.22, and 3.23, the uncertainty in a_1 can be written as,

$$U(a_1) = A_1 e^{-x/t_1} \sqrt{\left[\frac{U(A_1)}{A_1}\right]^2 + \left[\frac{x}{t_1^2} U(t_1)\right]^2} \tag{3.24}$$

From equation 3.24, the uncertainty in a_2 and a_3 can be written as,

$$U(a_2) = A_2 e^{-x/t_2} \sqrt{\left[\frac{U(A_2)}{A_2}\right]^2 + \left[\frac{x}{t_2^2} U(t_2)\right]^2} \tag{3.25}$$

$$U(a_3) = A_3 e^{-x/t_3} \sqrt{\left[\frac{U(A_3)}{A_3}\right]^2 + \left[\frac{x}{t_3^2} U(t_3)\right]^2} \tag{3.26}$$

Finally, the uncertainty in the absolute detector efficiency from the fitting function can be calculated in combination with equations 3.20, 3.21, and 3.22 as,

$$U(\varepsilon) = \sqrt{[U(a_1)]^2 + [U(a_2)]^2 + [U(a_3)]^2 + [U(y_0)]^2} \tag{3.27}$$

3.3.6 Uncertainty propagation for total cross section

The total cross-section ($4\pi a_0$) is calculated from the Legendre coefficient a_0. Therefore the uncertainty in a_0 needs to be calculated. In order to find the uncertainty in the total cross-section, the angular distribution function for 4.438 MeV ^{12}C is given by,

$$W(\theta) = a_0 + a_2 . \frac{1}{2}(3cos^2\theta - 1) + a_4 . \frac{1}{8}(35cos^4\theta - 30cos^2\theta + 3) \tag{3.28}$$

In this cross-section experiment, there were three different angular measurements (90^0, 130^0, and 140^0). Therefore, we have three equations in terms of angular measurements:

$$\left(\frac{d\sigma}{d\Omega}\right)_{90^0} = a_0 - a_2(0.5000) + a_4(0.3750) \tag{3.29}$$

$$\left(\frac{d\sigma}{d\Omega}\right)_{130^0} = a_0 + a_2(0.1198) + a_4(-0.4275) \tag{3.30}$$

$$\left(\frac{d\sigma}{d\Omega}\right)_{140^0} = a_0 + a_2(0.3801) + a_4(-0.3191) \tag{3.31}$$

From equations 3.24, 3.25, and 3.26 by solving the three simultaneous equations, the a_0 can be written as,

$$a_0 = 0.4501\left(\frac{d\sigma}{d\Omega}\right)_{90^0} - 0.0613\left(\frac{d\sigma}{d\Omega}\right)_{130^0} + 0.6112\left(\frac{d\sigma}{d\Omega}\right)_{140^0} \tag{3.32}$$

Thus, the uncertainty in a_0 can be written as,

$$U(a_0) = \sqrt{\left[0.4501 . \frac{U(\frac{d\sigma}{d\Omega})_{90^0}}{(\frac{d\sigma}{d\Omega})_{90^0}}\right]^2 + \left[0.0613 . \frac{U(\frac{d\sigma}{d\Omega})_{130^0}}{(\frac{d\sigma}{d\Omega})_{130^0}}\right]^2 + \left[0.6112 . \frac{U(\frac{d\sigma}{d\Omega})_{140^0}}{(\frac{d\sigma}{d\Omega})_{140^0}}\right]^2} \tag{3.33}$$

Since the total cross-section is calculated as,

$$\sigma = 4\pi a_0 \tag{3.34}$$

Therefore the uncertainty in the total cross-section for the 4.438 MeV ^{12}C can be calculated as,

$$U(\sigma) = \sigma . \frac{U(a_0)}{a_0} \tag{3.35}$$

To calculate the uncertainty in the total cross-section for the 6.129 MeV ^{16}O peak, we need four angular terms but only have three angular measurements. Therefore for this uncertainty calculation, the same formula 3.29 (instead of equation 3.9) was used ignoring the fourth term of the Legendre polynomial (this assumption was only used for the uncertainty calculation).

Chapter 4

Measurement of prompt gamma cross section using Geant4 AFRODITE model

This chapter explains how the Geant4 model of the AFRODITE detector system was employed in this simulation study. Firstly, it describes the Compton-suppression employed in the AFRODITE model and then it discusses validation of the AFRODITE model. Secondly, it explains the procedure to determine the absolute detection efficiency for the simulated AFRODITE clover detectors. Thirdly, the optimization of the simulated target thickness in order to decrease simulation time is described. Finally, this chapter discusses the techniques used to determine the simulated prompt gamma cross-section values for both the Carbon and Mylar targets.

4.1 Performance of Compton-suppression detector

In order to reduce background due to Compton scatter in gamma spectroscopy, a Compton suppression detector is the most effective way to achieve this. To evaluate the Compton suppression for the Geant4 AFRODITE model, three standard gamma emitting sources (^{137}Cs, ^{60}Co, and ^{152}Eu) were used. The sources were placed at the target position and 2.4×10^{8} gamma histories were used for both simulations with the Compton shield and with no Compton shielding. Figure 4.1 shows the AFRODITE geometry with an isotropic gamma source for testing the Compton shield with no Compton suppression and figure 4.2 shows the AFRODITE geometry with an isotropic gamma source for testing the Compton shield with Compton suppression. It is clear to see that inclusion of the Compton suppression BGO detectors significantly complicates the Geant4 geometry, and consequently increases the run time by 6-fold.

As described in Section 2.4.3, Compton suppression relies on the primary and suppression detectors operating in anti-coincidence, so that if a gamma appears in both at the same time, then the event is rejected. In the Geant4 AFRODITE model, the same principle applies. Gamma energy deposition events in the germanium clover detectors are stored in 10 ns time windows with a maximum time limit of 100 ns beyond the initial proton collision. The BGO energy deposition events are also in 10 ns time windows with a maximum time limit of 130 ns. At the end of each event, each gamma energy deposition in any of the 16 BGO detectors is compared to the gamma energy depositions in any of the 4 corresponding clover detectors. If these two energy depositions occurred with 30 ns of each other (BGO energy deposition must follow the clover energy deposition), then the event is rejected. A energy threshold is also used in the evaluation; either energy deposition must be above a 5.0 keV threshold.

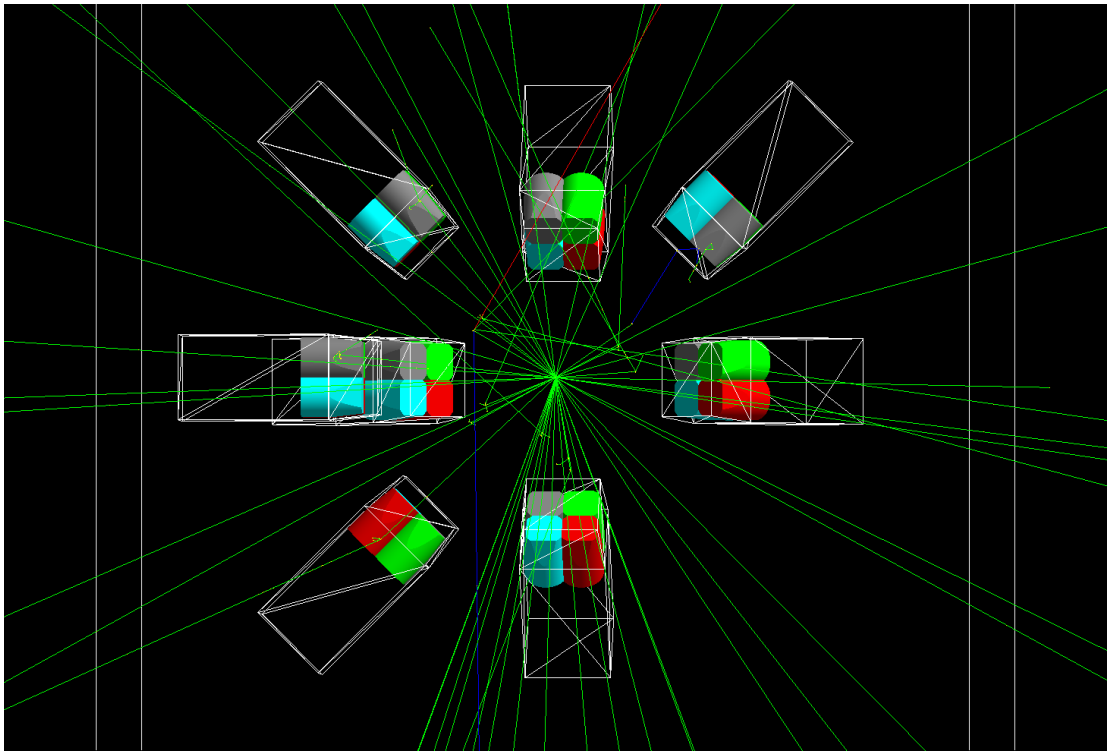

Figure 4.1: Clover detectors setup for testing Compton shield with no Compton shield and an isotropic gamma source.

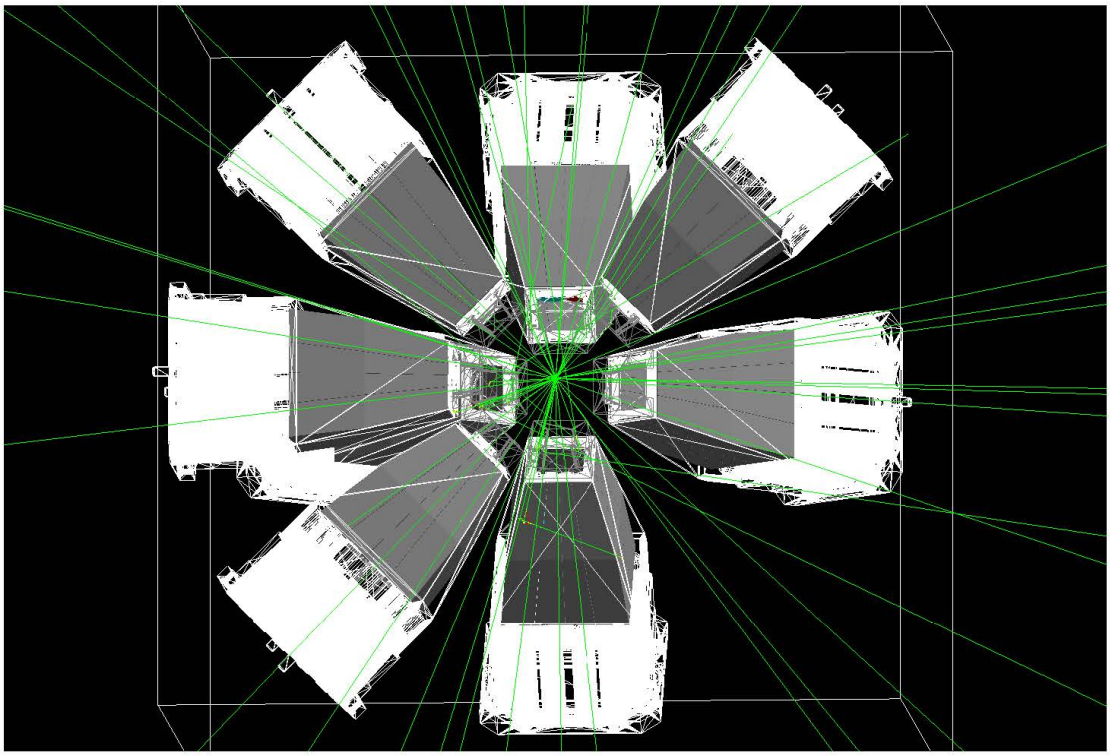

Figure 4.2: Clover detectors setup for testing Compton shield with Compton shield and an isotropic gamma source.

4.2 Validation of Geant4 AFRODITE model

In order to get accurate, reliable results from a Monte-carlo model, validation of the model is a requirement. Therefore, the Geant4 model of the AFRODITE system was tested by using the same three standard gamma emitting sources (^{152}Eu, ^{60}Co, and ^{137}Cs) as used in the experiment. As described in chapter 2, the Geant4 model of the AFRODITE detector system attempted to model the experimental setup as closely as possible.

Each standard gamma source was generated using the Geant4 General Particle Source package (GPS) and placed at the target position. The GPS package is able to describe the primary source particle with various spatial, spectral, and angular distribution specifications. Each source was modelled as an isotropic gamma source and was run with 1.5×10^9 histories. As described in the experimental method (chapter 2), the direct mode (single crystal events) was also used to accumulate the gamma events for the simulations.

4.3 Simulated absolute detector efficiency

In simulation studies, there is no need for an energy calibration since the energy of the detected gammas are immediately known unlike in the experiment. The next important step in the process is the absolute detector efficiency. In order to find the absolute detector efficiency of the Geant4 model of the AFRODITE detector system, three standard gamma emitting sources, ^{152}Eu, ^{60}Co, and ^{137}Cs were used in an identical method as for the measurements as explained in section 3.3. In these absolute detector efficiency measurements, one photo peak (662 keV) from ^{137}Cs, two photo peaks (1173 keV and 1332 keV) from ^{60}Co and 14 photo peaks (discussed further in Chapter 5) from ^{152}Eu were used.

The three standard gamma sources used to determine the absolute detector efficiencies for both the experiment and simulation were in the range of 120 keV to 1400 keV. In order to effectively use this efficiency curve for the prompt gamma cross-section measurements, this energy range needed to be extrapolated up to 7 MeV. To extrapolate a complete absolute detector efficiency response curve, simulated results for a single-energy point gamma source with energies from 0.2 MeV to 9.0 MeV were used. Each simulations required 10^9 incident gammas.

4.3.1 Calculating simulated detector efficiency

The absolute efficiency can be calculated by using the following formula as described in chapter 3,

$$\varepsilon = \frac{N}{N_0 P_\gamma(E) t e^{-\lambda t_d}} \tag{4.1}$$

where, N is the total area under the photo peak of γ ray energy E, N_0 is the activity of the gamma source in Becquerel, $P_\gamma(E)$ is the emission probability of the gamma ray at energy E, shown in table 5.1, t is the acquisition time, t_d is the decay time, and $\lambda = ln2/T_{1/2}$, is the decay constant. To find the absolute detector efficiency from the simulated data, this formula can be simplified since there is no radioactive decay in the simulations to,

$$\varepsilon = \frac{N}{N_0 P_\gamma(E)} \tag{4.2}$$

where N_0 is number of gamma histories used in the simulation and N and $P_\gamma(E)$ are the same as described above.

Uncertainty in the simulated absolute detector efficiency can also be calculated using a simplified equation since there is no uncertainty in the number of gamma histories in the simulation and the uncertainty in the emission probability of gamma rays can be neglected.

The resulting uncertainty equation is:

$$U(\varepsilon) = \varepsilon\Big(\frac{U(N)}{N}\Big) \tag{4.3}$$

where $U(N)$ was measured during the fitting of the photo peaks using OriginPro data analysis program.

4.4 Calculating simulated differential Cross-section

As discussed in chapter 1, the differential cross section can be calculated by using this formula,

$$\frac{d\sigma}{d\Omega} = \frac{N_{events(\Delta\Omega)}}{N_{incident}} \quad \frac{A}{dx\rho N_{Avo}\varepsilon} \tag{4.4}$$

Figure 6.21 shows how the number of detected events was measured 4.438 MeV peak of ^{12}C in simulation as done in the experimental measurement. Further details of peak measurement has been explained in section 3.3.4. The same method was used to measure peak area for 6.129 MeV peak of ^{16}O as shown in the figure 6.21. In simulation studies, prompt gamma spectra for each germanium crystal was not considered to measure differential cross-section as done in the experiment since absolute efficiency of all germanium crystal of Geant4 AFRODITE model was assumed as same. Therefore, in this measurement, all 90^0 (16 crystals), 130^0 (8 crystals), and 140^0 (8 crystals) were added to get prompt gamma spectra. Then, these spectra were used to measure the differential cross-sections. The above procedure was repeated all other four different proton energies.

As discussed in Chapter 3, the uncertainty in the differential cross section can be written as (assuming no uncertainty in A and N_{Avo}),

$$U\Big(\frac{d\sigma}{d\Omega}\Big) = \Big(\frac{d\sigma}{d\Omega}\Big)\sqrt{\Big[\frac{U(N_{events})}{N_{events}}\Big]^2 + \Big[\frac{U(N_{incident})}{N_{incident}}\Big]^2 + \Big[\frac{U(t_a)}{t_a}\Big]^2 + \Big[\frac{U(\varepsilon)}{\varepsilon}\Big]^2} \tag{4.5}$$

In simulation studies, there is no uncertainty in the target thickness and the number of incident particles. Therefore, the uncertainty in the simulated differential cross-section can be written as,

$$U\Big(\frac{d\sigma}{d\Omega}\Big) = \Big(\frac{d\sigma}{d\Omega}\Big)\sqrt{\Big[\frac{U(N_{events})}{N_{events}}\Big]^2 + \Big[\frac{U(\varepsilon)}{\varepsilon}\Big]^2} \tag{4.6}$$

4.5 Target thickness optimization for simulation

Experimental cross-section measurements typically use very thin targets so that the incident particles do not collide more than once in the target, thus producing accurate cross-section results. Unfortunately, as a Monte-Carlo simulation improves in geometric accuracy, there is a trade-off in computation time. For this Geant4 AFRODITE model, it was computationally impossible to replicate the number of incident protons (10^{14}) used in the experiment. So in order to both decrease the simulation time and provide reasonable statistics for the prompt gamma production, the simulation target thickness was increased. To ensure that changing the target thickness did not impact the prompt gamma production, a simple Geant4 cross-section simulation was run (Xsection). The Xsection code determined the cross section for the carbon 4.438 MeV photo peak at different thicknesses at the energies used in the experiment. The code measured the cross-section by counting the emitted prompt gammas over a 4π solid angle.

The experimental target thicknesses were 8.40±0.07 mg/cm^2 for the carbon target and 7.00±0.08 mg/cm^2 for the mylar target. In order to simulate the target, the thickness needed to be converted into units of mm, so the densities of carbon (2 g/cm^3) and mylar (1.4 g/cm^3) were taken from the Geant4 material database. Thus, the experimental target thickness for carbon was calculated as 0.042 mm and 0.050 mm for the mylar target.

The Xsection code is basically the AFRODITE code without the complex detectors; the physics and the proton beam of the Xsection code is identical to the AFRODITE code, as discussed in section 4.5.2. In order to only evaluate the target thickness, the inelastic cross-section for the 4.438 MeV gamma was calculated by measuring the peak area under the 4.438 MeV photo peak. Figure 4.3 shows the obtained spectrum for a 66 MeV proton beam on a 0.5 mm thickness ^{12}C target and includes the Gaussian peak fitting for the ^{12}C 4.438 MeV photo peak. As discussed in section 1.7, equation 1.9 was used to determine the total cross-section for 4.438 MeV photo peak. The above procedures were repeated for different thicknesses (0.005 mm to 5 mm) and five different energies (66, 80, 95, 110, and 125 MeV). The uncertainty in the cross-section values was calculated by considering the statistical uncertainty in the peak area measurements.

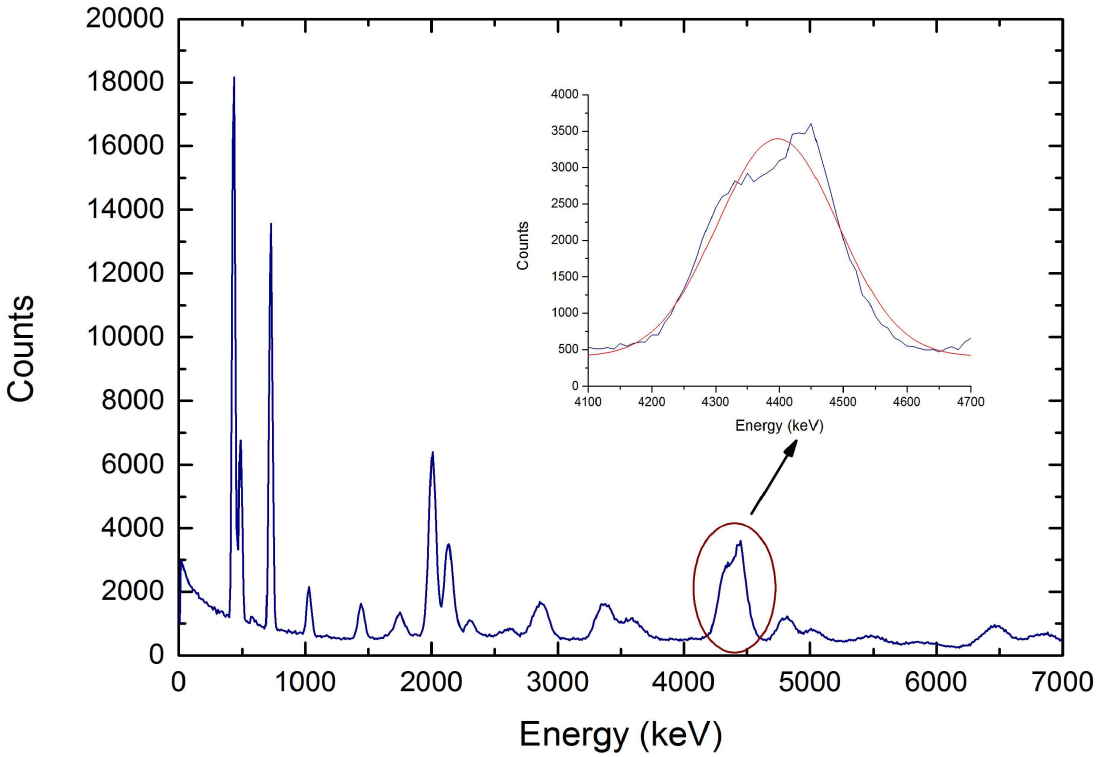

Figure 4.3: Prompt gamma spectrum for a 66 MeV proton bombardment on a 0.5 mm ^{12}C target. Inset: Gaussian peak fit for the 4.438 MeV photo peak using the OriginPro data analysis program.

Figure 4.4 shows the full results of the simulated cross-sections, and it is clear to see there is no significant difference in the cross-section values for target thicknesses less than 1 mm. Figure 4.5 shows the 66 MeV cross-section results with an enlarged value of the 0.005 to 0.6 mm thicknesses, showing very little change up to 0.6 mm. Therefore, a target thickness of 0.5 mm was selected for the carbon target in the full AFRODITE simulation. For the mylar target, none of the ^{16}O peaks (6.13 MeV, 6.92 MeV, and 7.12 MeV) were visible in the simulation as reported in section 6.4.2. Therefore, the same increased target thickness of 0.5 mm was used for the Mylar target in the prompt gamma production simulations.

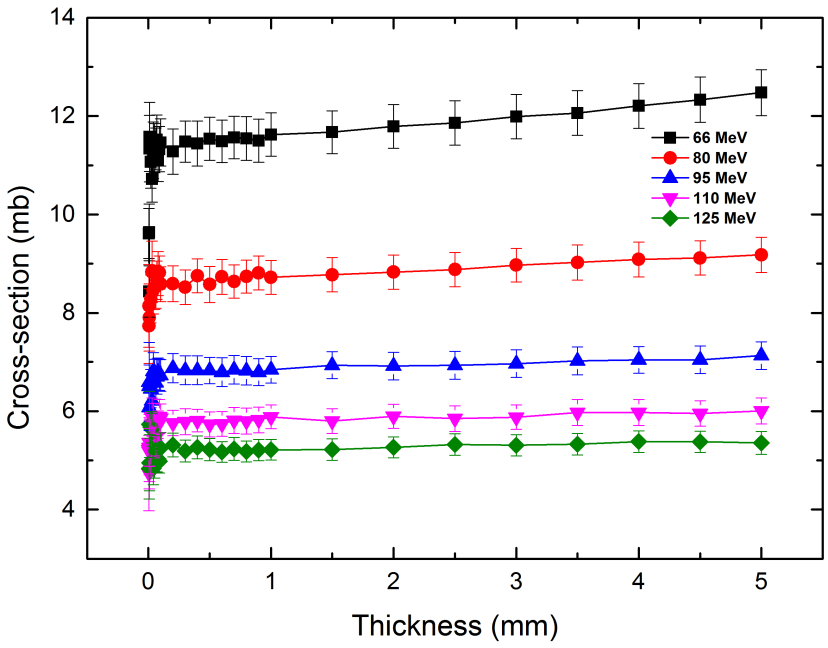

Figure 4.4: Simulated cross-section values versus thicknesses for 66, 80, 95, 110, and 125 MeV proton bombardments on a ^{12}C target.

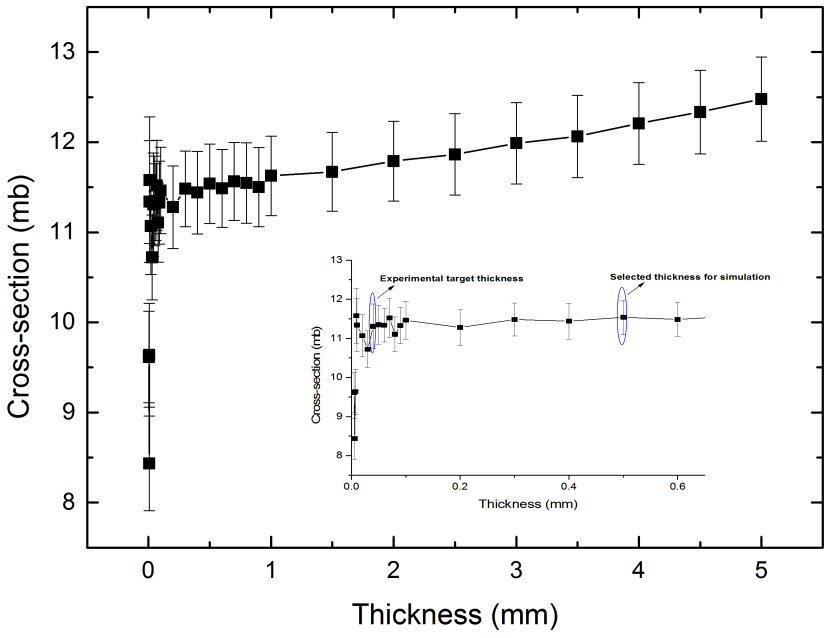

Figure 4.5: Simulated cross-section values versus thicknesses for a 66 MeV proton bombardment on a ^{12}C target. Inset: Zoomed picture of the experimental (0.04 mm) and the simulated (0.5 mm) target thicknesses.

Table 4.1: Calculated cross-section values using actual target thickness (0.042 mm) and simulated target thickness (0.5 mm) and percent difference. σ_{ATT}: cross-section value for actual target thickness. σ_{STT}: cross-section value for simulated target thickness

Energy (MeV)	σ_{ATT}	σ_{STT}	Percent difference
66	11.31± 0.57	11.54± 0.44	0.026%
80	8.46± 0.48	8.58± 0.48	0.010%
95	6.81± 0.38	6.83± 0.38	0.001%
110	5.84± 0.32	5.73± 0.32	0.010%
125	4.84± 0.33	5.22± 0.33	0.019%

For the AFRODITE code, using the simulated target thickness of 0.5 mm, about 1.2 x 10^{12} number of proton histories (1.8 x 10^5 CPU hours) are required to produce visible results. These simulations were performed at the Centre for High Performance Computing (CHPC), 15 Lower Hope Rd, Rosebank, Cape Town providing access to 720 CPU cores. A total of 1.8 x 10^5 CPU hours on 720 cores translates into about 250 hours per AFRODITE simulation. Using the actual target thickness, at least 2.0 x 10^{14} proton histories are needed to produce similar results. Therefore, increasing the target thickness saved approximately 3.2 x 10^7 CPU hours per prompt gamma spectrum. The total cross-section for the 4.438 MeV peak using the actual experimental thickness (0.042 mm), the simulated target thickness (0.5 mm), and the percentage difference of the total cross-section between these two targets are given in table 4.1. The percentage differences are all below 0.03% giving us confidence that the increased thickness did not impact the final cross-section results.

4.6 Simulation of prompt gamma production cross-section

When using the Geant4 Monte-Carlo code, it is important to select a suitable physics list. The Geant4 physics list reference page (G4Physics (2016)) recommends using the QGSP_BIC physics package for primary protons and neutrons below $\sim$ 10 GeV. It also states that "Binary Cascade better describes production of secondary particles produced in interactions of protons and neutrons with nuclei". The QGSP_BIC was the default package used, but other inelastic scattering models were explored. Therefore, this section explains how the physics lists were compared and describes the AFRODITE simulation procedures for prompt gamma production.

4.6.1 Comparison of physics list

As discussed above, the suggested physics list for 0 - 200 MeV protons is the binary cascade model, particularly the G4HadronPhysicsQGSP_BIC for inelastic scattering. There are a number of other inelastic scattering physics models as well as various inelastic cross-section data sets. In addition to the binary cascade physics list (default), the other options investigated for inelastic scattering were: the precompound model and the precompound model plus Fermi breakup. There are also two different inelastic cross-section data sets for inelastic scattering: the Geisha (default inelastic cross-section) and the Tripathi data sets. In addition, it is possible to modify the initial number of excitons in the Geant4 precompound model (G4PrecompoundModel), as described in Section 2.3.3. So based on previous work (Jeyasugiththan and Peterson (2015)), changing the initial exciton number from 2 (default) to 1 will also be explored. The Xsection code (described in section 4.4) was again used to investigate the various physics options using a 80 MeV proton beam on both the Carbon and Mylar targets.

4.6.2 Full AFRODITE simulations

For the simulations of prompt gamma production, the Geant4 model of the AFRODITE detector was used as in the experimental setup. The geometry setup of the AFRODITE model, the source of incident protons (a pencil beam) and the protons interactions with the target are shown in figure 4.6. The QGSP_BIC Physics list package was used and included the following models G4HadronPhysicsQGSP_BIC for the inelastic scattering, G4HadronElasticPhysics for the elastic scattering, G4EMStandardPhysics_option4 for the electromagnetic interactions, G4DecayPhysics and G4RadioactiveDecayPhysics for the radioactive processes. Additionally, the G4IonBinaryCascadePhysics, G4StoppingPhysics, and G4NeutronTrackingCut packages were also used. As discussed in the previous section, the thicknesses for the carbon and mylar targets was 0.5 mm in order to decrease the simulation time and to improve statistics. Each prompt gamma simulation required 1.2 x 10^{12} proton histories and 1.8 x 10^{5} CPU hours. A total of 10 AFRODITE simulations were run (five different energies for two different targets).

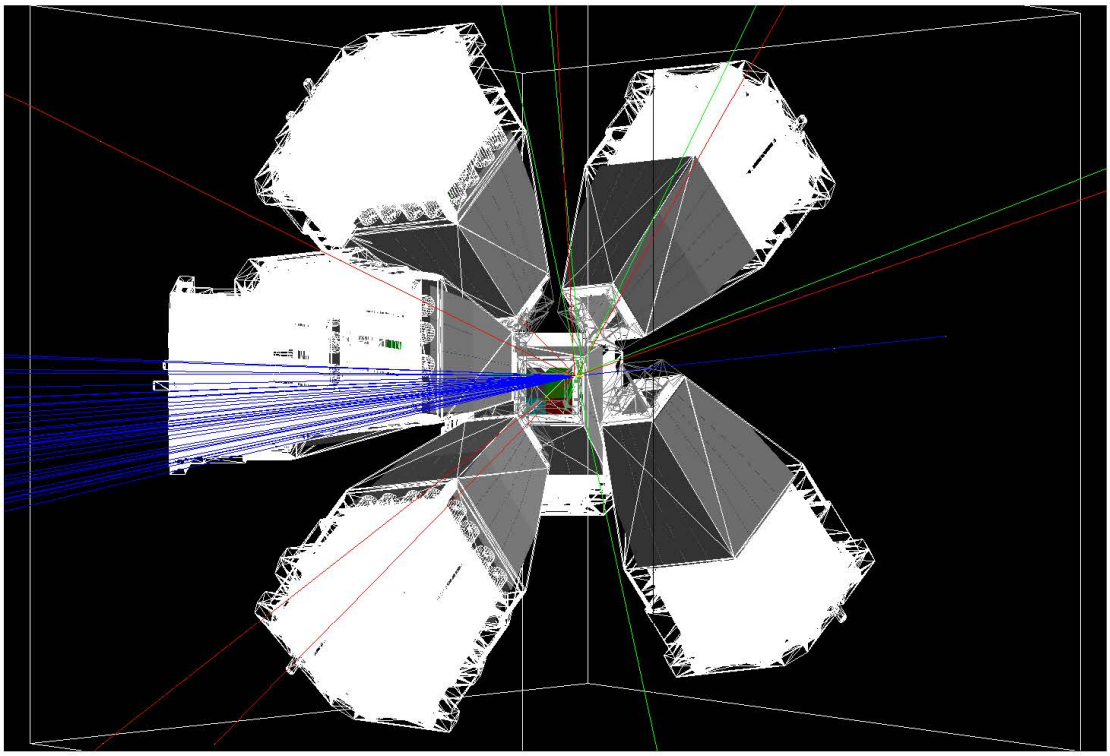

Figure 4.6: Geometry setup of the AFRODITE model for prompt gamma production with the incident proton entering as a pencil beam and interacting with the target. Track colours: blue - proton, green - gamma, and red - electron

Part III
Results and Discussion

Chapter 5

Results from experimental prompt gamma cross-section measurements

This chapter reports all measurements and calculations related to the prompt gamma production cross section experiment conducted at iThemba LABS in Faure, Cape Town, South Africa. It includes energy calibration procedures, absolute detector efficiency calculations and associated uncertainty propagation, absolute detector efficiency response curves for each high purity germanium crystals (32 crystals in total), differential cross section measurements for the Carbon and Mylar targets at three different angles for five different energies as discussed in chapter 3, and total cross section measurements for the Carbon and Mylar 4.438 MeV photo peaks and the Mylar (Oxygen) 6.129 MeV photo peak.

5.1 Energy calibration

As discussed in chapter 3, the Simsort program was used to extract the raw energy spectra data into ROOT TTrees for energy calibration. The TTree energy spectra were fed into OriginPro 9.0 (OriginLab, Northampton, MA) data analysis program to find the channel numbers according to the photo peaks from the three calibration source gamma spectra. The spectra for one of the crystals for ^{137}Cs, ^{60}Co, and ^{152}Eu (after the room background subtraction) are shown in figures 5.1, 5.2 and 5.3. The details of the expected photo peaks and emission probabilities are shown in table 5.1. To find the centroid of each photo peak, a Gaussian curve was fit to each peak using OriginPro. One photo peak from ^{137}Cs, two photo peaks from ^{60}Co, and 14 photo peaks from ^{152}Eu were used for the energy calibration for each of the high purity germanium crystals. Figures 5.4 and 5.5 show examples of using OriginPro for fitting the ^{137}Cs and ^{60}Co photo peaks. Since ^{152}Eu has so many photo peaks, each peaks needed to be fit individually. All of this data was compiled into peak energy against channel number graphs and fitted using a linear fit of the form $E = a + bX$ where E is the energy and X is the channel number. Figure 5.6 shows the energy calibration

curve for one of the high purity germanium crystals. This procedure was repeated for all 32 crystals and the full details for each crystal can be found in appendix B.1. These fitting parameters (slope and intercept) for each crystal was then loaded into the SimSort program (the gain and offset files) in order to correctly apply the energy calibrations to the final measurement spectra.

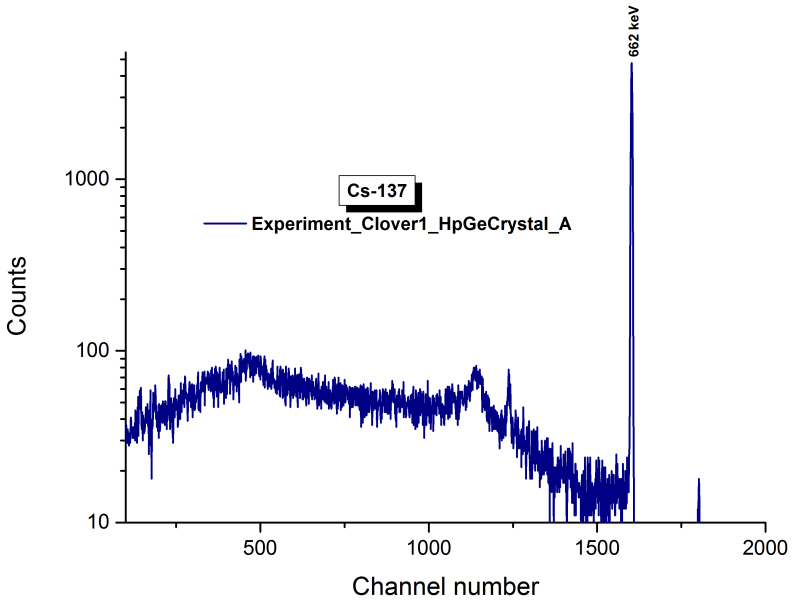

Figure 5.1: Identified photo peak in the ^{137}Cs spectrum from crystal A in clover 1. There were a total of 32 spectra for each calibration source.

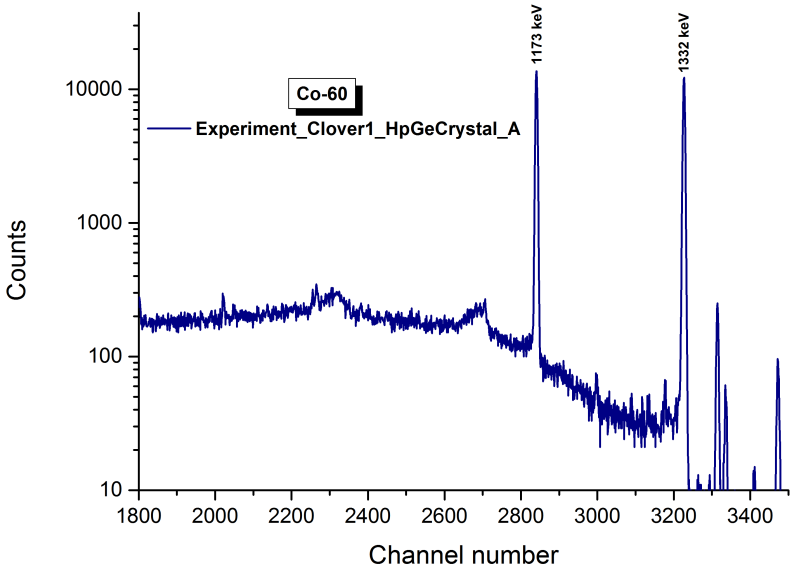

Figure 5.2: Identified photo peaks in the ^{60}Co spectrum from crystal A in clover 1.

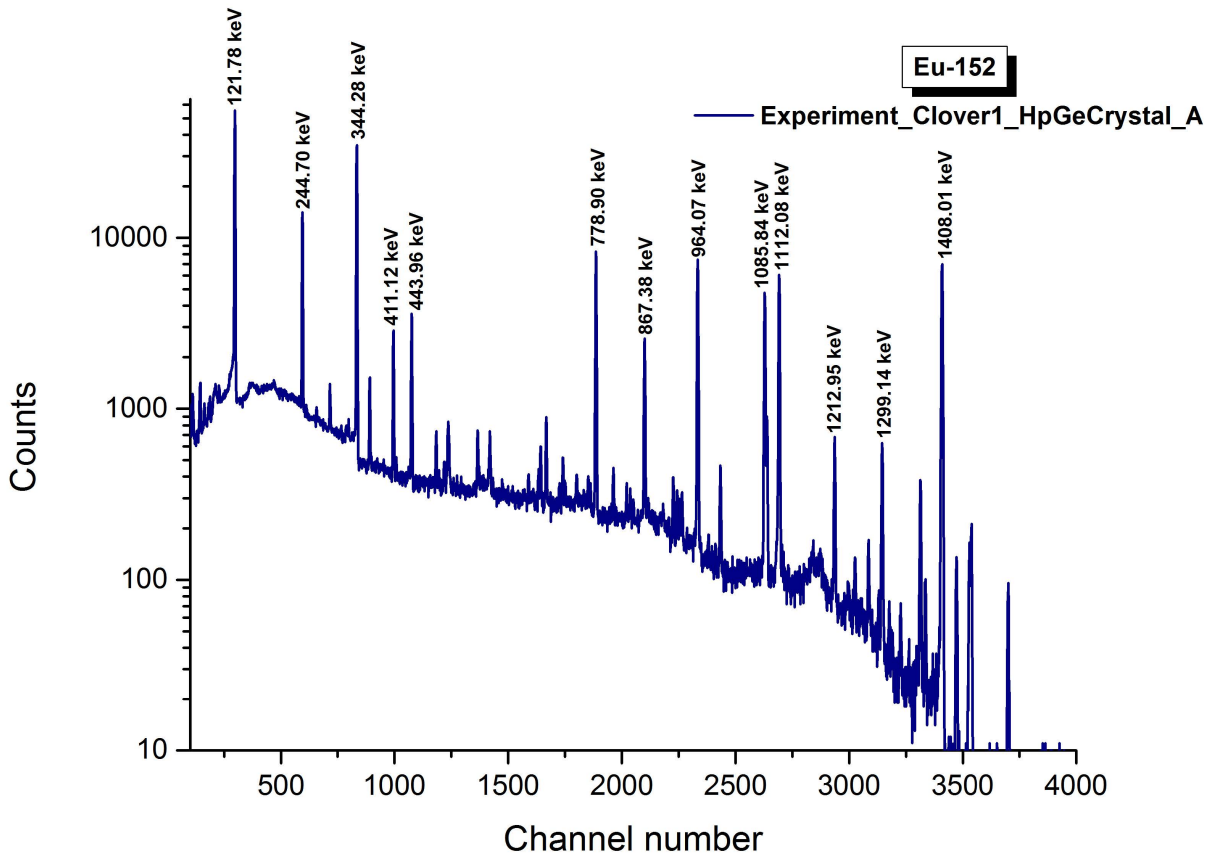

Figure 5.3: Identified photo peaks in the ^{152}Eu spectrum from crystal A in clover 1.

Table 5.1: The standard decay data for the three calibration sources. Source: IAEA (2016)

Radionuclide	Half-life (days)	Energy (keV)	Emission Probabilities
$^{60}Co_{27}$	1925.23 (27)	1173.228 (3)	0.9985 (3)
		1332.492 (4)	0.999826 (6)
$^{137}Cs_{55}$	1.099 (4) x 10+4	661.657 (3)	0.8499 (20)
$^{152}Eu_{63}$	4941 (7)	121.7817 (3)	0.2841 (13)
		244.6974 (8)	0.0755 (4)
		344.2785 (12)	0.2658 (12)
		411.1165 (12)	0.02237 (10)
		443.965 (3)	0.03125(14)
		778.9045 (24)	0.1296 (6)
		867.380 (3)	0.04241(23)
		964.072 (18)	0.1462 (6)
		1085.837 (10)	0.1013 (6)
		1089.737 (5)	0.01731 (10)
		1112.076 (3)	0.1340 (6)
		1212.948 (11)	0.01415 (9)
		1299.142 (8)	0.01632 (9)
		1408.013 (3)	0.2085 (9)

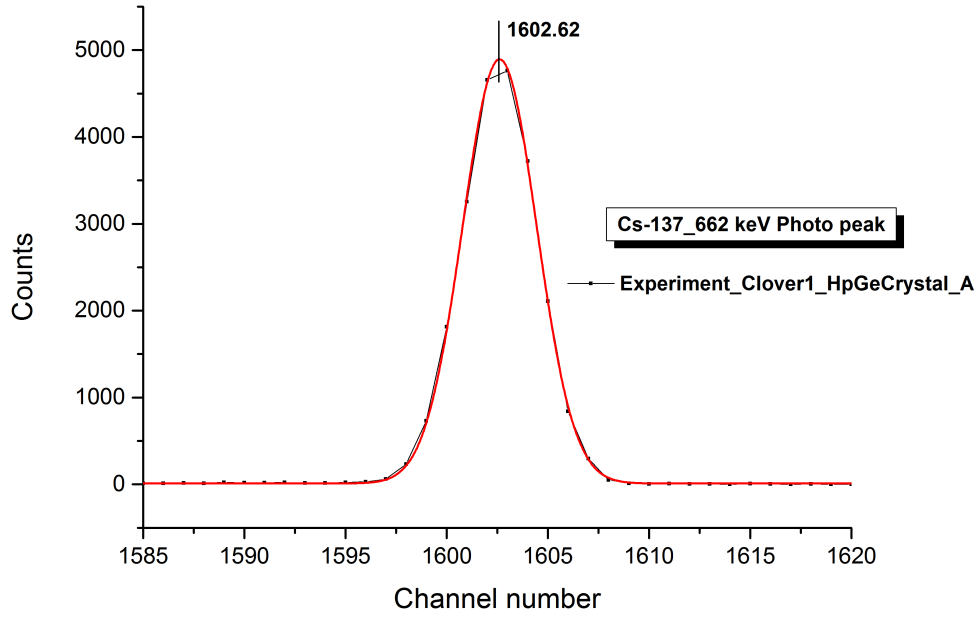

Figure 5.4: Peak fitting using OriginPro to find centroid of ^{137}Cs 662 keV photo peak in the spectrum from high purity germanium crystal A in clover 1.

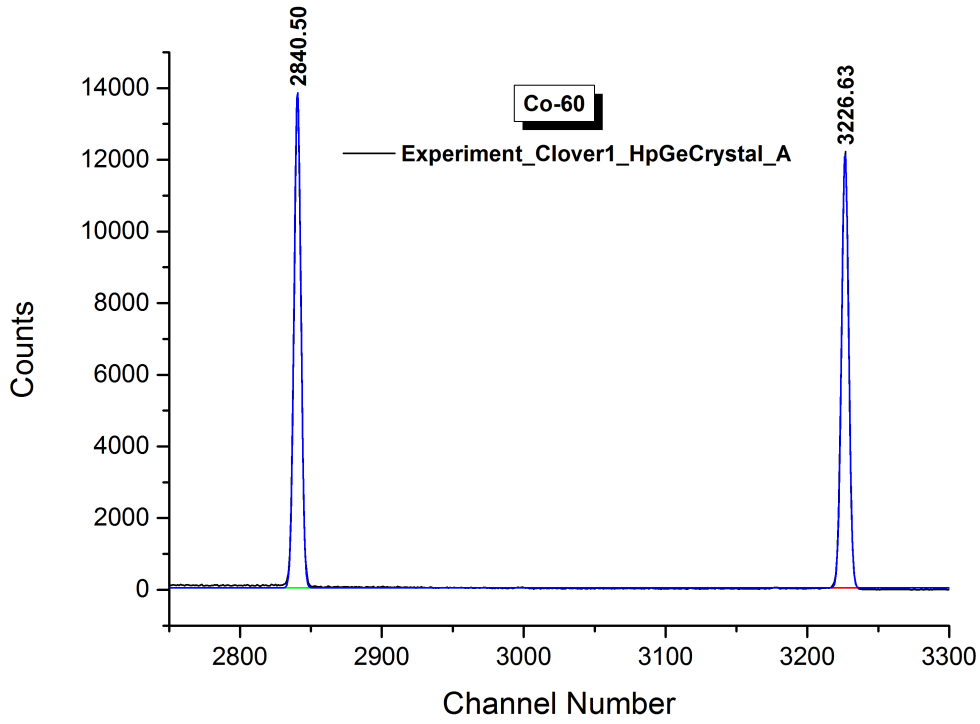

Figure 5.5: Peak fitting using OriginPro to find centroid of ^{60}Co 1173 keV and 1332 keV photo peaks in the spectrum from high purity germanium crystal A in clover 1.

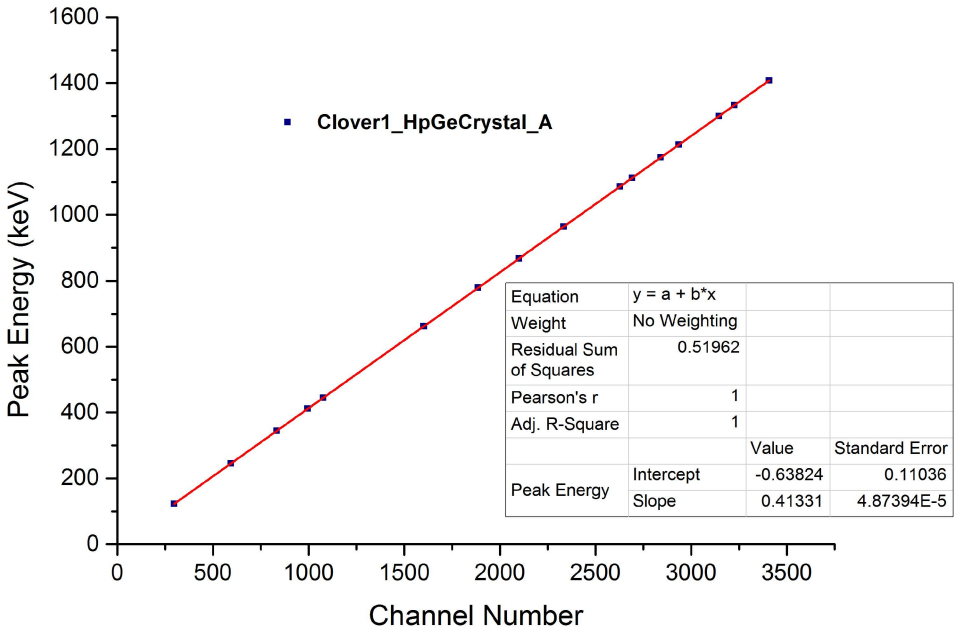

Figure 5.6: The energy calibration curve for crystal A in clover 1.

5.2 Absolute Detection efficiency

The absolute detection efficiency for a gamma ray detector varies with the energy of the detected gamma. For the germanium crystal efficiency calibration, three standard gamma emitting sources (^{152}Eu, ^{60}Co, and ^{137}Cs) were used as discussed in chapter 3. These sources only provided absolute detector efficiency data for the energies from 122 keV to 1408 keV. For the cross section measurement of ^{12}C and ^{16}O, the absolute efficiency response curve needed to be extrapolated up to 7000 keV since our interested peaks are 4.438 MeV from ^{12}C and 6.129 MeV from ^{16}O. Therefore, the absolute detector efficiencies at these energies needed to be determined.

Experimentally, the high purity germanium crystals have different absolute detector efficiencies. These differences could be due to the different ages of the high purity germanium crystals and also due to the alignment of the detectors. The largest differences were observed in clover 1. The variations of efficiencies of the four germanium crystals in clover 1 are shown in figure 5.7. It is clear to see that each crystal required individual fitting for the absolute efficiency response curves.

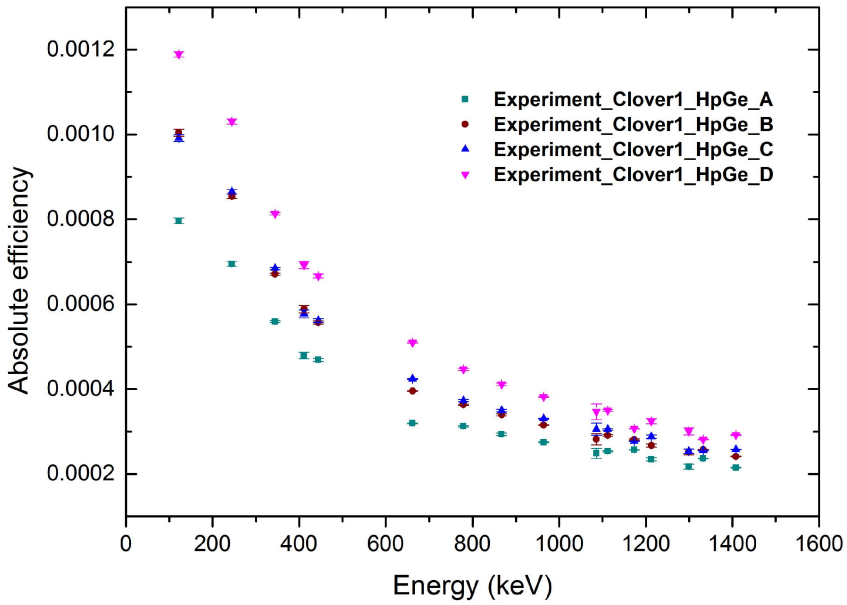

Figure 5.7: Absolute detection efficiency for the four high purity germanium crystals in clover 1.

The calculated absolute efficiencies for the three standard gamma emitting sources and the associated uncertainty for the high purity germanium crystal A in clover 1 are given in table 5.2. The procedure was repeated for all crystals. The measured efficiencies were fit to the Geant4 simulated data from the single-energy point gamma sources from 200 keV to 9000 keV and to the standard gamma emitting source (^{137}Cs, ^{60}Co, and ^{152}Eu) data. For the efficiency response curve fitting, a correction factor was needed since the Geant4 AFRODITE detector model had a higher efficiency than the experimental setup. The difference absolute efficiency between the experimental results and the simulated results is shown in figure 5.8. Each of the 30 high purity germanium crystal had a different correction factor and were in the range of 1.35 - 1.95. The correction factors for each high purity germanium crystal are shown in table 5.3. In order to find the function to fit the data, a third order exponential function provided the best fit. The fitting details for the absolute efficiency response curve for crystal A in clover 1 is shown in table 5.4. The corrected efficiency response curves for the high purity germanium crystals in clover 1 are shown in figures 5.9, 5.10, 5.11, and 5.12. The efficiency response curves for all other remaining crystals are included in appendix B.2. Crystal B in Clover 3 and crystal A in clover 6 were ignored because of insufficient data from the crystal and not functioning, respectively.

Table 5.2: Experimental absolute efficiencies and associated uncertainties for high purity germanium crystal A in clover 1.

Energy (keV)	Peak area	U(peak area)	Absolute efficiency(ϵ)	$U(\epsilon)$
662	22428.68	51.61	3.194×10^{-4}	7.350×10^{-7}
1173	80367.54	187.10	2.566×10^{-4}	5.974×10^{-7}
1333	74075.22	209.07	2.362×10^{-4}	6.667×10^{-7}
122	221212.24	1902.92	7.963×10^{-4}	6.850×10^{-6}
245	51326.45	375.63	6.952×10^{-4}	5.088×10^{-6}
344	145373.27	569.26	5.593×10^{-4}	2.190×10^{-6}
411	10484.33	156.86	4.793×10^{-4}	7.171×10^{-6}
444	14328.66	118.78	4.689×10^{-4}	3.887×10^{-6}
779	39556.60	180.76	3.121×10^{-4}	1.426×10^{-6}
867	12169.01	107.17	2.934×10^{-4}	2.584×10^{-6}
964	39262.46	129.18	2.746×10^{-4}	9.036×10^{-7}
1086	24604.87	1177.35	2.484×10^{-4}	1.189×10^{-5}
1112	33174.43	205.40	2.532×10^{-4}	1.568×10^{-6}
1213	3246.12	53.58	2.346×10^{-4}	3.872×10^{-6}
1299	3464.87	98.44	2.171×10^{-4}	6.168×10^{-6}
1408	43818.85	194.99	2.149×10^{-4}	9.564×10^{-7}

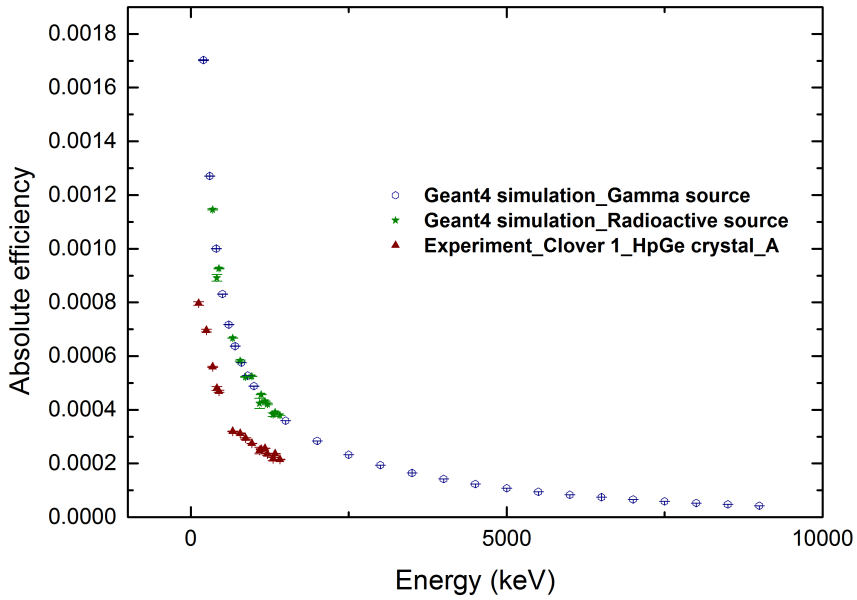

Figure 5.8: The absolute detector efficiency difference between the experimental results and the simulated results for high purity germanium crystal A in clover 1. This figure shows that the Geant4 model of the AFRODITE detector had a higher efficiency than the actual AFRODITE detector system.

Table 5.3: The correction factors for each high purity germanium crystal used to fit the efficiency response curves. Here, C - Clover, HpGe - High purity germanium crystal

Crystal	Correction factor	Crystal	Correction factor
C1_HpGe_A	1.85	C5_HpGe_A	1.80
C1_HpGe_B	1.65	C5_HpGe_B	1.80
C1_HpGe_C	1.55	C5_HpGe_C	1.55
C1_HpGe_D	1.35	C5_HpGe_D	1.70
C2_HpGe_A	1.75	C6_HpGe_A	not functioning
C2_HpGe_B	1.95	C6_HpGe_B	1.70
C2_HpGe_C	1.60	C6_HpGe_C	1.50
C2_HpGe_D	1.80	C6_HpGe_D	1.60
C3_HpGe_A	1.60	C7_HpGe_A	1.70
C3_HpGe_B	insufficient data	C7_HpGe_B	1.60
C3_HpGe_C	1.60	C7_HpGe_C	1.70
C3_HpGe_D	1.65	C7_HpGe_D	1.60
C4_HpGe_A	1.65	C8_HpGe_A	1.60
C4_HpGe_B	1.85	C8_HpGe_B	1.70
C4_HpGe_C	1.85	C8_HpGe_C	1.60
C4_HpGe_D	1.85	C4_HpGe_D	1.60

Table 5.4: Details of the functional fitting for the absolute efficiency response curve for crystal A in clover 1.

Model	ExpDec3		
Equation	$y = A_1 exp(-x/t_1) + A_2 exp(-x/t_2) + A_3 exp(-x/t_3) + y_0$		
Reduced Chi-Sqr	4.63772		
Adj. R-Square	0.99998		
		Value	Standard Error
Absolute efficiency	y_0	7.43×10^{-06}	5.25×10^{-07}
Absolute efficiency	A_1	0.00135	4.08×10^{-05}
Absolute efficiency	t_1	184.57007	4.45495
Absolute efficiency	A_2	3.11×10^{-04}	7.21×10^{-06}
Absolute efficiency	t_2	801.76261	24.94514
Absolute efficiency	A_3	2.15×10^{-04}	$4.24 \times 10{-}06$
Absolute efficiency	t_3	3447.60199	66.98161

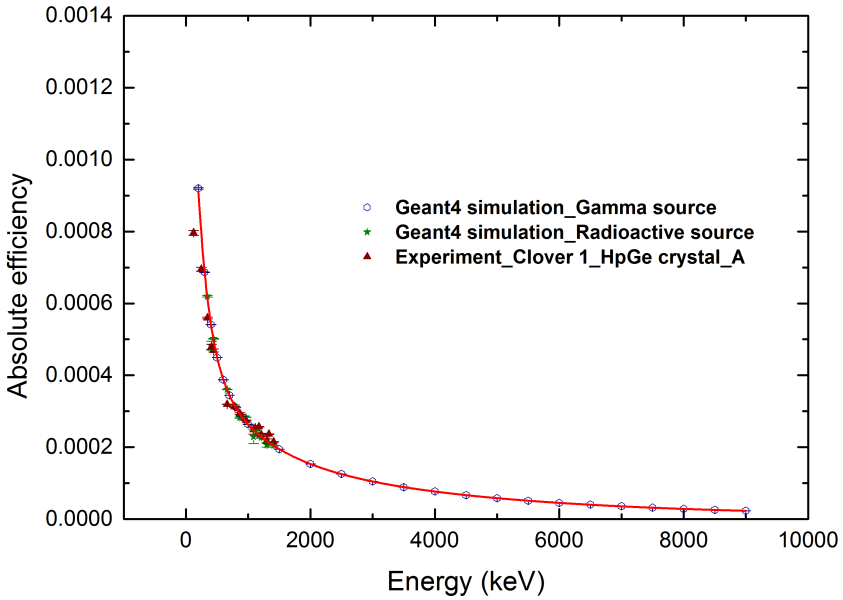

Figure 5.9: The absolute efficiency response curve for crystal A in a clover 1. The red triangle points are experimentally measured absolute detector efficiencies, the blue hollow circle points and green star points are simulated efficiencies using single-energy gamma sources and standard gamma emitting sources, respectively. Solid line is the third-order exponential fit.

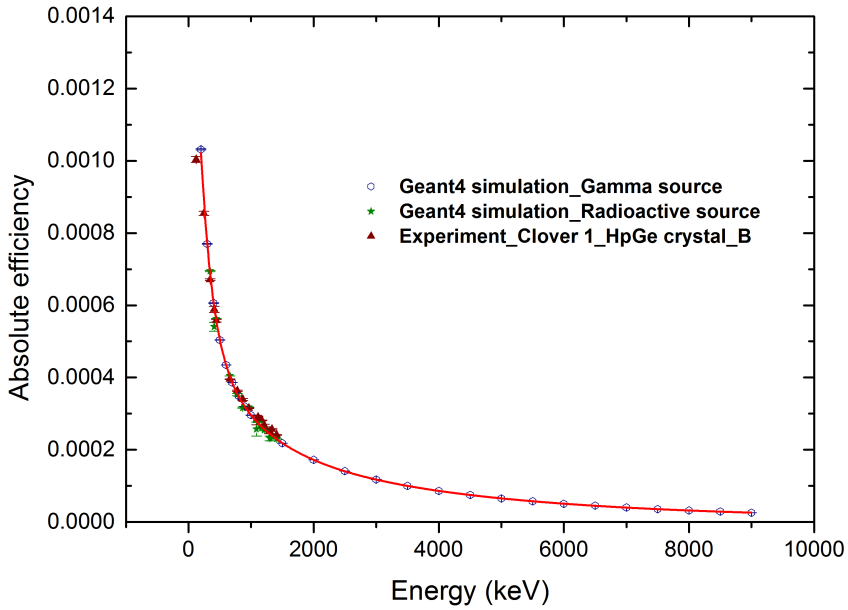

Figure 5.10: The absolute efficiency response curve for crystal B in a clover 1. The red triangle points are experimentally measured absolute detector efficiencies, the blue hollow circle points and green star points are simulated efficiencies using single-energy gamma sources and standard gamma emitting sources, respectively. Solid line is the third-order exponential fit.

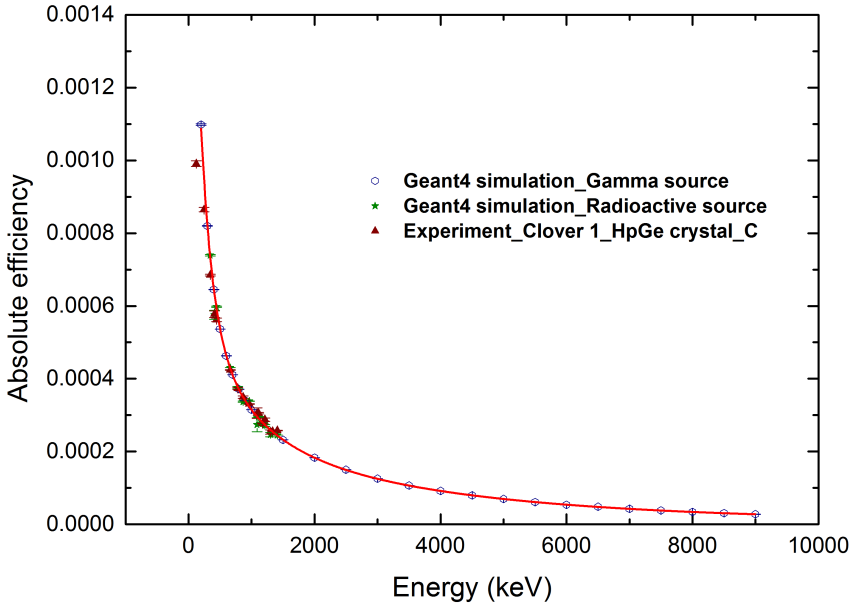

Figure 5.11: The absolute efficiency response curve for crystal C in a clover 1. The red triangle points are experimentally measured absolute detector efficiencies, the blue hollow circle points and green star points are simulated efficiencies using single-energy gamma sources and standard gamma emitting sources, respectively. Solid line is the third-order exponential fit.

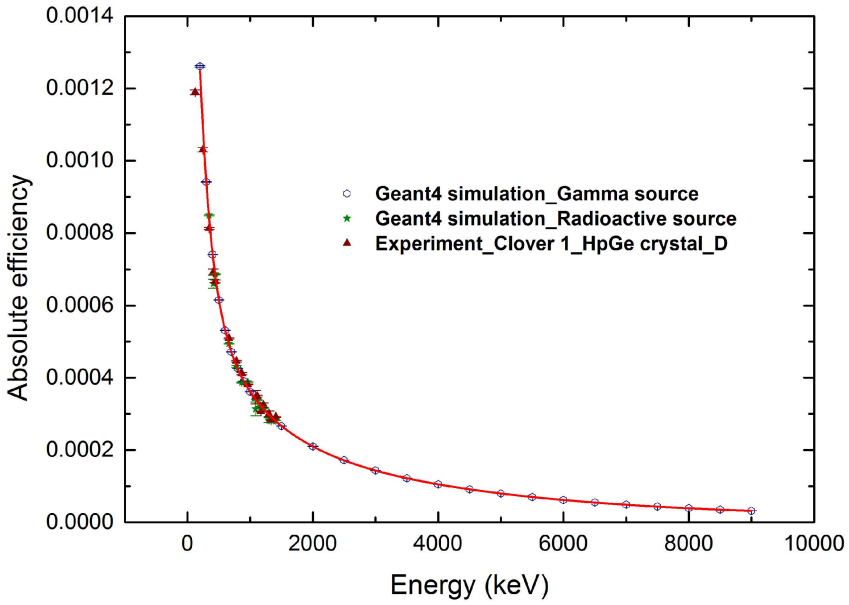

Figure 5.12: The absolute efficiency response curve for crystal D in a clover 1. The red triangle points are experimentally measured absolute detector efficiencies, the blue hollow circle points and green star points are simulated efficiencies using single-energy gamma sources and standard gamma emitting sources, respectively. Solid line is the third-order exponential fit.

5.3 Calculating prompt gamma cross section from experimental data

This section outlines the procedures for converting the measured data into total cross-section data. The gamma-ray line emission from the first excited state of the nucleus to its ground state is usually the strongest gamma-ray line. In this cross-section measurement study, this is true for the 4.438 MeV gamma from ^{12}C but not for 6.129 MeV gamma from ^{16}O. The first excited state of ^{16}O (0^+) at 6.049 MeV decays by electron and positron emission. The 6.129 MeV gamma from ^{16}O is the transition from the second excited state (3^-) to the ground state. This section reports all results regarding cross-section measurements for the 4.438 MeV peak from ^{12}C (natural carbon target) and the 4.438 and 6.129 MeV peaks from ^{16}O (mylar target) at five different energies 66, 80, 95, 110, 125 MeV.

5.3.1 Experimental prompt gamma spectra

Figures 5.13 and 5.14 show the raw data from the 95 MeV proton bombardment of the carbon and mylar targets as measured by the 4 clovers placed 90 degrees to the beam direction. These spectra include all backgrounds (room background, background radiations from empty frame with beam on and beam off) measured during the experiment. All background radiation measurements were normalized according to the time acquisition and the integrated proton charge. The final prompt gamma spectra at 90 degrees for the 95 MeV proton collision on the carbon and mylar targets are shown in figures 5.15 and 5.16. This procedure was repeated for all 30 (2 crystals were skipped) high purity germanium crystals of all five different energies and for both targets for a total of 300 (30 x 5 x 2) spectra used to determine the differential cross-sections.

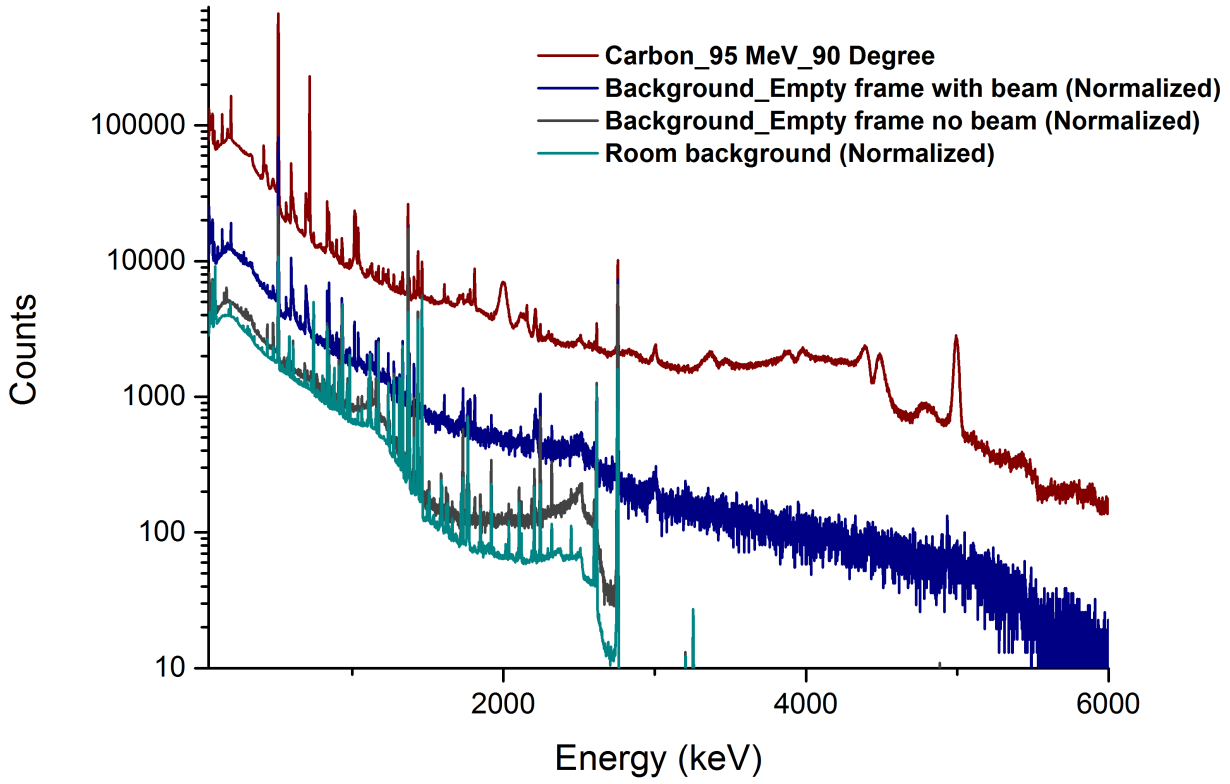

Figure 5.13: The red line shows the raw data for the 95 MeV proton bombardment of the carbon target, cyan color line is room background, the blue line indicates the background radiation from the frame with the beam on, and the gray line shows the background from the target frame with the beam off. These spectra were measured by the clovers placed at 90 degrees to the beam line.

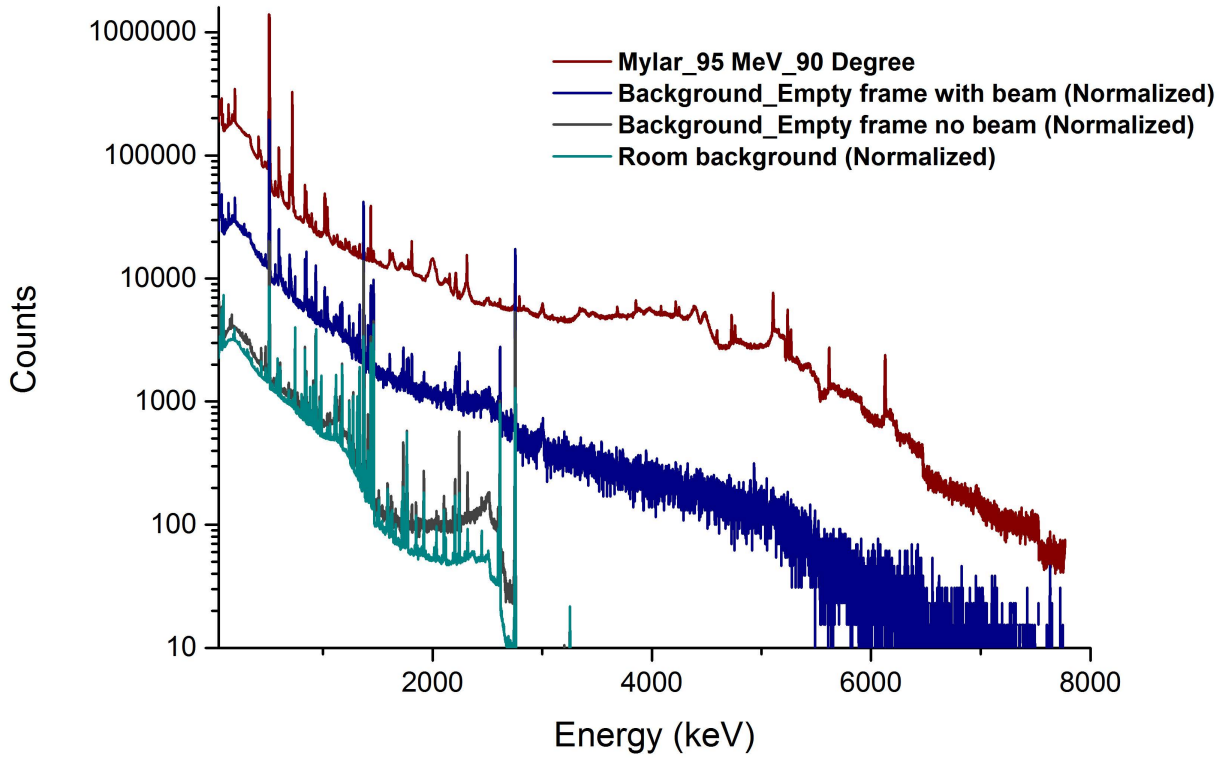

Figure 5.14: The red line shows the raw data for the 95 MeV proton bombardment of the mylar target, cyan color line is the room background, the blue line indicates the background radiation from the frame with the beam on, and the gray line shows the background from the target frame with the beam off. These spectra were measured by the clovers placed at 90 degrees to the beam line

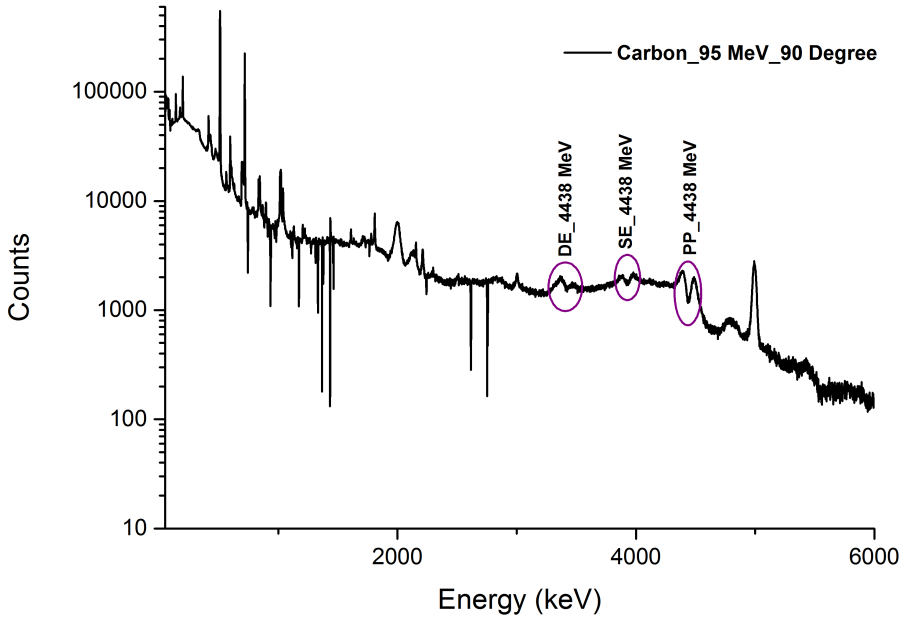

Figure 5.15: Prompt gamma spectrum for the 95 MeV proton collision with the carbon target measured by the clovers placed at 90 degrees to the beam direction. PP: Photo peak, SE: Single escape peak, and DE: Double escape peak.

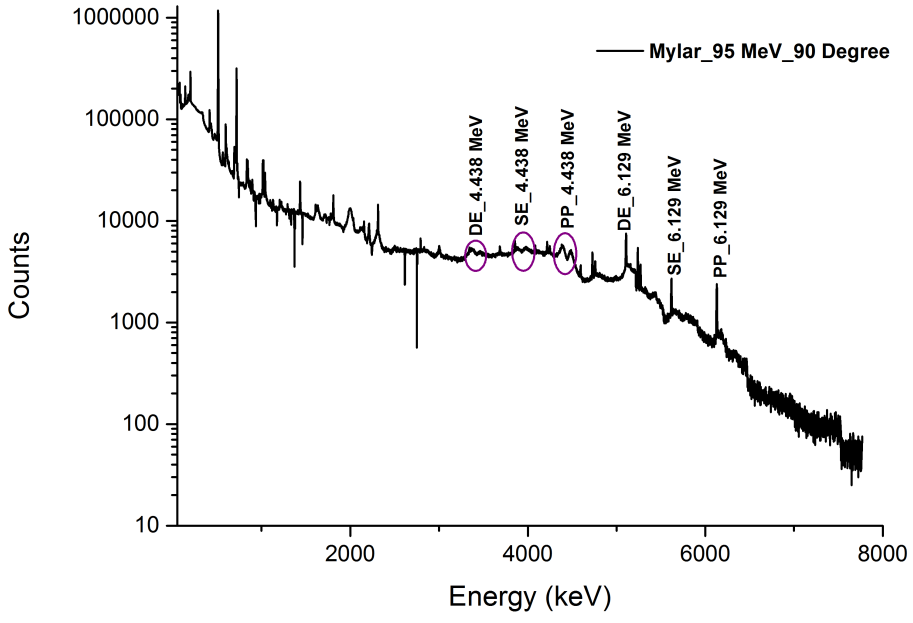

Figure 5.16: Prompt gamma spectrum for the 95 MeV proton collision with the mylar target measured by the clovers placed at 90 degrees to the beam direction. PP: Photo peak, SE: Single escape peak, and DE: Double escape peak.

5.3.2 Differential cross section

As described in section 3.3.4, the differential cross-section relies on determining the number of events for a given reaction i.e: the area under the relevant energy peak. Figure 5.17 shows the 4.438 MeV photo peak (with manually drawn background line) for the 95 MeV proton collisions on the carbon target for one of the high purity germanium crystals at 90^0, 130^0, and 140^0.

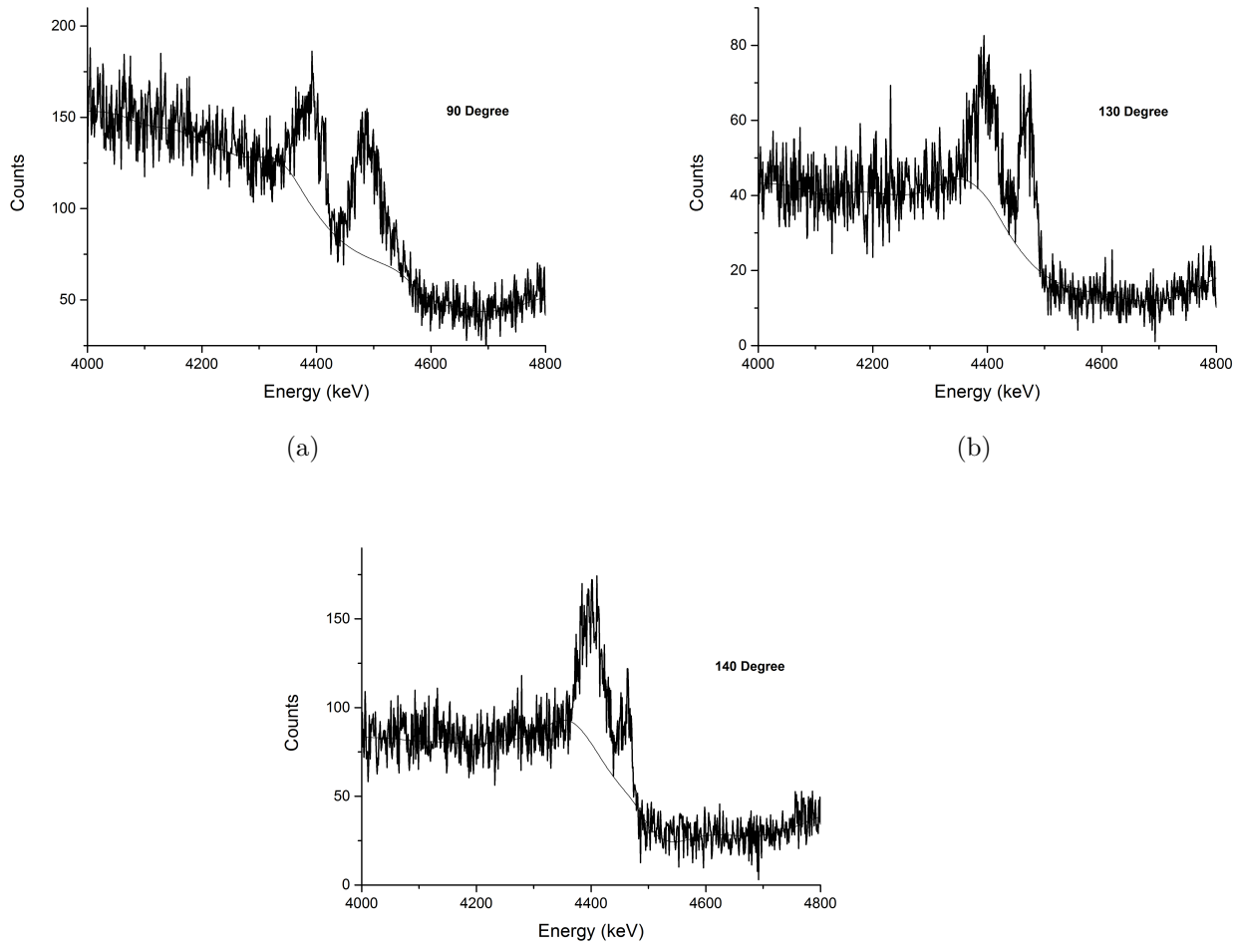

(a) (b)

(c)

Figure 5.17: The 4.438 MeV photo peak with manually added spectrum background line (black line) for the 95 MeV proton collisions on the carbon target for one of the high purity germanium crystals at 90^0 (a) - crystal A in clover 3, 130^0 (b) - crystal A in clover 1, and 140^0 (c) - crystal C in clover 1.

For oxygen (Mylar target), only the 6.129 MeV peak was observed. In addition, the 6.129 MeV photo peak of ^{16}O was only observed in 11 out of the 32 high purity germanium crystals. Since the observed 6.129 MeV peak had a Gaussian shape, Gaussian peak fitting in OriginPro was used to find the number of detected events in these photo peaks. Figures 5.18, 5.19, and 5.20 show the Gaussian peaks for the 6.129 MeV photo peak for the 95 MeV proton bombardment for the Mylar target.

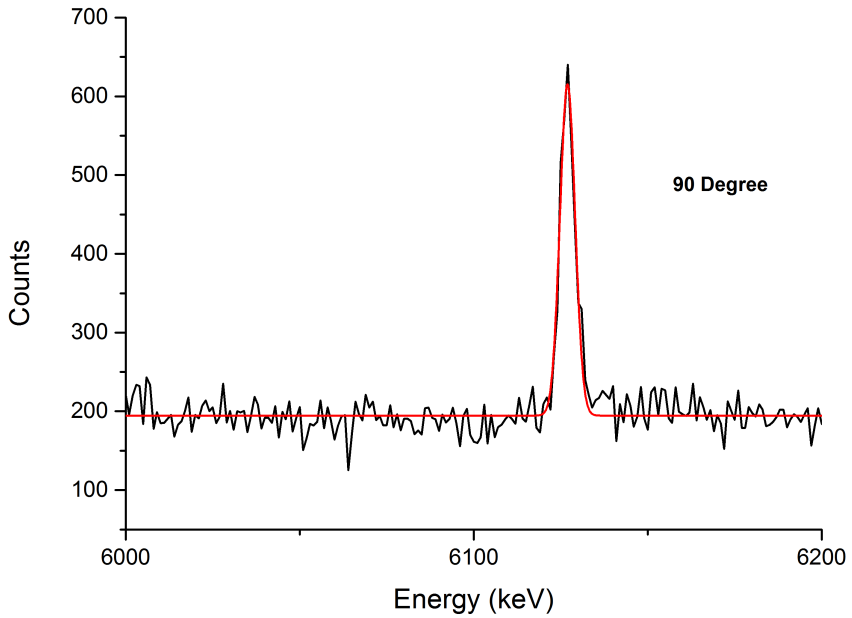

Figure 5.18: The 6.129 MeV photo peak with spectrum background subtraction for the 95 MeV proton collisions on Mylar target in a crystal C of clover 3 located at 90^0.

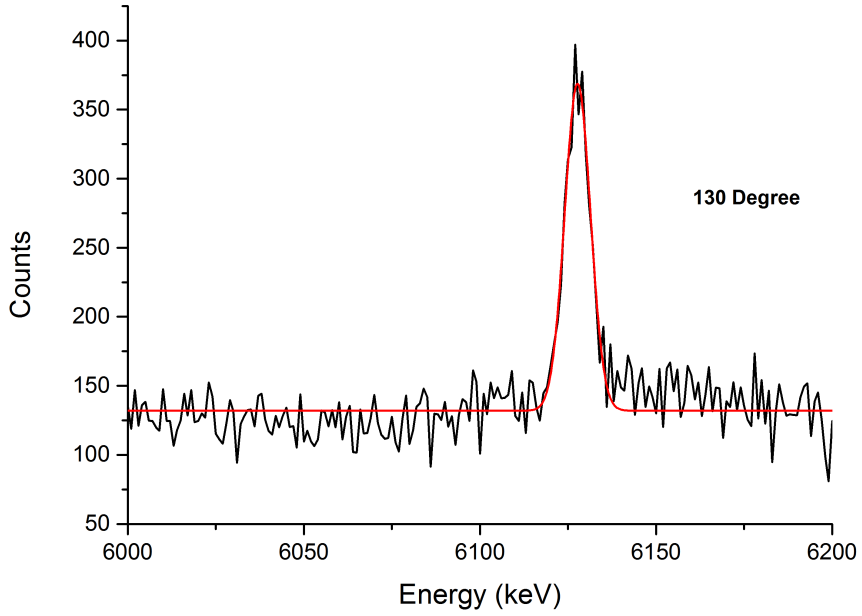

Figure 5.19: The 6.129 MeV photo peak with the spectrum background subtraction for the 95 MeV proton collisions on Mylar target in a crystal B of a clover 6 located at 130^0.

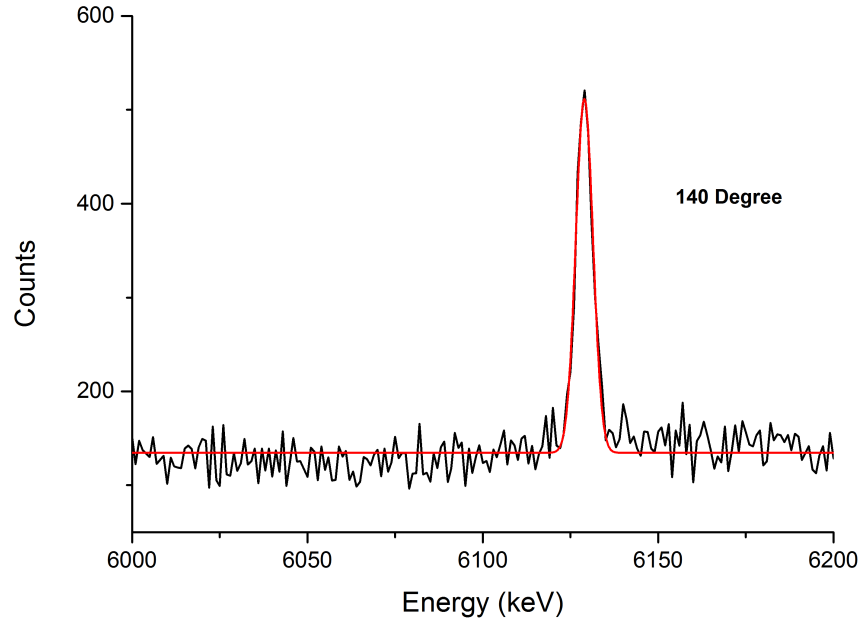

Figure 5.20: The 6.129 MeV photo peak with the spectrum background subtraction for the 95 MeV proton collisions on Mylar target in a crystal C of clover 6 located at 140^0.

These procedures were repeated for each high purity germanium crystal and the average values were calculated for the differential cross section at 90^0, 130^0, and 140^0 for the above mentioned peaks (4.438 MeV and 6.129 MeV) at five different proton energies (66, 80, 95, 110, and 125 MeV). The uncertainty in the differential cross section calculation was determined by using the method as discussed in section 3.3.5. The complete list of differential cross-sections (4.438 MeV and 6.129 MeV) for each crystal and five different energies with associated uncertainties are given in appendix B. The average values of differential cross section for 4.438 MeV peak from carbon and mylar targets are given in table 5.5 and 5.6, and for 6.129 MeV from mylar target are given in table 5.7.

Table 5.5: Average differential cross-section values for 4.438 MeV carbon target

Energy (MeV)	$\left(\frac{d\sigma}{d\Omega}\right)_{90^0}$	$\left(\frac{d\sigma}{d\Omega}\right)_{130^0}$	$\left(\frac{d\sigma}{d\Omega}\right)_{140^0}$
66	1.99 ± 0.12	1.89 ± 0.11	2.00 ± 0.12
80	1.59 ± 0.09	1.44 ± 0.08	1.53 ± 0.09
95	1.16 ± 0.07	0.99 ± 0.06	1.08 ± 0.06
110	0.93 ± 0.05	0.89 ± 0.05	0.91 ± 0.05
125	0.88 ± 0.04	0.76 ± 0.04	0.78 ± 0.04

Table 5.6: Average differential cross-section values for 4.438 MeV mylar target

Energy (MeV)	$\left(\frac{d\sigma}{d\Omega}\right)_{90^0}$	$\left(\frac{d\sigma}{d\Omega}\right)_{130^0}$	$\left(\frac{d\sigma}{d\Omega}\right)_{140^0}$
66	2.04 ± 0.12	1.98 ± 0.12	2.01 ± 0.12
80	1.78 ± 0.11	1.67 ± 0.10	1.72 ± 0.10
95	1.28 ± 0.08	1.16 ± 0.07	1.18 ± 0.07
110	1.11 ± 0.07	0.97 ± 0.06	0.99 ± 0.06
125	0.93 ± 0.06	0.83 ± 0.04	0.86 ± 0.05

Table 5.7: Average differential cross-section values for 6.129 MeV mylar target

Energy (MeV)	$\left(\frac{d\sigma}{d\Omega}\right)_{90^0}$	$\left(\frac{d\sigma}{d\Omega}\right)_{130^0}$	$\left(\frac{d\sigma}{d\Omega}\right)_{140^0}$
66	2.30 ± 0.15	2.06 ± 0.13	2.09 ± 0.14
80	1.99 ± 0.13	1.65 ± 0.11	1.72 ± 0.11
95	1.50 ± 0.10	1.20 ± 0.08	1.23 ± 0.08
110	1.12 ± 0.08	0.96 ± 0.07	0.97 ± 0.07
125	1.12 ± 0.08	0.82 ± 0.06	0.92 ± 0.07

5.3.3 Angular distribution of 4.438 MeV

The angular distribution of the 4.438 MeV gamma-ray line from ^{12}C was obtained by using a fourth order Legendre polynomial function (shown in equation 3.8). The fourth order Legendre polynomial function was fit to the measured differential cross-section values using the curve_fit function in the Scipy module of python. The fitting function produced the Legendre coefficients and the obtained values are shown in table 5.8. The angular distribution of the 4.438 MeV ^{12}C gamma for 66 MeV, 80 MeV, 95 MeV, 110 MeV, and 125 MeV proton energies are shown in figures 5.21(a), 5.21(b), 5.21(c), 5.21(d), and 5.21(e). Similar angular distribution patterns were obtained at each energy except for the 125 MeV proton energy. This is most likely due to the instability of the beam during the 125 MeV experimental run.

Table 5.8: Obtained Legendre coefficients during the angular distribution fit using python for the 4.438 MeV ^{12}C gamma

Energy (MeV)	a_0	a_2	a_4
66	1.998077	0.268328	0.327699
80	1.565181	0.224034	0.366764
95	1.124316	0.202178	0.375929
110	0.918018	0.030271	0.074713
125	0.827391	0.0128	0.152558

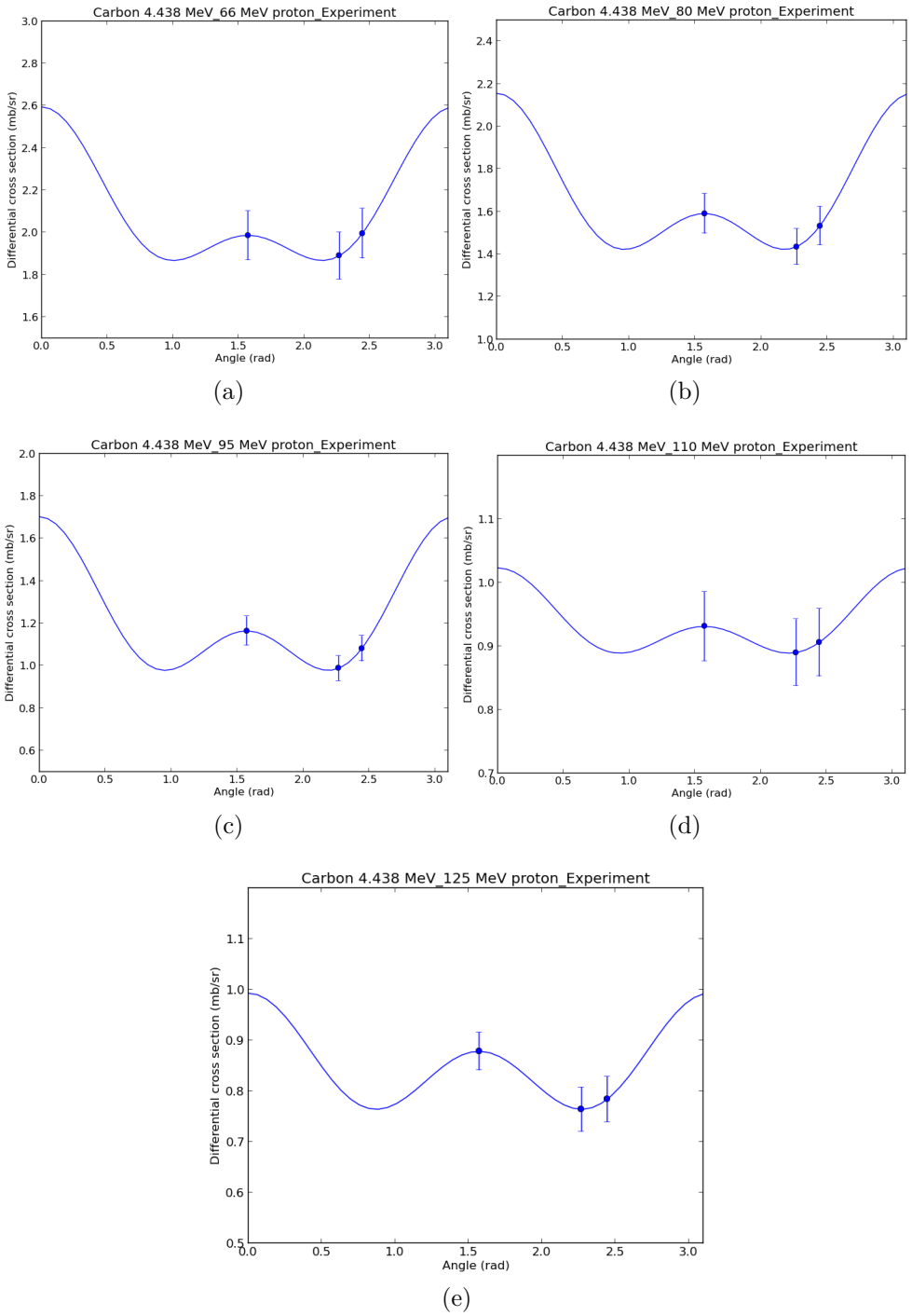

Figure 5.21: Angular distribution for the ^{12}C 4.438 MeV gamma-ray line at 66 (a), 80 (b), 95 (c), 110 (d), 125 (e) MeV proton energies. The solid lines are the fitted curves from the 4^{th} order Legendre polynomial python fit. The circle indicates the measured angular dependence term (differential cross section) with associated uncertainty.

The angular distribution of the 4.438 MeV gamma from the mylar target was also fit using the curve_fit function to determine the 4.438 MeV cross-section. The obtained Legendre coefficients from the fit are shown in table 5.9. The angular distributions of the 4.438 MeV gamma for the mylar target at 66 MeV, 80 MeV, 95 MeV, 110 MeV, and 125 MeV proton energies are shown in figures 5.22(a), 5.22(b), 5.22(c), 5.22(d), and 5.22(e).

Table 5.9: Obtained Legendre coefficients during the angular distribution fit using python for the 4.438 MeV gamma from the mylar target

Energy (MeV)	a_0	a_2	a_4
66	2.02448786	0.0790708	0.13719344
80	1.74892602	0.09724099	0.20318527
95	1.2251633	0.00725432	0.16310362
110	1.04732319	0.01087329	0.18296922
125	0.89072317	0.04000891	0.14528344

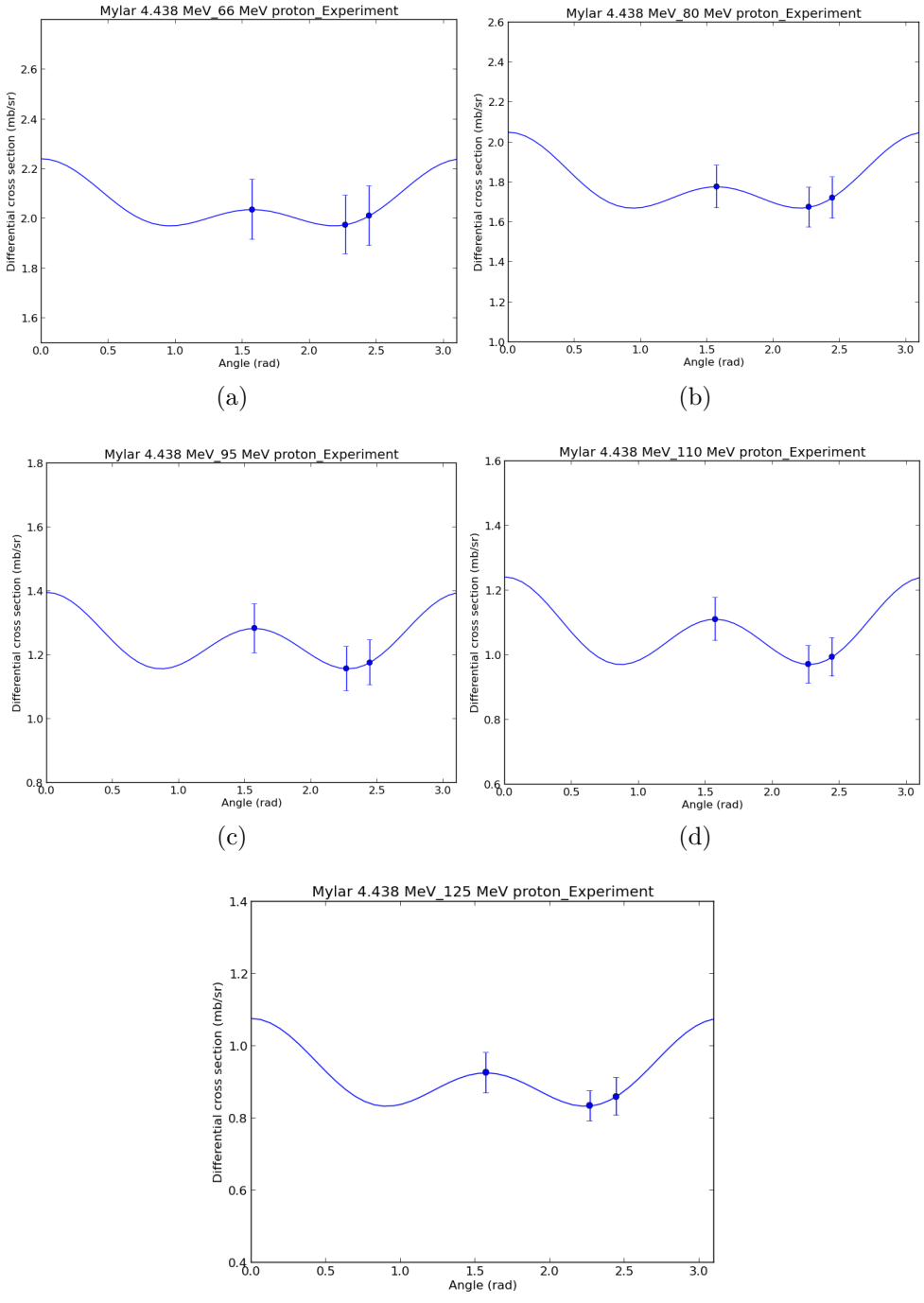

Figure 5.22: Angular distribution for the mylar 4.438 MeV gamma-ray line at 66 (a), 80 (b), 95 (c), 110 (d), 125 (e) MeV proton energies. The solid lines are the fitted curves from the 4^{th} order Legendre polynomial python fit. The circle indicates the measured angular dependence term (differential cross section) with associated uncertainty.

5.3.4 Angular distribution of 6.129 MeV

The angular distribution of the 6.129 MeV gamma-ray line from ^{16}O was obtained by using a sixth order Legendre polynomial function (shown in equation 3.9). In order to fit a sixth order Legendre polynomial function, at least four different angular measurements are required. Unfortunately, the detector arrangement only provides three different angular measurements (90^0, 130^0, and 140^0). Therefore, two virtual points at 50^0 (180^0-130^0) and 40^0 (180^0-140^0) were created to take advantage of the angular distribution of prompt gamma emission being symmetric about 90^0 [Dyer et al. (1981), Lang et al. (1987), Lesko et al. (1988)]. This is an approximate method used to obtain a fit to the polynomial. The angular distribution of the 6.129 MeV gamma from ^{16}O (Mylar) at 66 MeV, 80 MeV, 95 MeV, 110 MeV, and 125 MeV proton energies are shown in figures 5.23(a), 5.23(b), 5.23(c), 5.23(d), and 5.23(e). The obtained Legendre coefficients are shown in table 5.10.

Table 5.10: Obtained Legendre coefficients during the angular distribution fit using python for the 6.129 MeV ^{16}O gamma

Energy (MeV)	a0	a2	a4	a6
66	2.538665	1	1.540676	1.027579
80	2.183465	1	1.653824	0.989917
95	1.721195	1	1.65272	1.076689
110	1.409037	1	1.468962	1.078393
125	1.309166	1	1.544416	0.866311

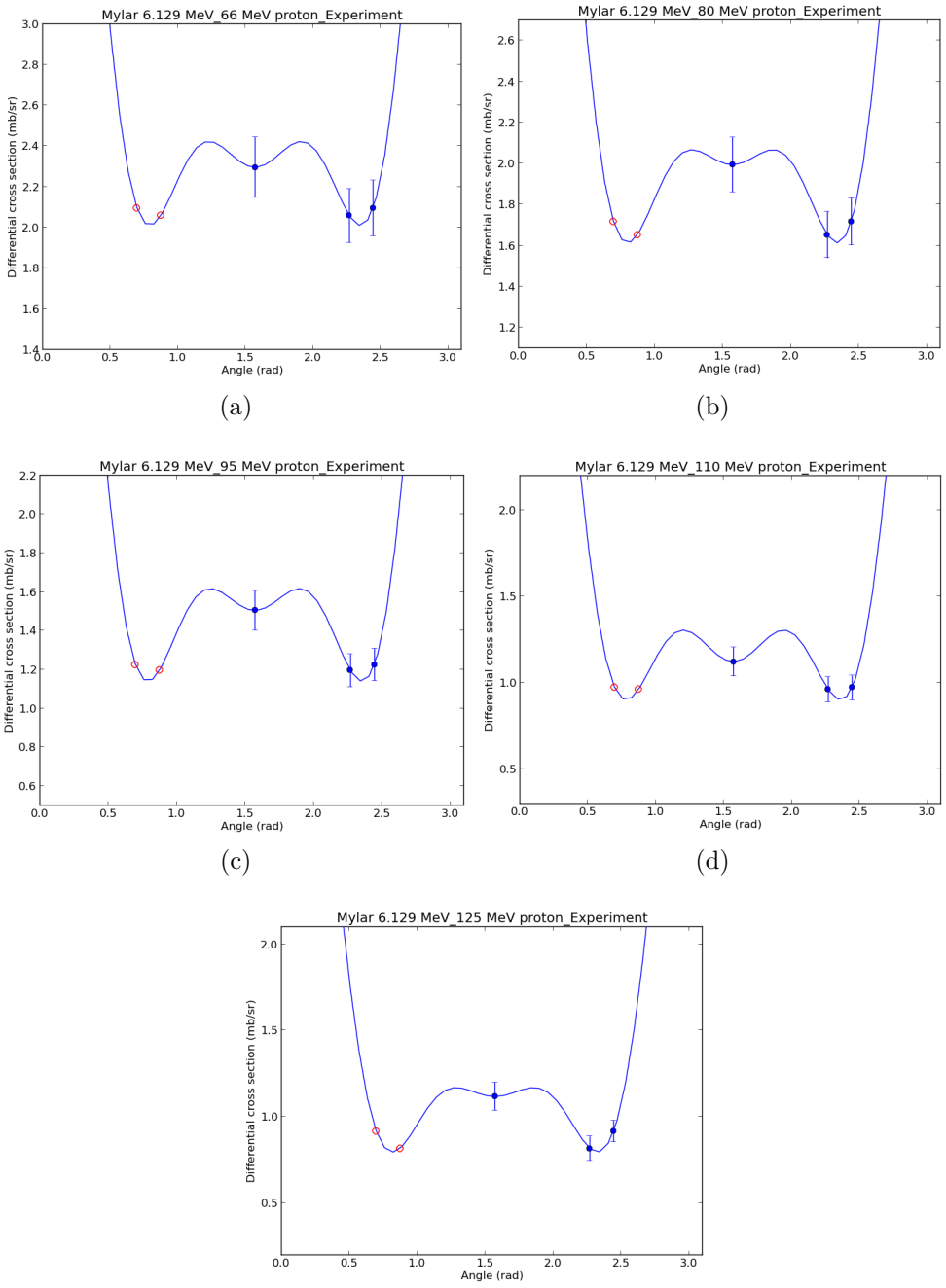

Figure 5.23: Angular distribution for the ^{16}O 6.129 MeV (Mylar) gamma-ray line at 66 (a), 80 (b), 95 (c), 110 (d), 125 (e) MeV proton energies. The solid lines are the fitted curves from the 6$^{\text{th}}$ order Legendre polynomial python fit. The blue circle indicates the measured angular dependence term (differential cross section) with associated uncertainty and red hollow circle indicates the virtual points.

5.3.5 Total cross-section measurement

As discussed in section 3.3.3, the Legendre polynomial coefficients were obtained by fitting Legendre polynomials to the differential cross-section data. The total cross-section is proportional to the zeroth-order Legendre coefficient a_0 and was calculated by multiplying a_0 by 4π. The measured total cross-sections for the 4.438 MeV gamma-ray line from the ^{12}C and mylar targets, and ^{16}O 6.129 MeV gamma-ray line from the mylar target are given in tables 5.11 and 5.12. The total cross-section versus energy plot for the 4.438 MeV gamma from carbon and mylar target is shown in figure 5.24, and for the 6.129 MeV gamma from mylar target is shown in figure 5.25.

Table 5.11: Experimental cross-section results for the 4.438 MeV gamma-ray line from ^{12}C and mylar targets

$E_p(MeV)$	σ(mb) (carbon)	σ(mb) (mylar)	Percent difference
66	25.1 ± 1.1	25.4 ± 1.2	1.20%
80	19.67 ± 0.88	21.98 ± 0.99	11.7%
95	14.13 ± 0.63	15.40 ± 0.70	8.99%
110	11.54 ± 0.51	13.16 ± 0.60	14.04%
125	10.40 ± 0.41	11.19 ± 0.51	7.60%

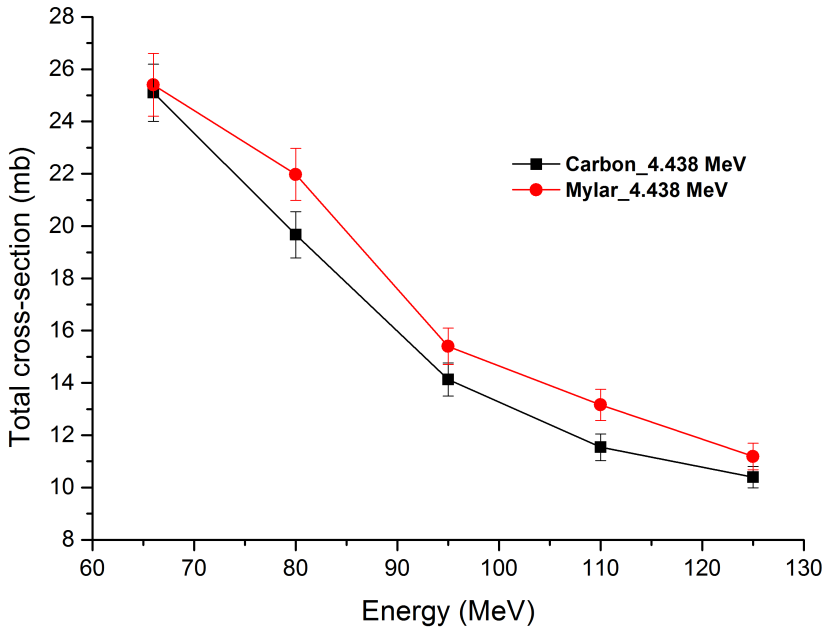

Figure 5.24: Experimental cross-section results for the 4.438 MeV gamma-ray line from ^{12}C and mylar targets

Table 5.12: Experimental cross-section results for the 6.129 MeV gamma-ray line from ^{16}O (Mylar)

$E_p(MeV)$	Total cross-section (σ)(mb)
66	31.9 ± 1.3
80	27.4 ± 1.2
95	21.63 ± 0.86
110	17.71 ± 0.72
125	16.45 ± 0.66

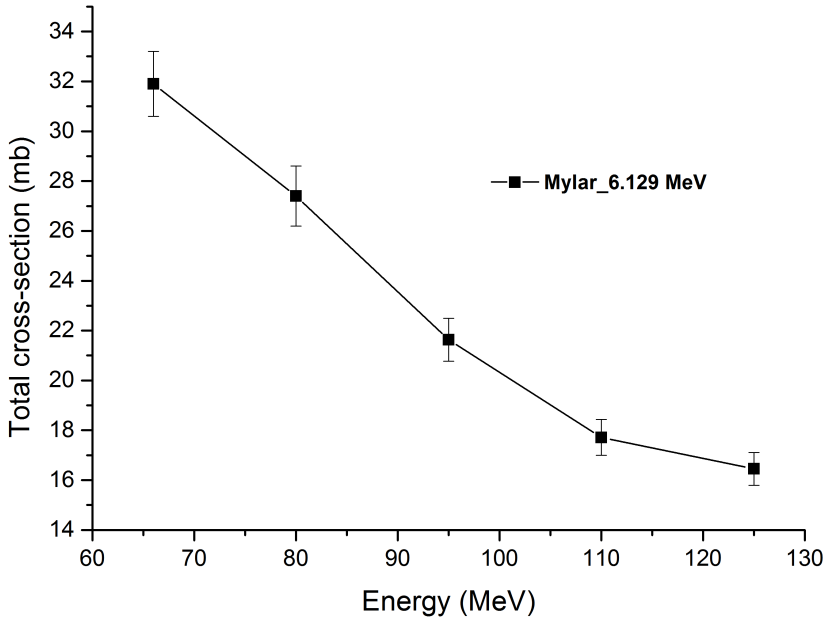

Figure 5.25: Experimental cross-section results for the 6.129 MeV gamma-ray line from ^{16}O (Mylar)

Chapter 6

Results from prompt gamma cross-section measurements

This chapter presents the results and data analysis for the simulations described in chapter 4. One of the primary aims of this work was to measure the prompt gamma cross-section for the 4.438 and 6.129 MeV gammas from the carbon and mylar targets using the Geant4 model for comparison with the experimental cross-section results. Firstly, this chapter describes the characteristics of the Compton suppression in the AFRODITE model. Secondly, it discusses the results of the validation of the Geant4 AFRODITE model. For this validation, the measured gamma spectra for ^{137}Cs, ^{60}Co, and ^{152}Eu were used to compare to the simulated gamma spectra. Thirdly, this chapter explains the calculations of the absolute detector efficiency using the AFRODITE model. Finally, it includes prompt gamma simulations for carbon and mylar targets at five different proton energies (66, 80, 95, 110, and 125 MeV), measurements of the differential cross-section, the angular distribution, and the total cross-section measurements for the 4.438 MeV and 6.129 MeV photo peaks.

6.1 Performance of the simulated Compton suppression

The standard gamma emitting sources (^{137}Cs, ^{60}Co, and ^{152}Eu) were simulated with and without the Compton suppression activated in the Geant4 AFRODITE model. In order to demonstrate the consistency of the simulated Compton suppression, the gamma spectra from one germanium crystal, one clover (for crystals), and the entire detector system (8 clovers) are also shown.

Figure 6.1 shows the simulated spectra for the ^{137}Cs source, and it is clear to see the difference between the suppressed and non-suppressed spectra. The suppressed spectra shows an improved photo peak, a reduced background, and a clear Compton edge. Based on the total gamma production by the Compton suppressed and non-suppressed spectra, there was a 45% less gammas in the suppressed spectra. The three sets of spectra from the crystal, clover, and entire system show virtually identical shape, indicating a consistent treatment of the Compton suppression in the AFRODITE code. Figure 6.2 shows the simulated spectra for ^{60}Co. This spectrum also has the same features as observed in the ^{137}Cs spectra, although the absence of the double escape peak from the 1173 keV gamma in the Compton suppressed spectra is missing. All above mentioned features were also seen in the ^{152}Eu spectra as shown in figure 6.3.

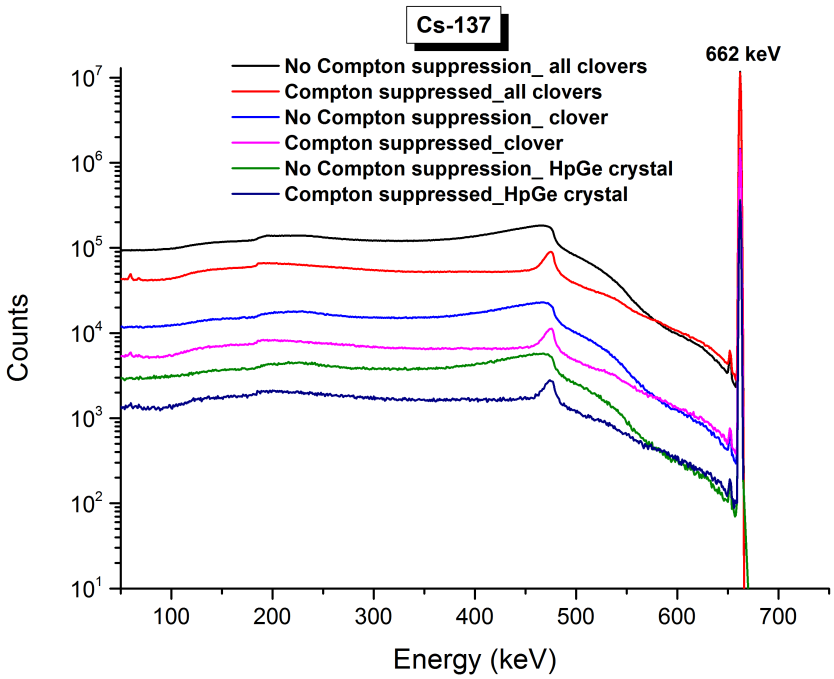

Figure 6.1: Spectra from the ^{137}Cs gamma source with Compton suppression and without Compton suppression in six different modes: crystal-green line, suppressed crystal-dark blue line, clover-blue line, suppressed clover-pink line, detector system (all clovers)-black line, and suppressed detector system-orange line. About 45% suppression was observed.

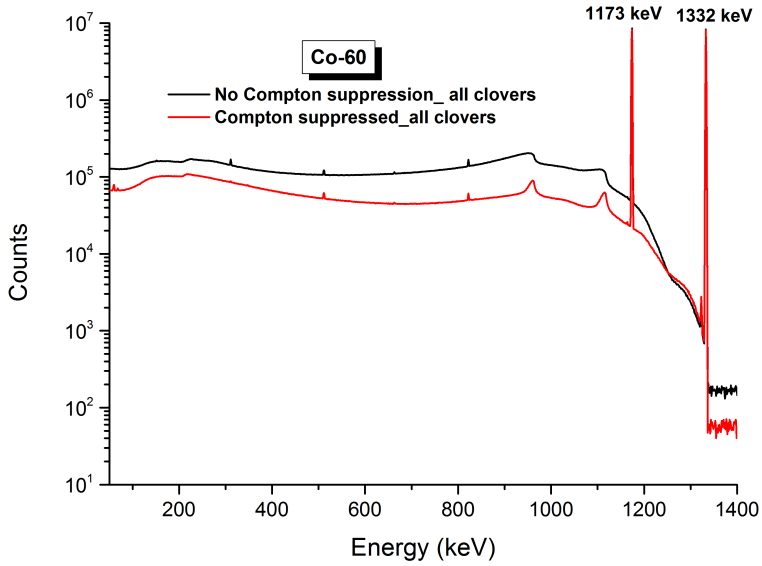

Figure 6.2: Spectra from ^{60}Co gamma source with Compton suppression and with no Compton suppression for entire AFRODITE detector system. Black line - No Compton suppressed spectrum. Red line - Compton suppressed spectrum.

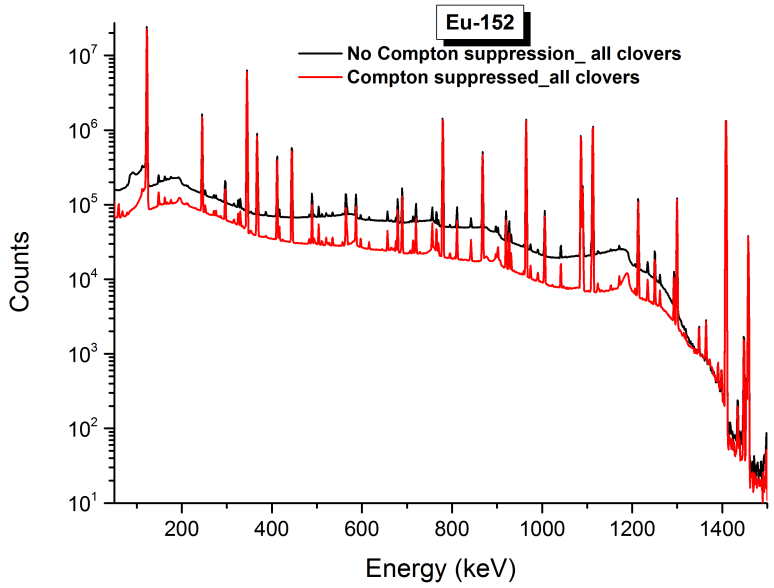

Figure 6.3: Spectra from ^{152}Eu gamma source with Compton suppression and with no Compton suppression for entire AFRODITE detector system. Black line - No Compton suppressed spectrum. Red line - Compton suppressed spectrum.

6.2 Validation of Geant4 AFRODITE model

The Geant4 Monte-Carlo model of the AFRODITE detector system was validated by using three standard gamma emitting sources (^{137}Cs, ^{60}Co, ^{152}Eu) as shown in figures 6.4, 6.5, and 6.6. The simulated gamma spectra were normalized against the experimentally obtained gamma spectra by comparing the number of gammas emitted by the gamma source (calculated from the source activity and the acquisition time) in the experiment and number of gamma histories used in the simulation. Both the experimental and simulated spectra have been Compton-suppressed.

Looking at the spectra in figures 6.4, 6.5, and 6.6, all of the photo peaks as well as the Compton edge and back scattered peaks are aligned. Comparing the simulated and experimental spectra shows that the Geant4 AFRODITE model had a higher efficiency than the experiment since the simulated photo peaks were higher than the experimental photo peaks. Based on the total gamma production in the experimental and simulated spectra, the Compton shielding of the Geant4 model was determined to work about 15% better than actual Compton shielding detector.

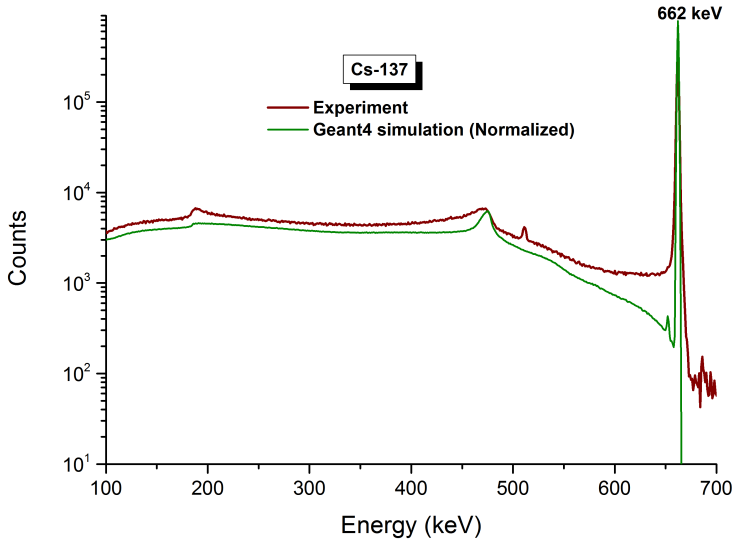

Figure 6.4: Comparison of the simulated and experimental gamma spectra from ^{137}Cs for the AFRODITE clover detector system. The green line shows the simulated spectrum and red line shows the experimental spectrum. Normalization was done according to the number of gammas emitted by the source in the experiment and number of gamma histories in the simulation.

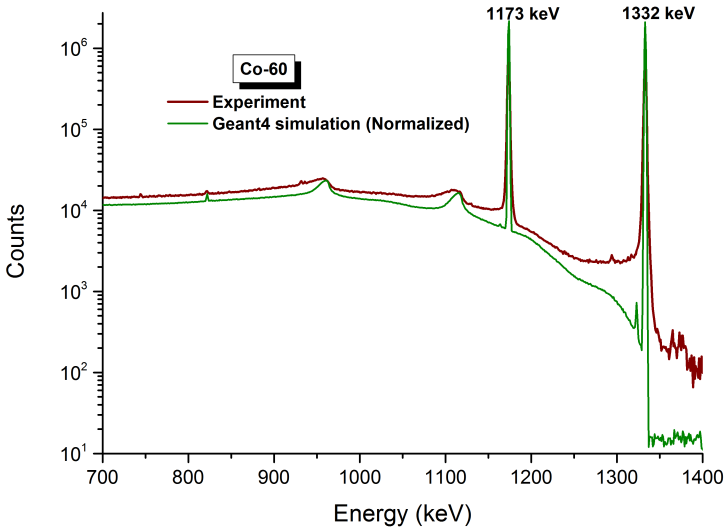

Figure 6.5: Comparison of the simulated and experimental gamma spectra from ^{60}Co for the AFRODITE clover detector system. The green line shows the simulated spectrum and red line shows the experimental spectrum. Normalization was done according to the number of gammas emitted by the source in the experiment and number of gamma histories in the simulation.

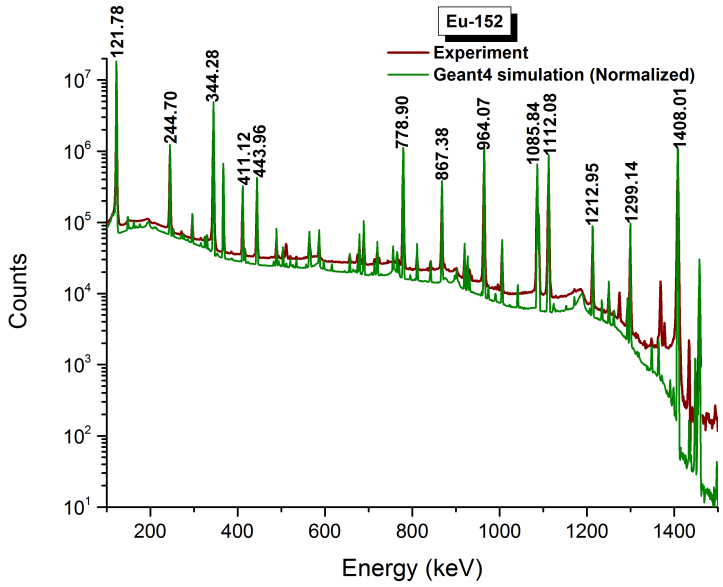

Figure 6.6: Comparison of the simulated and experimental gamma spectra from ^{152}Eu for the AFRODITE clover detector system. The green line shows the simulated spectrum and red line shows the experimental spectrum. Normalization was done according to the number of gammas emitted by the source in the experiment and number of gamma histories in the simulation.

6.3 Absolute detector efficiency for simulation

To measure the absolute detector efficiency for the simulations, the same procedures were repeated as for the experimental measurement of absolute detector efficiency as described in Chapter 5. In the experiment, the absolute detector efficiencies were calculated separately for each high purity germanium crystal since each crystal has a different efficiency. But, for the simulation the crystals are identically defined, so the efficiency for each crystal will be nearly identical. Therefore, there is no need for an efficiency response curve for each simulated germanium crystal. Only one germanium crystal was considered to find the efficiency response curve for all the simulated crystals. Figures 6.7, 6.8, and 6.9 show the Gaussian peak fitting using OriginPro data analysis program for the 662 keV photo peak from ^{137}Cs, both photo peaks for (1173 keV and 1332 keV) ^{60}Co, and two (779 keV and 867 keV) out of the 12 photo peaks from ^{152}Eu. The above peak fitting procedure was repeated for the remaining ^{152}Eu photo peaks for germanium crystal A in clover 1. For the simulation, the first two photo peaks (122 keV and 245 keV) of ^{152}Eu were ignored because of insufficient data. The simulated efficiency response curve for germanium crystal A in clover 1 is shown in figure 6.10. In order to find the function to fit the absolute efficiency response curve, a third order exponential function was used. Fitting details for germanium crystal A in clover 1 are shown in table 6.1.

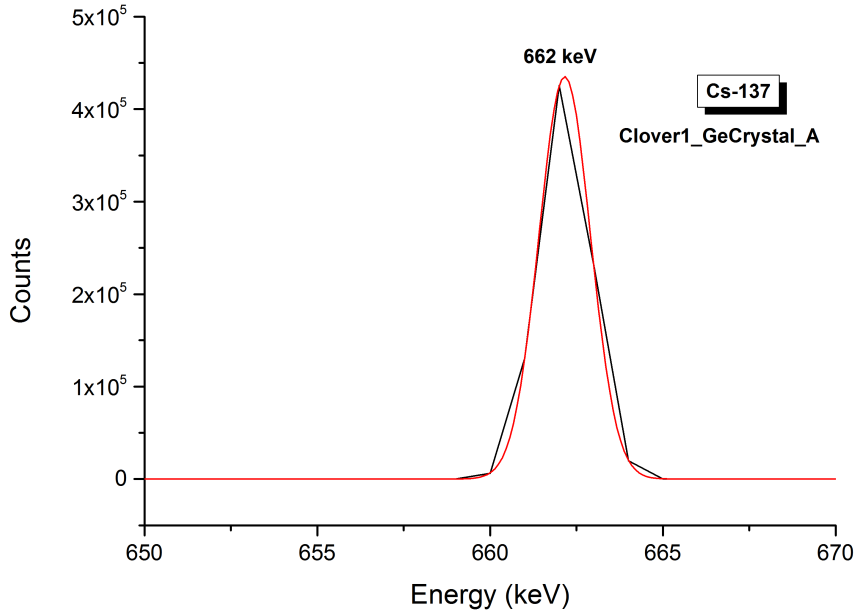

Figure 6.7: Fitted Gaussian photo peak (red line) to find area under the 662 keV peak from ^{137}Cs for germanium crystal A of clover 1.

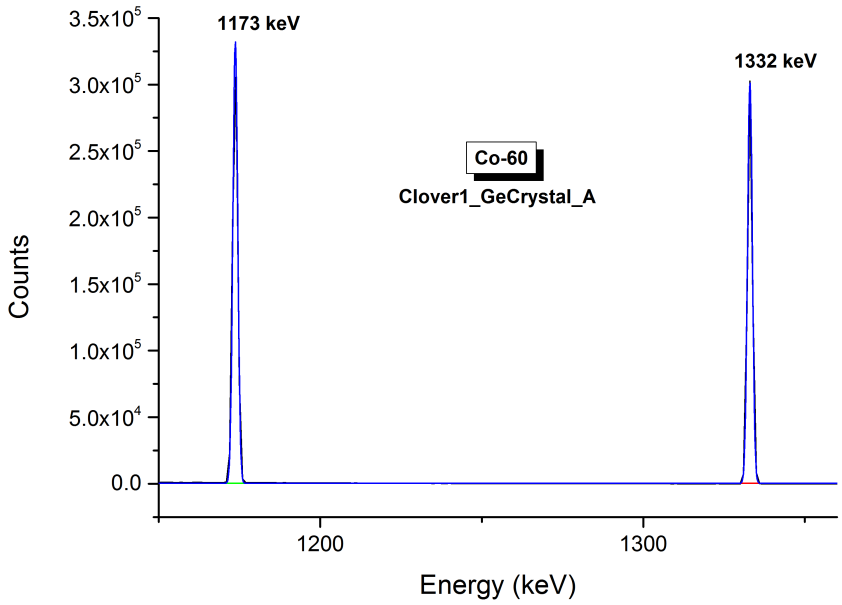

Figure 6.8: Fitted Gaussian photo peaks to find area under the 1173 keV and 1332 keV peaks from ^{60}Co for germanium crystal A of clover 1. Horizontal green and red lines are the background.

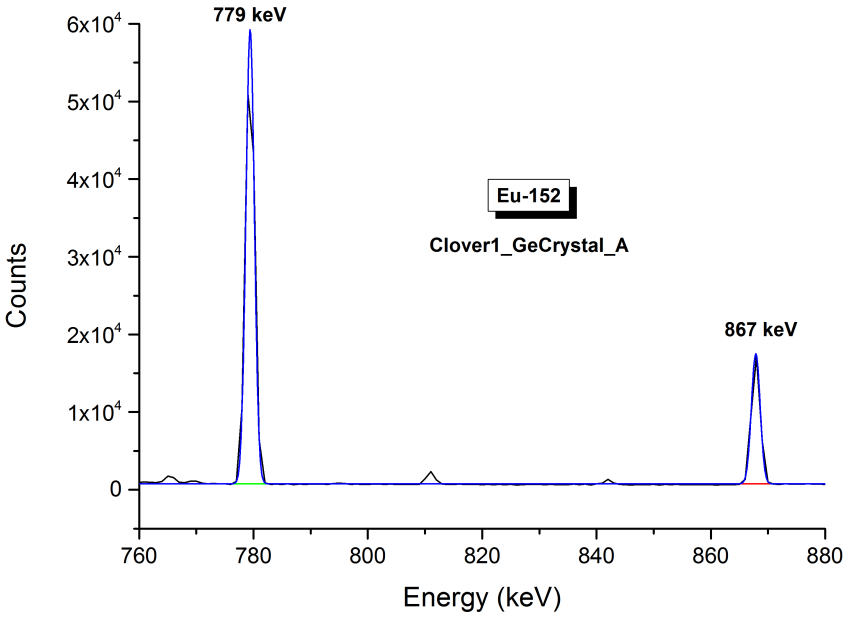

Figure 6.9: Fitted Gaussian photo peaks to find area under the 779 keV and 867 keV peaks from ^{152}Eu for germanium crystal A of clover 1. Horizontal green and red lines are the background.

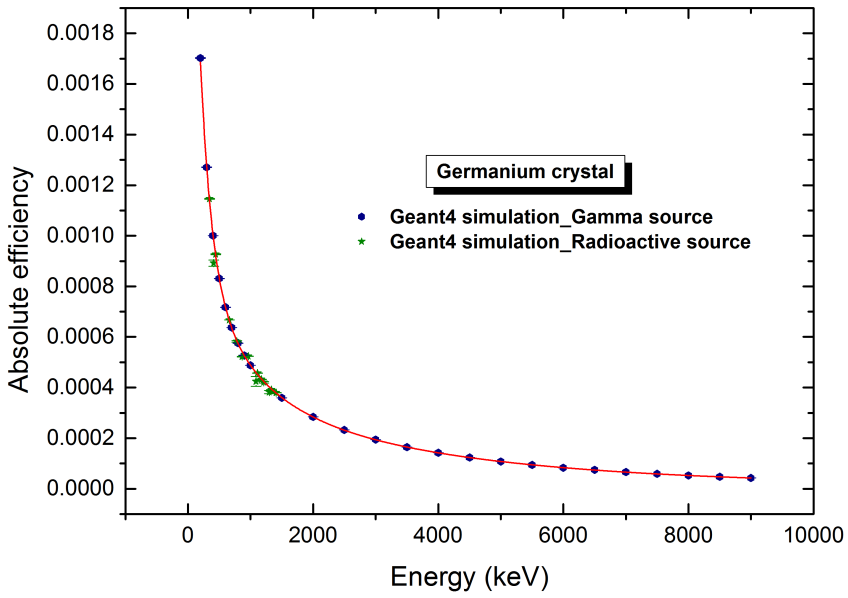

Figure 6.10: Absolute detector efficiency response curve for germanium crystal A of clover 1. The green points are the simulated efficiencies for the standard gamma emitting sources and the blue color points are the efficiencies for the single-energy gamma sources.

Table 6.1: Fitting details for the absolute detector efficiency response curve for germanium crystal A in clover 1 of the Geant4 model of the AFRODITE detector.

Model	ExpDec3		
Equation	$y = A_1 exp(-x/t_1) + A_2 exp(-x/t_2) + A_3 exp(-x/t_3) + y_0$		
Reduced Chi-Sqr	95.25416		
Adj. R-Square	0.99998		
		Value	Standard Error
Absolute efficiency	y_0	1.37×10^{-05}	9.72×10^{-07}
Absolute efficiency	A_1	5.76×10^{-04}	1.33×10^{-05}
Absolute efficiency	t_1	801.7626	24.94514
Absolute efficiency	A_2	3.98×10^{-04}	7.84×10^{-06}
Absolute efficiency	t_2	3447.60197	66.98161
Absolute efficiency	A_3	0.00251	7.54×10^{-05}
Absolute efficiency	t_3	184.57007	4.45495

6.4 Calculating prompt gamma cross section from simulated data

This section illustrates how the cross-section was measured with its associated uncertainty for the 4.438 MeV gamma-ray line from carbon and mylar and the 6.129 MeV gamma-ray line from ^{16}O in simulation studies. As described in Chapter 5, the same basic cross-section measurement methods which were applied in experimental cross-section calculation were used to measure the simulated differential cross-section and total cross-section with a few small changes. These changes will be described here.

6.4.1 Simulated prompt gamma spectra

As discussed in section 4.6, prompt gamma spectra were obtained by using the Geant4 model of the AFRODITE detector system with ^{12}C and Mylar targets at five different proton energies (66, 80, 95, 110, and 125 MeV). Figures 6.11 and 6.12 show the prompt gamma spectra obtained for an 80 MeV proton collision on the ^{12}C and Mylar targets, respectively. In these figures, the gamma spectra from the 90 and 130 degree germanium crystals are shown. The 140 degree gamma spectra are not included since these spectra are very similar to the 130 degree spectra.

For both of the prompt gamma spectra, the 130 degree spectra is higher than the 90 degree spectra. While we will see later in section 6.4 that the gamma peaks of interest (4.438 MeV and 6.129 MeV) at 90 degree have a larger number of counts than at 130 degree, the overall gamma production is higher at 130 degree. For the carbon target prompt gamma spectrum, the 4.438 MeV photo peak and the double escape peak are both clearly visible, but interestingly the single escape peak is not. Unlike the 4.438 MeV peaks from the mylar target (figure 6.12) where the photo peak, the single escape peak, and the double escape peak are all visible. Unfortunately, the 6.129 MeV photo peak from ^{16}O in the mylar target is virtually non-existent.

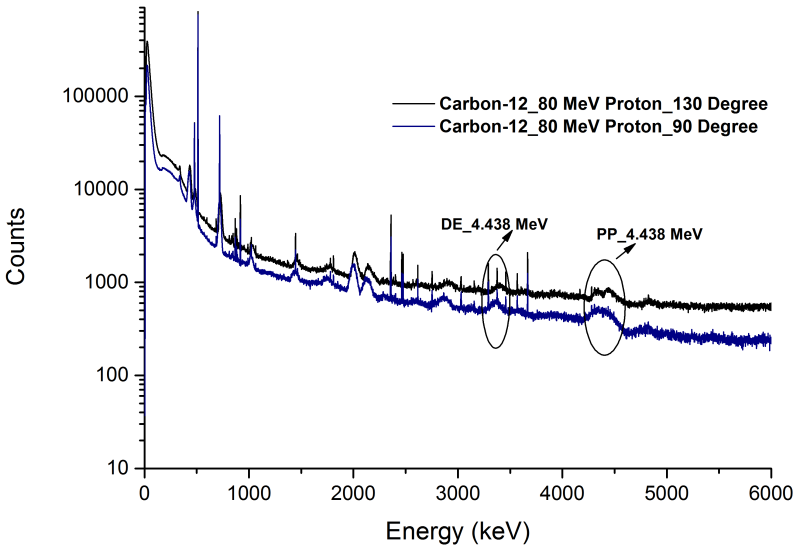

Figure 6.11: Simulated prompt gamma spectra from a 80 MeV proton collision with the carbon target. The blue line is the 90^0 spectrum and the black line is the 130^0 spectrum. The gap between two spectra shows a higher gamma production in crystals placed at 130^0 than at 90^0

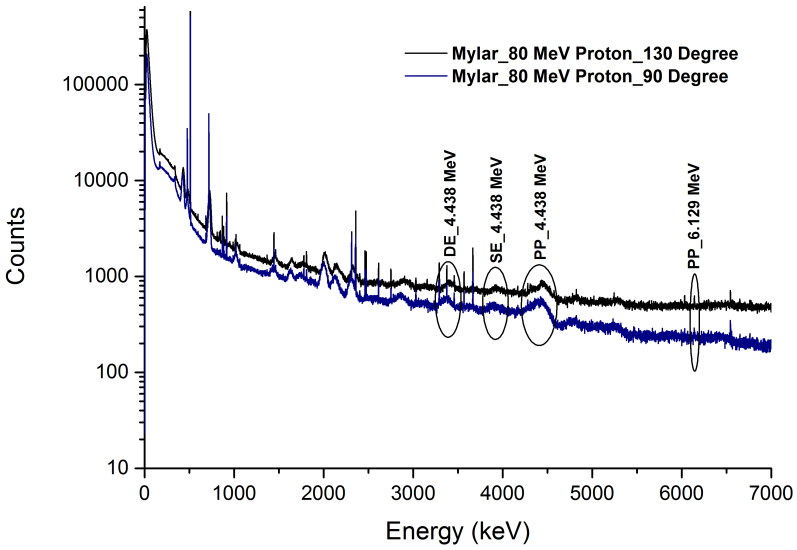

Figure 6.12: Simulated prompt gamma spectra from a 80 MeV proton collision with the mylar target. The blue line is the 90^0 spectrum and the black line is the 130^0 spectrum.

From these two prompt gamma spectra (Figures 6.11 and 6.12), two problems arose that required further investigation. First, the 4.438 MeV photo peak from the carbon target is broader than its experimental equivalent, as shown in figure 7.2. Second, as mentioned above, the 6.129 MeV photo peak from the mylar target does not appear in the simulations at any angle. These two problems are discussed in the following section.

6.4.2 Investigation into Geant4 Physics

Both of the aberrations found in the simulated prompt gamma spectra (the broad 4.438 MeV peak from ^{12}C and the suppressed 6.129 MeV photo peak from ^{16}O) point to issues within the physics of the AFRODITE code. The AFRODITE simulations were run using the binary cascade model (QGSP_BIC) with the default inelastic (Geisha) cross-section data set as the suggested model for proton collisions in the 0 - 200 MeV energy range (G4Physics (2016)). This section compares the prompt gamma spectrum obtained using this recommended physics model against other available models. The Xsection code (described in Section 4.4) was used to perform these comparisons. The physics model investigation consists of comparing the default values of the GQSP_BIC Physics list (specifically the inelastic scatter model, the inelastic cross-section data set and the exciton number setting) to the values suggested by the work of Jeyasugiththan (Jeyasugiththan and Peterson (2015)), as outlined in Section 4.5.1.

Let's start by looking at 80 MeV proton collisions with a carbon target. First, the default inelastic physics model (Binary Cascade) remains fixed, while comparing the inelastic cross-section data sets. Figure 6.13 shows the default data set (Geisha) against the Tripathi data set, and the two spectra are basically identical, indicating that the cross-section data set has no bearing on the Binary Cascade inelastic scatter model. Next, the precompound model (PRECO) was compared against the binary cascade model (BC) using the default cross-section data set (Geisha), shown in figure 6.14. The number of gamma counts was suppressed for the PRECO model (both overall and in the 4.438 MeV peak) while the width of the 4.438 MeV peak was unchanged. Figure 6.14 also shows that the same broad (and suppressed) peak is observed when the Tripathi cross-section data set is used with the precompound model.

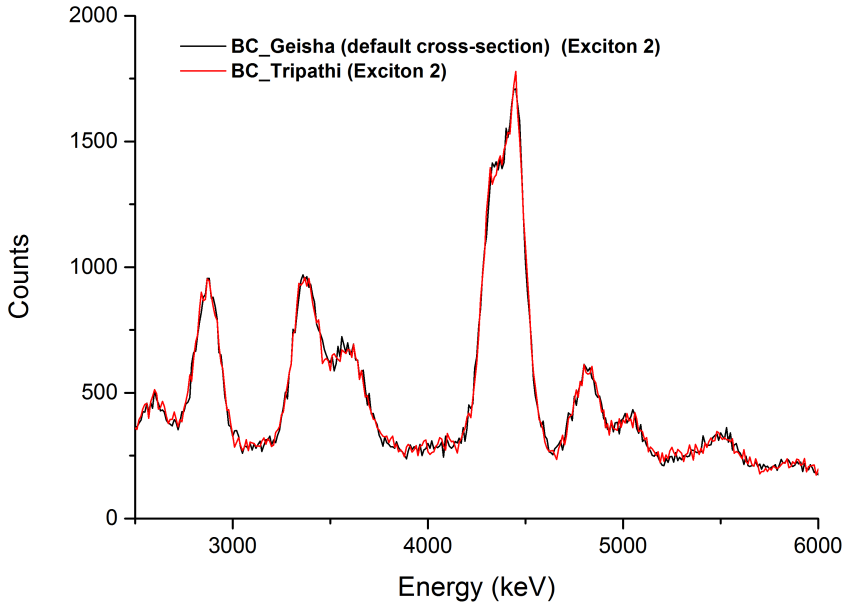

Figure 6.13: Prompt gamma spectrum comparison for binary cascade with two different inelastic cross-section data set (Geisha and Tripathi).

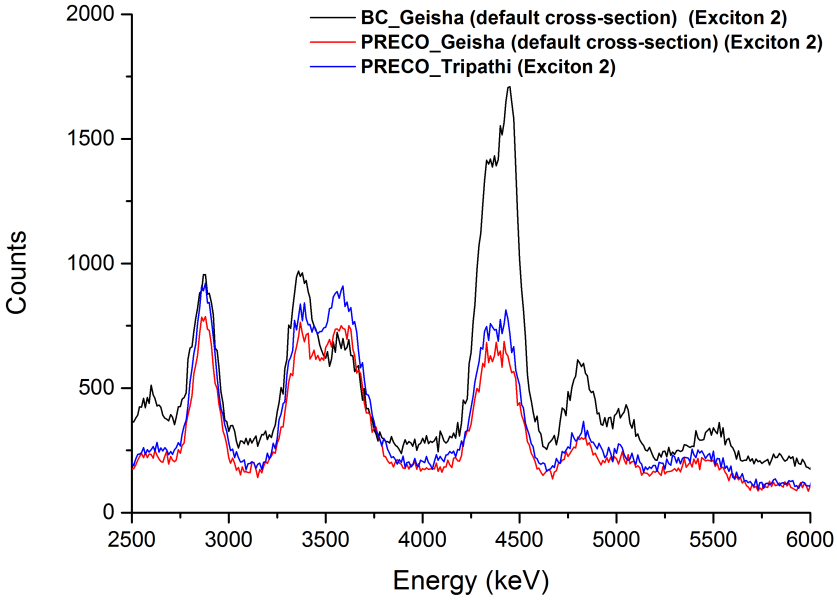

Figure 6.14: Binary cascade prompt gamma spectrum comparison against the precompound model using the Tripathi and Geisha cross-section data set.

Finally, the exciton number was changed in the precompound model from the default value of 2 to 1 with the results shown in figure 6.15. The precompound model with exciton 1 is

able to significantly narrow the 4.438 MeV photo peak for both inelastic cross-section data sets. The spectra from the precompound model with the two different cross-section data sets are very similar with the only difference being a slightly higher number of prompt gammas from the Tripathi data set. While this difference is slight, using the Geisha cross-section data set is recommended due to the tendency for Geant4 simulations to overestimate prompt gamma production values. Based on these comparisons, the precompound model using an exciton number of 1 and the Geisha cross-section data set provides a 4.438 MeV photo peak that is closer to the experimental result, both due to the narrower peak and the suppressed prompt gamma production. This appears to be a better choice for 66 to 125 MeV proton collisions with carbon than the recommended QGSP_BIC physics list for Geant4 (version 10.01.p03).

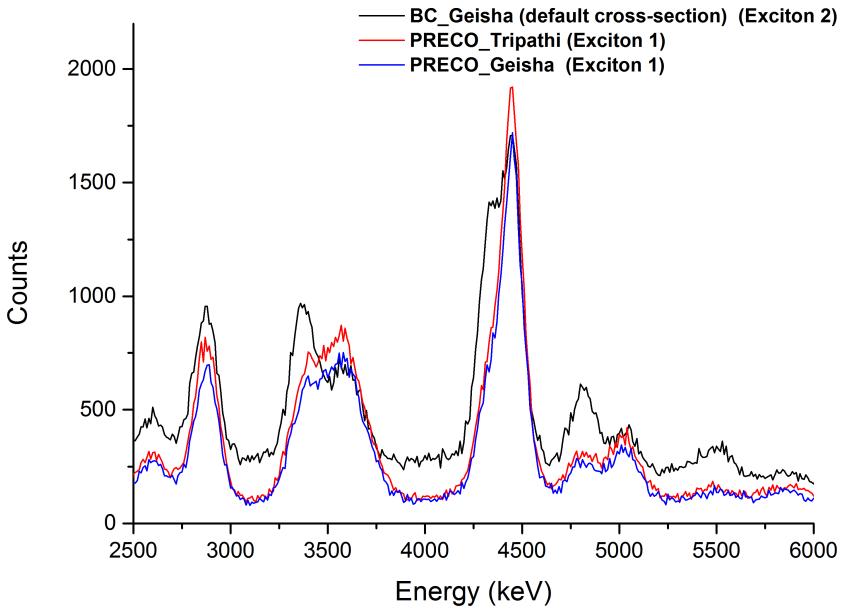

Figure 6.15: Binary cascade prompt gamma spectrum comparison against the precompound model with modified number of exciton as 1 using the Tripathi and Geisha cross-section data set.

While the precompound model (with exciton number of 1) provides a narrower peak, the reason for the broad peak using the default physics lists is still not clear. Figure 6.16 provides a glimpse into the reason behind the broad peak by disabling the Doppler Broadening of the prompt gammas, producing sharp gamma peaks. The 4.438 MeV gamma peak is very noticeable, particular for the exciton = 1 spectra, but there is a second peak at 4.33 MeV that is equally prominent in the exciton = 2 spectra. This peak comes from the following simulated reactions [^{12}C(p, d)^{11}C* or ^{12}C(p, np)^{11}C*], which have been artificially amplified through the Geant4 Physics processes. Unfortunately, no option exists to disable Doppler Broadening for the Binary Cascade model, but simulations have shown that the ^{11}C reactions listed above also occur at a equal rate to the expected ^{12}C(p, x)^{12}C* reaction, thus explaining the broad 4.438 MeV gamma peak.

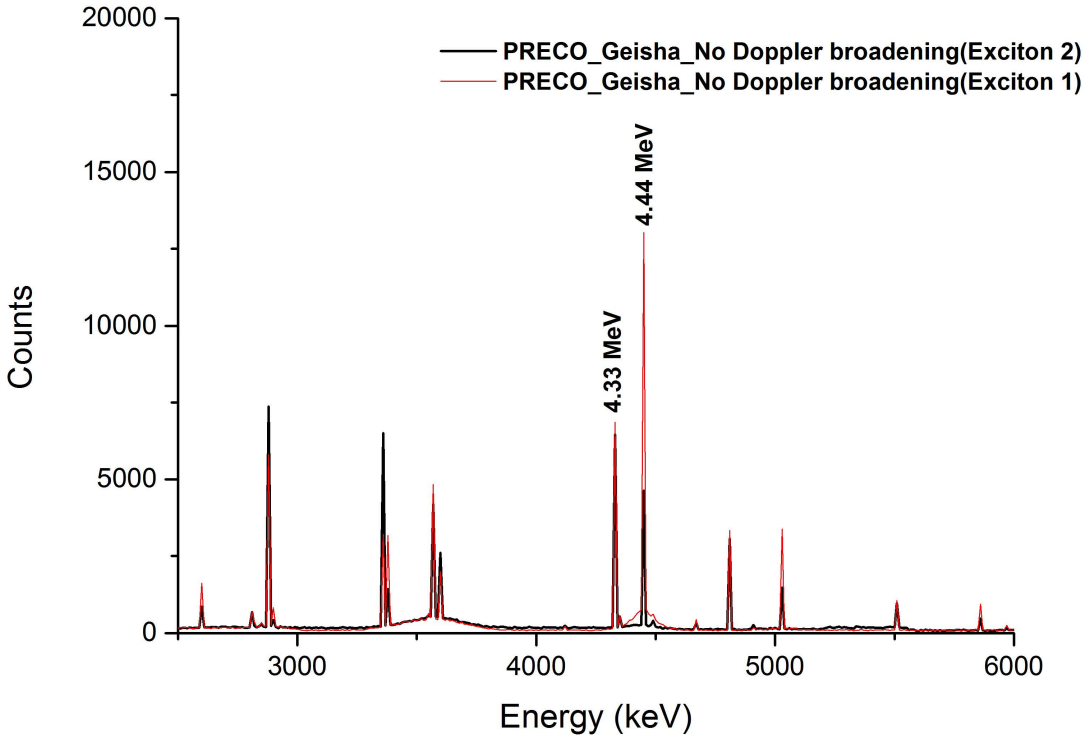

Figure 6.16: Prompt gamma spectrum with Doppler broadening ignored for the precompound model using the Geisha inelastic cross-section data set with the carbon target and 80 MeV incident proton. Note the sharp increase in the 4.438 MeV peak when the exciton number is changed to 1.

Now, looking at 80 MeV proton collisions with the Mylar target. All of the various physics options used with the carbon target have been repeated for the Mylar target, as shown in figure 6.17. One additional physics option (the precompound model plus Fermi breakup) was included. The Fermi breakup model was used in previous work (Jeyasugiththan and Peterson (2015)) to successfully produce the 6.129 MeV gamma peak from proton collisions with Oxygen. Unfortunately, none of the physics options were able to produce a 6.129 MeV gamma peak in version 10.01.p03. As shown in figure 6.17, most of the physics models produced a broad peak around 6.5 MeV, which appears to come from a mixture of reaction (^{16}O(p, n)^{15}O*, ^{16}O(p, d)^{14}N*, ^{16}O(p, an)^{11}C*), instead of the expected reaction (^{16}O(p, x)^{16}O*) as shown by the grouping of peaks near 6.5 MeV in figure 6.18. It is not clear at this time why the 6.129 MeV peak does not appear for this version of Geant4 (v10.01.p03) when previous versions (v09.06.p04) were able to produce the peaks.

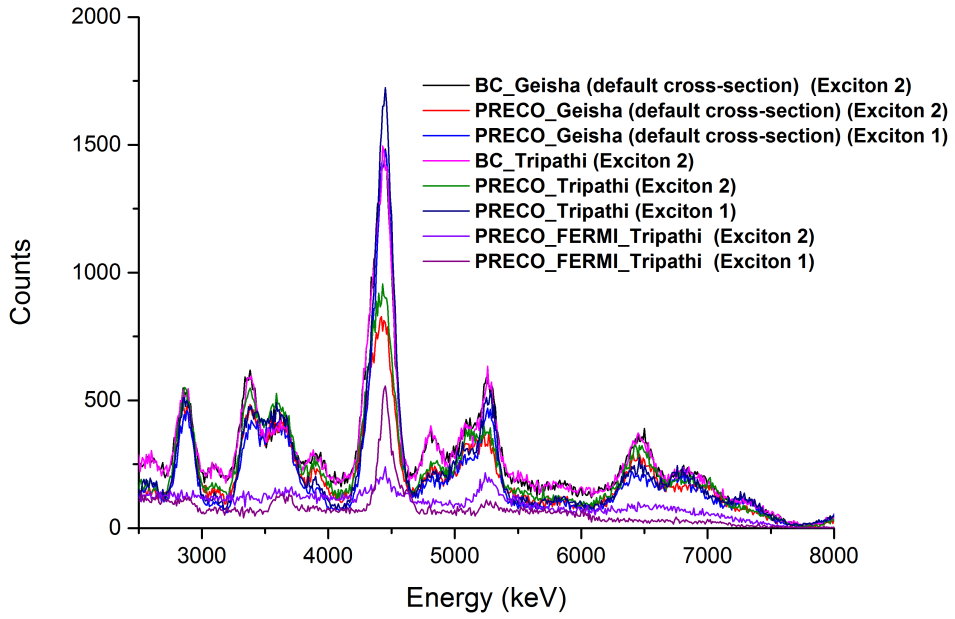

Figure 6.17: Prompt gamma spectra comparison for mylar target using different physics lists with available cross-section data set and modified and default exciton number.

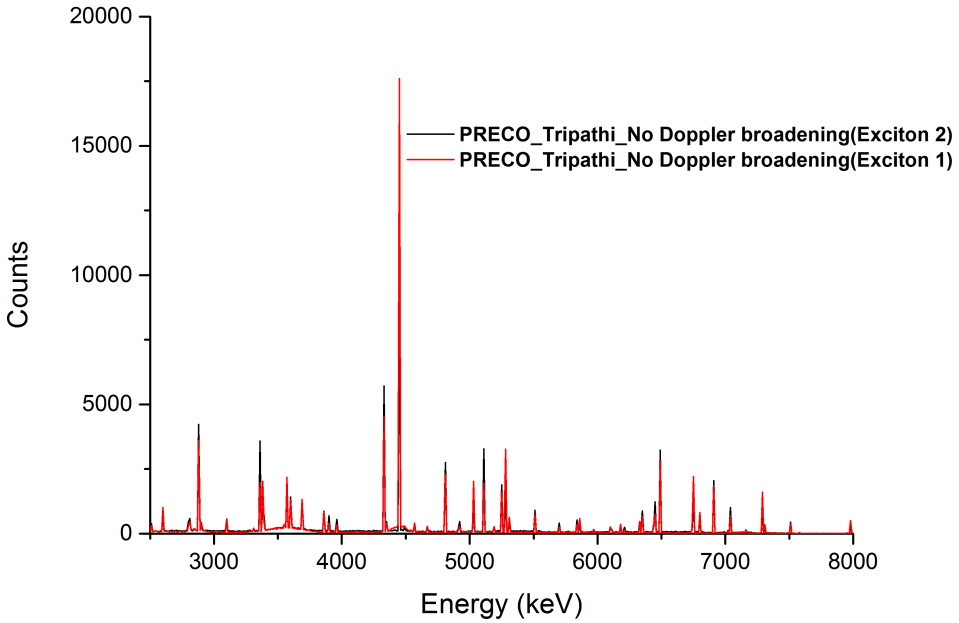

Figure 6.18: Prompt gamma spectrum with Doppler broadening ignored for the precompound model using the Tripathi inelastic cross-section data set with the Mylar target.

NOTE: On 09 December 2016, the latest version of Geant4 (v10.03) was released by the Geant4 Collaboration. We decided to run 80 MeV proton collisions on the Mylar target using the Xsection code. The results are shown in figure 6.19. There are a number of differences to the spectra from figure 6.17 using the previous version of Geant4 (v10.01.p03), but the most striking feature is the presence of the 6.129 MeV gamma peak, as well as peaks at 6.129 and 7.115 MeV. According to the Geant4 10.3 Release Notes (G4.10.3 (2016)), two changes most likely contributed to the appearance of the 6.129 MeV peak. First, they "achieved consistent set of data - G4ENSDFSTATE-2.1, G4RadioactiveDecay-5.1, G4PhotonEvaporation-4.3, in terms of isomer excitation levels - and physics models which use these data - radioactive-decay and photon-evaporation, in terms of energy and lifetime of excited nuclides". Second, the "precompound/de-excitation code has been restructured in order to use the same data as radioactive-decay model and former, internal hard-coded data are not used any longer". This was only a very brief investigation into the latest version of Geant4, but it looks like the latest updates to the code might be a good start toward producing high-quality prompt gamma simulations using Geant4.

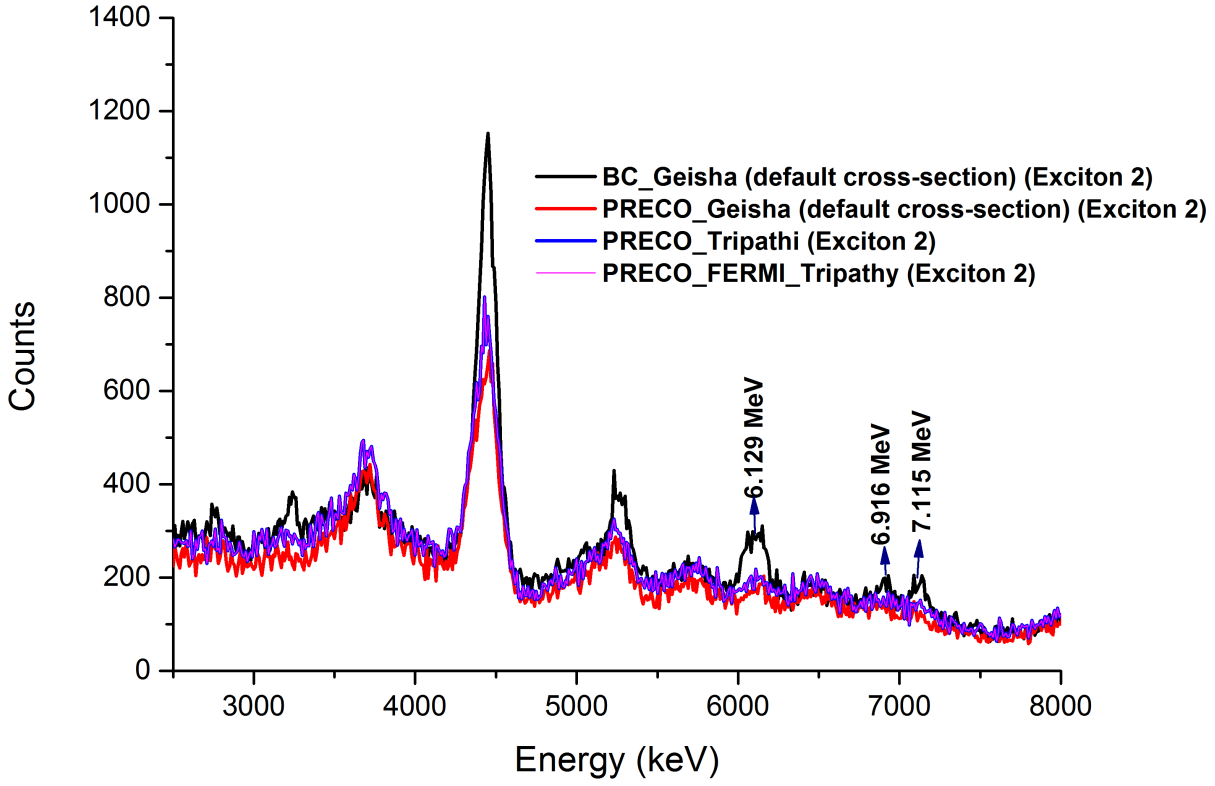

Figure 6.19: Prompt gamma spectra comparison for the mylar target using different physics lists with the latest version of Geant4 (10.3)

6.4.3 Calculating simulated differential cross-section

As discussed in section 5.2.2, the same method was used to calculate the simulated differential cross-sections. For the simulations, the differential cross sections were only measured for the 4.438 MeV gamma peak from the carbon and mylar targets. Figure 6.20 shows the 4.438 MeV photo peaks. Figure 6.21 shows the suppressed 6.129 MeV photo peaks. The results for the averaged differential cross-section at three different angles at five different energies are shown in table 6.2. Due to the suppressed 6.129 MeV peak, the differential cross-section for the 6.129 MeV ^{16}O gamma was not calculated.

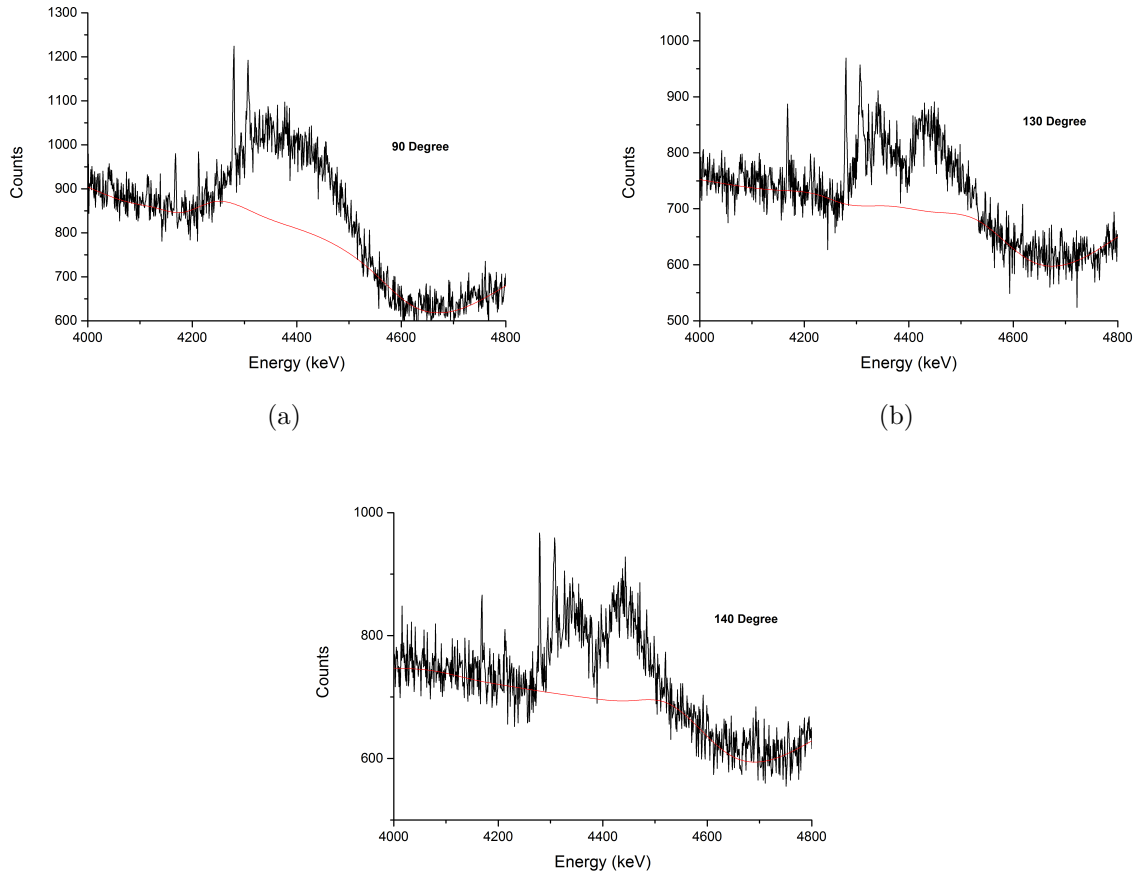

(a) (b)

(c)

Figure 6.20: 4.438 MeV photo peak with a manually added background line (red line) for the 95 MeV proton collision with the Carbon target for germanium crystals placed at 90^0, germanium crystals placed at 130^0, and germanium crystals placed at 140^0 respectively.

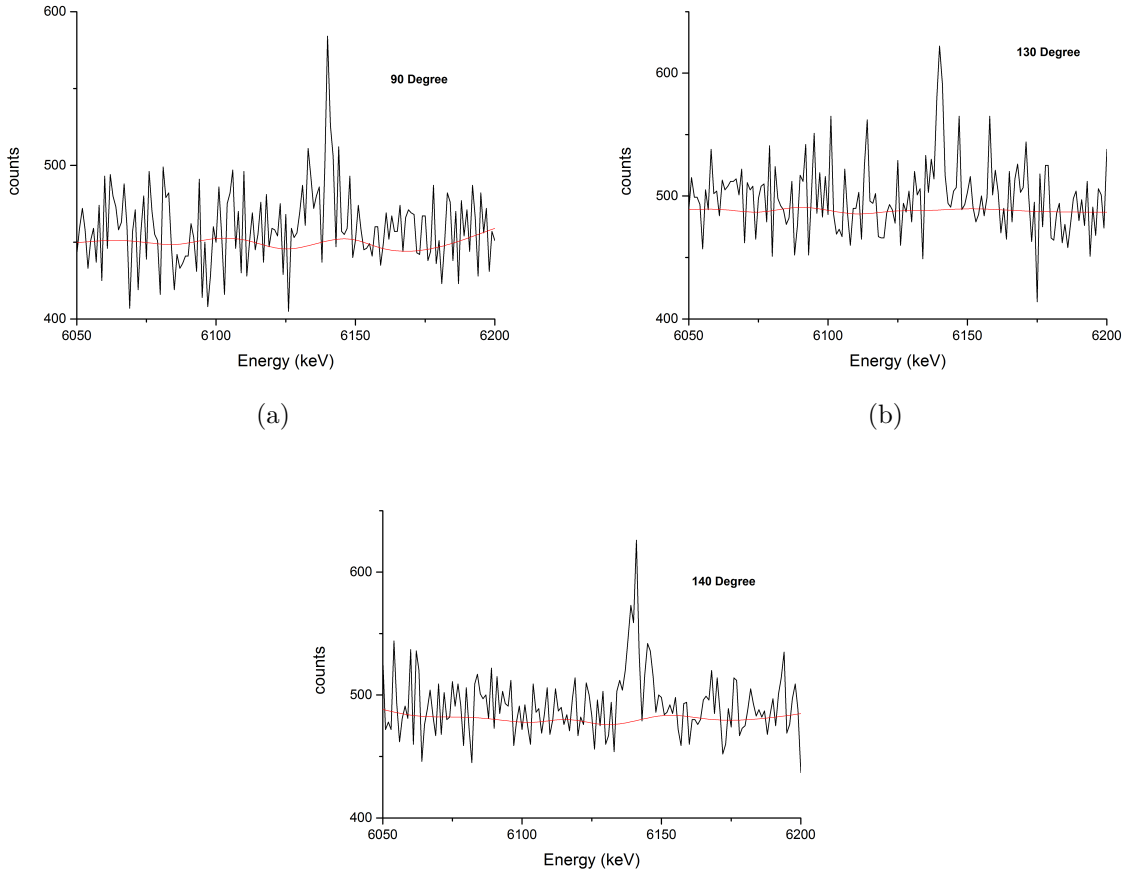

(a) (b) (c)

Figure 6.21: 6.129 MeV photo peak with a manually added background line (red line) for the 95 MeV proton collision with the Carbon target for germanium crystals placed at 90^0, germanium crystals placed at 130^0, and germanium crystals placed at 140^0 respectively.

Table 6.2: Average differential cross-section values for 4.438 MeV carbon target

Energy (MeV)	$\left(\frac{d\sigma}{d\Omega}\right)_{90^0}$	$\left(\frac{d\sigma}{d\Omega}\right)_{130^0}$	$\left(\frac{d\sigma}{d\Omega}\right)_{140^0}$
66	2.99 ± 0.16	2.81 ± 0.14	2.95 ± 0.15
80	2.37 ± 0.12	2.18 ± 0.11	2.32 ± 0.12
95	1.75 ± 0.10	1.46 ± 0.08	1.60 ± 0.08
110	1.60 ± 0.09	1.34 ± 0.07	1.42 ± 0.07
125	1.37 ± 0.07	1.15 ± 0.04	1.17 ± 0.07

Table 6.3: Average differential cross-section values for 4.438 MeV mylar target

Energy (MeV)	$\left(\frac{d\sigma}{d\Omega}\right)_{90^0}$	$\left(\frac{d\sigma}{d\Omega}\right)_{130^0}$	$\left(\frac{d\sigma}{d\Omega}\right)_{140^0}$
66	2.97 ± 0.15	2.36 ± 0.14	2.48 ± 0.15
80	2.24 ± 0.12	1.97 ± 0.11	2.16 ± 0.12
95	1.61 ± 0.09	1.44 ± 0.08	1.52 ± 0.08
110	1.46 ± 0.07	1.33 ± 0.07	1.35 ± 0.07
125	1.22 ± 0.07	1.10 ± 0.06	1.18 ± 0.06

6.4.4 Angular distribution of 4.438 MeV in Geant4 simulation

As described in section 5.3.3, the angular distribution of the 4.438 MeV gamma-ray line from ^{12}C was obtained by using a fourth order Legendre polynomial function (see equation 3.8). The fourth order Legendre polynomial function was fit with measured differential cross-section values. Using the curve_fit function in the Scipy module in python, the Legendre coefficients were obtained and are shown in table 6.4. The angular distribution of 4.438 MeV ^{12}C for 66 MeV, 80 MeV, 95 MeV, 110 MeV, and 125 MeV proton energies are shown in figures 6.23(a), 6.23(b), 6.23(c), 6.23(d), and 6.23(e), respectively.

The angular distribution of the 4.438 MeV from mylar target was also fitted using python to measure the cross-section of 4.438 MeV. The obtained Legendre coefficients during the fit are shown in table 6.5. The angular distribution of 4.438 MeV of mylar target for 66 MeV, 80 MeV, 95 MeV, 110 MeV, and 125 MeV proton energies are shown in figures 6.24(a), 6.24(b), 6.24(c), 6.24(d), and 6.24(e), respectively.

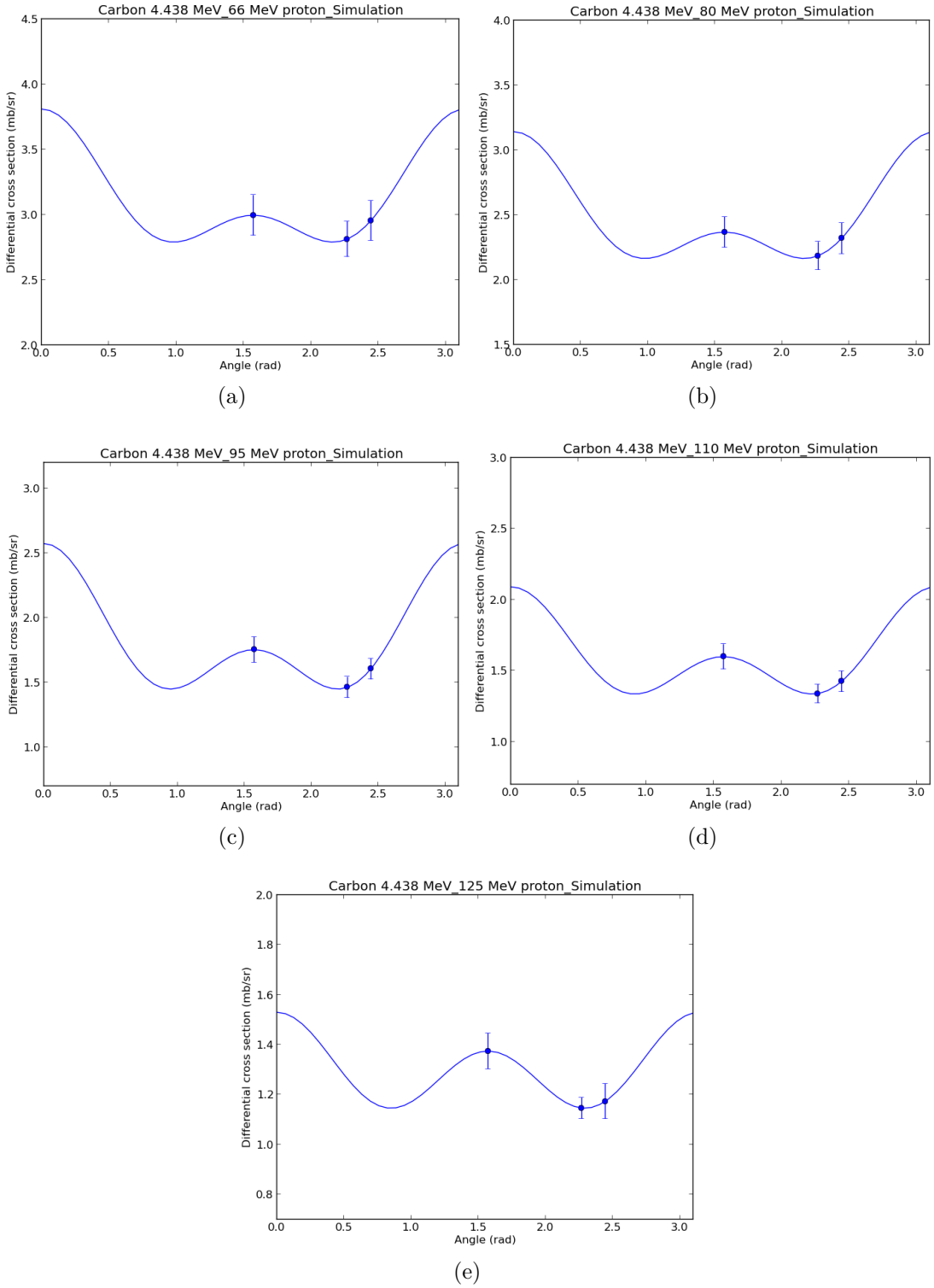

Figure 6.22: Angular distribution for the simulated ^{12}C 4.438 MeV gamma-ray line at 66 (a), 80 (b), 95 (c), 110 (d), 125 (e) MeV proton energies. The solid line are the fitted curve according to the 4th order Legendre polynomial using python. The circle are the differential cross section values with their associated uncertainty.

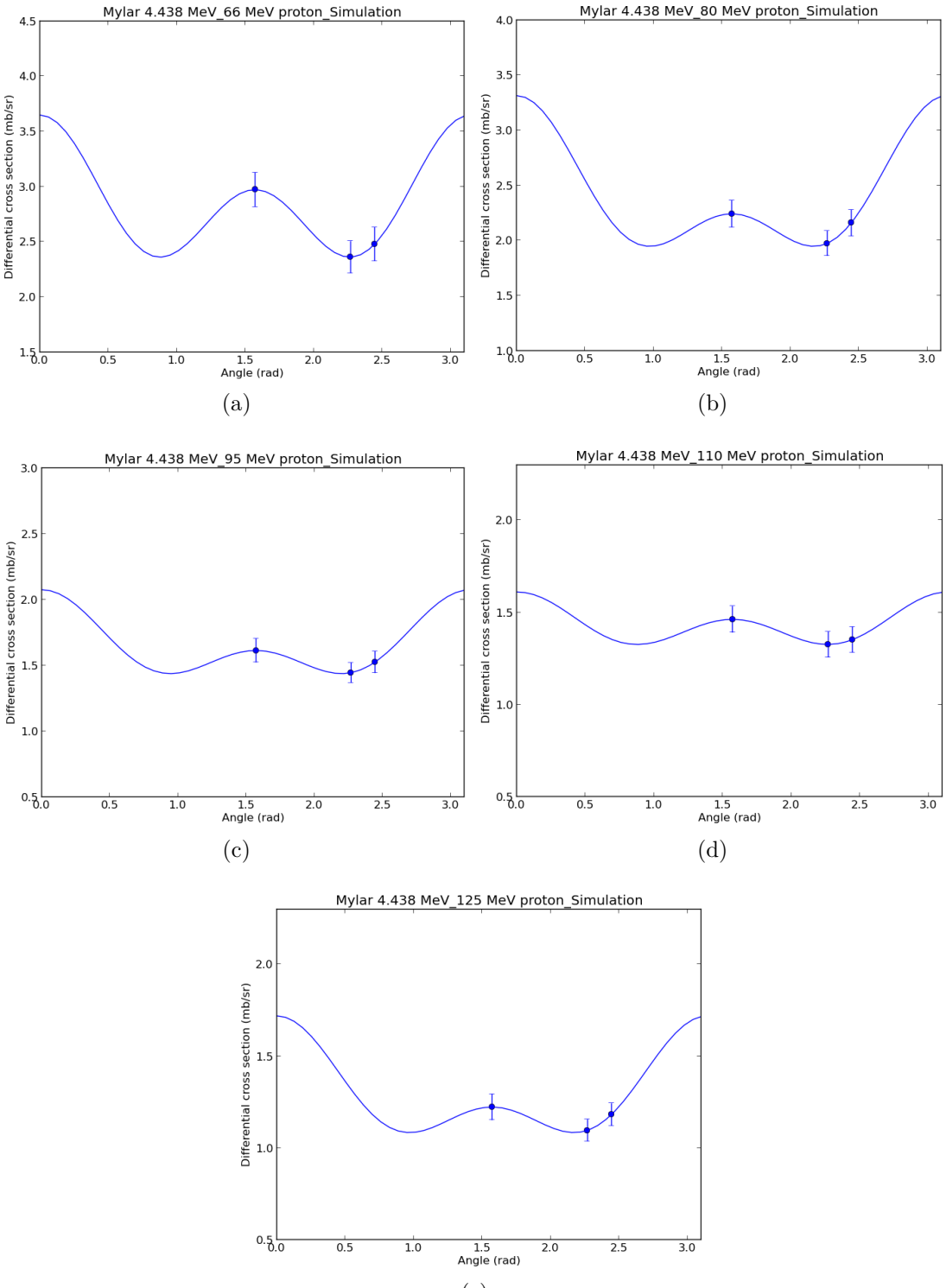

Figure 6.23: Angular distribution for the simulated mylar 4.438 MeV gamma-ray line at 66 (a), 80 (b), 95 (c), 110 (d), 125 (e) MeV proton energies. The solid line are the fitted curve according to the 4^{th} order Legendre polynomial using python. The circle are the differential cross section values with their associated uncertainty.

Table 6.4: Legendre coefficients from the angular distribution fit using python for the simulated 4.438 MeV gamma from the carbon target

Energy (MeV)	a_0	a_2	a_4
66	2.98067671	0.3390689	0.48948732
80	2.34856505	0.31886259	0.47350998
95	1.68026179	0.29964268	0.59386548
110	1.50809289	0.14581975	0.43657863
125	1.26519136	-0.01132849	0.27585171

Table 6.5: Legendre coefficients from the angular distribution fit using python for the simulated 4.438 MeV gamma from the mylar target

Energy (MeV)	a_0	a_2	a_4
66	2.7079386	0.100824	0.84019573
80	2.20902807	0.43555683	0.67053426
95	1.5693157	0.16711294	0.33850871
110	1.40312295	0.02169636	0.18646728
125	1.20573854	0.20071812	0.31312138

6.4.5 Total cross-section measurement in Geant4 simulation

As discussed in section 5.3.5, the Legendre polynomial coefficients were obtained by fitting Legendre polynomials to the differential cross-section data. The total cross-section is proportional to the zeroth-order Legendre coefficient a_0 and was calculated by multiplying a_0 by 4π. The simulated total cross-sections for the 4.438 MeV gamma-ray line from the ^{12}C and mylar targets at five different energies are given in the table 6.6. The total cross-section versus energy plot for the 4.438 MeV gamma from the carbon and mylar targets is shown in figure 6.23

Table 6.6: Simulated cross-section results for the 4.438 MeV gamma-ray line for ^{12}C and mylar targets

$Energy(MeV)$	σ(mb) (carbon)	σ(mb) (mylar)	Percent difference
66	37.5 ± 1.5	34.0 ± 1.5	9.33%
80	29.5 ± 1.2	27.8 ± 1.2	5.76%
95	21.11 ± 0.83	19.72 ± 0.82	6.58%
110	18.95 ± 0.69	17.63 ± 0.68	6.97%
125	15.90 ± 0.63	15.15 ± 0.62	4.72%

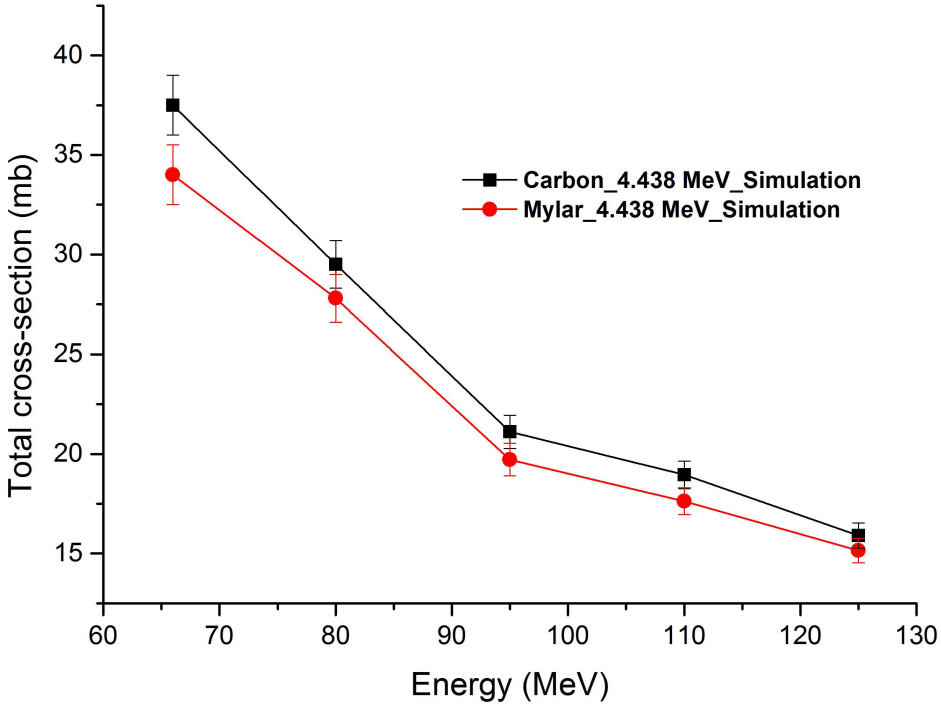

Figure 6.24: Simulated cross-section results for the 4.438 MeV gamma-ray line for ^{12}C and mylar targets

Chapter 7

Comparison of experimental and simulated results

This section focuses on comparison of the simulated and experimental results. It includes an absolute comparison of the simulated and experimental prompt gamma spectra for the carbon and mylar targets. There is also a comparison of the 4.438 MeV photo peaks from both the carbon and mylar targets using experimental and simulated data. Next, the simulated total cross-section results for the 4.438 MeV photo peak are compared to the experimental results. Finally, the measured and simulated results are compared against available experimental cross-section data.

7.1 Prompt gamma spectra from carbon target

The prompt gamma energy spectra were simulated and experimentally measured at five different energies (66, 80, 95, 110, 125 MeV). For this absolute comparison, the prompt gamma spectra for the 95 MeV proton beam was considered. The other four energies produced similar results. In order to make an absolute comparison between the experimental and simulated results, three primary factors were considered: the difference in the number of incident protons, the difference in the target thickness and the absolute detector efficiency correction factor. Each of these elements resulted in a correction to the simulated spectra. First, the difference in the number of incident protons was corrected by multiplying the simulated spectra by the ratio of the total number of protons from the experimental run to the total number of simulated protons. Next, the difference in the target thickness was corrected by multiplying the simulated spectra by the ratio of the experimental target thickness to the simulated target thickness. This is based on the dependence of the cross-section on target thickness as shown in Equation 1.9. Lastly, the difference in the absolute detector efficiency (described in Section 5.2) needed to be corrected for each crystal individually based in the absolute detector efficiency correction factors listed in Table 5.3. The

simulated spectra from each crystal was divided by its respective correction factor. The combination of these corrections provided a way to make an absolute comparison of the experimental and simulated spectra, as shown in figure 7.1 and figure 7.3.

The absolute comparison of the prompt gamma spectra for the carbon target between the simulation and the experiment is shown in figure 7.1. Overall, the two spectra align quite well, showing good peak agreement along the energy scale, particularly for the 4.438 MeV peak. The spectra also agree reasonably well in the number of counts with a two noticeable gaps (between 2.0 and 3.5 MeV and above 4.5 MeV) where the simulation spectra is higher than the experimental spectra. The stretches where the simulations spectra are higher could be a result of the historic overestimation of the prompt gamma production in Geant4 or possibly the timing settings of the simulated Compton suppression. Looking more closely at the 4.438 MeV ^{12} photo peak, the simulated peak is broader than the experimental peak. And as mentioned in Chapter 6, the single escape peak from the 4.438 MeV gamma is missing from the simulated spectra, while it appears in the experimental, as well as the double escape peak in both spectra. The shape of the 4.438 MeV ^{12} photo peak will be discussed further in the next section.

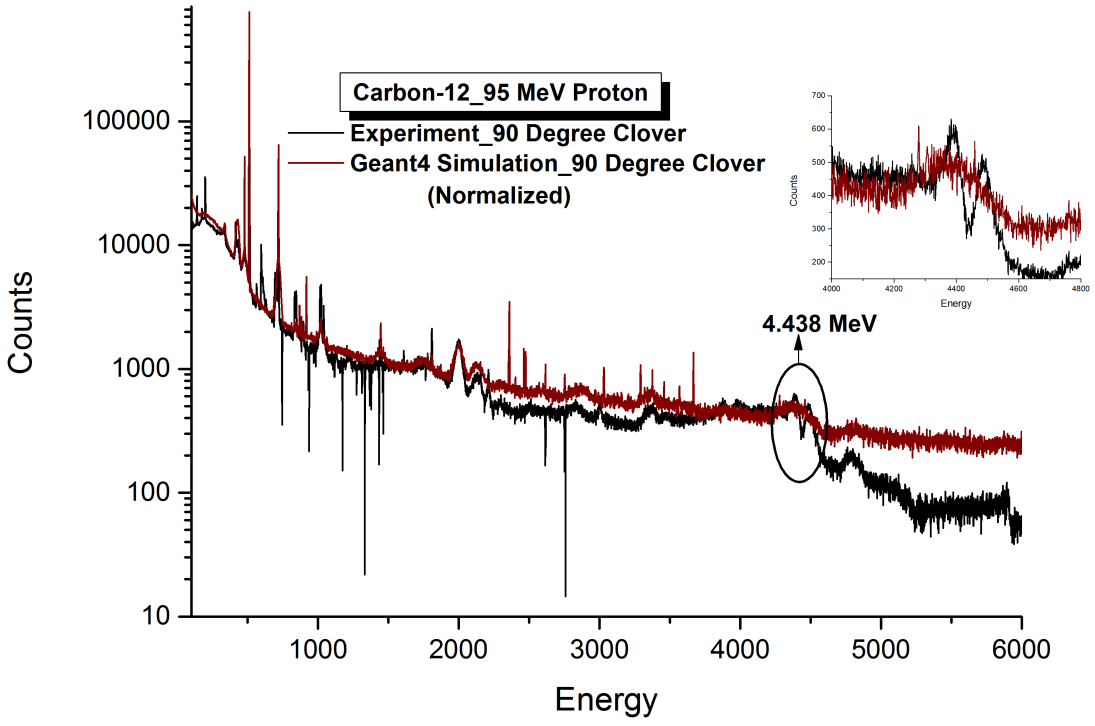

Figure 7.1: Prompt gamma spectra comparison of the experimental and simulated results for a 95 MeV proton collision on the carbon target. The red line shows the corrected Geant4 simulated spectrum and the black line shows the experimental spectrum. Inset: Enlarged view of the 4.438 MeV gamma peak.

7.1.1 Comparison of simulated and experimental 4.438 MeV photo peak from ^{12}C

An enlarged view of the simulated and experimental 4.438 MeV photo peaks from ^{12}C at 90°, 130°, and 140° are shown in figure 7.2. The shape of the 4.438 MeV peaks have some unique characteristics and significant differences. Starting with the experimental results, the 4.438 MeV photon peak is relatively wide and has a distinct double peak appearance that changes with angle. Both of these attributes are a product of Doppler Broadening. The life time of the 4.438 MeV gamma-ray line emission of ^{12}C is 6.1×10^{-14} second or 61 femto-seconds. In a (p, p$'\gamma$) reaction, the produced gamma ray line width depends on whether the life-time of γ-ray emitting state is less than or greater than the slowing time of the recoiling-ion in the target. If the life time of the excited nucleus is on the order of pico-seconds or longer in a solid target, there will not be Doppler broadening, but the gamma-ray transition will be a narrow line. On the contrary, if the life time is in femto-second or shorter (as the 4.438 MeV from ^{12}C), the gamma-ray line will be a broader line [Lang et al. (1987)], as observed in figure 7.2. The double peak, also a product of the de-excitation life-time, comes from the "coherent Doppler shift" (Kolata et al. (1967)). For specific types of de-excitations (including 2^+ to 0) with short life-times, the Doppler shift produces a symmetric double peak at 90 degrees, as seen in figure 7.2. The double peak fades as the detector shifts away from 90 degrees, which is also observed in the experimental spectra.

Now, for the simulated 4.438 MeV gamma peak, the peak is also a broad peak with a hint of a double peak, but does not do a good job replicating the experimental results. As discussed in Section 6.4.2, the simulated 4.438 photo peak is unusually broad due to additional reactions such as ^{12}C(p, d)^{11}C* or ^{12}C(p, np)^{11}C* being incorrectly simulated by the Geant4 physics list. The presence of the double peak indicates that Geant4 seems to have incorporated the Doppler shift mentioned above into their physics models but unfortunately, the shift moves in the wrong direction. Instead of being symmetric at 90 degrees and then decreasing as the angle increases, the opposite effect is observed. It is

possible that there is a compounding effect occurring that is skewing the results, but it is difficult to determine from these plots. Either way, the simulated shape of the 4.438 MeV photo peak from ^{12}C does not adequately match the shape of the experimental peak.

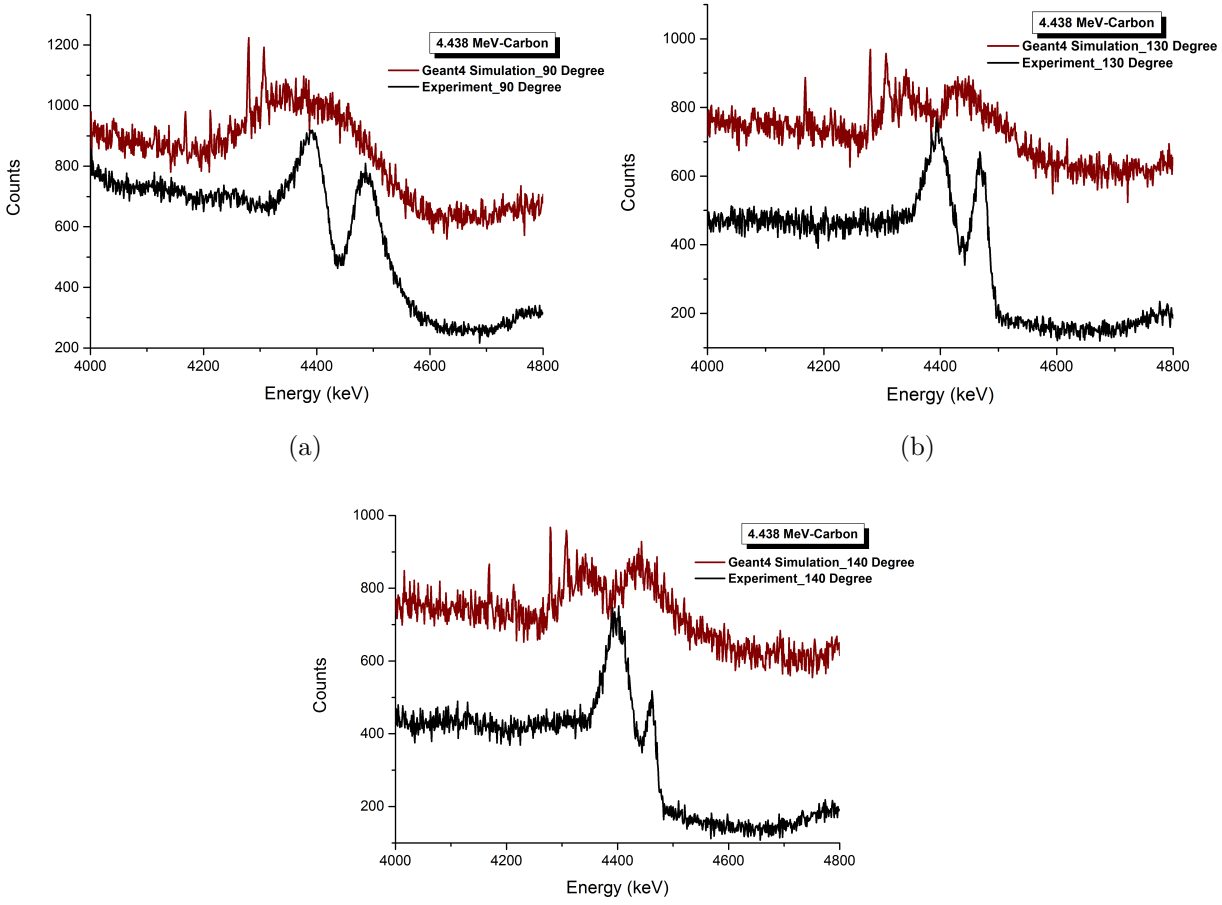

Figure 7.2: Simulated and experimental 4.438 MeV photo peak comparison for a 95 MeV proton collision on the Carbon target at 90°, 130°, and 140° clovers, respectively. The simulated spectra was not corrected for absolute comparison in this figure in order to better see the shape of the two spectra.

7.2 Prompt gamma spectra from mylar target

For the absolute prompt gamma spectra comparison for the mylar target, the energy spectra for the 95 MeV proton beam was again considered. In order to make an absolute comparison between the experimental and simulated results, the same procedures were followed as explained above. The absolute prompt gamma spectra comparison for 95 MeV protons on the mylar target is shown in figure 7.3. As with the spectra for the carbon target, the spectra align well along the energy scale, particularly for the 4.438 MeV peak (and the single and double escape peaks). As for alignment of the number of counts, the mylar spectra align considerably better than the carbon spectra, with no major gaps between the spectra except for around 6.0 MeV. Looking more closely at the 4.438 MeV ^{12} photo peak, the simulated peak is again broader than the experimental peak as seen in the carbon spectra. The experimental 6.129 MeV ^{16}O photo peak (with single and double escape peaks) is very sharp, but unfortunately there is no simulated 6.129 MeV peak for comparison. The shape of the 4.438 MeV ^{12} photo peak will be discussed further in the next section.

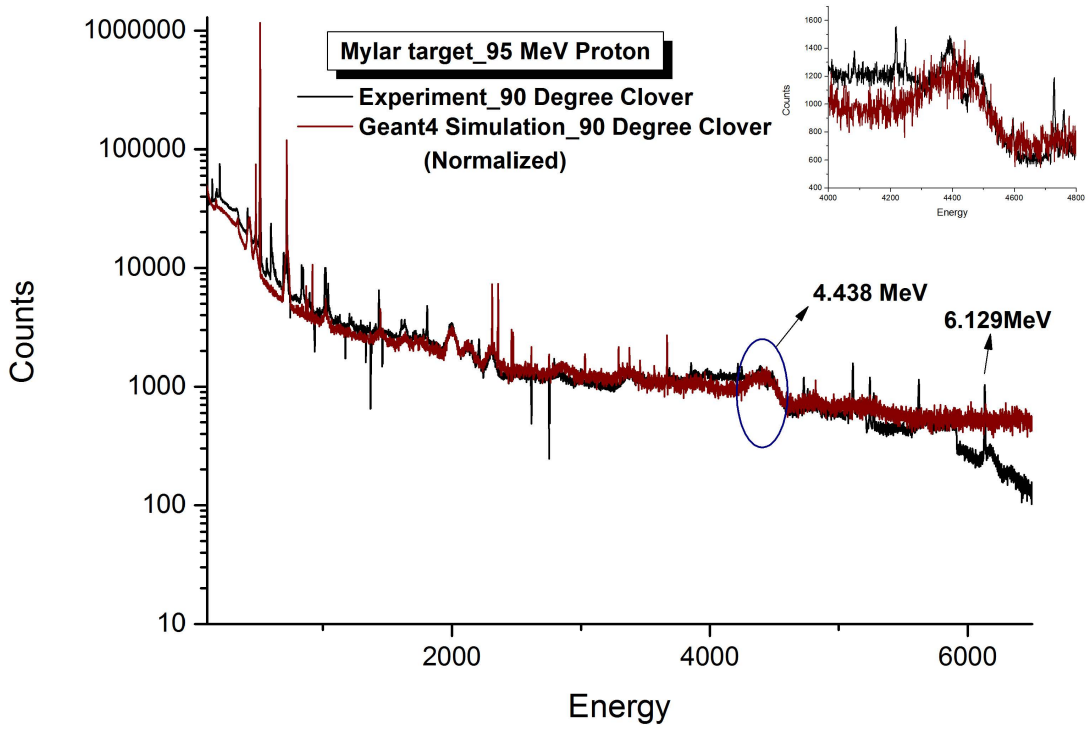

Figure 7.3: Prompt gamma spectra comparison of the experimental and simulated results for a 95 MeV proton collision on the mylar target. The red line shows the corrected Geant4 simulated spectrum and the black line shows the experimental spectrum. Inset: Enlarged view of the 4.438 MeV gamma peak.

7.2.1 Comparison of simulated and experimental 4.438 MeV photo peak from Mylar target

An enlarged view of the simulated and experimental 4.438 MeV photo peaks from the mylar target at 90°, 130°, and 140° is shown in figure 7.4. The shape of the peaks from the mylar target exhibit the same characterisitcis as the 4.438 MeV peaks from the carbon target, broadened and double peaks. For the experimental peaks, the shape of the 4.438 MeV gamma peak from the mylar target is virtually identical to the peaks from the carbon target, as shown in figure 7.5. While the carbon peaks appear to be a bit taller, the width of the peaks and the behavior of the double peaks is exactly the same. For the simulated peaks, the 4.438 MeV gamma peak has a slight shift towards higher energies, shown most

prominent in the 90 degrees panel of figure 7.6. Simulations confirmed that this shift can be attributed to a decreased number of the additional reactions [^{12}C(p, d)^{11}C* or ^{12}C(p, np)^{11}C*] that resulted in the broadening of the 4.438 MeV gamma peak from the carbon target. This also seems to decrease the appearance of the double peak at 130 and 140 degrees, suggesting that there is an angular Doppler shift occurring for the 4.438 MeV gamma in the Geant4 simulation.

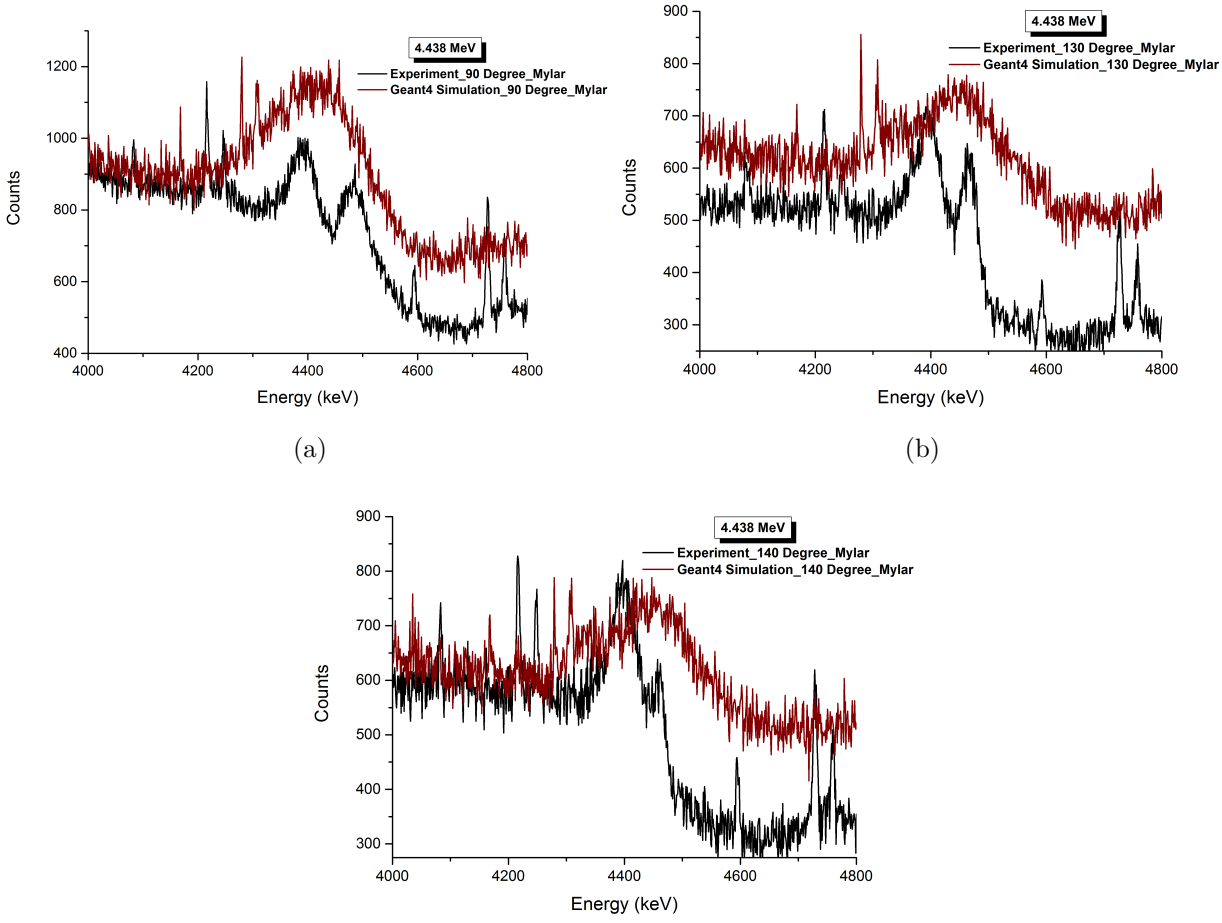

Figure 7.4: Simulated and experimental 4.438 MeV photo peak comparison for a 95 MeV proton collision on the Mylar target at 90°, 130°, and 140° clovers, respectively. The simulated spectra was not corrected for absolute comparison in this figure in order to better see the shape of the two spectra.

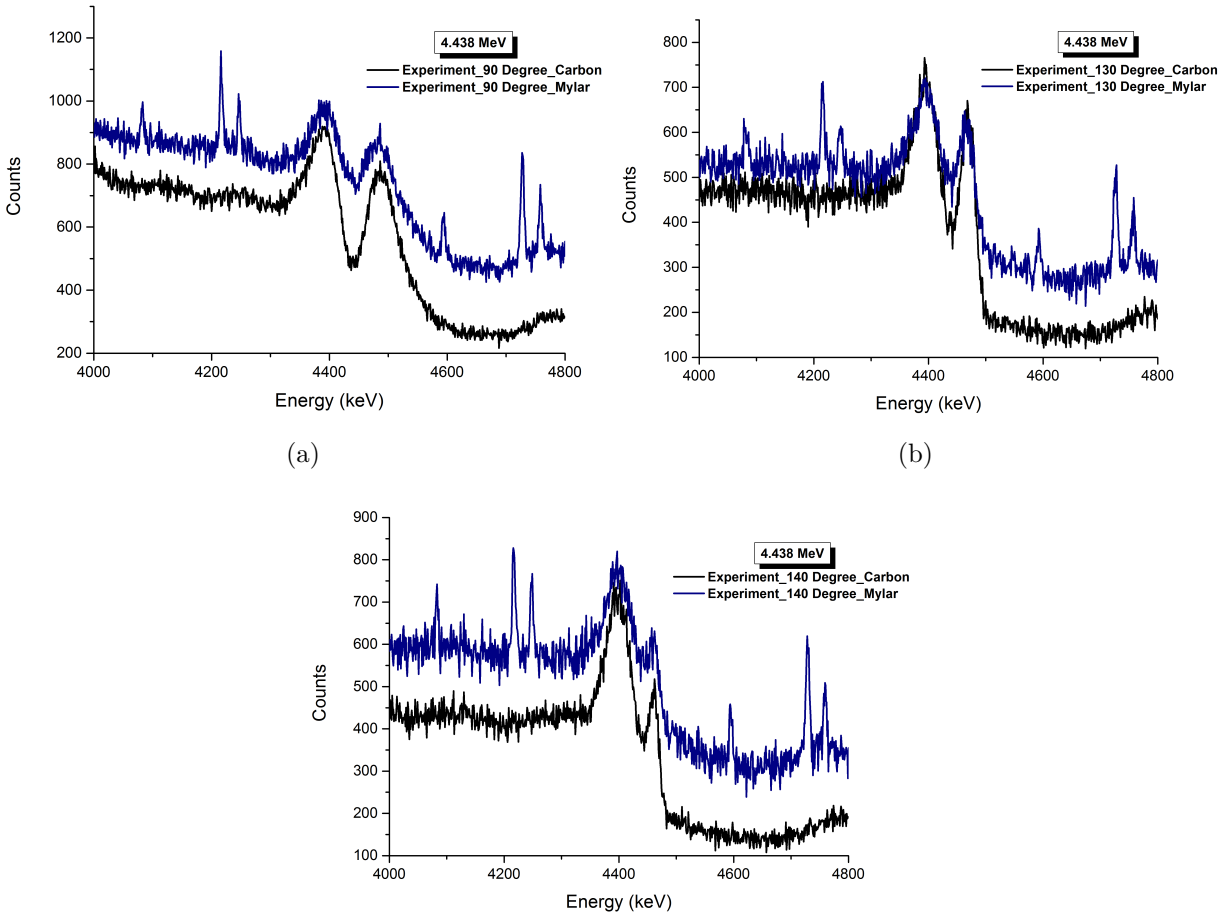

Figure 7.5: Experimental 4.438 MeV photo peak comparison for a 95 MeV proton collision on the Carbon and Mylar targets at 90°, 130°, and 140° clovers, respectively. The spectra were intentionally shifted in order to better see the shape of the two spectra.

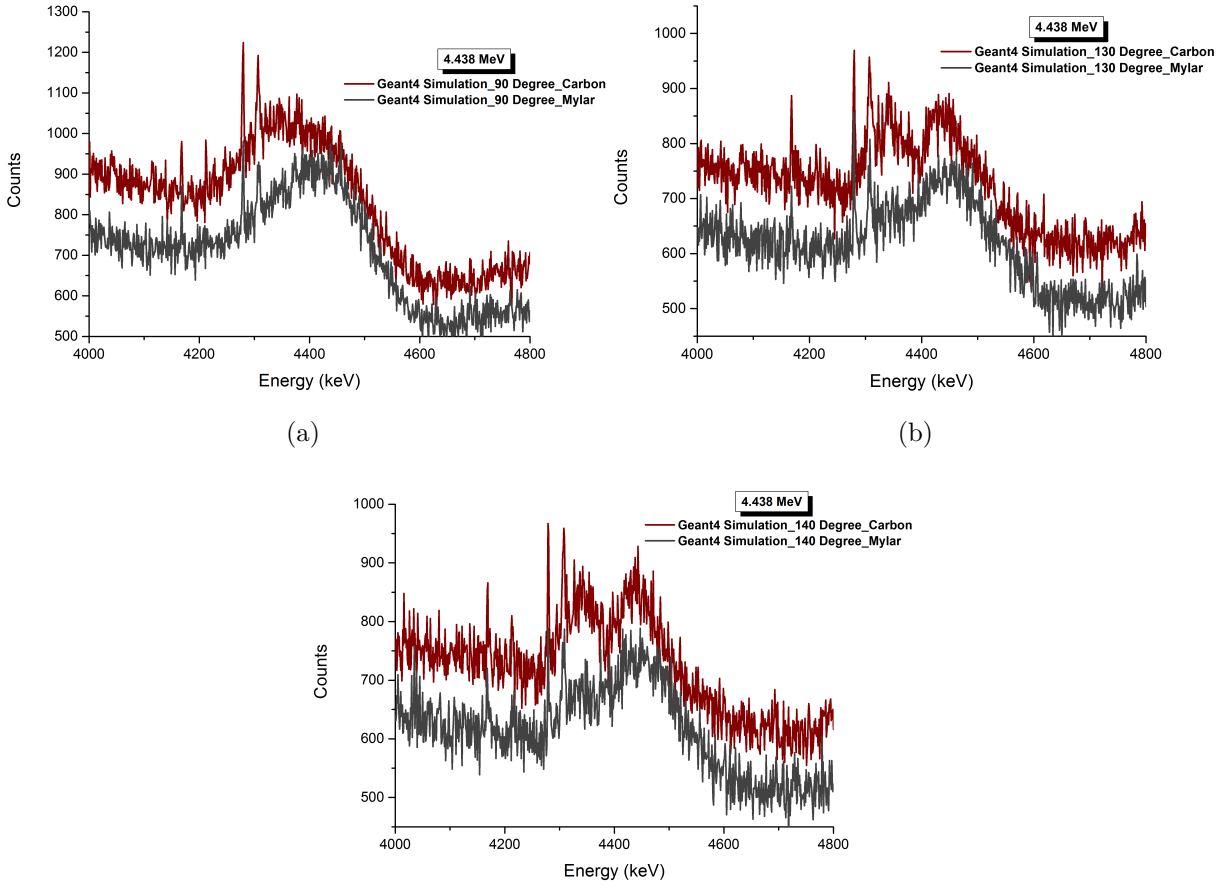

Figure 7.6: Simulated 4.438 MeV photo peak comparison for a 95 MeV proton collision on the Carbon and Mylar targets at 90°, 130°, and 140° clovers, respectively. The spectra were intentionally shifted in order to better see the shape of the two spectra.

7.3 Comparison of experimental and simulated total cross section results

This section compares the total cross-section results for the 4.438 MeV gamma photo peak from both the carbon and mylar targets and the 6.129 MeV gamma photo peak from the mylar target. The experimental total cross-section results were originally discussed in Section 5.3.5 and the simulated total cross-section results were originally discussed in Section 6.4.5. The total cross-section results are also compared to existing published cross-section results for both the 4.438 MeV and 6.129 MeV gamma peaks.

7.3.1 Experimental and simulated cross-section comparison for the 4.438 MeV photo peak

The total cross-section results for the 4.438 MeV gamma peak from the carbon target as shown in 7.1 and from the mylar target in 7.2. These results are also shown in figure 7.7. Comparing the experimental and simulated results reveals that the difference between the results at each energy vary from 26% to 64% with the simulated results being higher than the experimental at all energies and for both targets. The reason for the significantly higher simulated total cross-section values to two-fold. First, the 4.438 MeV gamma peak from the carbon target included additional 4.33 MeV gammas from the ^{12}C(p, d)^{11}C* or ^{12}C(p, np)^{11}C* reactions thus increasing the reaction cross-section. Although a contributing factor, it is unlikely to have produced the full (up to 64%) difference between the simulated and experimental results. Second, and probably a larger contributor to the difference, there is an overestimation in the 4.438 MeV gamma produced by the ^{12}C(p,x)^{12}C* reaction in physics of Geant4.

Comparing the carbon and mylar cross-section shows that, on average, the percent difference for the 4.438 MeV peak from the carbon target (52.1%) is greater than the percent difference from the mylar target (31.2%). This can also be seen in figure 7.7 where the

Table 7.1: Comparison of experimental total cross-section (σ) results against simulated results for 4.438 MeV gamma-ray line for ^{12}C

$Energy(MeV)$	σ (mb) (Exp)	σ (mb) (Sim)	Percent difference
66	25.1 ± 1.1	37.5 ± 1.5	49.40%
80	19.67 ± 0.88	29.5 ± 1.2	49.97%
95	14.13 ± 0.63	21.11 ± 0.83	49.39%
110	11.54 ± 0.51	18.95 ± 0.69	64.21%
125	10.40 ± 0.41	15.90 ± 0.63	52.88%

Table 7.2: Comparison of experimental total cross-section results against simulated results for 4.438 MeV gamma-ray line for mylar target

$Energy(MeV)$	σ (mb) (Exp)	σ (mb) (Sim)	Percent difference
66	25.4 ± 1.2	34.0 ± 1.5	33.86%
80	21.98 ± 0.99	27.8 ± 1.2	26.48%
95	15.40 ± 0.70	19.72 ± 0.82	28.05%
110	13.16 ± 0.60	17.63 ± 0.68	33.97%
125	11.19 ± 0.51	15.15 ± 0.62	35.39%

gap between the two mylar lines is smaller than the gap between the carbon lines. First, looking at the simulated results reveals that the carbon values are about 7.6% higher than the mylar values. As discussed in Section 6.4.2, the number of 4.33 MeV gammas that were counted as part of the 4.438 MeV gamma peak is significantly less for the mylar target than for the carbon target, supporting the assertion that these additional gammas did not fully contribute to the 52.1% difference between simulated and experimental cross-section values for the carbon target. Second, looking at the experimental results shows that the mylar values are about 7.8% higher than the carbon values. These higher values are likely due to the fact that mylar is a compound target, containing both carbon and oxygen, thus the 4.438 MeV gamma peak contains gammas from two reactions, the ^{12}C(p,x)^{12}C* and ^{16}O(p,ax)^{12}C* reactions. But, again, this is not the sole contributor to the difference between the experimental and simulated cross-section values, pointing to a systematic difference between the two set of values, possibly due to the physics models in Geant4.

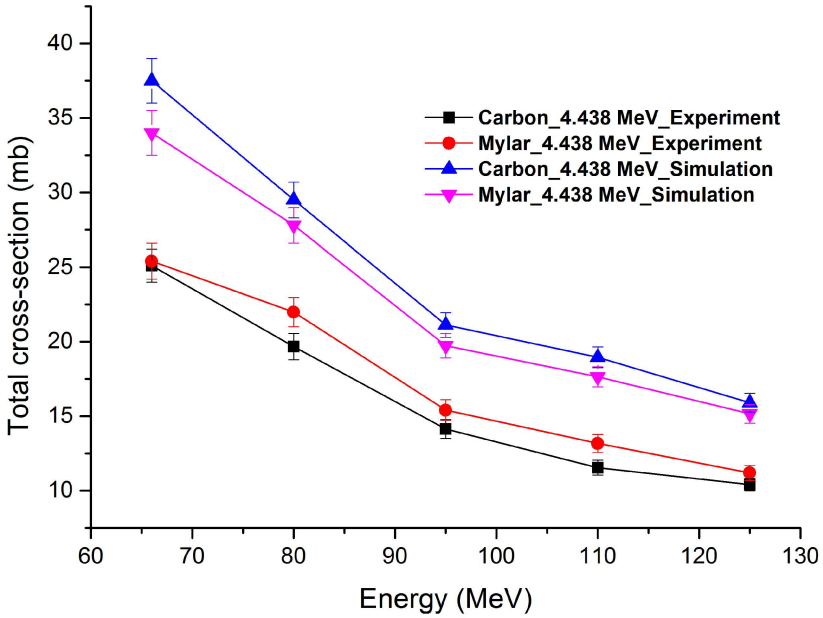

Figure 7.7: Comparison of experimental total cross-section results against simulated results for 4.438 MeV gamma from carbon and mylar targets.

Figure 7.8 shows the total cross-section comparison of simulated and experimental total cross-section data with available experimental cross-section data for the 4.438 MeV photo peak from both the carbon and mylar targets. At first glance, the gap between the simulated and experimental results from this work can be clearly seen. The cross-section results from this work also appear to be higher than what would be expected from the available experimental data. Due to the sparsity of the data in the 66 to 125 MeV energy range (only two previously measured points fall into that energy range), it is difficult to determine if these new cross-section values are out-of-line with the existing data.

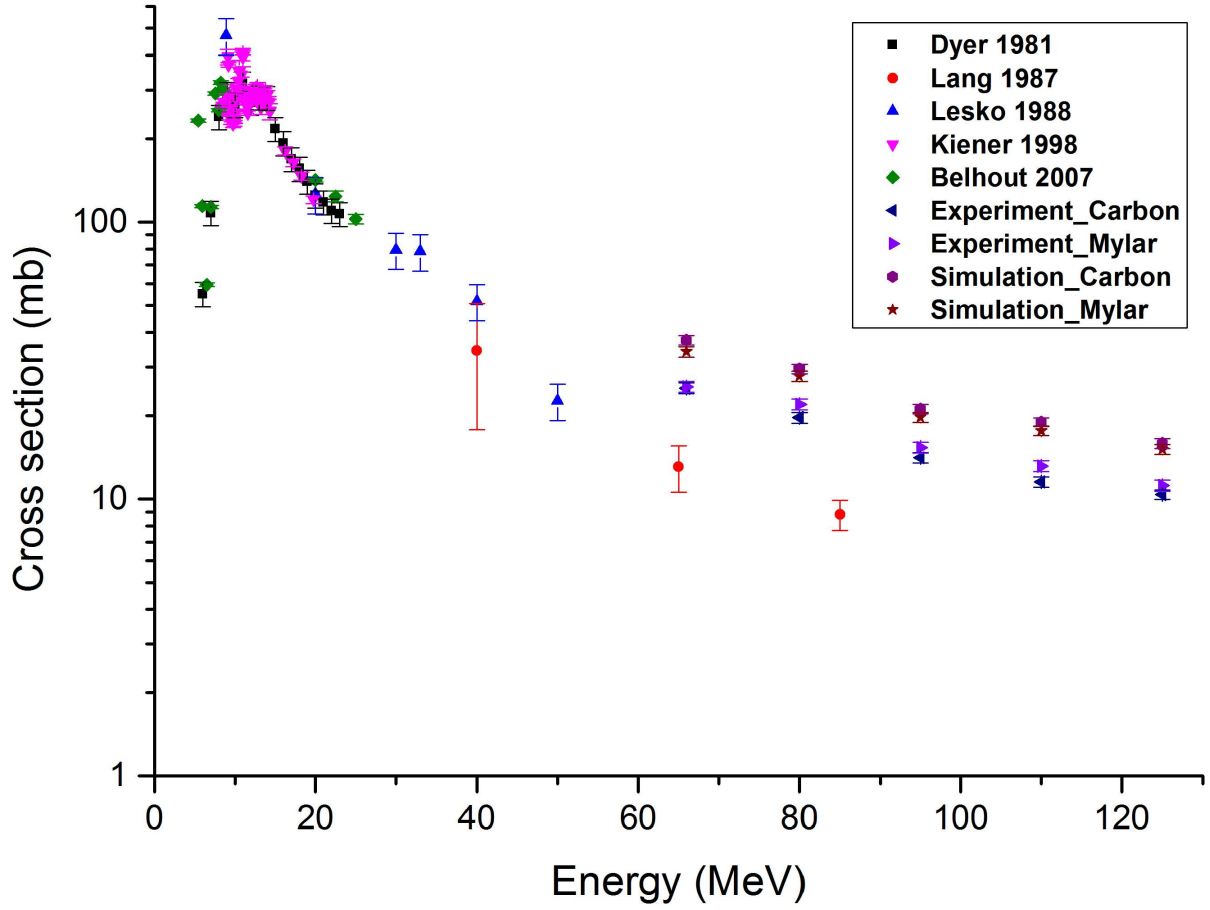

Figure 7.8: Comparison of measured and simulated total cross-section values for the 4.438 MeV photo peak with available experimental cross-section data.

7.3.2 Experimental and published cross-section comparison for the 6.129 MeV photo peak

For the 6.129 MeV cross-section data, only the experimental results are available to compare to the available experimental results. Figure 7.9 shows the total cross-section comparison of the experimental total cross-section data with available experimental cross-section data for the 6.129 MeV photo peak from the mylar target. As with the 4.438 MeV peak, these new cross-section results appear to be higher than the expected values, but due to the sparsity of the data, it is hard to determine if these data points are indeed too high.

Although, particularly for the 6.129 MeV photo peak measurements, the lack of a fourth angular measurement does cast some uncertainty on this data set. Both the mylar and carbon targets would benefit from additional angular measurements.

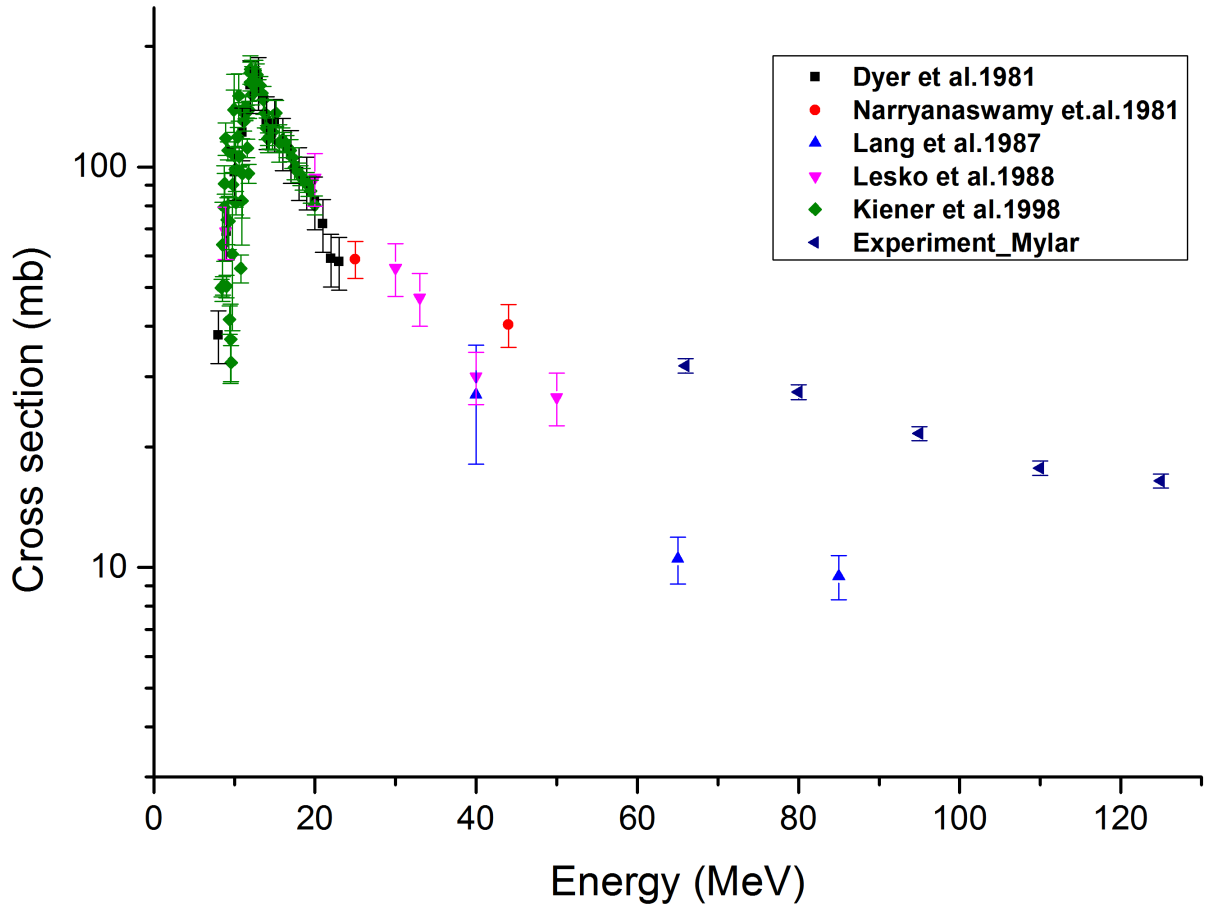

Figure 7.9: Comparison of measured total cross-section values for the 6.129 MeV photo peak from ^{16}O with available experimental cross-section data.

Chapter 8

Conclusion

This thesis presents a comparison of prompt gamma cross-section data from both experiment and simulation. In this dissertation, there were two specific aims. The first specific aim was to measure the prompt gamma cross-section reactions from carbon and oxygen using the AFRODITE clover detectors. The second aim was to model the AFRODITE detector system using the Geant4 Monte-Carlo transport code for analyzing the feasibility of the Geant4 hadronic interaction physics list for the application of prompt gamma production in the therapeutic range by comparing to experimental results.

For the experimental study, the prompt gamma cross-sections were measured for the 4.438 MeV gamma peak from ^{12}C (carbon and mylar) and the 6.129 MeV gamma peak from ^{16}O (mylar) at five different energies 66 MeV, 80 MeV, 95 MeV, 110 MeV and 125 MeV. The cross-section calculation faced some difficulties, like a broad and split 4.438 MeV ^{12}C peak due to Doppler broadening and a lack of sufficient angular measurements for the 6.129 MeV ^{16}O peak.

For the simulation study, the AFRODITE detector system was modeled using the Geant4 Monte-Carlo code (version 10.01.p03) and was validated by comparing to experimentally measured gamma spectrum using three standard gamma emitting sources, ^{137}Cs, ^{60}Co, and ^{162}Eu. This validation of the AFRODITE model led to the conclusion our Geant4 AFRODITE model had a slightly higher efficiency than the actual detector setup. The reason for this higher efficiency was determined to be due to the fact that the simulated Compton suppression detectors worked about 15% better than the actual Compton suppression detectors. This increased efficiency doesn't impact the prompt gamma cross-section calculations since the efficiency response curves are determined individually for the experiment and simulation studies.

For the prompt gamma simulations, the target thickness was increased to 0.5 mm in order to optimize the computation time while increasing the prompt gamma cross-section statistics. As in the experimental study, the prompt gamma spectra were simulated for five different energies (66 MeV, 80 MeV, 95 MeV, 110 MeV and 125 MeV) and two targets (carbon

and mylar). The recommended physics model for proton collisions below 10 GeV (the Geant4 binary cascade model for hadronic inelastic reactions) was used for the AFRODITE simulations. The total cross-section values were calculated for the 4.438 MeV ^{12}C peak using the carbon and mylar targets. While using the Geant4 binary cascade model, two problems arose during the simulations. First, the 4.438 MeV ^{12}C photo peak was unusually broad and, second, the 6.129 MeV ^{16}O photo peak was very suppressed in the simulated prompt gamma spectra.

The above mentioned problems were analysed with the Xsection code, which measured the prompt gamma production over a 4π solid angle using different physics models and inelastic cross-section data sets. Prompt gamma spectra were simulated for the carbon target using the Geant4 binary cascade and the precompound model, while selecting two different inelastic cross-section data sets (Geisha-default and Tripathi) and modifying the exciton number in the precompound model between 1 and 2 (default). According to the simulated prompt gamma spectra, the precompound model with an exciton number of 1 and the default (Geisha) cross-section data set significantly narrow the 4.438 MeV photo peak. The same procedures were repeated to try and finding a solution for the suppressed 6.129 MeV ^{16}O peak, but unfortunately, the 6.129 MeV ^{16}O peak could not be observed in any of the tested Geant4 physics lists.

The total cross-section values for the 4.438 MeV ^{12}C photo peak were measured from the carbon and mylar targets in both the experiment and the simulation and the obtained results were compared. For the 4.438 MeV cross-section values from the carbon target, the Geant4 simulated results were up to 64% higher than the experimental cross-section values due to additional reactions [^{12}C(p, d)^{11}C*, ^{12}C(p, np)^{11}C*] contributing to the 4.438 MeV peak. The simulated cross-section results for the 4.438 MeV peak from the mylar target were also higher than the experimental results, but only up to 35%. The experimental 4.438 MeV cross-section values from the mylar target had slightly higher values (7%) than the experimental values from the carbon target because mylar contains both carbon and oxygen, thus getting contribution from the ^{16}O(p,x)^{12}C* reaction as well. By contrast, the simulated mylar results for the 4.438 MeV peak were above 7% lower than the carbon results due to a lack of the additional reactions [^{12}C(p, d)^{11}C*, ^{12}C(p, np)^{11}C*] that boosted the simulated carbon target results.

The total cross-section results (both experimental and simulated 4.438 MeV peak results from carbon and mylar as well as experimental 6.129 MeV peak results from mylar) results were compared to the available experimental data. Due to the scarcity of the available data, it is difficult to make any direct comparisons to existing data, but all of the total cross-section data from the work appears to be higher than the expected values based on what is currently available. While it is unclear why these results might be higher than previous measured results, it is quite clear that the Geant4 simulated cross-section results are 30% to 40% higher than the measured cross-section results. Since the energy spectra from the AFRODITE detector (both experimental and simulated) went through the same calculation procedures, this difference is not a product of the cross-section calculations, but

of the Geant4 code itself. The two candidates are the geometry model of the AFRODITE detector or the Geant4 physics models in the AFRODITE code. Based on previous reports, the second seems to the the most likely prospect.

Looking to the future, the two recommended areas of further work would be: First, to repeat the experimental AFRODITE measurements with additional clover detectors placed at more than three angles, with at least four angles suggested in order to improve the fitting of the angular distribution. Second, to re-run the AFRODITE simulations in order to recalculate the cross-section values for the 4.438 MeV peak using the suggested physics list from the Xsection code and to use the latest version of the Geant4 code (v10.03) for the 6.129 MeV cross-sections from the mylar target. The Geant4 improvements are already being implemented and will appear in the publication of this work.

Bibliography

Agostinelli, S., Allison, J., Amako, K., Apostolakis, J., Araujo, H., Arce, P., Asai, M., Axen, D., Banerjee, S., Barrand, G., Behner, F., Bellagamba, L., Boudreau, J., Broglia, L., Brunengo, A., Burkhardt, H., Chauvie, S., Chuma, J., Chytracek, R., Cooperman, G., Cosmo, G., Degtyarenko, P., Dell'Acqua, A., Depaola, G., Dietrich, D., Enami, R., Feliciello, A., Ferguson, C., Fesefeldt, H., Folger, G., Foppiano, F., Forti, A., Garelli, S., Giani, S., Giannitrapani, R., Gibin, D., Cadenas, J. G., GonzÃ¡lez, I., Abril, G. G., Greeniaus, G., Greiner, W., Grichine, V., Grossheim, A., Guatelli, S., Gumplinger, P., Hamatsu, R., Hashimoto, K., Hasui, H., Heikkinen, A., Howard, A., Ivanchenko, V., Johnson, A., Jones, F., Kallenbach, J., Kanaya, N., Kawabata, M., Kawabata, Y., Kawaguti, M., Kelner, S., Kent, P., Kimura, A., Kodama, T., Kokoulin, R., Kossov, M., Kurashige, H., Lamanna, E., LampÃ©n, T., Lara, V., Lefebure, V., Lei, F., Liendl, M., Lockman, W., Longo, F., Magni, S., Maire, M., Medernach, E., Minamimoto, K., de Freitas, P. M., Morita, Y., Murakami, K., Nagamatu, M., Nartallo, R., Nieminen, P., Nishimura, T., Ohtsubo, K., Okamura, M., O'Neale, S., Oohata, Y., Paech, K., Perl, J., Pfeiffer, A., Pia, M., Ranjard, F., Rybin, A., Sadilov, S., Salvo, E. D., Santin, G., Sasaki, T., Savvas, N., Sawada, Y., Scherer, S., Sei, S., Sirotenko, V., Smith, D., Starkov, N., Stoecker, H., Sulkimo, J., Takahata, M., Tanaka, S., Tcherniaev, E., Tehrani, E. S., Tropeano, M., Truscott, P., Uno, H., Urban, L., Urban, P., Verderi, M., Walkden, A., Wander, W., Weber, H., Wellisch, J., Wenaus, T., Williams, D., Wright, D., Yamada, T., Yoshida, H., Zschiesche, D., 2003. Geant4 a simulation toolkit. Nuclear Instruments and Methods in Physics Research Section A: Accelerators, Spectrometers, Detectors and Associated Equipment 506 (3), 250 – 303.

Alburger.D.E, Perlman.I, Rasmussen.J.O, Hyde, E. K., T.Seaborg, G., R.Bishop, G., Wilson, R., Devons.S, Goldfarb.L.J.B, Blin-Stoyle.R.J, Grace.M.A, 2012. Nuclear Reactions III. Springer Science and Business Media.

Amako, K., 1994. Methodologies, languages and too;s session summary. Proceedinds of CHEP94, San Francisco, CA, USA CONF-940492 (LBL-35822).

Aubrecht, G., 2003. Nuclear science- a guide to the nuclear science wall chart. Tech. rep., Contemporary Physics Education Project (CPEP).

Belhout, A., Kiener, J., Coc, A., Duprat, J., Engrand, C., Fitoussi, C., Gounelle, M., Lefebvre-Schuhl, A., Séréville, N. d., Tatischeff, V., Thibaud, J.-P., Chabot, M., Ham-

mache, F., Benhabiles-Mezhoud, H., Sep 2007. γ-ray production by proton and α-particle induced reactions on ^{12}C, ^{16}O, ^{24}Mg, and fe. Phys. Rev. C 76, 034607.

Bennett.G.W, Archambeau.J.O, Archambeau.B.E, Meltzer.J.I, Wingate.C.L, 1978. Visualization and transport of positron emission from proton activation in vivo. Science 200 (4346), 1151–1153.

Beyer, G. P., Scarantino, C. W., Prestidge, B. R., Sadeghi, A. G., Anscher, M. S., Miften, M., Carrea, T. B., Sims, M., Black, R. D., 2007. Technical evaluation of radiation dose delivered in prostate cancer patients as measured by an implantable mosfet dosimeter. International Journal of Radiation Oncology*Biology*Physics 69, 925 – 935.

Biggs.F, L., 1990. Preprint Sandia Laboratory, SAND 87-0070.

Black, R. D., Scarantino, C. W., Mann, G. G., Anscher, M. S., Ornitz, R. D., Nelms, B. E., 2005. An analysis of an implantable dosimeter system for external beam therapy. International Journal of Radiation Oncology*Biology*Physics 63, 290 – 300.

Bom, V., Joulaeizadeh, L., Beekman, F., 2012. Real-time prompt gamma monitoring in spot-scanning proton therapy using imaging through a knife-edge-shaped slit. Physics in Medicine and Biology 57, 297.

Brune, C., 2002. Gaussian quadrature applied to experimental gamma-ray yields. Nuclear Instruments and Methods in Physics Research Section A- Accelerators, Spectrometers, Detectors and Associated Equipment 493, 106 – 110.

Butcher.J.C, Messel.H, 1960. Nucl.Phys. 202, 15.

Dedes, G., Pinto, M., Dauvergne, D., Freud, N., Krimmer, J., LÃ©tang, J. M., Ray, C., Testa, E., 2014. Assessment and improvements of geant4 hadronic models in the context of prompt-gamma hadrontherapy monitoring. Physics in Medicine and Biology 59 (7), 1747.

Diblen, F., Espana, S., Holen, R. V., Vandenberghe, S., 2012. Detector design for range monitoring in hadron therapy by means of image reconstruction. In: 2012 IEEE Nuclear Science Symposium and Medical Imaging Conference Record (NSS/MIC). pp. 3887–3889.

Duchene.G, Beck.F.A, Twin.P.J, de France.G, Curien.D, Han.L, Beausang.C.W, Bentley.M.A, Nolan.P.J, Simpson.J, 1999. The clover: a new generation of composite ge detectors. Nuclear Instruments and Methods in Physics Research Section A: Accelerators, Spectrometers, Detectors and Associated Equipment 432 (1), 90 – 110.

Dyer, P., Bodansky, D., Seamster, A. G., Norman, E. B., Maxson, D. R., May 1981. Cross sections relevant to gamma-ray astronomy: Proton induced reactions. Phys. Rev. C 23, 1865–1882.

Essers, M., Mijnheer, B., 1999. In vivo dosimetry during external photon beam radiotherapy. International Journal of Radiation Oncology*Biology*Physics 43 (2), 245 – 259.

Ferguson.A.J, 1965. Angular correlation methods in gamma-ray spectroscopy. North-Holland, Amsterdam.

Folger, G., Ivanchenko, V. N., Wellisch, J. P., 2004. The binary cascade. The European Physical Journal A - Hadrons and Nuclei 21.

Ford.R, Nelson.W, 1985. SLAC-265, UC-32.

Frandes, M., Zoglauer, A., Maxim, V., Prost, R., 2010. A tracking compton-scattering imaging system for hadron therapy monitoring. IEEE TRANSACTIONS ON NUCLEAR SCIENCE 57 (1).

G4.10.3, 2016. Geant4 10.3 release notes.
URL `http://geant4.cern.ch/support/ReleaseNotes4.10.3.html`

G4HadModels, 2015. Geant4 hadronic models.
URL `http://llr.in2p3.fr/activites/physique/atf2/Geant4_hadronic_models.html`

G4Physics, 2016. Reference physics lists.
URL `http://geant4.cern.ch/support/proc_mod_catalog/physics_lists/referencePL.shtml`

Galt.J.C, 2005. Gamma radiation spectroscopy and the ^{12}c$(\alpha,\gamma)^{16}$o reaction with dragon. Tech. rep., TRIUMF:Canada's national laboratory for particle and nuclear physics and accelerator-based science.

Geant4, 2015. Physics Reference Manual. Geant4 collaborators.

Gilmore, G., D.Hemingway, J., 1996. Practical gamma-ray spectroscopy. John Wiley and Sons.

Goitein, M., 2008. Radiation Oncology:A Physicist's-Eye View. Springer.

Gottschalk, B., 2004. Passive beam spreading in proton radiation therapy. Tech. rep., Harvard High Energy Physics Laboratory.

Gottschalk, B., S, T., EH, B., EW, C., D, P., HM, L., 2011. Water equivalent path length measurement in proton radiotherapy using time resolved diode dosimetry. Med Phys 38, 2282–88.

Griffin.J.J, 1966. Semiclassical model of intermediate structure. Phys.Rev.Lett 17, 478 – 481.

Gudima.K.K, Mashnik.S.G, Toneev.V.D, 1983. Cascade-exciton model of nuclear reactions. Nuclear Physics A 401 (2), 329 – 361.

Heitler.W, 1954. The Quantum Theory of Radiation.

Heitler.W, 1957. The Quantum Theory of Radiation. Oxford University Press.

Hubbell, Gimm, Overbo, 1980. J.Phys.Chem.Ref.Data 9, 1023.

IAEA, 2016. X-ray and gamma-ray decay data standards for detector calibration and other applications.
URL http://daq.tlabs.ac.za/facilities/ddas-1/setup-guide

ICRU, 1993. Stopping Powers and Ranges for Protons and Alpha Particles. International Commission on Radiation Units and Measurements.

Iliadis, C., 2007. Nuclear Physics of Stars. Wiley-VCH.

iThemba LABS, 2016. Digital data acquisition system.
URL http://daq.tlabs.ac.za/facilities/ddas-1/setup-guide

Jayaraman, S., Lanzl, L. H., 2011. Clinical radiotherapy physics. Springer Science & Business Media.

Jeyasugiththan, J., 2014. Experimental investigation of the characteristics of prompt gammas produced in tissue during proton therapy treatment. Ph.D. thesis, Uninersity of cape Town.

Jeyasugiththan, J., Peterson, S. W., 2015. Evaluation of proton inelastic reaction models in geant4 for prompt gamma production during proton radiotherapy. Physics in Medicine and Biology 60 (19), 7617.

Jones.P.M, Wei.L, Beck.F.A, Butler.P.A, Byrski.T, DuchÃ[a]ne.G, de France.G, Hannachi.F, Jones.G.D, Kharraja.B, 1995. Calibration of the new composite clover detector as a compton polarimeter for the eurogam array. Nuclear Instruments and Methods in Physics Research Section A: Accelerators, Spectrometers, Detectors and Associated Equipment 362 (2), 556 – 560.

Jongen, Y., Stichelbaut, F., 2003. Verification of the proton beam position in the patient by the detection of prompt gamma-rays emission. In: 42nd Meet. Particle Therapy Co-Operative Group (PTCOG).

Kabuki, S., Ueno, K., Kurosawa, S., Iwaki, S., Kubo, H., Miuchi, K., Fujii, Y., Kim, D., Kim, J., Kohara, R., Osamu Miyazaki, T. S., Shirahata, T., Takayanagi, T., Terunuma, T., Tsukahara, Y., Yamamoto, E., Yasuoka, K., Tanimori, T., 2009. Study on the use of electron-tracking compton gamma-ray camera tomonitor the therapeutic proton dose distribution in real time. IEEE Nuclear Science Symposium Conference Record.

Kiener, J., Berheide, M., Achouri, N. L., Boughrara, A., Coc, A., Lefebvre, A., de Oliveira Santos, F., Vieu, C., Oct 1998. γ-ray production by inelastic proton scattering on ^{16}O and ^{12}C. Phys. Rev. C 58, 2174–2179.

Kim, D., Yim, H., Kim, J.-W., 2009. Pinhole camera measurements of prompt gammarays for detection of beam range variation in proton therapy. Journal of the Korean Physical Society 55(4), 1673.

Klein.O, Nishina.Y, 1929. Z.Physik 52, 853.

Knoll.F.G, 2010. Radiation detection and measurement. Wiley.

Knopf, A.-C., Lomax, A., 2013. In vivo proton range verification: a review. Physics in Medicine and Biology 58 (15), R131.

Knopf, A.-C., Parodi, K., Paganetti, H., Bortfeld, T., Daartz, J., Engelsman, M., Liebsch, N., Shih, H., 2011. Accuracy of proton beam range verification using post-treatment positron emission tomography computed tomography as function of treatment site. International Journal of Radiation Oncology Biology Physics 79 (1), 297 – 304.

Kolata, J. J., Auble, R., Galonsky, A., Oct 1967. Excitation energy of the first excited state of c^{12}, and observation of a coherent doppler effect. Phys. Rev. 162, 957–962.

Kormoll, T., Fiedler, F., Schone, S., Wustemann, J., Zuber, K., Enghardt, W., 2011. A compton imager for in-vivo dosimetry of proton beams: A design study. Nuclear Instruments and Methods in Physics Research Section A: Accelerators, Spectrometers, Detectors and Associated Equipment 626-627, 114–119.

Kozlovsky, B., Murphy, R. J., Ramaty, R., 2002. Nuclear deexcitation gamma-ray lines from accelerated particle interactions. The Astrophysical Journal Supplement Series 141 (2), 523.

Kraan, A. C., july 2015. Range verification methods in particle therapy: Underlying physics and monte carlo modeling. Frontiers in Oncology 5.

Kurosawa, S., Kubo, H., Ueno, K., Kabuki, S., Iwaki, S., Takahashi, M., Taniue, K., Higashi, N., Miuchi, K., Tanimori, T., Kim, D., Kim, J., 2012. Prompt gamma detection for range verification in proton therapy. Current Applied Physics 12 (2), 364 – 368.

Kutner, M. L., 2003. Astronomy: A physical perspective. Cambridge University press.

Lang, F. L., Werntz, C. W., Crannell, C. J., Trombka, J. I., Chang, C. C., Apr 1987. Cross sections for production of the 15.10-mev and other astrophysically significant gamma-ray lines through excitation and spallation of ^{12}C and ^{16}O with protons. Phys. Rev. C 35, 1214–1227.

Lee, H. R., Park, J. H., Kim, C. H., Min, C. H., 2012. Design optimization of a 2d prompt-gamma measurement system for proton dose verification. Journal of the Korean Physical Society 61, 239–242.

Lesko, K. T., Norman, E. B., Larimer, R.-M., Kuhn, S., Meekhof, D. M., Crane, S. G., Bussell, H. G., May 1988. Measurements of cross sections relevant to gamma-ray line astronomy. Phys. Rev. C 37, 1808–1817.

Li, K., 2015. Afrodite-pr239a.
URL `https://github.com/KevinCWLi/AFRODITE-PR239A`

Litzenberg, D. W., Bajema, J. F., Becchetti, F. D., Brown, J. A., Raymond, R. S., Roberts, D. A., Caraher, J., Hutchins, G., Ronningen, R., Smith, R., Abbott, M., Oct 1992. On-

line monitoring and pet imaging of proton radiotherapy beams. In: IEEE Conference on Nuclear Science Symposium and Medical Imaging. pp. 954–956 vol.2.

Litzenberg, D. W., Bajema, J. F., Becchetti, F. D., Roberts, D. A., Ronningen, R., der Molen, S. V., Brown, J. A., Haken, R. K. T., Caraher, J., Hazard, C., Chawla, M., Oct 1994. On-line monitoring and pet imaging of proton radiotherapy beams. In: Nuclear Science Symposium and Medical Imaging Conference, 1994., 1994 IEEE Conference Record. Vol. 4. pp. 1672–1676 vol.4.

Lu, H.-M., 2007. A potential method for range verification in proton therapy treatment using range-modulated passive scattering fields. 46th meet of the particle therapy co-operative group(Wanjie).

Lu, H.-M., 2008a. A point dose method for in vivo range verification in proton therapy. Physics in Medicine and Biology 53 (23), N415.

Lu, H.-M., 2008b. A potential method for in vivo range verification in proton therapy treatment. Physics in Medicine and Biology 53 (5), 1413.

Mackin, D., Polf, J., Peterson, S., Beddar, S., 2013. The effects of doppler broadening and detector resolution on the performance of three stage compton cameras. Medical Physics 40, 012402.

Messel.H, Crawford.D, 1970. Electron-photon shower distribution. Pergamon Press.

Min, C. H., 2011. Development of prompt gamma measurement system for in vivo proton beam range verification. Ph.D. thesis, Hanyang University, Seoul (KR).

Min, C. H., Lee, H. R., Kim, C. H., Lee, S. B., 2012. Development of array-type prompt gamma measurement system for in vivo range verification in proton therapy. Medical physics.

Min.C, Kim.C.H, Youn.M, Kim.J, 2006. Prompt gamma measurements for locating the dose falloff region in the proton therapy. Applied Physics Letters. 89, 183517.

Moteabbed, M., Espana, S., Paganetti, H., 2011. Monte carlo patient study on the comparison of prompt gamma and pet imaging for range verification in proton therapy. Physics in Medicine and Biology 56 (4), 1063.

Mumot, M., Algranati, C., Hartmann, M., Schippers, J. M., Hug, E., Lomax, A. J., 2010. Proton range verification using a range probe: definition of concept and initial analysis. Physics in Medicine and Biology 55 (16), 4771.

Narayanaswamy, J., Dyer, P., Faber, S. R., Austin, S. M., Dec 1981. Production of 6.13-mev gamma rays from the ^{16}O$(p,p'\gamma)^{16}$O reaction at 23.7 and 44.6 mev. Phys. Rev. C 24, 2727–2730.

Newhauser, W. D., Zhang, R., 2014. The physics of proton therapy. Physics in Medicine and Biology 60, 155–209.

Newman.R.T, Lawrie.J.J, S, B. R., V, F., Naguleswaran.S, V, P., Rigollet.C, F, S.-S., D, S., J, S., F, S., Beetge, W. R., Mabala.G, Roux.D, Whittaker.W, Ncapayi.N.J, 1995. High-spin studies with the afrodite array. Nuclear Instruments and Methods in Physics Research Section A: Accelerators, Spectrometers, Detectors and Associated Equipment 362 (2), 556 – 560.

Nikolic, J. D., Jokovic, D., Todorovic, D., Rajacic, M., 2014. Application of geant4 simulation on calibration of hpge detectors for cylindrical environmental samples. Journal of Radiological Protection 34 (2), N47.

Paans, A. M. J., Schippers, J. M., 1992. Proton therapy in combination with pet as monitor: a feasibility study. In: IEEE Conference on Nuclear Science Symposium and Medical Imaging. pp. 957–959 vol.2.

Paganetti, H., 2012. Range uncertainties in proton therapy and the role of monte carlo simulations. Physics in Medicine and Biology 57 (11).

Paganetti, H., Bortfeld, T., 2005. Proton beam radiotherapy-the state of the art. New Technologies in Radiation Oncology (Medical Radiology Series) 3, 540.

Papka.P, 2007. Simsort. Unpublished.

Parodi, K., Bortfeld, T., 2006. A filtering approach based on gaussian powerlaw convolutions for local pet verification of proton radiotherapy. Physics in Medicine and Biology 51 (8), 1991.

Parodi, K., Enghardt, W., 2000. Potential application of pet in quality assurance of proton therapy. Physics in Medicine and Biology 45 (11), N151.

Parodi, K., Enghardt, W., Haberer, T., 2002. In-beam pet measurements of beta plus radioactivity induced by proton beams. Physics in Medicine and Biology 47 (1), 21.

Parodi, K., Ponisch, F., Enghardt, W., 2005. Experimental study on the feasibility of in-beam pet for accurate monitoring of proton therapy. IEEE Transactions on Nuclear Science 52 (3), 778–786.

Perkins, S., Cullen, D., Seltzer, S., 1991. Tables and graphs of electron-interaction cross sections from 10 eV to 100 GeV derived from the LLNL Evaluated Electron Data Library (EEDL), Z = 1–100.

Peterson, S. W., Robertson, D., Polf, J., 2010. Optimizing a three-stage compton camera for measuring prompt gamma rays emitted during proton radiotherapy. Physics in Medicine and Biology 55 (22), 6841.

Polf, J. C., Peterson, S., McCleskey, M., Roeder, B. T., Spiridon, A., Beddar, S., Trache, L., 2009. Measurement and calculation of characteristic prompt gamma ray spectra emitted during proton irradiation. Physics in Medicine and Biology 54 (22), N519.

Polf.J.C, Peterson.S, Ciangaru.G, Gillin.M, Beddar.S, 2009a. Prompt gamma-ray emission from biological tissues during proton irradiation: a preliminary study. Physics in Medicine and Biology 54, 731.

Poole, C. M., Cornelius, I., Trapp, J. V., Langton, C. M., 2012. A cad interface for geant4. Australasian Physical & Engineering Sciences in Medicine 35 (3), 329–334.

Poole.C, 2012. Cadmesh.
URL `https://github.com/christopherpoole/CADMesh`

Rajput, M. U., Mahmud, A., Waqar, A., 2002. Characteristic absolute efficiency response curves of a high purity germanium detector in the energy range 50–1500 kev. Journal of Radioanalytical and Nuclear Chemistry 251 (3), 457–462.

Ramaty, R.and Kozlovsky, B. S. A. N., June 1977. The solar gamma-ray spectrum between 4 and 8 mev. Astrophysical Journal 214, 617–631.

Richard, M. H., Chevallier, M., Dauvergne, D., Freud, N., Henriquet, P., Foulher, F. L., Letang, J. M., Montarou, G., Ray, C., Roellinghoff, F., Testa, E., Testa, M., Walenta, A. H., 2011. Design guidelines for a double scattering compton camera for prompt-gamma imaging during ion beam therapy: A monte carlo simulation study. IEEE Transactions on Nuclear Science 58, 87–94.

Robertson, D., Polf, J. C., Peterson, S. W., Gillin, M. T., Beddar, S., 2011. Material efficiency studies for a compton camera designed to measure characteristic prompt gamma rays emitted during proton beam radiotherapy. Physics in Medicine and Biology 56, 3047.

Roellinghoff, F., Richard, M.-H., Chevallier, M., Constanzo, J., Dauvergne, D., Freud, N., Henriquet, P., Foulher, F. L., Letang, J., Montarou, G., Ray, C., Testa, E., Testa, M., Walenta, A., 2011. Design of a compton camera for 3d prompt- imaging during ion beam therapy. Nuclear Instruments and Methods in Physics Research Section A: Accelerators, Spectrometers, Detectors and Associated Equipment 648, Supplement 1, S20 – S23.

Romero, J., Osborne, J., Brady, F., Caskey, W., Cebra, D., Partlan, M., Kusko, B., King, R., Mirshad, I., Kubo, H., Daftari, I., Chu, W., 1995. Patient positioning for proton-therapy using a proton range telescope. Nuclear Instruments and Methods in Physics Research Section A: Accelerators, Spectrometers, Detectors and Associated Equipmen 356 (2), 558 – 565.

Rose, M. E., Aug 1953. The analysis of angular correlation and angular distribution data. Phys. Rev. 91, 610–615.

Scarantino, C. W., Prestidge, B. R., Anscher, M. S., Ferree, C. R., Kearns, W. T., Black, R. D., Bolick, N. G., Beyer, G. P., 2008. The observed variance between predicted and measured radiation dose in breast and prostate patients utilizing an in vivo dosimeter. International Journal of Radiation Oncology*Biology*Physics 72, 597 – 604.

Schulte, R. W., Penfold, S. N., 2012. Proton ct for improved stopping power determination in proton therapy, invited. American nuclear society 106, 55–58.

Seo, H., An, S. H., Kim, J. K., Kim, C. H., 2007. Monte carlo study of a double-scattering compton camera with {GEANT4}. Nuclear Instruments and Methods in Physics Research Section A: Accelerators, Spectrometers, Detectors and Associated Equipment 580, 314 – 317.

S.Krane, K., 1987. Introductory Nuclear Physics. John Wiley and Sons.

Smeets, J., Roellinghoff, F., Janssens, G., Perali, I., Celani, A., Fiorini, C., Freud, N., Testa, E., Prieels, D., 2016. Experimental comparison of knife-edge and multi-parallel slit for prompt gamma imaging of proton pencil beams. Frontiers in Oncology 6, 156.

Smeets, J., Roellinghoff, F., Prieels, D., Stichelbaut, F., Benilov, A., Busca, P., Fiorini, C., Peloso, R., Basilavecchia, M., Frizzi, T., Dehaes, J. C., Dubus, A., 2012. Prompt gamma imaging with a slit camera for real-time range control in proton therapy. Physics in Medicine and Biology 57, 3371.

Sober, 2005. An introduction to cross section.

Storm.H, Israel.H.I, 1970. Nucl.Data Tables A7, 565.

Szücs, T., Bemmerer, D., Broggini, C., Caciolli, A., Confortola, F., Corvisiero, P., Elekes, Z., Formicola, A., Fülöp, Z., Gervino, G., Guglielmetti, A., Gustavino, C., Gyürky, G., Imbriani, G., Junker, M., Lemut, A., Marta, M., Mazzocchi, C., Menegazzo, R., Prati, P., Roca, V., Rolfs, C., Rossi Alvarez, C., Somorjai, E., Straniero, O., Strieder, F., Terrasi, F., Trautvetter, H. P., 2010. An actively vetoed clover gamma detector for nuclear astrophysics at luna. The European Physical Journal A 44, 513–519.

Tavernier, S., 2010. Experimental techniques in nuclear and particle physics. Springer.

Testa, E., Bajard, M., Chevallier, M., Dauvergne, D., Le Foulher, F., Freud, N., Letang, Poizat, Ray, C., Testa, M., 2008. Monitoring the bragg peak location of 73 MeV/u carbon ions by means of prompt gamma-ray measurements. Applied Physics Letters 93, 093506.

Verburg, J. M., Riley, K., Bortfeld, T., Seco, J., 2013. Energy- and time-resolved detection of prompt gamma-rays for proton range verification. Physics in Medicine and Biology 58 (20), L37.

Verburg, J. M., Shih, H. A., Seco, J., 2012. Simulation of prompt gamma-ray emission during proton radiotherapy. Physics in Medicine and Biology 57 (17), 5459.

Vynckier, S., Derreumaux, S., Richard, F., Bol, A., Michel, C., Wambersie, A., 1993. Is it possible to verify directly a proton-treatment plan using positron emission tomography? Radiotherapy and Oncology 26 (3), 275 – 277.

Weisskopf, V. F., Ewing, D. H., 1940. On the yield of nuclear reactions with heavy elements. Phys. Rev. 57, 472–485.

WHO, 2015. World health organization, cancer statistics.
URL http://www.who.int/mediacentre/factsheets/fs297/en/

Wilson, R. R., 1946. Radiological use of fast protons. Radiology 47, 487–491.

Wright, D. H., Koi, T., Folger, G., Ivanchenko, V., Kossov, M., Starkov, N., Heikkinen, A., Wellisch, H., 2006. Low and high energy modeling in geant4. AIP conference procedings.

Yahia-Cherif, W., Ouichaoui, S., Kiener, J., Tatischeff, V., Lawrie, E., Lawrie, J., Belhout, A., Benhabiles, H., Bucher, T., Chafa, A., Damache, S., Debabi, M., Deloncle, I., Easton, J., Hamadache, C., Hammache, F., P. Jones, B.V. Kheswa, N. K. T. L. S. M. D. N. J. N. S. N., Moussa, D., Nchodu, R., Papka, P., de Sereville, N., Sharpey-Schafer, J., Shirinda, O., Wiedeking, M., Wyngaardt, S., 2015. Gamma ray production cross sections in proton induced reactions on natural mg, si and fe targets over the proton energy range 30 up to 66 mev. In: IOP Institute of Physics Conference Nuclear Physics in Astrophysics VII, 28th EPF Nuclear Physics Divisional Conference, May 18-22 2015, York, UK.

Yock, T. I., Tarbell, N. J., 2004. Technology insight: Proton beam radiotherapy for treatment in pediatric brain tumors. Nat Clin Pract Oncol. 1, 97–103.

Ziegler.J.F, 1999. The stopping of energetic light ions in elemental matter. J.Appl.Phys/Rev.Appl.Phys. 85, 1249–1272.

Appendix

Appendix A

Geant4 Electromagnetic processes

A.0.3 Photoelectric effect

The photo electric effect is defined as the ejection of electron from the matter after the absorption of photon in the material. For the simulation of this process, parameterized photon absorption cross section is used to find mean free path. Data set of atomic shell is used to determine the ejected electron energy and K-shell angular distribution to find the direction of electron. The equation for the parameterized photon absorption cross section is given by [Biggs.F (1990)],

$$\sigma\left(Z, E_{\gamma}\right) = \frac{a\left(Z, E_{\gamma}\right)}{E_{\gamma}} + \frac{b\left(Z, E_{\gamma}\right)}{E_{\gamma}^{2}} + \frac{c\left(Z, E_{\gamma}\right)}{E_{\gamma}^{3}} + \frac{d\left(Z, E_{\gamma}\right)}{E_{\gamma}^{4}} \tag{A.1}$$

To generate the coefficients a, b, c, and d, an experimental data set is used to fit in some energy intervals. Least squares method is employed for fitting. The boundaries of these energy intervals are equal to the related photoabsorption edges.

The mean free path for photoelectric interaction is given by,

$$\lambda\left(E_{\gamma}\right) = \frac{1}{\Sigma_{i} n_{ati}.\sigma\left(Z_{i}, E_{\gamma}\right)} \tag{A.2}$$

where, n_{ati} is the number of atoms per volume for i^{th} element in compound material. The mean free path and cross section are calculated on the fly since both are discontinuous. The probability of photon interaction with i^{th} element is given by,

$$Prob\left(Z_{i}, E_{\gamma}\right) = \frac{n_{ati}\sigma\left(Z_{i}, E_{\gamma}\right)}{\Sigma_{i}[n_{ati}.\sigma_{i}(E_{\gamma})]} \tag{A.3}$$

The photon can be absorbed if $E_{\gamma} > B_{shell}$, where B_{shell} is the shell energy which depends

on atomic number Z of the material. The kinetic energy of emitted photoelectron is:

$$T_{photoelectron} = E_\gamma - B_{shell}\left(Z_i\right) \tag{A.4}$$

More details of this process can be found in the Geant4 physics reference manual [Geant4 (2015)].

A.0.4 Compton scattering

The Compton scattering is defined as an inelastic scattering of photon on the atom with releasing an electron. Compton scattering of a photon is simulated by using an empirical cross section formula which reproduces the scattering cross section data for $E_\gamma > 10$ keV.

$$\sigma\left(Z, E_\gamma\right) = \Big[P_1(Z). \quad \frac{log(1+2X)}{X} + \quad \frac{P_2(Z) + P_3(Z)X + P_4(Z)X^2}{1 + aX + bX^2 + cX^3}\Big] \tag{A.5}$$

where, Z is the atomic number of the medium, E_γ is the energy of photon, $X = E_\gamma/mc^2$, m is mass of electron, and $P_i(Z) = Z(d_i + e_i Z + f_i Z^2)$. The parameters are determined within the method which evaluate the cross section per atom. To extract the parameters, over 511 data points [Hubbell et al. (1980), Storm.H and Israel.H.I (1970)] are chosen for fitting in the intervals $1 \leq$ Z ≤ 100 and $E_\gamma \in$ [10 keV, 100 GeV]. The scattering angle and energy of photon are determined by using Klein-Nishina differential cross section formula for this simulation.

The Klein-Nishina differential cross section per atom is given by [Klein.O and Nishina.Y (1929)],

$$\frac{d\sigma}{d\epsilon} = \pi r_e^2 \frac{m_e c^2}{E_0} Z\Big[\frac{1}{\epsilon} + \epsilon\Big]\Big[1 - \frac{\epsilon sin^2\theta}{1+\epsilon^2}\Big] \tag{A.6}$$

where, r_e is an radius of classical electron, $m_e c^2$ is an electron mass, E_0 is an incident photon energy, $\epsilon = E_1/E_0$, and E_1 is scattered photon energy. Assuming an elastic collision, scattering angle θ is given by Compton formula:

$$E_1 = E_0 \quad \frac{m_e c^2}{m_e c^2 + E_0(1 - cos\theta)} \tag{A.7}$$

At minimum energy of photon (backward scattering, $\theta = 180°$), ϵ is given by

$$\epsilon = \frac{m_e c^2}{m_e c^2 + 2E_0} \tag{A.8}$$

The function can be set to sample the photon energy by using combination of composition and rejection Monte Carlo method [Butcher.J.C and Messel.H (1960), Messel.H and

Crawford.D (1970), Ford.R and Nelson.W (1985)].

$$\Phi(\epsilon) \simeq \left[\frac{1}{\epsilon} + \epsilon\right]\left[1 - \frac{\epsilon sin^2\theta}{1+\epsilon^2}\right] = f(\epsilon).g(\epsilon) \tag{A.9}$$

$$f(\epsilon) = \alpha_1 f_1(\epsilon) + \alpha_2 f_2(\epsilon) \tag{A.10}$$

where, $f_1(\epsilon) = 1/(\alpha_1\epsilon)$, $\alpha_1 = ln(1/\epsilon)$, $f_2(\epsilon) = \epsilon/\alpha_2$, and $\alpha_2 = (1-\epsilon^2)/2$, f_1 and f_2 are probability density functions and $g(\epsilon)$ is the rejection function which satisfies $0 < g(\epsilon) \leq 1$

$$g(\epsilon) = \left[1 - \frac{\epsilon}{1+\epsilon^2} sin^2\theta\right] \tag{A.11}$$

The sampling procedures are following for ϵ in a given set of three random numbers r, r', and r'' which are uniformly distributed on the interval [0,1].

Step 1: If $r < \alpha_1/\alpha_1 + \alpha_2$, $f_1(\epsilon)$ will be selected otherwise $f_2(\epsilon)$

Step 2: ϵ will be sampled from the following distributions corresponding to f_1 and f_2.

For f_1: $\epsilon = \epsilon_0^{r'}$ $\quad (\equiv exp(-r'\alpha_1))$

For f_2: $\epsilon^2 = \epsilon_0^2 + (1-\epsilon_0^2)r'$

Step 3: The angle θ will be calculated using the following formula

$sin^2\theta = t(2-t)$ where, $t \equiv (1 - cos\theta) = m_e c^2(1-\epsilon)/(E_0\epsilon)$

Step 4: To test the rejection function, if $g(\epsilon) \geq r''$ ϵ will be accepted otherwise it will start again from step 1 [Geant4 (2015)].

A.0.5 Gamma conversion

If the gamma ray has an energy greater than rest mass of pair ($2m_e = 1.022$ MeV), it can produce an electron and positron pair. In order to conserve energy and momentum, this interaction must be taken place in the Coulomb field of the target material. If the photon has the energy larger than 1.022 MeV, the remaining energy is divided between the pair as kinetic energy.

The total cross section per atom for a gamma conversion into an electron positron pair is given by [Hubbell et al. (1980), Heitler.W (1957)]

$$\sigma\,(Z, E_\gamma) = Z(Z+1) \quad \left[F_1(X) + F_2(X)Z + \frac{F_3(X)}{Z}\right] \tag{A.12}$$

where, $X = ln(E_\gamma/m_e c^2)$, Z and E_γ are atomic number of the nuclei and incident gamma

energy respectively and the functions of F_n are given by

$$F_1(X) = a_0 + a_1X + a_2X^2 + a_3X^3 + a_4X^4 + a_5X^5 \tag{A.13}$$

$$F_2(X) = b_0 + b_1X + b_2X^2 + b_3X^3 + b_4X^4 + b_5X^5 \tag{A.14}$$

$$F_3(X) = c_0 + c_1X + c_2X^2 + c_3X^3 + c_4X^4 + c_5X^5 \tag{A.15}$$

The parameters a_i, b_i, and c_i can be found by using least-squares fit to the data set [Hubbell et al. (1980)]. The parameters are in the following range, $1 \leq \mathrm{Z} \leq 100$ and $E_\gamma \in$ [1.5 MeV, 100 GeV]. To extrapolate the data, the following equation is used

$$\sigma\left(E\right) = \sigma\left(E_low\right).\left(\frac{E - 2m_ec^2}{E_low - 2m_ec^2}\right)^2 \tag{A.16}$$

The mean free path for the photon conversion into an electron and positron pair (e^-, e^+) in a given material is given by the equation 2.2.

The electron cloud leads to additional contribution to the pair production which is given by,

$$\xi\left(Z\right) = \frac{ln(1440/Z^{2/3})}{ln(183/Z^{1/3}) - f_c(Z)} \tag{A.17}$$

The Bethe-Heitler formula for the cross section after some corrections and algebraic manipulation can be written:

$$\frac{d\sigma\left(Z,\epsilon\right)}{d\epsilon} = \alpha r_e^2 Z[Z + \xi\left(Z\right)]\frac{2}{9}\left[\frac{1}{2} - \epsilon_{min}\right] \times \left[N_1 f_1\left(\epsilon\right) g_1\left(\epsilon\right) + N_2 f_2\left(\epsilon\right) g_2\left(\epsilon\right)\right] \tag{A.18}$$

where, $N_1 = \left[\frac{1}{2} - \epsilon_{min}\right]^2 F_{10}$, $f_1\left(\epsilon\right) = \frac{3}{[\frac{1}{2}-\epsilon_{min}]^2}[\frac{1}{2} - \epsilon]^2$, $g_1\left(\epsilon\right) = \frac{F_1(\epsilon)}{F_{10}}$, $N_2 = \frac{3}{2}F_{20}$, $f_2\left(\epsilon\right) = const = \frac{1}{[\frac{1}{2}-\epsilon min]}$, and $g_2\left(\epsilon\right) = \frac{F_2(\epsilon)}{F_{20}}$.

$f_1\left(\epsilon\right)$ and $f_2\left(\epsilon\right)$ are probability density functions and $g_1\left(\epsilon\right)$ and $g_2\left(\epsilon\right)$ are rejection functions. The interval for probability density function is $\epsilon \in [\epsilon_{min}, 1/2]$ and the rejection function is valid only if $0 < g_i(\epsilon) \leq 1$.

The probability of gamma conversion interaction for i^{th} element in compound material can be written as,

$$Prob\left(Z_i, E_\gamma\right) = \frac{n_{ati}\sigma\left(Z_i, E_\gamma\right)}{\Sigma_i[n_{ati}.\sigma_i(E_\gamma)]} \tag{A.19}$$

Sampling procedures for this interaction is following,

let (r_a, r_b, r_c) are uniformly distributed random numbers.

Step 1: The random number r_a will be used to choose decomposition term in the equation 2.18. If $r_a < N_1/(N_1 + N_2)$, $f_1\left(\epsilon\right) g_1\left(\epsilon\right)$ will be selected otherwise $f_2\left(\epsilon\right) g_2\left(\epsilon\right)$.

Step 2: ϵ will be sampled from $f_1(\epsilon)$ or $f_2(\epsilon)$ with r_b:

$\epsilon = \frac{1}{2} - \left(\frac{1}{2} - \epsilon_{min}\right) r_b^{1/3}$ or $\epsilon = \epsilon_{min} + \left(\frac{1}{2} - \epsilon_{min}\right) r_b$

Step 3: If $g_1(\epsilon)$ or $g_2(\epsilon) < r_c$, ϵ will be rejected.

More details of this process can be found in the Geant4 physics reference manual [Geant4 (2015)].

A.0.6 Ionization

The Geant4 handles the energy loss processes for e^+/e^-, μ^+, μ^- and the charged hadrons in a similar way. The continuous and discrete energy loss must be considered for any of energy loss processes. The energy loss below a given threshold is continuous and the energy above the threshold is simulated by the production of secondary particles (gammas, positrons, and electrons). The transferable maximum energy to free electron is given by,

$$T_{max} = \begin{cases} E - mc^2 & \text{for} \quad e^+ \\ (E - mc^2) & \text{for} \quad e^- \end{cases} \tag{A.20}$$

where, mc^2 is the electron mass. The energy loss above a given threshold is simulated by the delta rays production by Möller scattering (e^-e^-), or Bhabha scattering (e^+e^-). Below the threshold energy, the ejected soft electrons are simulated as continuous energy loss.

Setting

$$\frac{d\sigma(Z, E, T)}{dT} \tag{A.21}$$

be the differential cross section per atom to eject a secondary particle with kinetic energy E by an incident particle of total energy E in a material of density ρ. The mean rate of energy loss can be written as:

$$\frac{dE_{soft}(E, T_{cut})}{dx} = n_{at}. \int_0^{T_{cut}} \frac{d\sigma(Z, E, T)}{dT} T dT \tag{A.22}$$

where, T_{cut} is the production threshold / cut off kinetic energy and n_{at} is the number of atoms per volume.

The total cross section per atom for the ejection of secondary particle energy $T > T_{cut}$ is

$$\sigma(Z, E, T_{cut}) = \int_{T_{cut}}^{T_{max}} \frac{d\sigma(Z, E, T)}{dT} dT \tag{A.23}$$

where, T_{max} is the transferable maximum energy to the secondary particle. In case of multiple processes of energy loss for a given particle, then the energy loss for the total

continuous part is the sum:

$$\frac{dE^{tot}_{soft}(E, T_{cut})}{dx}) \quad = \quad \sum_i \frac{dE_{soft,i}(E, T_{cut})}{dx} \tag{A.24}$$

The total cross section per atom for Möller (e^-e^-) and Bhabha (e^+e^-) scattering is obtained by integrating the equation 2.23. T_{cut} is always 1 keV or larger in Geant4 simulation. If delta rays energies much larger than excitation energy of the material ($T \gg I$), the total cross section is considered as Möller scattering [Messel.H and Crawford.D (1970)].

$$\sigma(Z, E, T_{cut}) = \frac{2\pi r_e^2 Z}{\beta^2(\gamma-1)} \times \Big[\frac{(\gamma-1)^2}{\gamma^2}\Big(\frac{1}{2} - x\Big) + \frac{1}{x} - \frac{1}{1-x} - \frac{2\gamma-1}{\gamma^2} ln\frac{1-x}{x}\Big], \tag{A.25}$$

and for Bhabha scattering,

$$\sigma(Z, E, T_{cut}) = \frac{2\pi r_e^2 Z}{(\gamma-1)} \times \Big[\frac{1}{\beta^2}\Big(\frac{1}{x} - 1\Big) + B_1 lnx + B_2(1-x) - \frac{B_3}{2}(1-x^2) + \frac{B_4}{3}(1-x^3)\Big]. \tag{A.26}$$

where,

$$\gamma = \tfrac{E}{mc^2} \qquad B_1 = 2 - y^2$$
$$\beta^2 = 1 - (1/\gamma^2) \qquad B_2 = (1-2y)(3+y^2)$$
$$x = T_{cut}/(E - mc^2) \qquad B_3 = (1-2y)^2 + (1-2y)^3$$
$$y = 1/(\gamma+1) \qquad B_4 = (1-2y)^3$$

These formulae give total cross section above the threshold ($T^{thr}_{Moller} = 2T_{cut}$, $T^{thr}_{Bhabha} = T_{cut}$). The mean free path is given by,

$$\lambda = (n_{at}.\sigma)^{-1} \qquad or \qquad \lambda = (\Sigma_i n_{ati}.\sigma_i)^{-1} \tag{A.27}$$

During the initialization stage of simulation, these values are determined and stored in the differential cross section table. According the material, the ranges of the particle can be determined and stored. The continuous energy loss and range can be retrieved during run time [Geant4 (2015)].

A.0.7 Bremsstrahlung

Bremsstrahlung is a braking radiation produces when the charged particle is deflected through by another charged particle influence. The energy loss of electrons or positrons due to the Bremsstrahlung radiation are determined as explained in section A.0.6.

Let,

$$\frac{d\sigma(Z,T,k)}{dk} \tag{A.28}$$

be the differential cross section for the Bremsstrahlung radiation energy of k and kinetic energy of electron T in the Coulomb field of atomic charge Z. If the photon energy is below the cut-off value (k_c), the soft photons are treated as continuous energy loss. The mean value of electron energy loss is given by,

$$E^{brem}_{Loss}(Z,T,k_c) = \int_0^{k_c} k\frac{d\sigma(Z,T,k)}{dk}dk. \tag{A.29}$$

For the photon radiation energy above the cut off value, the total cross section is given by,

$$\sigma_{brem}(Z,T,k_c) = \int_{k_c}^{T} \frac{d\sigma(Z,T,k)}{dk}dk. \tag{A.30}$$

The energy loss and the cross section have been parameterized in EEDL (Evaluated Electrons Data Library) data set [Perkins et al. (1991)].

A.0.8 Positron-electron annihilation

This process simulates in-flight annihilation of an electron and positron. It is assumed that the electron is initially free and rest. If annihilation process produce one, three or more which are ignored since these processes are negligible comparing with production of two photons.

The cross section per atom for the annihilation in flight of positron and electron is given by the Heitler formula [Heitler.W (1954), Ford.R and Nelson.W (1985)],

$$\sigma(Z,E) = \frac{Z\pi r_e^2}{\gamma+1} \quad \Big[\frac{\gamma^2+4\gamma+1}{\gamma^2-1} ln\Big(\gamma+\sqrt{\gamma^2-1}\Big) - \frac{\gamma+3}{\sqrt{\gamma^2-1}}\Big] \tag{A.31}$$

where, E is total energy of incident positron, $\gamma = E/mc^2$, and r_e is the classical electron radius. The mean free path for positron with annihilation of electron is given by,

$$\lambda(E) = \Big(\sum_i n_{ati}.\sigma(Z_i,E)\Big)^{-1} \tag{A.32}$$

where, n_{ati} is the number of atoms per volume of the i^{th} element in a compound material [Geant4 (2015)].

Appendix B

Experimental results

B.1 Energy calibration results

Energy calibration details for each high purity germanium crystals of first four clover detectors are given in table B.1.

Table B.1: The energy calibration curve details for each high purity germanium crystals for first four clover detectors

Crystal	Slope	Intercept
Clover1_HpGeCrystal_A	0.41331	-0.65728
Clover1_HpGeCrystal_B	0.38088	-0.68969
Clover1_HpGeCrystal_C	0.40747	-0.21988
Clover1_HpGeCrystal_D	0.41421	-0.88325
Clover2_HpGeCrystal_A	0.55486	-0.62601
Clover2_HpGeCrystal_B	0.53782	-2.41356
Clover2_HpGeCrystal_C	0.37220	-1.20114
Clover2_HpGeCrystal_D	0.42239	-1.8097
Clover3_HpGeCrystal_A	0.38918	-1.62867
Clover3_HpGeCrystal_B	insufficient data	insufficient data
Clover3_HpGeCrystal_C	0.46231	-1.47148
Clover3_HpGeCrystal_D	0.39428	-1.63946
Clover4_HpGeCrystal_A	0.39203	-1.61165
Clover4_HpGeCrystal_B	0.39505	-1.47363
Clover4_HpGeCrystal_C	0.66803	-1.19519
Clover4_HpGeCrystal_D	0.37477	-0.76558

Energy calibration details for each high purity germanium crystals of last four clover detectors are given in table B.2.

Table B.2: The energy calibration curve details for each high purity germanium crystals for remaining four clover detectors

Crystal	Slope	Intercept
Clover5_HpGeCrystal_A	0.36778	-1.5564
Clover5_HpGeCrystal_B	0.37212	-1.14521
Clover5_HpGeCrystal_C	0.35864	-1.07525
Clover5_HpGeCrystal_D	0.36635	-1.60916
Clover6_HpGeCrystal_A	0.56715	-1.34462
Clover6_HpGeCrystal_B	0.56667	-1.92714
Clover6_HpGeCrystal_C	0.5468	-1.58229
Clover6_HpGeCrystal_D	0.57148	-2.80283
Clover7_HpGeCrystal_A	0.56878	-2.76433
Clover7_HpGeCrystal_B	0.53932	-1.69768
Clover7_HpGeCrystal_C	0.36144	-1.58643
Clover7_HpGeCrystal_D	0.52747	-3.16963
Clover8_HpGeCrystal_A	0.37258	-1.48711
Clover8_HpGeCrystal_B	0.38188	-1.77789
Clover8_HpGeCrystal_C	0.5929	-1.03273
Clover8_HpGeCrystal_D	0.36868	-0.8365

B.2 Experimental absolute detector efficiency results

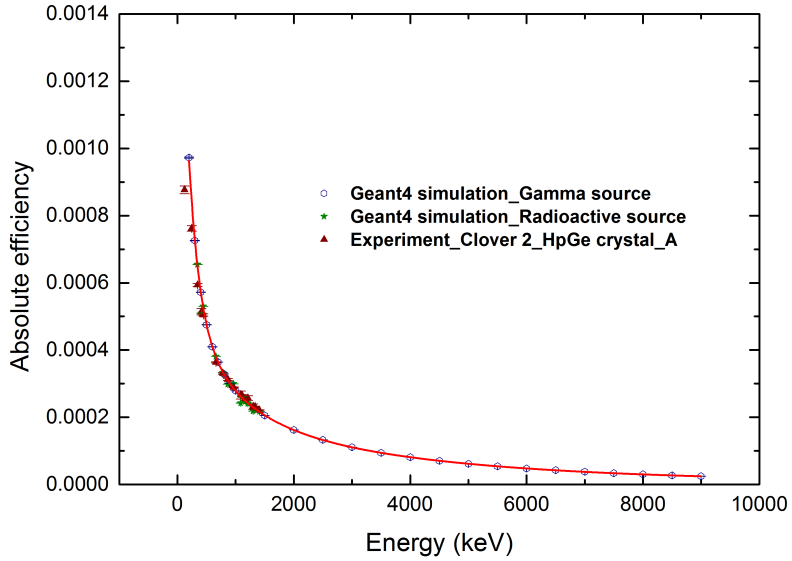

Figure B.1: The absolute efficiency response curve for crystal A in a clover 2. The red triangle points are experimentally measured absolute detector efficiencies the blue hollow circle points and green star points are simulated efficiencies using single-energy gamma sources and standard gamma emitting sources, respectively. Solid line is the third-order exponential fit.

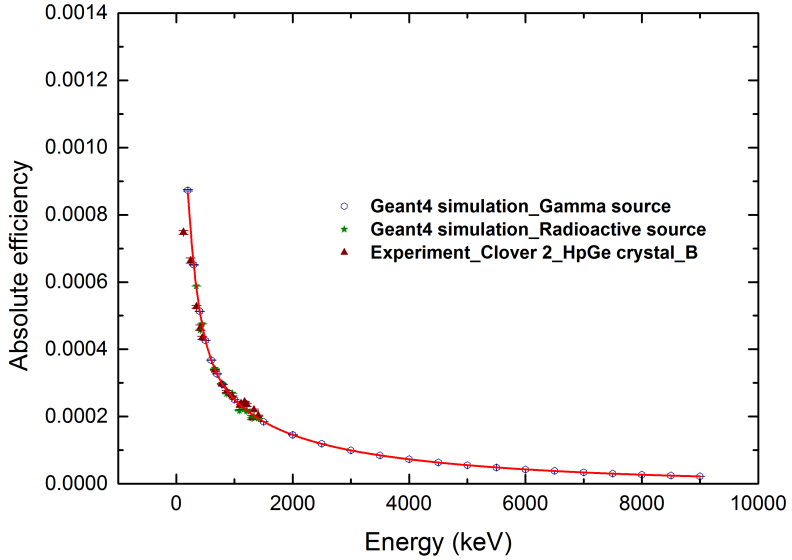

Figure B.2: The absolute efficiency response curve for crystal B in a clover 2. The red triangle points are experimentally measured absolute detector efficiencies the blue hollow circle points and green star points are simulated efficiencies using single-energy gamma sources and standard gamma emitting sources, respectively. Solid line is the third-order exponential fit.

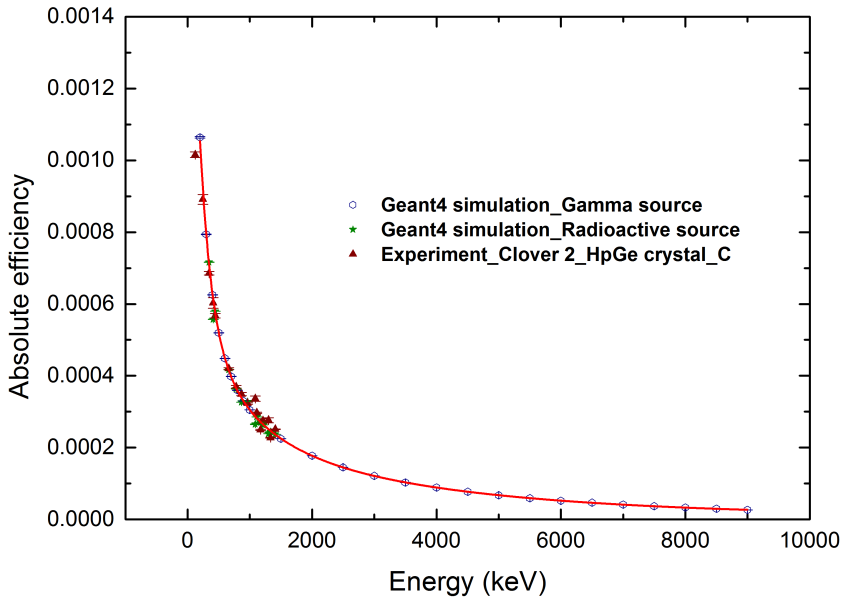

Figure B.3: The absolute efficiency response curve for crystal C in a clover 2. The red triangle points are experimentally measured absolute detector efficiencies the blue hollow circle points and green star points are simulated efficiencies using single-energy gamma sources and standard gamma emitting sources, respectively. Solid line is the third-order exponential fit.

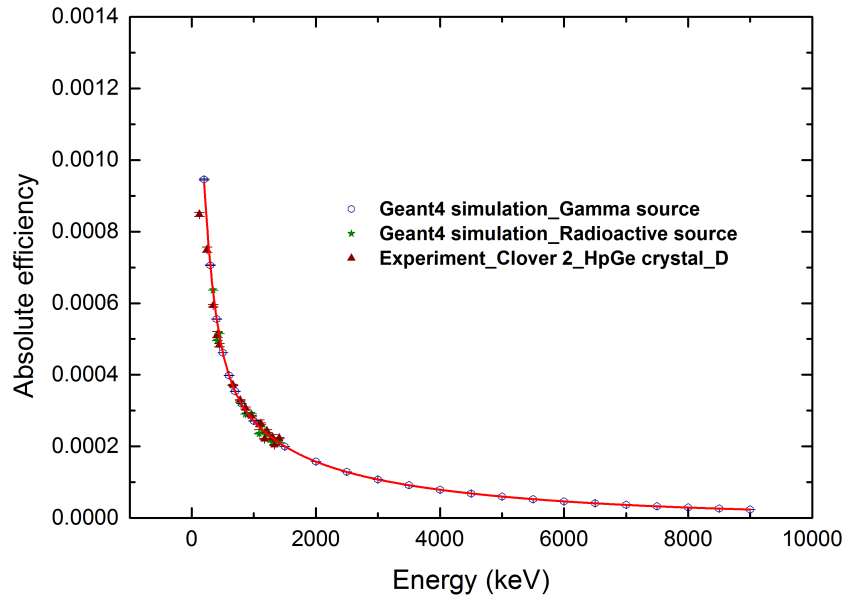

Figure B.4: The absolute efficiency response curve for crystal D in a clover 2. The red triangle points are experimentally measured absolute detector efficiencies the blue hollow circle points and green star points are simulated efficiencies using single-energy gamma sources and standard gamma emitting sources, respectively. Solid line is the third-order exponential fit.

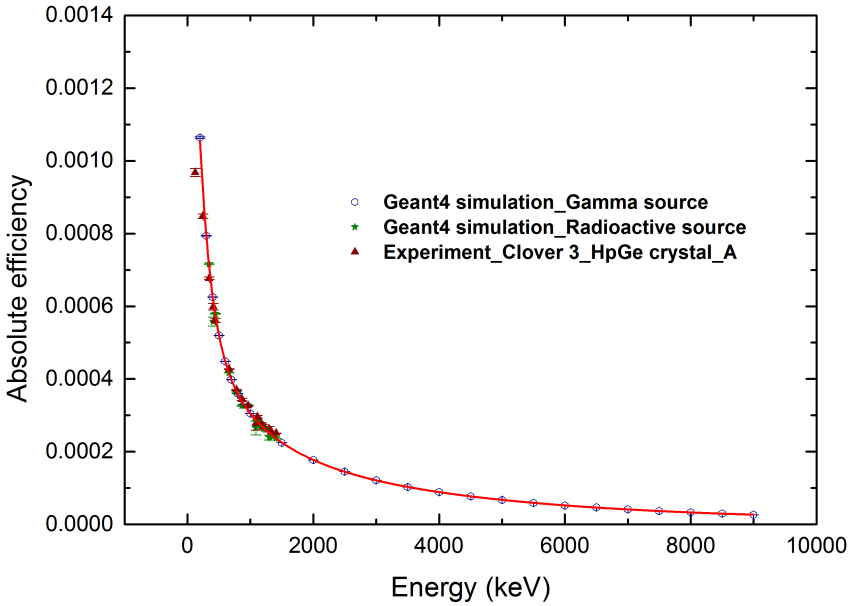

Figure B.5: The absolute efficiency response curve for crystal A in a clover 3. The red triangle points are experimentally measured absolute detector efficiencies the blue hollow circle points and green star points are simulated efficiencies using single-energy gamma sources and standard gamma emitting sources, respectively. Solid line is the third-order exponential fit.

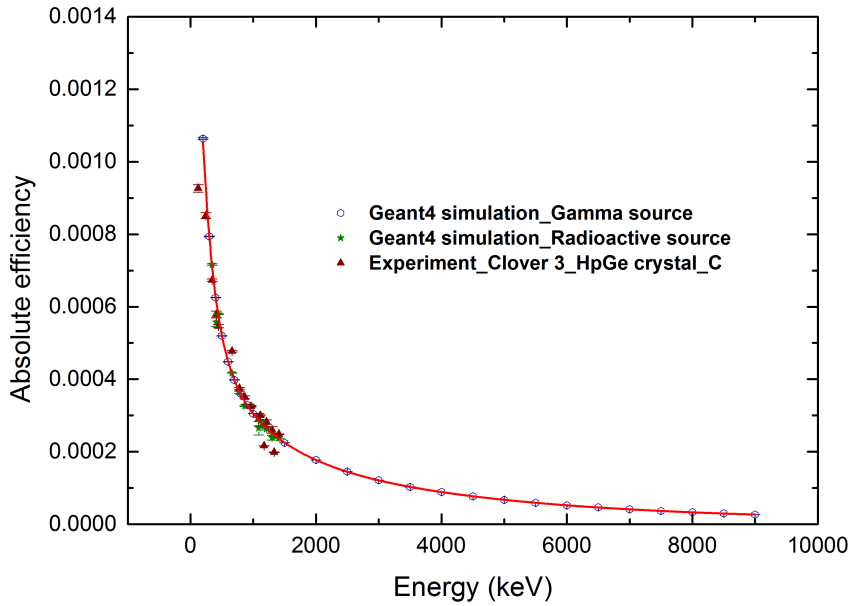

Figure B.6: The absolute efficiency response curve for crystal C in a clover 3. The red triangle points are experimentally measured absolute detector efficiencies the blue hollow circle points and green star points are simulated efficiencies using single-energy gamma sources and standard gamma emitting sources, respectively. Solid line is the third-order exponential fit.

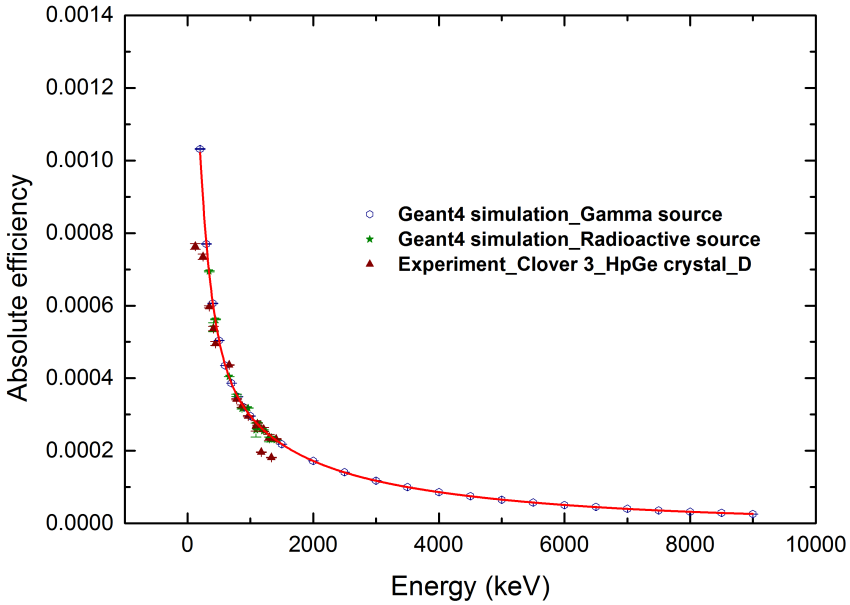

Figure B.7: The absolute efficiency response curve for crystal D in a clover 3. The red triangle points are experimentally measured absolute detector efficiencies the blue hollow circle points and green star points are simulated efficiencies using single-energy gamma sources and standard gamma emitting sources, respectively. Solid line is the third-order exponential fit.

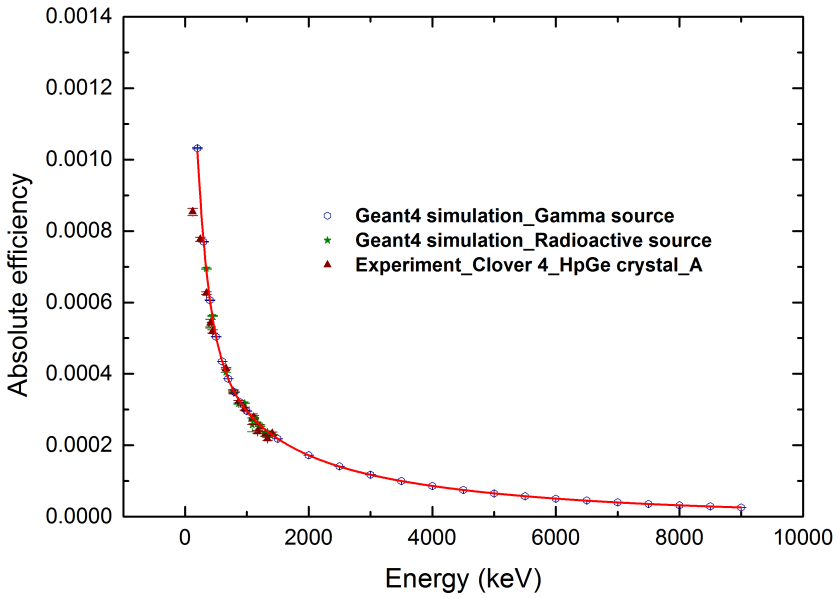

Figure B.8: The absolute efficiency response curve for crystal A in a clover 4. The red triangle points are experimentally measured absolute detector efficiencies the blue hollow circle points and green star points are simulated efficiencies using single-energy gamma sources and standard gamma emitting sources, respectively. Solid line is the third-order exponential fit.

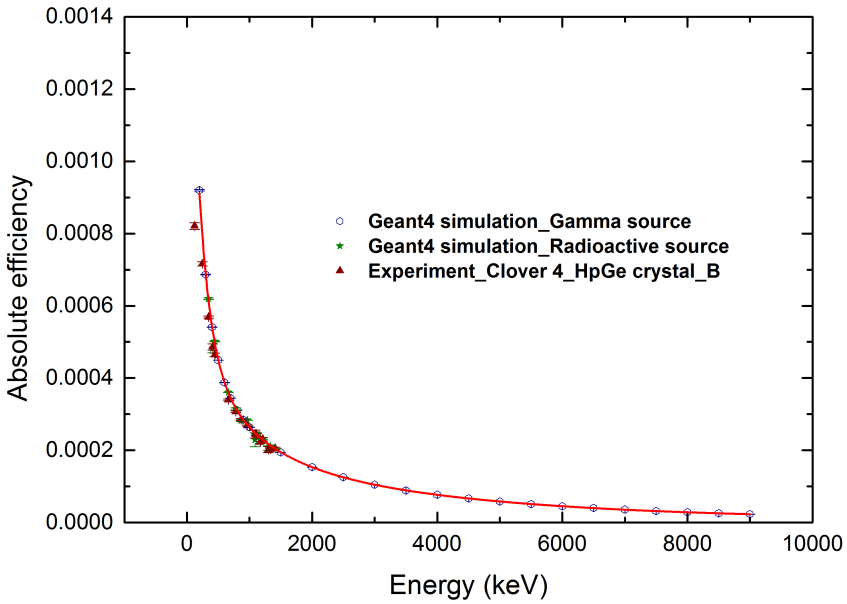

Figure B.9: The absolute efficiency response curve for crystal B in a clover 4. The red triangle points are experimentally measured absolute detector efficiencies the blue hollow circle points and green star points are simulated efficiencies using single-energy gamma sources and standard gamma emitting sources, respectively. Solid line is the third-order exponential fit.

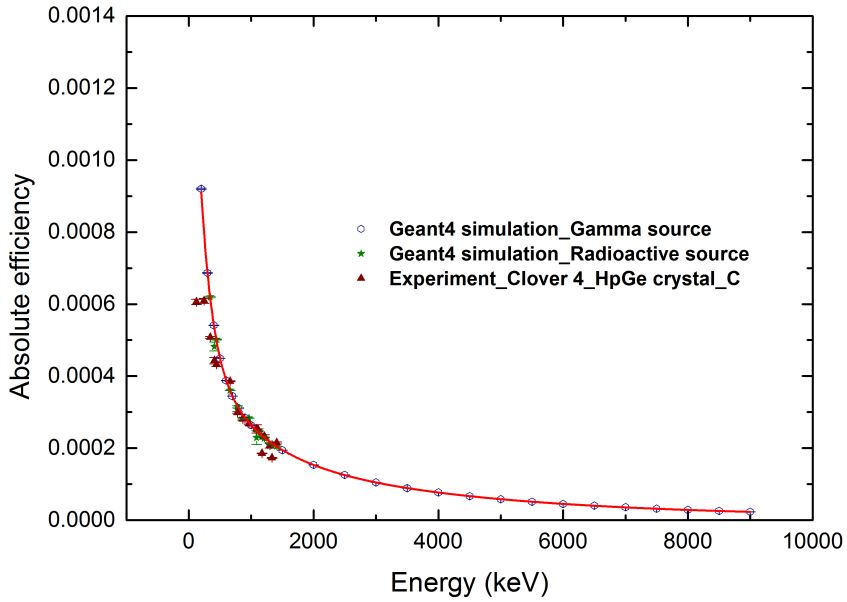

Figure B.10: The absolute efficiency response curve for crystal C in a clover 4. The red triangle points are experimentally measured absolute detector efficiencies the blue hollow circle points and green star points are simulated efficiencies using single-energy gamma sources and standard gamma emitting sources, respectively. Solid line is the third-order exponential fit.

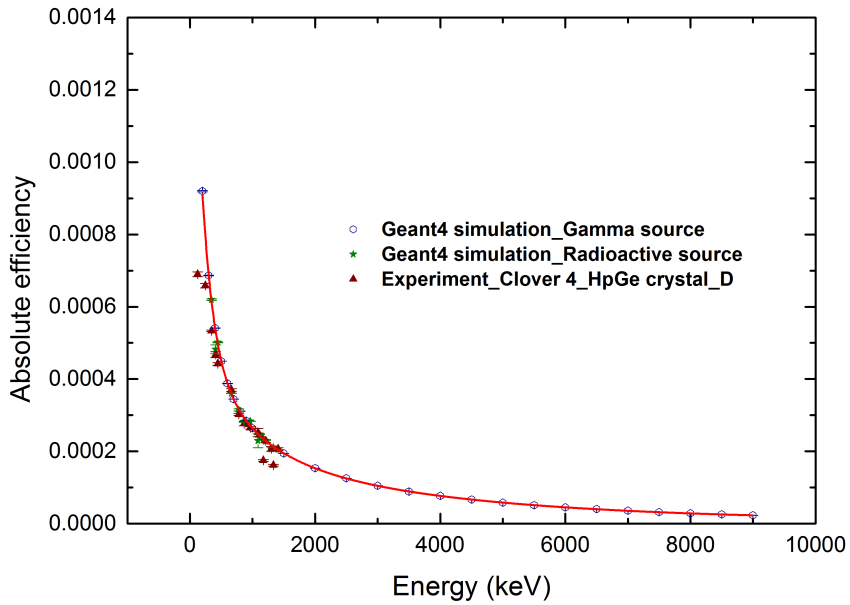

Figure B.11: The absolute efficiency response curve for crystal D in a clover 4. The red triangle points are experimentally measured absolute detector efficiencies the blue hollow circle points and green star points are simulated efficiencies using single-energy gamma sources and standard gamma emitting sources, respectively. Solid line is the third-order exponential fit.

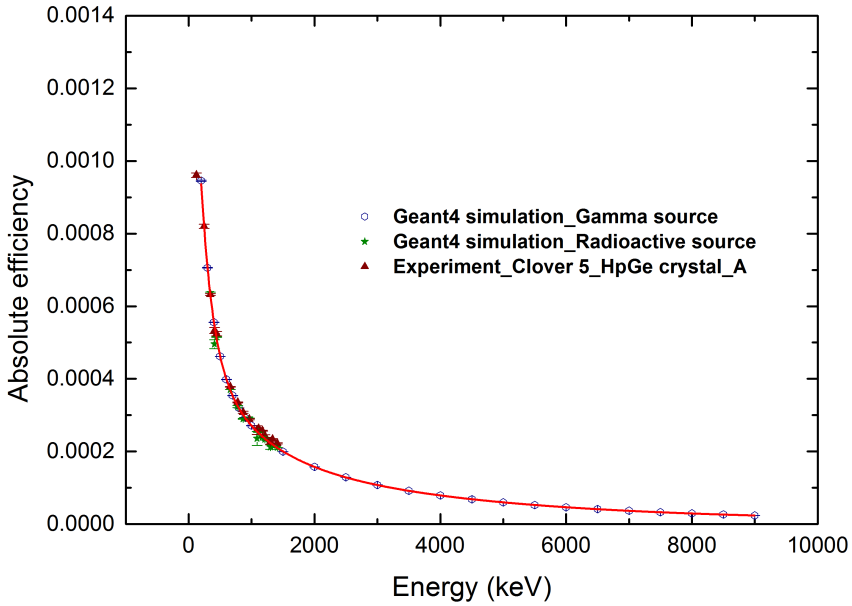

Figure B.12: The absolute efficiency response curve for crystal A in a clover 5. The red triangle points are experimentally measured absolute detector efficiencies the blue hollow circle points and green star points are simulated efficiencies using single-energy gamma sources and standard gamma emitting sources, respectively. Solid line is the third-order exponential fit.

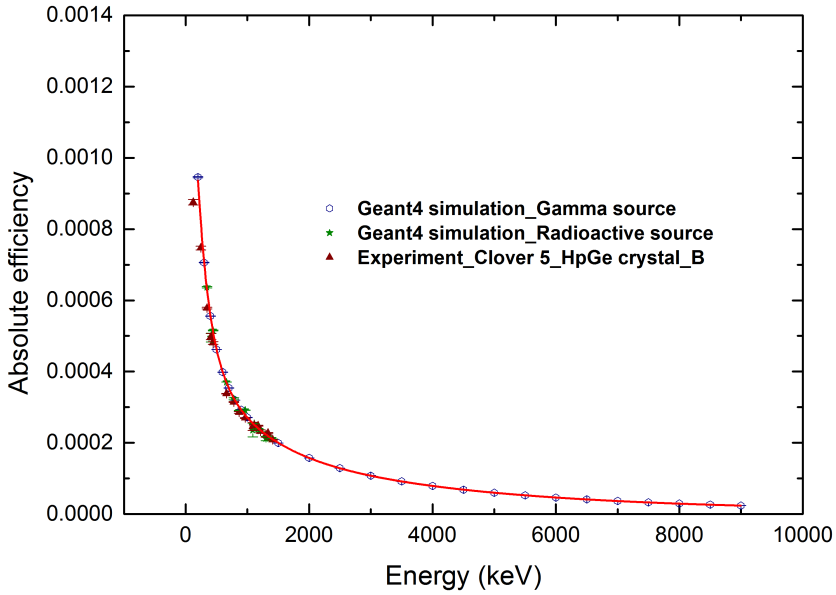

Figure B.13: The absolute efficiency response curve for crystal B in a clover 5. The red triangle points are experimentally measured absolute detector efficiencies the blue hollow circle points and green star points are simulated efficiencies using single-energy gamma sources and standard gamma emitting sources, respectively. Solid line is the third-order exponential fit.

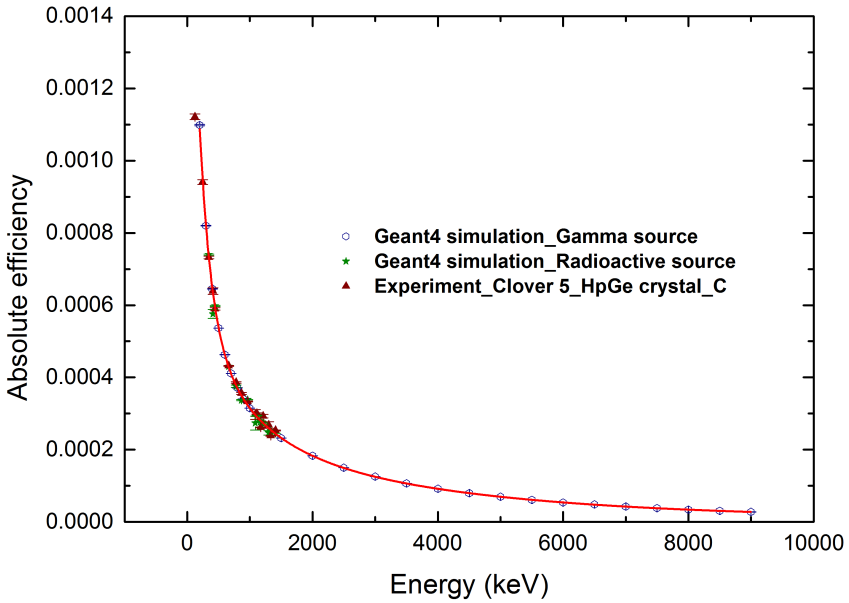

Figure B.14: The absolute efficiency response curve for crystal C in a clover 5. The red triangle points are experimentally measured absolute detector efficiencies the blue hollow circle points and green star points are simulated efficiencies using single-energy gamma sources and standard gamma emitting sources, respectively. Solid line is the third-order exponential fit.

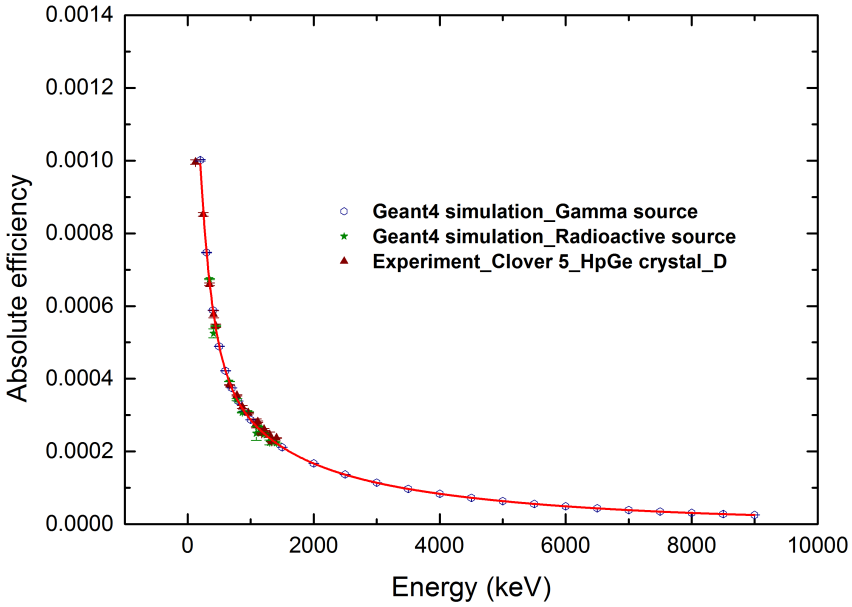

Figure B.15: The absolute efficiency response curve for crystal D in a clover 5. The red triangle points are experimentally measured absolute detector efficiencies the blue hollow circle points and green star points are simulated efficiencies using single-energy gamma sources and standard gamma emitting sources, respectively. Solid line is the third-order exponential fit.

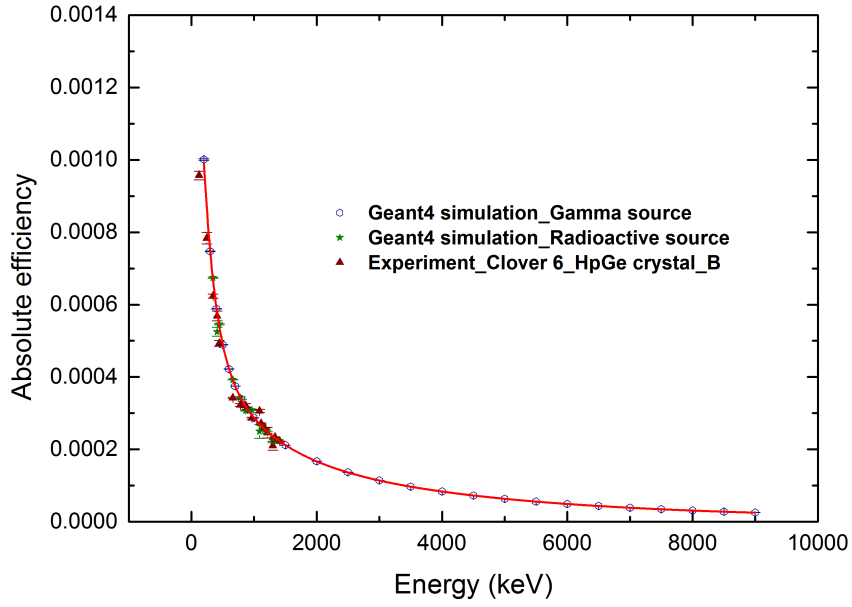

Figure B.16: The absolute efficiency response curve for crystal B in a clover 6. The red triangle points are experimentally measured absolute detector efficiencies the blue hollow circle points and green star points are simulated efficiencies using single-energy gamma sources and standard gamma emitting sources, respectively. Solid line is the third-order exponential fit.

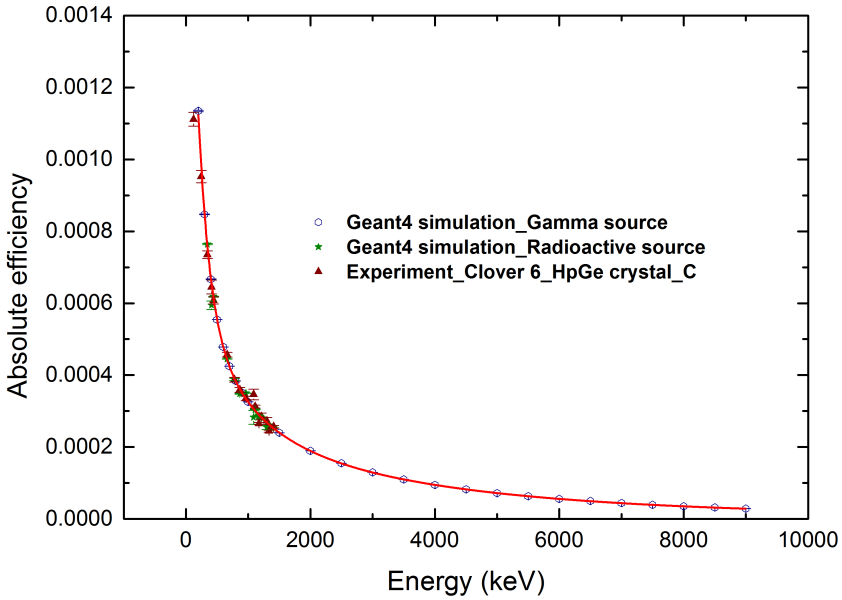

Figure B.17: The absolute efficiency response curve for crystal C in a clover 6. The red triangle points are experimentally measured absolute detector efficiencies the blue hollow circle points and green star points are simulated efficiencies using single-energy gamma sources and standard gamma emitting sources, respectively. Solid line is the third-order exponential fit.

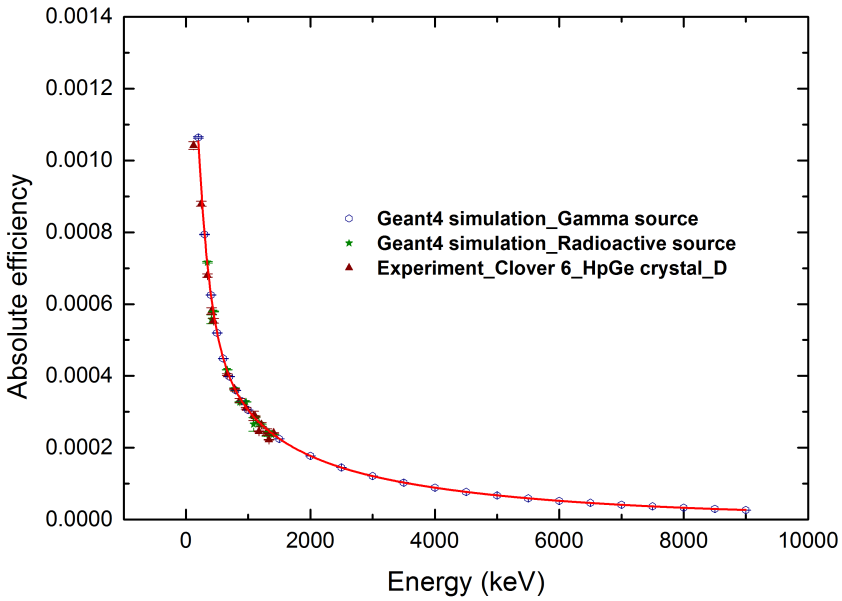

Figure B.18: The absolute efficiency response curve for crystal D in a clover 6. The red triangle points are experimentally measured absolute detector efficiencies the blue hollow circle points and green star points are simulated efficiencies using single-energy gamma sources and standard gamma emitting sources, respectively. Solid line is the third-order exponential fit.

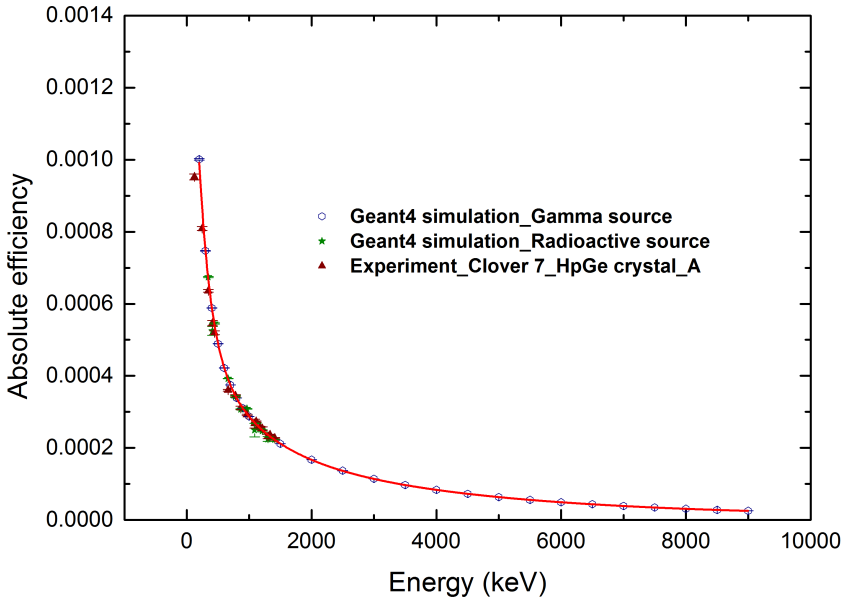

Figure B.19: The absolute efficiency response curve for crystal A in a clover 7. The red triangle points are experimentally measured absolute detector efficiencies the blue hollow circle points and green star points are simulated efficiencies using single-energy gamma sources and standard gamma emitting sources, respectively. Solid line is the third-order exponential fit.

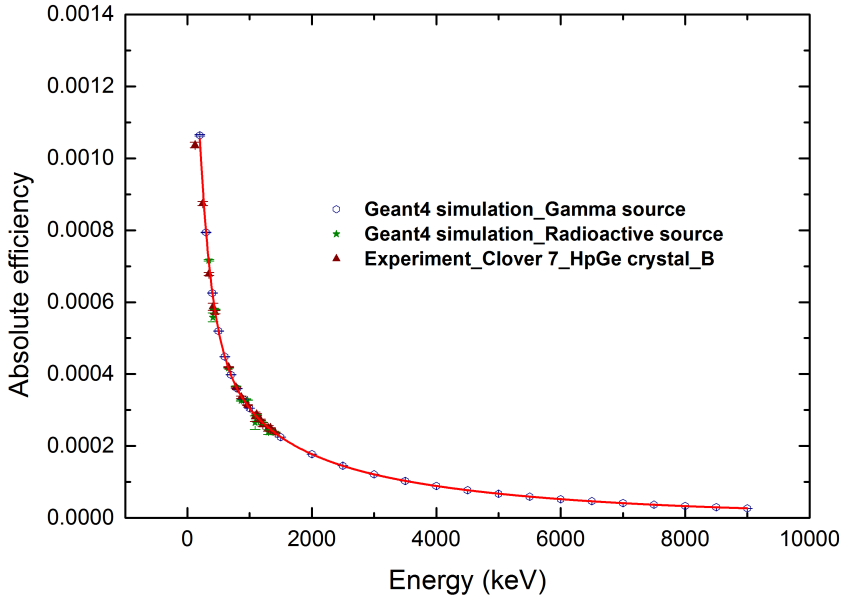

Figure B.20: The absolute efficiency response curve for crystal B in a clover 7. The red triangle points are experimentally measured absolute detector efficiencies the blue hollow circle points and green star points are simulated efficiencies using single-energy gamma sources and standard gamma emitting sources, respectively. Solid line is the third-order exponential fit.

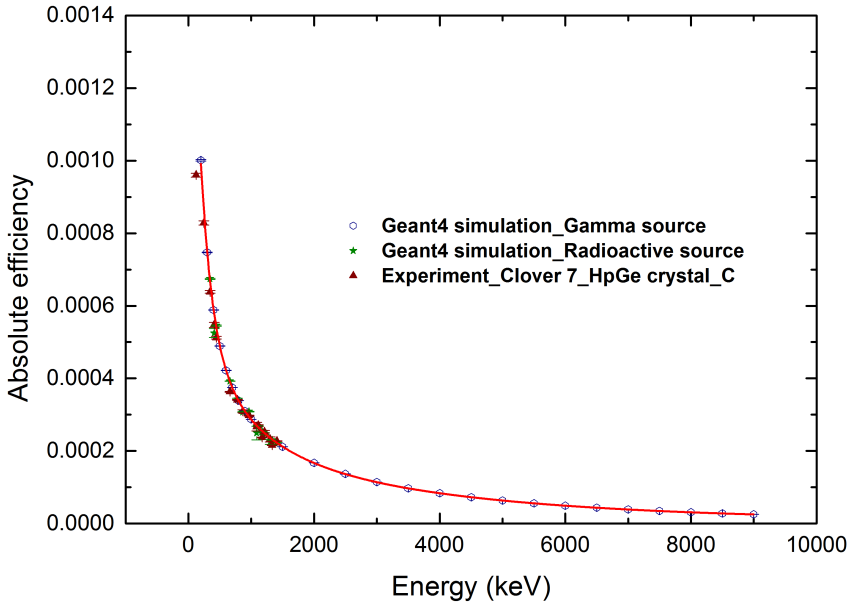

Figure B.21: The absolute efficiency response curve for crystal C in a clover 7. The red triangle points are experimentally measured absolute detector efficiencies the blue hollow circle points and green star points are simulated efficiencies using single-energy gamma sources and standard gamma emitting sources, respectively. Solid line is the third-order exponential fit.

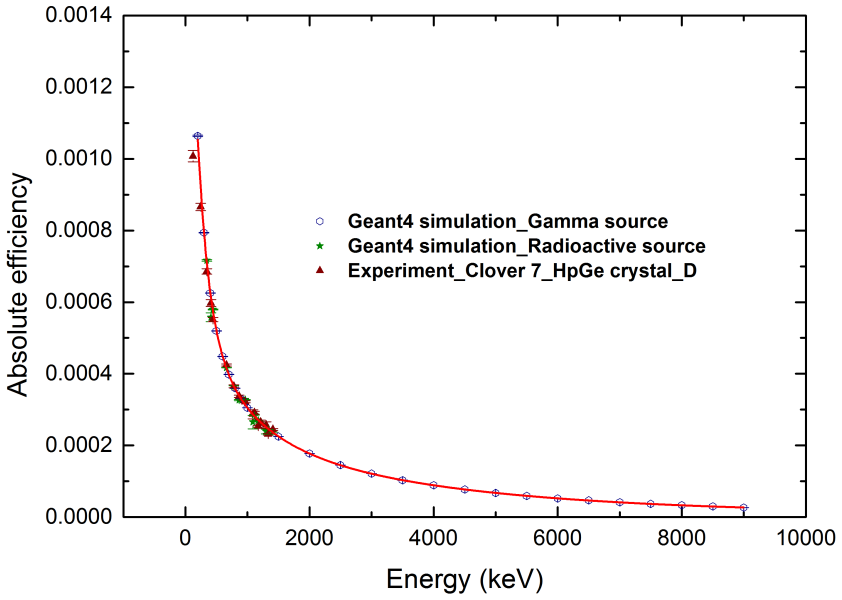

Figure B.22: The absolute efficiency response curve for crystal D in a clover 7. The red triangle points are experimentally measured absolute detector efficiencies the blue hollow circle points and green star points are simulated efficiencies using single-energy gamma sources and standard gamma emitting sources, respectively. Solid line is the third-order exponential fit.

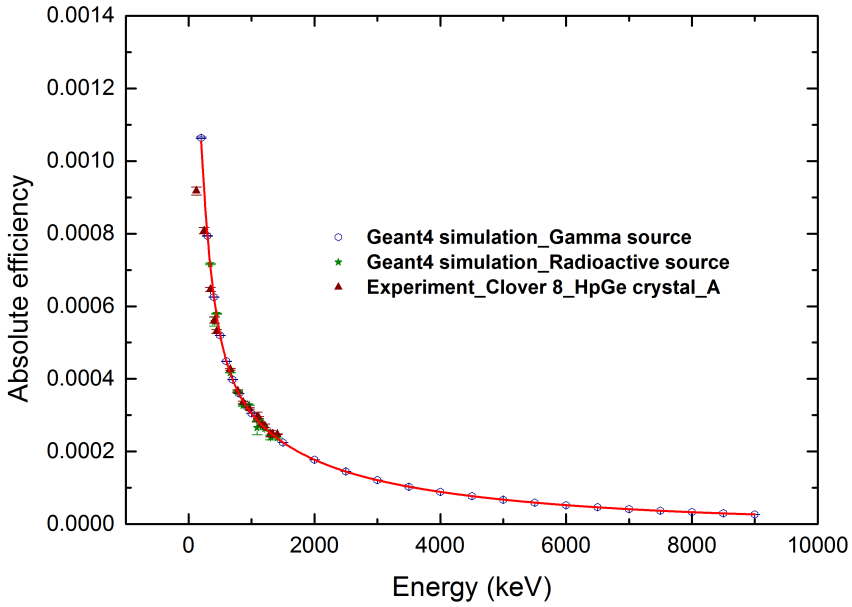

Figure B.23: The absolute efficiency response curve for crystal A in a clover 8. The red triangle points are experimentally measured absolute detector efficiencies the blue hollow circle points and green star points are simulated efficiencies using single-energy gamma sources and standard gamma emitting sources, respectively. Solid line is the third-order exponential fit.

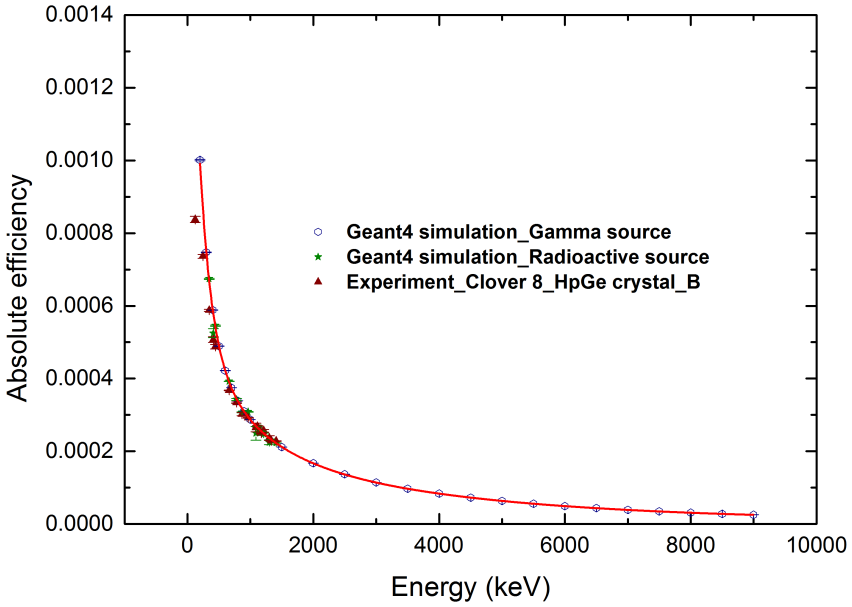

Figure B.24: The absolute efficiency response curve for crystal B in a clover 8. The red triangle points are experimentally measured absolute detector efficiencies the blue hollow circle points and green star points are simulated efficiencies using single-energy gamma sources and standard gamma emitting sources, respectively. Solid line is the third-order exponential fit.

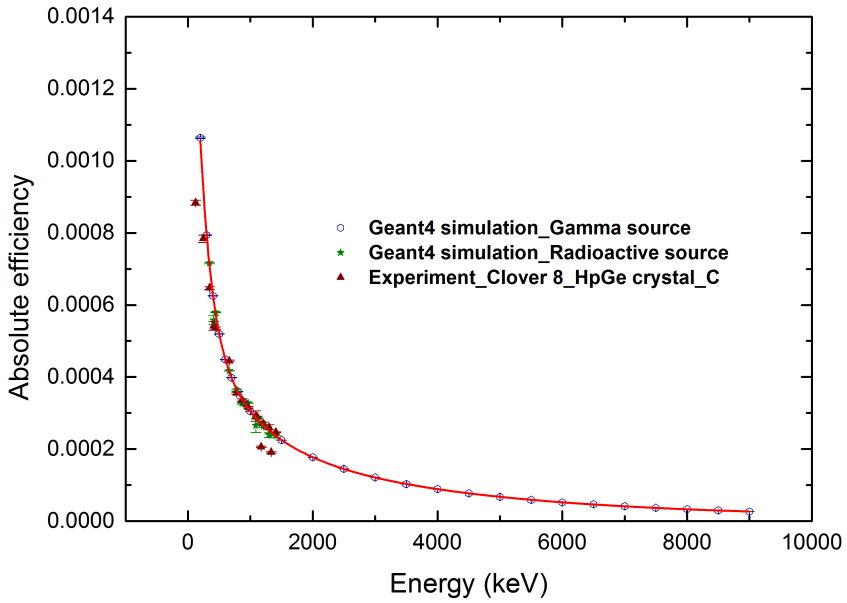

Figure B.25: The absolute efficiency response curve for crystal C in a clover 8. The red triangle points are experimentally measured absolute detector efficiencies the blue hollow circle points and green star points are simulated efficiencies using single-energy gamma sources and standard gamma emitting sources, respectively. Solid line is the third-order exponential fit.

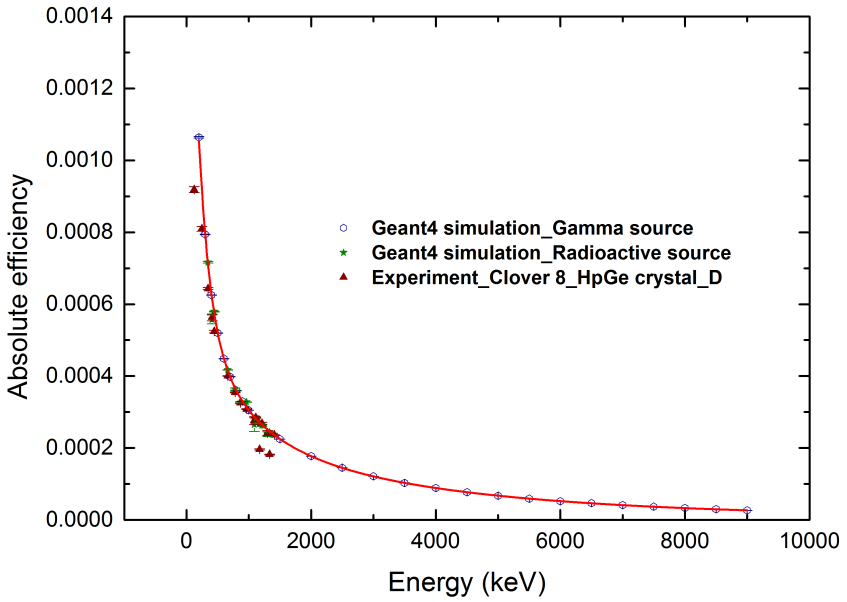

Figure B.26: The absolute efficiency response curve for crystal D in a clover 8. The red triangle points are experimentally measured absolute detector efficiencies the blue hollow circle points and green star points are simulated efficiencies using single-energy gamma sources and standard gamma emitting sources, respectively. Solid line is the third-order exponential fit.

Table B.3: Absolute detector efficiency for the 4.438 MeV energy for each high purity germanium crystals with associated uncertainty

Crystal	Angle (Degree)	$\epsilon_{4.438}$	U($\epsilon_{4.438}$)
C1_HpGe_A	130	6.80×10^{-05}	1.97×10^{-06}
C1_HpGe_B	130	7.62×10^{-05}	2.21×10^{-06}
C1_HpGe_C	140	8.11×10^{-05}	2.35×10^{-06}
C1_HpGe_D	140	9.31×10^{-05}	2.70×10^{-06}
C2_HpGe_A	90	7.19×10^{-05}	2.08×10^{-06}
C2_HpGe_B	90	6.45×10^{-05}	1.87×10^{-06}
C2_HpGe_C	90	7.86×10^{-05}	2.28×10^{-06}
C2_HpGe_D	90	6.99×10^{-05}	2.03×10^{-06}
C3_HpGe_A	90	7.86×10^{-05}	2.28×10^{-06}
C3_HpGe_B	90	insufficient data	insufficient data
C3_HpGe_C	90	7.86×10^{-05}	2.28×10^{-06}
C3_HpGe_D	90	7.62×10^{-05}	2.21×10^{-06}
C4_HpGe_A	90	7.62×10^{-05}	2.21×10^{-06}
C4_HpGe_B	90	6.80×10^{-05}	1.97×10^{-06}
C4_HpGe_C	90	6.80×10^{-05}	1.97×10^{-06}
C4_HpGe_D	90	6.80×10^{-05}	1.97×10^{-06}
C5_HpGe_A	130	6.99×10^{-05}	2.03×10^{-06}
C5_HpGe_B	130	6.99×10^{-05}	2.03×10^{-06}
C5_HpGe_C	140	8.11×10^{-05}	2.35×10^{-06}
C5_HpGe_D	140	7.40×10^{-05}	2.15×10^{-06}
C6_HpGe_A	130	not functioning	not functioning
C6_HpGe_B	130	7.40×10^{-05}	2.15×10^{-06}
C6_HpGe_C	140	8.38×10^{-05}	2.43×10^{-06}
C6_HpGe_D	140	7.86×10^{-05}	2.28×10^{-06}
C7_HpGe_A	130	7.40×10^{-05}	2.15×10^{-06}
C7_HpGe_B	130	7.86×10^{-05}	2.28×10^{-06}
C7_HpGe_C	140	7.40×10^{-05}	2.15×10^{-06}
C7_HpGe_D	140	7.86×10^{-05}	2.28×10^{-06}
C8_HpGe_A	90	7.86×10^{-05}	2.28×10^{-06}
C8_HpGe_B	90	7.40×10^{-05}	2.15×10^{-06}
C8_HpGe_C	90	7.86×10^{-05}	2.28×10^{-06}
C8_HpGe_D	90	7.86×10^{-05}	2.28×10^{-06}

Table B.4: Absolute detector efficiency for the 6.129 MeV energy for each high purity germanium crystals with associated uncertainty

Crystal	Angle (Degree)	$\epsilon_{6.129}$	U($\epsilon_{6.129}$)
C1_HpGe_A	130	4.39×10^{-05}	1.54×10^{-06}
C1_HpGe_B	130	4.92×10^{-05}	1.72×10^{-06}
C1_HpGe_C	140	5.24×10^{-05}	1.83×10^{-06}
C1_HpGe_D	140	6.02×10^{-05}	2.11×10^{-06}
C2_HpGe_A	90	4.64×10^{-05}	1.63×10^{-06}
C2_HpGe_B	90	4.16×10^{-05}	1.46×10^{-06}
C2_HpGe_C	90	5.08×10^{-05}	1.78×10^{-06}
C2_HpGe_D	90	4.51×10^{-05}	1.58×10^{-06}
C3_HpGe_A	90	5.08×10^{-05}	1.78×10^{-06}
C3_HpGe_B	90	insufficient data	insufficient data
C3_HpGe_C	90	5.08×10^{-05}	1.78×10^{-06}
C3_HpGe_D	90	4.92×10^{-05}	1.72×10^{-06}
C4_HpGe_A	90	4.92×10^{-05}	1.72×10^{-06}
C4_HpGe_B	90	4.39×10^{-05}	1.54×10^{-06}
C4_HpGe_C	90	4.39×-05	1.54×10^{-06}
C4_HpGe_D	90	4.39×10^{-05}	1.54×10^{-06}
C5_HpGe_A	130	4.51×10^{-05}	1.58×10^{-06}
C5_HpGe_B	130	4.51×10^{-05}	1.58×10^{-06}
C5_HpGe_C	140	5.24×10^{-05}	1.83×10^{-06}
C5_HpGe_D	140	4.78×10^{-05}	1.67×10^{-06}
C6_HpGe_A	130	not functioning	not functioning
C6_HpGe_B	130	4.78×10^{-05}	1.67×10^{-06}
C6_HpGe_C	140	5.41×10^{-05}	1.90×10^{-06}
C6_HpGe_D	140	5.08×10^{-05}	1.78×10^{-06}
C7_HpGe_A	130	4.78×10^{-05}	1.67×10^{-06}
C7_HpGe_B	130	5.08×10^{-05}	1.78×10^{-06}
C7_HpGe_C	140	4.78×10^{-05}	1.67×10^{-06}
C7_HpGe_D	140	5.08×10^{-05}	1.78×10^{-06}
C8_HpGe_A	90	5.08×10^{-05}	1.78×10^{-06}
C8_HpGe_B	90	4.78×10^{-05}	1.67×10^{-06}
C8_HpGe_C	90	5.08×10^{-05}	1.78×10^{-06}
C8_HpGe_D	90	5.08×10^{-05}	1.78×10^{-06}

Table B.5: Measured differential cross-section values(4.438 MeV) for each high purity germanium crystals for the 66 MeV proton collision on natural carbon target

Crystal	Angle (Degree)	$\frac{d\sigma}{d\Omega}$ (mb)	U($\frac{d\sigma}{d\Omega}$) (mb)
C1_HpGe_A	130	1.039	0.061
C1_HpGe_B	130	2.197	0.129
C1_HpGe_C	140	2.074	0.122
C1_HpGe_D	140	1.950	0.115
C2_HpGe_A	90	1.820	0.107
C2_HpGe_B	90	2.149	0.127
C2_HpGe_C	90	1.972	0.116
C2_HpGe_D	90	1.786	0.105
C3_HpGe_A	90	2.179	0.128
C3_HpGe_B	90	insufficient data	insufficient data
C3_HpGe_C	90	1.896	0.112
C3_HpGe_D	90	2.007	0.118
C4_HpGe_A	90	2.315	0.136
C4_HpGe_B	90	1.958	0.115
C4_HpGe_C	90	1.834	0.108
C4_HpGe_D	90	1.737	0.102
C5_HpGe_A	130	2.016	0.119
C5_HpGe_B	130	2.075	0.122
C5_HpGe_C	140	2.044	0.121
C5_HpGe_D	140	2.167	0.128
C6_HpGe_A	130	not functioning	not functioning
C6_HpGe_B	130	2.034	0.120
C6_HpGe_C	140	1.884	0.111
C6_HpGe_D	140	1.927	0.114
C7_HpGe_A	130	2.045	0.121
C7_HpGe_B	130	1.825	0.108
C7_HpGe_C	140	1.943	0.115
C7_HpGe_D	140	1.976	0.117
C8_HpGe_A	90	2.119	0.125
C8_HpGe_B	90	2.316	0.136
C8_HpGe_C	90	1.826	0.107
C8_HpGe_D	90	1.889	0.111

Table B.6: Measured differential cross-section values(4.438 MeV) for each high purity germanium crystals for the 80 MeV proton collision on natural carbon target

Crystal	Angle (Degree)	$\frac{d\sigma}{d\Omega}$ (mb)	U($\frac{d\sigma}{d\Omega}$) (mb)
C1_HpGe_A	130	0.916	0.054
C1_HpGe_B	130	1.468	0.087
C1_HpGe_C	140	1.688	0.100
C1_HpGe_D	140	1.426	0.084
C2_HpGe_A	90	1.770	0.104
C2_HpGe_B	90	1.796	0.106
C2_HpGe_C	90	1.546	0.091
C2_HpGe_D	90	1.662	0.098
C3_HpGe_A	90	1.513	0.089
C3_HpGe_B	90	insufficient data	insufficient data
C3_HpGe_C	90	1.551	0.092
C3_HpGe_D	90	1.531	0.090
C4_HpGe_A	90	1.867	0.110
C4_HpGe_B	90	1.668	0.098
C4_HpGe_C	90	1.725	0.101
C4_HpGe_D	90	1.560	0.092
C5_HpGe_A	130	1.599	0.094
C5_HpGe_B	130	1.443	0.086
C5_HpGe_C	140	1.697	0.100
C5_HpGe_D	140	1.592	0.094
C6_HpGe_A	130	not functioning	not functioning
C6_HpGe_B	130	1.569	0.093
C6_HpGe_C	140	1.439	0.085
C6_HpGe_D	140	1.224	0.073
C7_HpGe_A	130	1.623	0.096
C7_HpGe_B	130	1.429	0.085
C7_HpGe_C	140	1.697	0.100
C7_HpGe_D	140	1.503	0.089
C8_HpGe_A	90	1.573	0.093
C8_HpGe_B	90	1.538	0.091
C8_HpGe_C	90	1.193	0.071
C8_HpGe_D	90	1.366	0.081

Table B.7: Measured differential cross-section values(4.438 MeV) for each high purity germanium crystals for the 95 MeV proton collision on natural carbon target

Crystal	Angle (Degree)	$\frac{d\sigma}{d\Omega}$ (mb)	U($\frac{d\sigma}{d\Omega}$) (mb)
C1_HpGe_A	130	0.636	0.038
C1_HpGe_B	130	1.117	0.066
C1_HpGe_C	140	1.134	0.067
C1_HpGe_D	140	1.038	0.061
C2_HpGe_A	90	1.024	0.061
C2_HpGe_B	90	1.076	0.064
C2_HpGe_C	90	1.482	0.087
C2_HpGe_D	90	1.215	0.072
C3_HpGe_A	90	1.180	0.070
C3_HpGe_B	90	insufficient data	insufficient data
C3_HpGe_C	90	1.290	0.076
C3_HpGe_D	90	1.377	0.081
C4_HpGe_A	90	1.208	0.071
C4_HpGe_B	90	1.453	0.085
C4_HpGe_C	90	1.110	0.065
C4_HpGe_D	90	0.966	0.057
C5_HpGe_A	130	1.125	0.066
C5_HpGe_B	130	0.960	0.057
C5_HpGe_C	140	1.153	0.068
C5_HpGe_D	140	1.365	0.080
C6_HpGe_A	130	not functioning	not functioning
C6_HpGe_B	130	1.094	0.065
C6_HpGe_C	140	1.005	0.060
C6_HpGe_D	140	0.787	0.048
C7_HpGe_A	130	0.959	0.057
C7_HpGe_B	130	1.023	0.061
C7_HpGe_C	140	1.111	0.066
C7_HpGe_D	140	1.057	0.063
C8_HpGe_A	90	1.167	0.069
C8_HpGe_B	90	1.182	0.070
C8_HpGe_C	90	0.985	0.058
C8_HpGe_D	90	0.746	0.044

Table B.8: Measured differential cross-section values(4.438 MeV) for each high purity germanium crystals for the 110 MeV proton collision on natural carbon target

Crystal	Angle (Degree)	$\frac{d\sigma}{d\Omega}$ (mb)	U($\frac{d\sigma}{d\Omega}$) (mb)
C1_HpGe_A	130	0.631	0.037
C1_HpGe_B	130	0.946	0.056
C1_HpGe_C	140	0.950	0.056
C1_HpGe_D	140	0.858	0.051
C2_HpGe_A	90	1.007	0.059
C2_HpGe_B	90	1.137	0.067
C2_HpGe_C	90	0.804	0.047
C2_HpGe_D	90	0.895	0.053
C3_HpGe_A	90	0.991	0.058
C3_HpGe_B	90	insufficient data	insufficient data
C3_HpGe_C	90	0.764	0.045
C3_HpGe_D	90	0.718	0.042
C4_HpGe_A	90	0.990	0.058
C4_HpGe_B	90	1.088	0.064
C4_HpGe_C	90	1.017	0.060
C4_HpGe_D	90	1.047	0.061
C5_HpGe_A	130	1.158	0.068
C5_HpGe_B	130	0.909	0.054
C5_HpGe_C	140	1.029	0.061
C5_HpGe_D	140	0.948	0.056
C6_HpGe_A	130	not functioning	not functioning
C6_HpGe_B	130	0.853	0.051
C6_HpGe_C	140	0.790	0.047
C6_HpGe_D	140	0.804	0.047
C7_HpGe_A	130	0.891	0.052
C7_HpGe_B	130	0.839	0.050
C7_HpGe_C	140	1.044	0.061
C7_HpGe_D	140	0.823	0.049
C8_HpGe_A	90	0.938	0.055
C8_HpGe_B	90	0.957	0.056
C8_HpGe_C	90	0.879	0.052
C8_HpGe_D	90	0.730	0.043

Table B.9: Measured differential cross-section values(4.438 MeV) for each high purity germanium crystals for the 125 MeV proton collision on natural carbon target

Crystal	Angle (Degree)	$\frac{d\sigma}{d\Omega}$ (mb)	U($\frac{d\sigma}{d\Omega}$) (mb)
C1_HpGe_A	130	0.525	0.040
C1_HpGe_B	130	0.904	0.043
C1_HpGe_C	140	0.703	0.039
C1_HpGe_D	140	0.821	0.042
C2_HpGe_A	90	0.770	0.039
C2_HpGe_B	90	0.892	0.039
C2_HpGe_C	90	0.992	0.037
C2_HpGe_D	90	0.908	0.038
C3_HpGe_A	90	1.234	0.040
C3_HpGe_B	90	insufficient data	insufficient data
C3_HpGe_C	90	1.084	0.039
C3_HpGe_D	90	1.083	0.038
C4_HpGe_A	90	0.927	0.035
C4_HpGe_B	90	0.905	0.035
C4_HpGe_C	90	0.771	0.028
C4_HpGe_D	90	0.816	0.035
C5_HpGe_A	130	0.768	0.055
C5_HpGe_B	130	0.846	0.031
C5_HpGe_C	140	0.706	0.043
C5_HpGe_D	140	0.786	0.045
C6_HpGe_A	130	not functioning	not functioning
C6_HpGe_B	130	0.691	0.043
C6_HpGe_C	140	0.718	0.046
C6_HpGe_D	140	0.837	0.045
C7_HpGe_A	130	0.852	0.048
C7_HpGe_B	130	0.761	0.046
C7_HpGe_C	140	0.873	0.048
C7_HpGe_D	140	0.823	0.051
C8_HpGe_A	90	1.058	0.048
C8_HpGe_B	90	0.923	0.041
C8_HpGe_C	90	0.826	0.038
C8_HpGe_D	90	0.736	0.032

Table B.10: Measured differential cross-section values(4.438 MeV) for each high purity germanium crystals for the 66 MeV proton collision on mylar target

Crystal	Angle (Degree)	$\frac{d\sigma}{d\Omega}$ (mb)	U($\frac{d\sigma}{d\Omega}$) (mb)
C1_HpGe_A	130	1.335	0.080
C1_HpGe_B	130	2.335	0.139
C1_HpGe_C	140	2.071	0.124
C1_HpGe_D	140	2.310	0.137
C2_HpGe_A	90	2.543	0.151
C2_HpGe_B	90	2.500	0.148
C2_HpGe_C	90	2.442	0.145
C2_HpGe_D	90	1.766	0.105
C3_HpGe_A	90	1.943	0.116
C3_HpGe_B	90	insufficient data	insufficient data
C3_HpGe_C	90	1.717	0.102
C3_HpGe_D	90	2.163	0.128
C4_HpGe_A	90	1.986	0.118
C4_HpGe_B	90	1.883	0.112
C4_HpGe_C	90	2.243	0.133
C4_HpGe_D	90	1.815	0.108
C5_HpGe_A	130	2.190	0.130
C5_HpGe_B	130	2.021	0.120
C5_HpGe_C	140	2.071	0.123
C5_HpGe_D	140	2.305	0.138
C6_HpGe_A	130	not functioning	not functioning
C6_HpGe_B	130	1.834	0.109
C6_HpGe_C	140	1.872	0.112
C6_HpGe_D	140	2.061	0.124
C7_HpGe_A	130	1.976	0.117
C7_HpGe_B	130	2.135	0.127
C7_HpGe_C	140	1.766	0.105
C7_HpGe_D	140	1.631	0.097
C8_HpGe_A	90	1.713	0.102
C8_HpGe_B	90	2.055	0.122
C8_HpGe_C	90	1.949	0.115
C8_HpGe_D	90	1.829	0.109

Table B.11: Measured differential cross-section values(4.438 MeV) for each high purity germanium crystals for the 80 MeV proton collision on mylar target

Crystal	Angle (Degree)	$\frac{d\sigma}{d\Omega}$ (mb)	U($\frac{d\sigma}{d\Omega}$) (mb)
C1_HpGe_A	130	1.007	0.060
C1_HpGe_B	130	1.694	0.101
C1_HpGe_C	140	1.696	0.101
C1_HpGe_D	140	1.797	0.107
C2_HpGe_A	90	1.927	0.115
C2_HpGe_B	90	1.809	0.108
C2_HpGe_C	90	1.559	0.093
C2_HpGe_D	90	1.811	0.108
C3_HpGe_A	90	1.853	0.111
C3_HpGe_B	90	insufficient data	insufficient data
C3_HpGe_C	90	1.641	0.099
C3_HpGe_D	90	1.340	0.080
C4_HpGe_A	90	1.837	0.109
C4_HpGe_B	90	1.722	0.104
C4_HpGe_C	90	1.754	0.104
C4_HpGe_D	90	1.793	0.107
C5_HpGe_A	130	1.724	0.103
C5_HpGe_B	130	1.961	0.117
C5_HpGe_C	140	1.806	0.108
C5_HpGe_D	140	1.783	0.107
C6_HpGe_A	130	not functioning	not functioning
C6_HpGe_B	130	2.024	0.120
C6_HpGe_C	140	1.435	0.086
C6_HpGe_D	140	1.744	0.104
C7_HpGe_A	130	1.572	0.094
C7_HpGe_B	130	1.733	0.103
C7_HpGe_C	140	1.820	0.109
C7_HpGe_D	140	1.688	0.101
C8_HpGe_A	90	2.245	0.133
C8_HpGe_B	90	2.023	0.121
C8_HpGe_C	90	1.422	0.085
C8_HpGe_D	90	1.911	0.114

Table B.12: Measured differential cross-section values(4.438 MeV) for each high purity germanium crystals for the 95 MeV proton collision on mylar target

Crystal	Angle (Degree)	$\frac{d\sigma}{d\Omega}$ (mb)	U($\frac{d\sigma}{d\Omega}$) (mb)
C1_HpGe_A	130	0.813	0.048
C1_HpGe_B	130	1.426	0.085
C1_HpGe_C	140	1.233	0.074
C1_HpGe_D	140	1.203	0.072
C2_HpGe_A	90	1.346	0.080
C2_HpGe_B	90	1.475	0.088
C2_HpGe_C	90	1.085	0.065
C2_HpGe_D	90	1.133	0.068
C3_HpGe_A	90	1.316	0.079
C3_HpGe_B	90	insufficient data	insufficient data
C3_HpGe_C	90	1.262	0.076
C3_HpGe_D	90	1.014	0.061
C4_HpGe_A	90	1.640	0.097
C4_HpGe_B	90	1.682	0.100
C4_HpGe_C	90	1.139	0.068
C4_HpGe_D	90	1.257	0.075
C5_HpGe_A	130	1.177	0.070
C5_HpGe_B	130	1.253	0.075
C5_HpGe_C	140	1.317	0.079
C5_HpGe_D	140	1.363	0.082
C6_HpGe_A	130	not functioning	not functioning
C6_HpGe_B	130	1.020	0.062
C6_HpGe_C	140	0.928	0.057
C6_HpGe_D	140	0.929	0.056
C7_HpGe_A	130	1.240	0.074
C7_HpGe_B	130	1.166	0.069
C7_HpGe_C	140	1.244	0.074
C7_HpGe_D	140	1.190	0.071
C8_HpGe_A	90	1.234	0.074
C8_HpGe_B	90	1.648	0.098
C8_HpGe_C	90	1.067	0.064
C8_HpGe_D	90	0.944	0.056

Table B.13: Measured differential cross-section values(4.438 MeV) for each high purity germanium crystals for the 110 MeV proton collision on mylar target

Crystal	Angle (Degree)	$\frac{d\sigma}{d\Omega}$ (mb)	U($\frac{d\sigma}{d\Omega}$) (mb)
C1_HpGe_A	130	0.724	0.043
C1_HpGe_B	130	1.283	0.077
C1_HpGe_C	140	1.065	0.064
C1_HpGe_D	140	0.924	0.055
C2_HpGe_A	90	1.248	0.075
C2_HpGe_B	90	1.001	0.060
C2_HpGe_C	90	0.957	0.057
C2_HpGe_D	90	1.087	0.067
C3_HpGe_A	90	1.199	0.072
C3_HpGe_B	90	insufficient data	insufficient data
C3_HpGe_C	90	1.251	0.075
C3_HpGe_D	90	1.268	0.076
C4_HpGe_A	90	0.916	0.055
C4_HpGe_B	90	1.331	0.080
C4_HpGe_C	90	0.800	0.048
C4_HpGe_D	90	1.112	0.066
C5_HpGe_A	130	0.972	0.059
C5_HpGe_B	130	0.876	0.052
C5_HpGe_C	140	1.092	0.066
C5_HpGe_D	140	0.913	0.056
C6_HpGe_A	130	not functioning	not functioning
C6_HpGe_B	130	1.062	0.064
C6_HpGe_C	140	0.939	0.057
C6_HpGe_D	140	0.830	0.050
C7_HpGe_A	130	0.965	0.058
C7_HpGe_B	130	0.911	0.055
C7_HpGe_C	140	1.174	0.070
C7_HpGe_D	140	1.008	0.060
C8_HpGe_A	90	1.118	0.067
C8_HpGe_B	90	1.408	0.084
C8_HpGe_C	90	0.965	0.058
C8_HpGe_D	90	0.996	0.059

Table B.14: Measured differential cross-section values(4.438 MeV) for each high purity germanium crystals for the 125 MeV proton collision on mylar target

Crystal	Angle (Degree)	$\frac{d\sigma}{d\Omega}$ (mb)	U($\frac{d\sigma}{d\Omega}$) (mb)
C1_HpGe_A	130	0.496	0.030
C1_HpGe_B	130	1.009	0.060
C1_HpGe_C	140	0.909	0.055
C1_HpGe_D	140	1.021	0.061
C2_HpGe_A	90	0.756	0.046
C2_HpGe_B	90	1.125	0.067
C2_HpGe_C	90	0.879	0.053
C2_HpGe_D	90	1.033	0.062
C3_HpGe_A	90	1.300	0.078
C3_HpGe_B	90	insufficient data	insufficient data
C3_HpGe_C	90	1.108	0.067
C3_HpGe_D	90	0.995	0.060
C4_HpGe_A	90	0.755	0.046
C4_HpGe_B	90	1.082	0.065
C4_HpGe_C	90	0.941	0.056
C4_HpGe_D	90	0.605	0.038
C5_HpGe_A	130	0.972	0.058
C5_HpGe_B	130	1.017	0.061
C5_HpGe_C	140	0.697	0.042
C5_HpGe_D	140	0.994	0.060
C6_HpGe_A	130	not functioning	not functioning
C6_HpGe_B	130	0.631	0.039
C6_HpGe_C	140	0.738	0.045
C6_HpGe_D	140	0.639	0.040
C7_HpGe_A	130	0.968	0.058
C7_HpGe_B	130	0.742	0.045
C7_HpGe_C	140	0.778	0.050
C7_HpGe_D	140	1.101	0.066
C8_HpGe_A	90	1.110	0.067
C8_HpGe_B	90	0.897	0.054
C8_HpGe_C	90	0.641	0.039
C8_HpGe_D	90	0.652	0.039

Table B.15: Measured differential cross-section values(6.129 MeV) for each high purity germanium crystals for the 66 MeV proton collision on mylar target

Crystal	Angle (Degree)	$\frac{d\sigma}{d\Omega}$ (mb)	U($\frac{d\sigma}{d\Omega}$) (mb)
C1_HpGe_A	130	no peak	no peak
C1_HpGe_B	130	no peak	no peak
C1_HpGe_C	140	no peak	no peak
C1_HpGe_D	140	no peak	no peak
C2_HpGe_A	90	2.454	0.158
C2_HpGe_B	90	2.576	0.165
C2_HpGe_C	90	no peak	no peak
C2_HpGe_D	90	no peak	no peak
C3_HpGe_A	90	no peak	no peak
C3_HpGe_B	90	insufficient data	insufficient data
C3_HpGe_C	90	1.982	0.129
C3_HpGe_D	90	no peak	no peak
C4_HpGe_A	90	no peak	no peak
C4_HpGe_B	90	no peak	no peak
C4_HpGe_C	90	2.585	0.167
C4_HpGe_D	90	no peak	no peak
C5_HpGe_A	130	no peak	no peak
C5_HpGe_B	130	no peak	no peak
C5_HpGe_C	140	no peak	no peak
C5_HpGe_D	140	no peak	no peak
C6_HpGe_A	130	not functioning	not functioning
C6_HpGe_B	130	2.195	0.143
C6_HpGe_C	140	2.308	0.148
C6_HpGe_D	140	2.194	0.142
C7_HpGe_A	130	2.060	0.132
C7_HpGe_B	130	1.919	0.123
C7_HpGe_C	140	no peak	no peak
C7_HpGe_D	140	1.783	0.120
C8_HpGe_A	90	no peak	no peak
C8_HpGe_B	90	no peak	no peak
C8_HpGe_C	90	1.880	0.124
C8_HpGe_D	90	no peak	no peak

Table B.16: Measured differential cross-section values(6.129 MeV) for each high purity germanium crystals for the 80 MeV proton collision on mylar target

Crystal	Angle (Degree)	$\frac{d\sigma}{d\Omega}$ (mb)	U($\frac{d\sigma}{d\Omega}$) (mb)
C1_HpGe_A	130	no peak	no peak
C1_HpGe_B	130	no peak	no peak
C1_HpGe_C	140	no peak	no peak
C1_HpGe_D	140	no peak	no peak
C2_HpGe_A	90	2.110	0.139
C2_HpGe_B	90	2.362	0.155
C2_HpGe_C	90	no peak	no peak
C2_HpGe_D	90	no peak	no peak
C3_HpGe_A	90	no peak	no peak
C3_HpGe_B	90	insufficient data	insufficient data
C3_HpGe_C	90	1.695	0.115
C3_HpGe_D	90	no peak	no peak
C4_HpGe_A	90	no peak	no peak
C4_HpGe_B	90	no peak	no peak
C4_HpGe_C	90	2.104	0.141
C4_HpGe_D	90	no peak	no peak
C5_HpGe_A	130	no peak	no peak
C5_HpGe_B	130	no peak	no peak
C5_HpGe_C	140	no peak	no peak
C5_HpGe_D	140	no peak	no peak
C6_HpGe_A	130	not functioning	not functioning
C6_HpGe_B	130	1.780	0.128
C6_HpGe_C	140	1.785	0.117
C6_HpGe_D	140	1.756	0.118
C7_HpGe_A	130	1.661	0.110
C7_HpGe_B	130	1.515	0.101
C7_HpGe_C	140	no peak	no peak
C7_HpGe_D	140	1.606	0.109
C8_HpGe_A	90	no peak	no peak
C8_HpGe_B	90	no peak	no peak
C8_HpGe_C	90	1.700	0.114
C8_HpGe_D	90	no peak	no peak

Table B.17: Measured differential cross-section values(6.129 MeV) for each high purity germanium crystals for the 95 MeV proton collision on mylar target

Crystal	Angle (Degree)	$\frac{d\sigma}{d\Omega}$ (mb)	U($\frac{d\sigma}{d\Omega}$) (mb)
C1_HpGe_A	130	no peak	no peak
C1_HpGe_B	130	no peak	no peak
C1_HpGe_C	140	no peak	no peak
C1_HpGe_D	140	no peak	no peak
C2_HpGe_A	90	1.643	0.110
C2_HpGe_B	90	1.691	0.112
C2_HpGe_C	90	no peak	no peak
C2_HpGe_D	90	no peak	no peak
C3_HpGe_A	90	no peak	no peak
C3_HpGe_B	90	insufficient data	insufficient data
C3_HpGe_C	90	1.276	0.088
C3_HpGe_D	90	no peak	no peak
C4_HpGe_A	90	no peak	no peak
C4_HpGe_B	90	no peak	no peak
C4_HpGe_C	90	1.582	0.108
C4_HpGe_D	90	no peak	no peak
C5_HpGe_A	130	no peak	no peak
C5_HpGe_B	130	no peak	no peak
C5_HpGe_C	140	no peak	no peak
C5_HpGe_D	140	no peak	no peak
C6_HpGe_A	130	not functioning	not functioning
C6_HpGe_B	130	1.279	0.092
C6_HpGe_C	140	1.205	0.083
C6_HpGe_D	140	1.249	0.086
C7_HpGe_A	130	1.315	0.088
C7_HpGe_B	130	1.083	0.073
C7_HpGe_C	140	no peak	no peak
C7_HpGe_D	140	1.132	0.081
C8_HpGe_A	90	no peak	no peak
C8_HpGe_B	90	no peak	no peak
C8_HpGe_C	90	1.331	0.091
C8_HpGe_D	90	no peak	no peak

Table B.18: Measured differential cross-section values(6.129 MeV) for each high purity germanium crystals for the 110 MeV proton collision on mylar target

Crystal	Angle (Degree)	$\frac{d\sigma}{d\Omega}$ (mb)	U($\frac{d\sigma}{d\Omega}$) (mb)
C1_HpGe_A	130	no peak	no peak
C1_HpGe_B	130	no peak	no peak
C1_HpGe_C	140	no peak	no peak
C1_HpGe_D	140	no peak	no peak
C2_HpGe_A	90	1.288	0.090
C2_HpGe_B	90	1.268	0.089
C2_HpGe_C	90	no peak	no peak
C2_HpGe_D	90	no peak	no peak
C3_HpGe_A	90	no peak	no peak
C3_HpGe_B	90	insufficient data	insufficient data
C3_HpGe_C	90	1.052	0.079
C3_HpGe_D	90	no peak	no peak
C4_HpGe_A	90	no peak	no peak
C4_HpGe_B	90	no peak	no peak
C4_HpGe_C	90	1.245	0.092
C4_HpGe_D	90	no peak	no peak
C5_HpGe_A	130	no peak	no peak
C5_HpGe_B	130	no peak	no peak
C5_HpGe_C	140	no peak	no peak
C5_HpGe_D	140	no peak	no peak
C6_HpGe_A	130	not functioning	not functioning
C6_HpGe_B	130	1.053	0.084
C6_HpGe_C	140	1.069	0.076
C6_HpGe_D	140	0.979	0.071
C7_HpGe_A	130	0.917	0.066
C7_HpGe_B	130	0.914	0.068
C7_HpGe_C	140	no peak	no peak
C7_HpGe_D	140	0.837	0.064
C8_HpGe_A	90	no peak	no peak
C8_HpGe_B	90	no peak	no peak
C8_HpGe_C	90	0.961	0.069
C8_HpGe_D	90	no peak	no peak

Table B.19: Measured differential cross-section values(6.129 MeV) for each high purity germanium crystals for the 125 MeV proton collision on mylar target

Crystal	Angle (Degree)	$\frac{d\sigma}{d\Omega}$ (mb)	U($\frac{d\sigma}{d\Omega}$) (mb)
C1_HpGe_A	130	no peak	no peak
C1_HpGe_B	130	no peak	no peak
C1_HpGe_C	140	no peak	no peak
C1_HpGe_D	140	no peak	no peak
C2_HpGe_A	90	1.138	0.082
C2_HpGe_B	90	1.380	0.097
C2_HpGe_C	90	no peak	no peak
C2_HpGe_D	90	no peak	no peak
C3_HpGe_A	90	no peak	no peak
C3_HpGe_B	90	insufficient data	insufficient data
C3_HpGe_C	90	1.080	0.080
C3_HpGe_D	90	no peak	no peak
C4_HpGe_A	90	no peak	no peak
C4_HpGe_B	90	no peak	no peak
C4_HpGe_C	90	1.147	0.084
C4_HpGe_D	90	no peak	no peak
C5_HpGe_A	130	no peak	no peak
C5_HpGe_B	130	no peak	no peak
C5_HpGe_C	140	no peak	no peak
C5_HpGe_D	140	no peak	no peak
C6_HpGe_A	130	not functioning	not functioning
C6_HpGe_B	130	0.992	0.078
C6_HpGe_C	140	0.775	0.060
C6_HpGe_D	140	0.809	0.062
C7_HpGe_A	130	0.865	0.063
C7_HpGe_B	130	0.892	0.069
C7_HpGe_C	140	no peak	no peak
C7_HpGe_D	140	0.868	0.065
C8_HpGe_A	90	no peak	no peak
C8_HpGe_B	90	no peak	no peak
C8_HpGe_C	90	0.943	0.066
C8_HpGe_D	90	no peak	no peak